COO/1198-1279

MASTER

UNIVERSITY OF ILLINOIS AT URBANA-CHAMPAIGN

THE GRADUATE COLLEGE

WE HEREBY RECOMMEND THAT THE THESIS BY

NESTOR JOHN ZALUZEC

ENTITLED AN ANALYTICAL ELECTRON MICROSCOPE STUDY OF THE OMEGA PHASE TRANSFORMATION IN A ZIRCONIUM-NIOBIUM ALLOY

BE ACCEPTED IN PARTIAL FULFILLMENT OF THE REQUIREMENTS FOR THE DEGREE OF DOCTOR OF PHILOSOPHY

Director of Thesis Research

Head of Department

Committee on Final Examination†

Chairman

† Required for doctor's degree but not for master's.

0-317

DISCLAIMER

THIS PAGE

WAS INTENTIONALLY

LEFT BLANK

ACKNOWLEDGMENTS

The author wishes to express a sincere thanks to his advisor, Professor Hamish L. Fraser, for his enthusiasm, constant support, and guidance during this research, and even more so for the friendship which has grown between them. A special note of gratitude is extended to John B. Woodhouse and Ian D. Ward for their invaluable assistance in developing and modifying the instrumentation used during this work, to Professor Harry E. Cook whose lectures and many beneficial discussions on phase transformations influenced this study, and to Peggy Mochel for her help in assembly language programming. To his fellow graduate students, particularly Robert D. Trohsdrun Field, the author wishes to acknowledge many hours of valuable assistance and to Frances Scarboro and the Radiation Effects and Microstructural Analysis Group at the Oak Ridge National Laboratory for their contribution to the preparation of this thesis. Finally, a special thanks to the author's family and friends for their continued patience, understanding and help over the years, and to his wife, Karen, and sons, Christiaan and Nicholaus, whose love makes it all worthwhile.

This research project was supported by the Department of Metallurgy and Mining Engineering and the Materials Research Laboratory at the University of Illinois at Urbana-Champaign under Energy Research and Development contract ERDA(11-1)-1198.

TABLE OF CONTENTS

Page

INTRODUCTION

When alloys of the group IV-B elements Ti, Zr, and Hf and other transition metals, most notably V, Nb, Cr, Mo, and Fe, are quenched from the high-temperature bcc solid solution, the formation of the equilibrium hcp alpha (α) phase is often partially or completely suppressed. Instead, a metastable phase, termed omega (ω) is formed. Two different types of ω structures have been identified: first, there is reversible athermal transformation which is thought to be a diffusionless displacement controlled reaction; and second, that which develops only upon isothermal aging. Initially, interest in this transformation was generated from the observed embrittlement effects and enhancement of superconducting properties accompanying the precipitation of ω. However, the more recent interest in the athermal transformation stems from the inherent mechanical instabilities of the bcc lattice and its relationship to the bcc-hcp transition. Furthermore, it has been suggested that the ω-like fluctuations serve as precursors to some bcc martensitic transformations. Over the last twenty years several experimental and theoretical studies have been undertaken in an attempt to determine the precise nature of the athermal transformation. The research presented here was initiated in order to test one of those theories.

During the course of this study, several techniques of microstructural analysis were developed, refined, and standardized. Grouped under the general classification of *Analytical Electron Microscopy* they provide the experimentalist with a unique tool for the microcharacterization of solids, allowing semiquantitative to quantitative analyses of

the morphology, crystallography, elemental composition, and electronic structure of regions as small as 20 Å in diameter. As these tools were still in their infancy when this work was initiated, it was necessary to spend considerable time and effort in developing these methods into state-of-the-art analytical techniques, and this work comprises a major portion of the research described herein. The microanalytical techniques employed during this study include: energy dispersive x-ray spectroscopy (EDS) using both conventional and scanning transmission electron micrsocopy (CTEM, STEM), transmission scanning electron diffraction (TSED), the stationary diffraction pattern technique, and electron energy loss spectroscopy (ELS) using a dedicated scanning transmission electron microscope (DSTEM).

CHAPTER 1

1. GENERAL PROPERTIES OF THE OMEGA PHASE IN ZIRCONIUM-NIOBIUM

1.1 Background

A partial phase diagram for the Zr-Nb system is shown in Fig. 1. At high temperatures there is a continuous series of bcc solid solutions (β) from pure zirconium to pure niobium. On the niobium-rich side of the diagram above the eutectoid temperature there is a miscibility gap extending from 17.5 to approximately 85% Nb. The terminal zirconium-rich solid solution (α) phase is hexagonal, but for alloys of less than 7% Nb the hcp phase is replaced by a martensitic form (α') of α. On quenching the higher niobium concentration alloys from the bcc solid solution, the α and α' transformations can be partially or completely suppressed and a bcc phase can be retained. This solid solution then decomposes into a metastable structure called the omega (ω) phase. The transition temperature (T_ω) for this transformation[1] is also shown in Fig. 2.

Early studies using x-ray diffraction techniques have shown that ω is an hexagonal phase with the following orientation relationships[2–4] to the parent bcc matrix:

$$[0001]_\omega \parallel [111]_\beta \qquad \text{and} \qquad [11\bar{2}0]_\omega \parallel [110]_\beta$$

The unit cell can be indexed hexagonally with three atoms at the positions (000) and $\pm\left(\frac{1}{3}, \frac{2}{3}, \frac{1}{3} + u\right)$. Here u is the displacement necessary

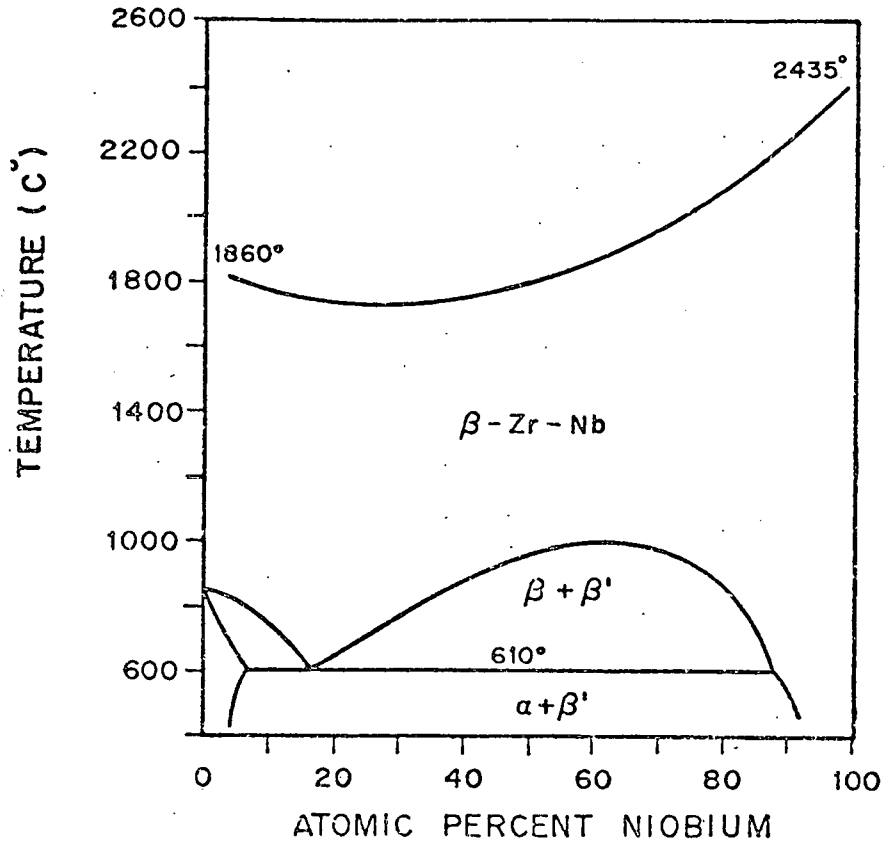

Fig. 1. Phase Diagram for the Zirconium-Niobium System.

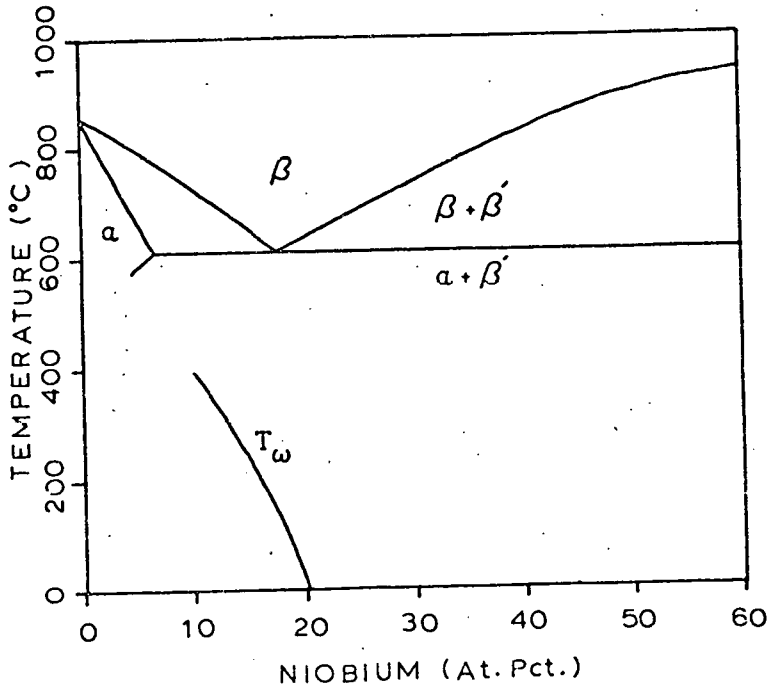

Fig. 2. Partial Phase Diagram for the Zr-Nb System Showing the Omega Phase Transformation Temperature (T_ω).

along a <111> direction to convert the bcc (u=0) to the hexagonal lattice $\left(u = \frac{1}{6}\right)$. Figure 3 is a sketch of a {110} section of a bcc lattice illustrating the relationship between ω and β. From this figure, one can see that the rearrangement necessary to convert β to ω involves only the collapse of two adjacent {111} planes while the third plane remains fixed. Since there are four equivalent <111> directions in bcc, four different variants of ω can develop.[4] Two forms of ω have been reported: (1) the athermal transformation which occurs by a diffusionless structural change of the bcc lattice, and (2) the aged formed by annealing specimens containing either the athermal or as-quenched bcc phases at temperatures between 200–400°C.

Using transmission electron microscopy, studies of the fully aged omega phase in Zr-Nb[5] and Ti-Nb[6] systems have shown that this phase consists of incoherent precipitates lying on {111} planes of the retained β phase. All four variants were seen to develop equally in both systems; however, the morphology of the precipitate shape varied with alloy system. In Zr-Nb, the precipitates were in the form of platelets ∿1000 Å in diameter and ∿200 Å thick, while in Ti-Nb ellipsoidal particles (∿1300 Å long and 500 Å in diameter), with the major axis parallel to $[0001]_\omega = [111]_\beta$, were observed.

The athermal transformation in alloys of Zr-Nb, Ti-Nb, and Ti-V has been under investigation for a number of years by Sass and his coworkers.[7–13] From their dark-field TEM observations they concluded that the morphology of the as-quenched athermal ω consists of 10–15 Å diameter

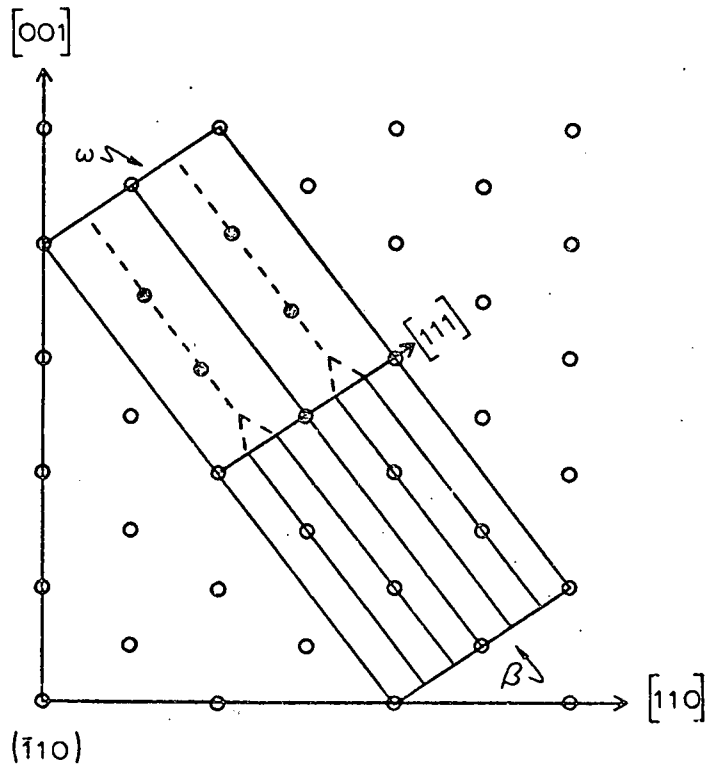

Fig. 3. Schematic Diagram Illustrating the Crystallographic Relationship between the β and ω Phases in an $(\bar{1}10)$ Plane.

particles spaced 15–25 Å apart arranged in rows along the <111> directions of the bcc lattice. Furthermore, these rows tended to cluster into different domains, the domain size and number of particles/row decreasing with increasing solute content.

The results of diffraction experiments are summarized in Fig. 4, where a sketch of a typical {110} electron diffraction pattern (x-ray and neutron diffraction display similar characteristics) with reflections corresponding to a single [111] ω variant is shown. Two types of reflections are observed: (1) sharp diffraction spots which are common to both the bcc and ω structures (solid circles in Fig. 4), and (2) reflections due only to the presence of the ω phase, hereafter referred to as the ω reflections. Above and immediately below the transition temperature (T_ω) these ω reflections appear as diffuse peaks elongated perpendicular to the [111] direction. These peaks are also offset from the ideal hexagonal ω position (k_ω), the displacement (Δk) being away from the bcc matrix reflections along the [111] direction. Upon cooling the sample below the transformation temperature, these peaks shift toward their ideal positions and corresponding increases in intensity and sharpness have been observed.[14]

Using neutron diffraction, Moss et al.[15] have observed diffuse peaks at the ω positions at temperatures of 1000°C ($\sim$975° above T_ω). Their measurements indicated the existence of a strong elastic component in the diffuse ω peaks; this result led them to conclude that a quasi-static ω-like particle exists even in the bcc solid solution. They also pointed out that the displacements of the diffuse ω peaks

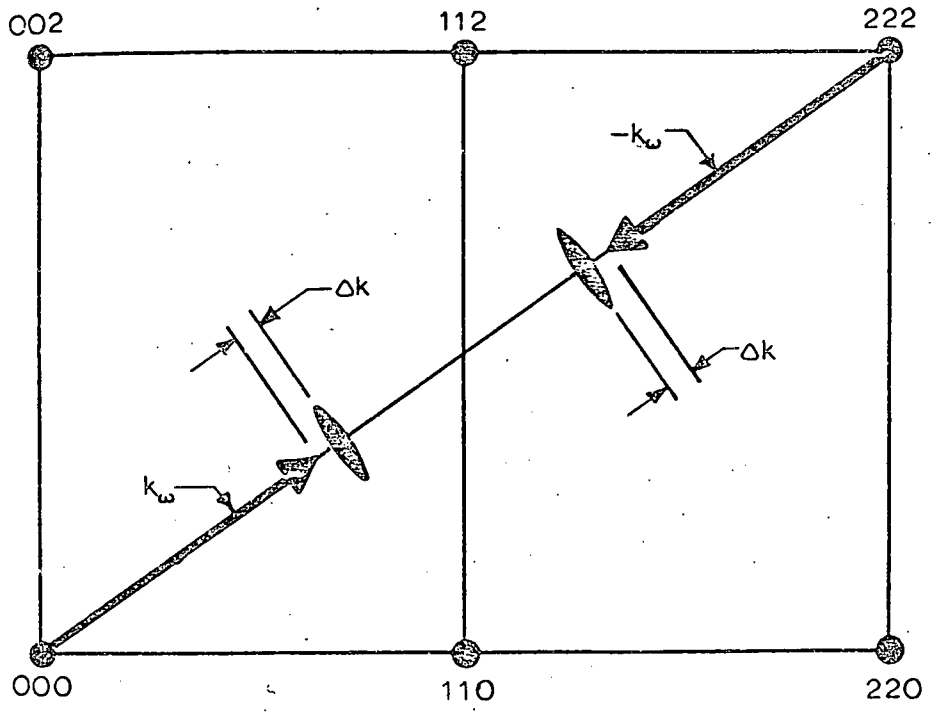

Fig. 4. Schematic Diagram of a {110} Electron Diffraction Pattern of a Sample Containing Both the β and ω Phases. Only one <111> ω variant is shown for clarity.

observed are near a point in k-space (k_m) which is a minimum in the phonon dispersion curves of the pure bcc transition metals, such as niobium, the suggestion being that lattice vibrations play an important role in determining the nature of the transformation.

Batterman et al.[16] confirmed the existence of elastic scattering at the ω positions using a Mossbauer scattering technique. In addition they also detected an inelastically scattered peak which was revealed by the higher (energy) resolution of this technique compared to neutron scattering (10^{-8} versus 10^{-5} eV). They were able to show that the inelastic scattering was not merely thermal diffuse scattering (TDS) but was inherently related to the ω producing phenomenon. In an extension of this study Lin et al.[17] determined that in alloys of Zr-Nb the elastic scattering is peaked at the positions which corresponded to the offset ω reflections (k_m) while the inelastic scattering was always centered at the exact hexagonal positions (k_ω). This implies that not only are quasi-static, particle-like distributions present but also that dynamical (time-dependent) fluctuations exist in the bcc lattice.

1.2 Models of the Omega Transformation

The first model of the ω transformation was proposed by Hatt and Roberts[4] in 1960. Based on their x-ray diffraction measurements, they suggested that the transformation was accomplished by gliding {112} planes along $\langle 111 \rangle_\beta$ directions in a cooperative manner. Figure 5 is a sketch of the $(110)_\beta$ plane of the bcc structure showing the {112} packing sequence of six planes (labeled 1,2,3,4,5,6,1,2,3,-----). The

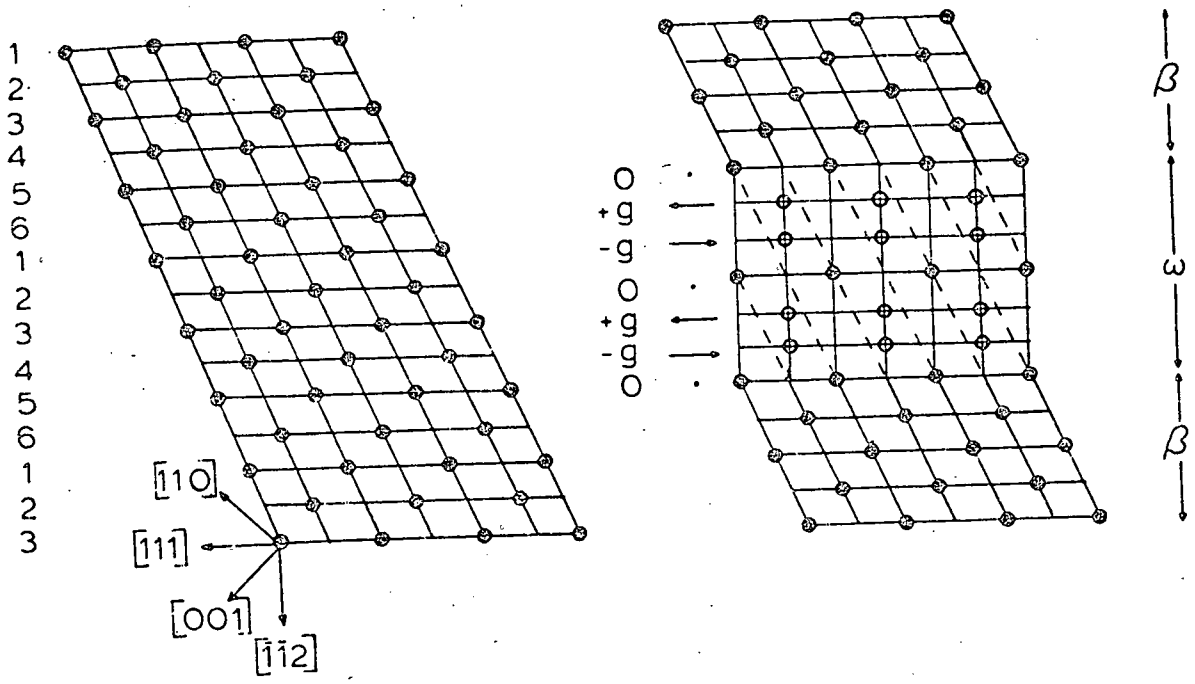

Fig. 5. Glide Sequence Proposed by Hatt and Roberts for the Formation of the ω Phase.

ω structure can be obtained by gliding specific pairs of {112} planes in the [111] and $[\bar{1}\bar{1}\bar{1}]$ directions alternately as shown in Fig. 5. The glide component g is the displacement necessary along <111> to create the ω phase and for the ideal hexagonal structure is equal to $\frac{1}{12} d_{111} = \frac{1}{6}\sqrt{\frac{3}{2}}\, a_\beta$. In the interpretation of their x-ray results they also showed that the ω morphology was rod-like with the major dimension being parallel to a <111> direction.

In 1970 deFontaine[18] formulated a geometrical description of the ω phase transformation which serves as the basis for all the current theoretical treatments. In this description a $\frac{2}{3}$ <111> longitudinal displacement wave (or equivalently a $\frac{1}{3}$ <112> transverse wave) modulates the bcc lattice by causing a collapse of {111} planes as illustrated in Fig. 6. The amplitude of the displacement wave necessary to produce the $\beta \rightarrow \omega$ transformation is a/6 ($\sim$0.5 Å). This description has the advantage that it lends itself readily to a lattice dynamics interpretation of the phase transformation.

In the same paper deFontaine[18] outlined a theory explaining why such an interplanar collapse model was feasible. Expressing the elastic free energy of the bcc solid solution in a harmonic form, he demonstrated that vibrational instabilities (i.e., atomic displacement waves whose amplitude increases with time) would develop for those waves with wave vectors in the vicinity of $k_\omega \left[\frac{2}{3} <111>\right]$.

In order to arrive at these results deFontaine had to assume specific sets of atomic force constants which were obtained by using the long wavelength relations of the microscopic theory of inelasticity.[19,20]

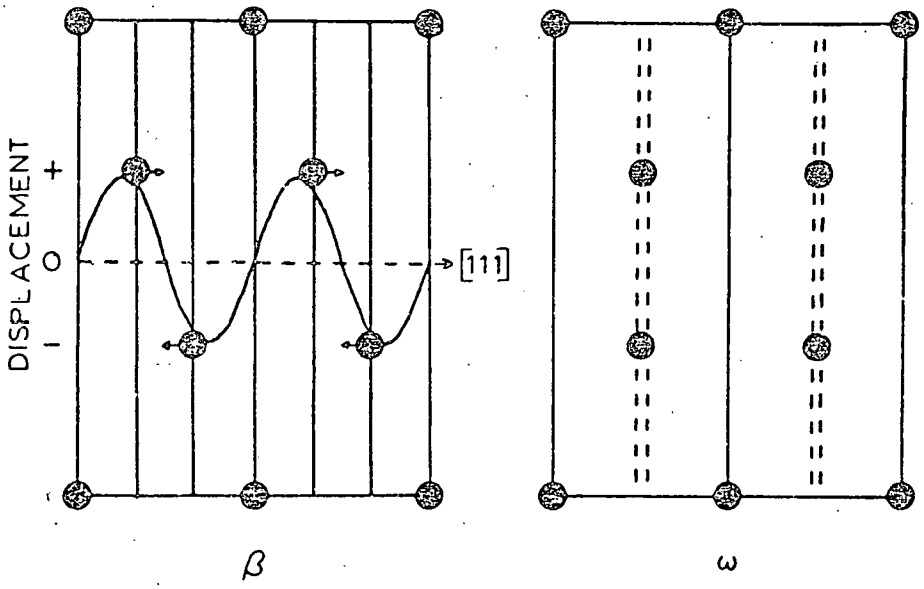

Fig. 6. DeFontaine's Displacement Wave Description for the Formation of the ω Phase.

He then showed that such combinations corresponded to a softening or vanishing of the elastic moduli C_{44} and $C' (= [C_{11} - C_{12}]/2)$. At virtually the same time Fisher and Dever[21] presented evidence showing that the magnitude of the shear modulus C' was closely related to the stability of the bcc transition metals, particularly with regard to the occurrence of martensitic and omega phase transformations. They pointed out (1) that the value of C' is related to the electron population of the d shell of the transition metals and their alloys, and (2) that the $\beta \rightarrow \alpha$ and $\beta \rightarrow \omega$ phase transformations were clearly associated with a reduction or vanishing of C'. Further work by deFontaine et al.[22] pointed out that the transformation is not in fact a lattice instability but rather a metastable state of the β structure. If the bcc structure were truly unstable, which would correspond to a vanishing of the elastic constants, then the entire crystal would transform catastrophically to ω once the transition temperature is crossed. In fact, this is never observed experimentally; instead, only localized events are observed. Using the measurements of Fisher and Dever,[21] deFontaine et al.[22] then obtained a consistent set of atomic force constants which yielded contours of low elastic energy in the k-space regions near k_ω without forcing the drastic softening of C'.

Although deFontaine's theory qualitatively explains the diffraction effects observed in ω forming alloys, three additional models have been proposed in an attempt to accurately describe the transformation mechanism. They are: (1) Vandermeulen and Deruyttere's[23] proposal where ideal ω particles are formed having faulted structures at their

ends, (2) Borie, Sass and Andreassen's[24,25] model of ordered sub-variants within a single variant, and (3) Cook's[26,27] anharmonic Landau model of first-order phase transformations. Each of these will be discussed in succession.

In a study of a Cu–16.5 at. % Sn alloy, Vandermeulen and Deruyttere[23] noted that when the high-temperature bcc phase is quenched to room temperature an ω-type transformation occurs, and electron diffraction patterns similar to those reported in titanium and zirconium alloys are observed. In order to explain the diffraction effects (i.e., shifts of the ω reflections away from k_ω) they proposed a physical model of the ω phase which consists of a periodic distribution of ideal ω-like particles separated by small faulted regions. This faulting of the ω structure is accomplished by disrupting the ω-forming displacement wave periodically by a displacement function which is incommensurate with the k_ω vibrational wave. This is shown schematically in Fig. 7. The usual ω wave which modulates the (111) planes of the bcc lattice is shown in Figs. 7(a) and (b). If the displacement wave is interrupted by the insertion of a displacement function with wavelength $\frac{1}{3} k_\omega$ $\left(\text{or } \frac{2}{3} k_\omega\right)$, the structure of Fig. 7(c) and (d) [7(e) and (f)] is obtained. These two incommensurate displacement functions are essentially faults in the ω structure and are designated as type 1 $\left(k = \frac{1}{3} k_\omega\right)$ and type 2 $\left(k = \frac{2}{3} k_\omega\right)$ faults, respectively. If one assumes that these faults occur in a periodic manner throughout the crystal, then it is possible to calculate the effects on an electron diffraction pattern. The results of such a

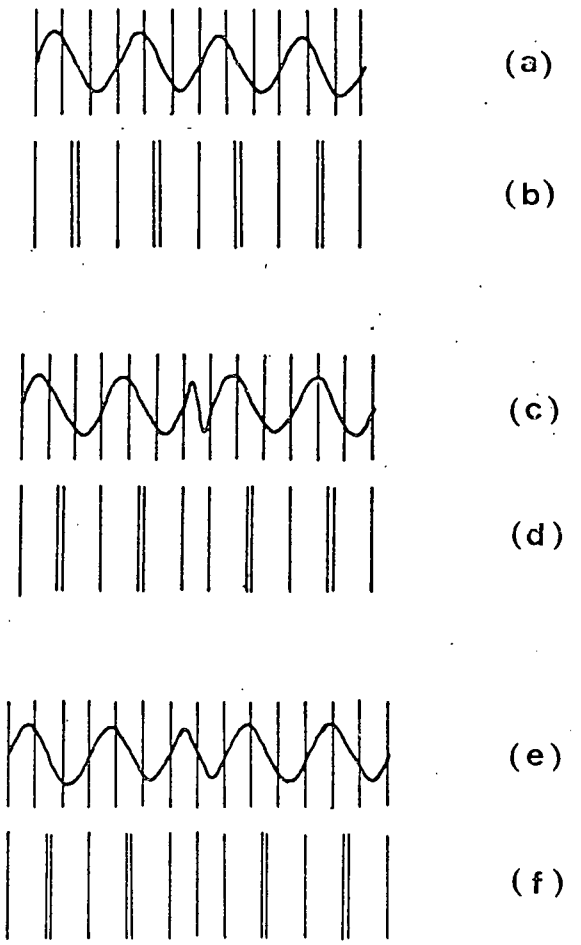

Fig. 7. Vandermeulen and Deruyttere's[23] Model for the Formation of a Faulted Omega Structure.

calculation of the diffracted intensity for a type 2 fault is illustrated in Fig. 8, where the diffracted intensity along a <111> direction is plotted for regions about the $[0001]_\omega$, $[0002]_\omega$, and $[0003]_\omega \equiv [222]_\beta$ reciprocal lattice points. Although the model does correctly predict a shift of the $[0001]_\omega$ and $[0002]_\omega$ reflections away from the ideal k_ω positions, it also unambiguously predicts the development of satellite peaks off these shifted reflections. In the electron diffraction patterns presented in their work no such satellite intensity is apparent nor to date have such observations been reported in the literature. In addition, Vanderneulen and Deruyttere fail to explain the mechanism of the formation of such faults and their required periodicity.

In a similar attempt to explain the diffraction patterns observed from the athermal ω, Borie et al.[24,25] have proposed another purely geometrically based model of ω. Their analysis was based on two assumptions: (1) the entire sample transforms into the ω phase (which as pointed out previously has never been achieved experimentally), and (2) within a single <111> variant of ω a preferential ordering of subvariants occurs. The possibility of the existence of subvariants can be easily demonstrated by the drawing in Fig. 9. Shown here is the ABC packing sequence of {111} planes in bcc materials. Clearly there are three equivalent ways in which a given <111> variant of ω can form – that is, the unshifted bcc plane can be either A, B, or C and the feasibility of subvariants is apparent. Calculations of diffuse intensity by Borie et al. showed that if a preferred order of subvariants occurs along the $[0001]_\omega = [111]_\beta$ direction then shifts of the ω reflections as experimentally

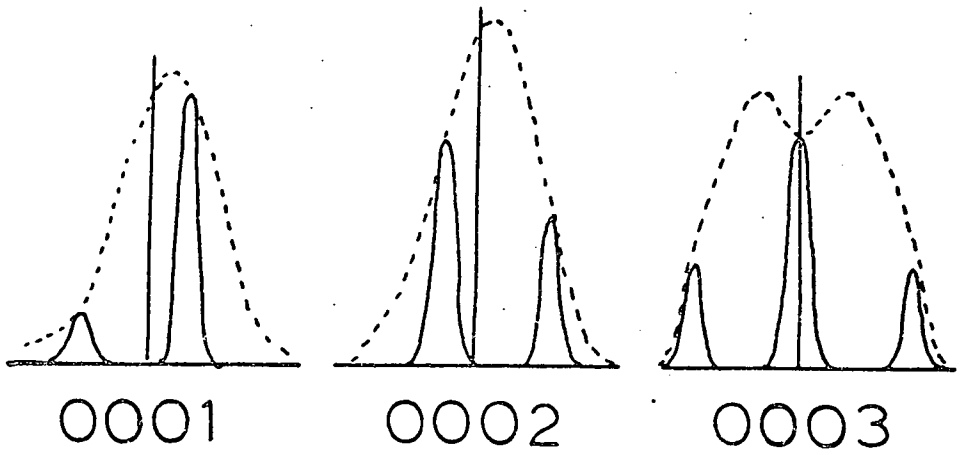

Fig. 8. Calculated Diffraction Intensity Along $\langle 222 \rangle_\beta$ Direction in an {011} Reciprocal Lattice Plane after Vandermeulen and Deruyttere.[23]

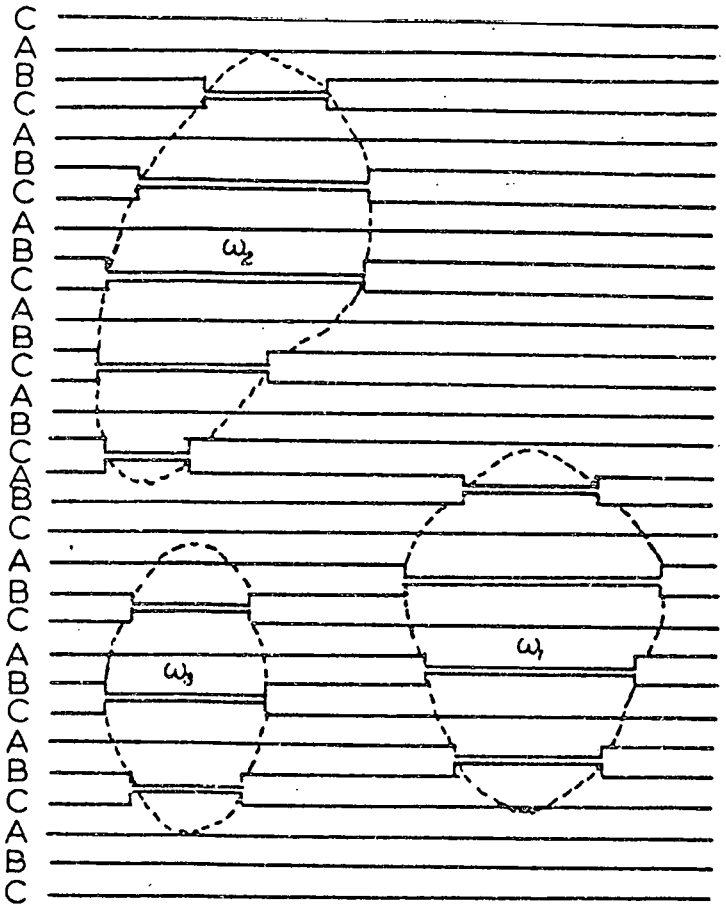

Fig. 9. Formation of Subvariants in the ω to β Transformation after Borie et al.[24]

observed can be obtained. The ordering sequence of subvariants necessary to produce this effect is as follows: ω_1, ω_3, ω_2, ... Here an ω_1 subvariant corresponds to the subvariant formed by fixing the A plane and allowing the B and C planes to collapse; likewise the ω_2 and ω_3 subvariants correspond to the B and C planes remaining fixed, respectively. Recently, using a high-resolution lattice imaging technique, Chang, Krakow and Sass[13] have observed the existence of subvariants within a single $[111]_\omega$ variant; however, they were not able to show the existence of any ordering between subvariants. Although such a purely crystallographic solution to the diffuse intensity problem is valid, it is not unique nor, as with the model of Vandermeulen and Deruyttere, have arguments been presented to justify the existence of such an ordering phenomenon.

In a series of papers published from 1973 through 1975 Cook[26–29] has presented one of the most unified explanations of the ω phase transformation. Beginning with thermodynamic principles he accounts not only for the observed experimental details but also presents a mechanism by which the transformation can develop. For brevity's sake an earlier one-dimensional anharmonic planar lattice model[27] will be outlined instead of the three-dimensional formalism presented in his more recent publication.[29]

Of significant importance to the understanding of any phase change in materials is the nature of the transformation – namely, is it of first or second order? Based on symmetry arguments and the Landau criterion for the nature of phase transitions, Cook points out that the

ω transformation cannot be of second order. The arguments supporting this assertion are that in the Landau formalism the free energy of the system and hence the structure of the lattice must be symmetric with respect to interchange of the order parameter (η) from positive to negative values (Fig. 10). The order parameter is a means of indicating the degree of completion of the transformation and for the case of omega η can be related to the amount of collapse of the {111} planes of the bcc phase; when $\eta = 1$ the ω structure is obtained. deFontaines' displacement wave model is readily adapted to this treatment by allowing the amplitude of the displacement wave (hence the degree of collapse) to be governed by the modified expression

$$u_{<111>} = \eta \frac{a}{6} \sin (k_\omega \cdot x) \quad . \quad (1.1)$$

One can see from Fig. 11 that the structure obtained by modulating the bcc lattice using a positive η (omega) versus negative η (anti-omega), is clearly different and hence the transformation cannot be of second order.

As in any change of state the most stable structure is that which minimizes the free energy of the system. For the case of ω, the change in free energy (ΔF) in going from the β to ω phases can be written in the form

$$\Delta F = \frac{1}{2!} \phi_{ij} u_i u_j + \frac{1}{3!} \phi_{ijk} u_i u_j u_k + \frac{1}{4!} \phi_{ijkl} \cdots \quad (1.2)$$

where u_i represents the displacement away from the bcc configuration and ϕ_{ij}'s are the isothermal coupling parameters (or force constants)

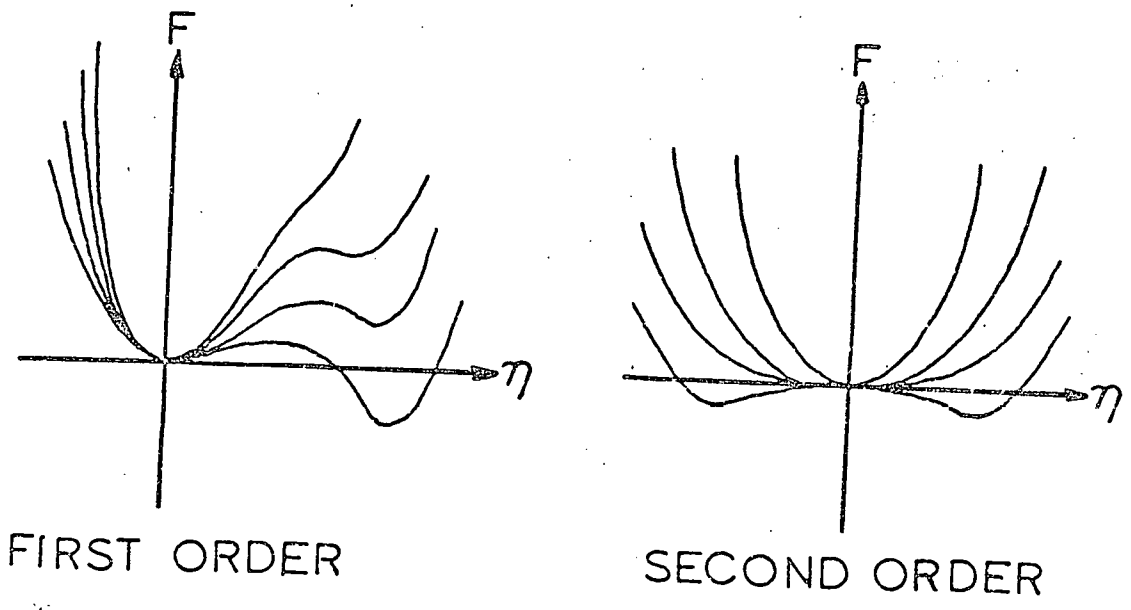

Fig. 10. Free Energy as a Function of Order Parameter for a First- and Second-Order Phase Transformation.

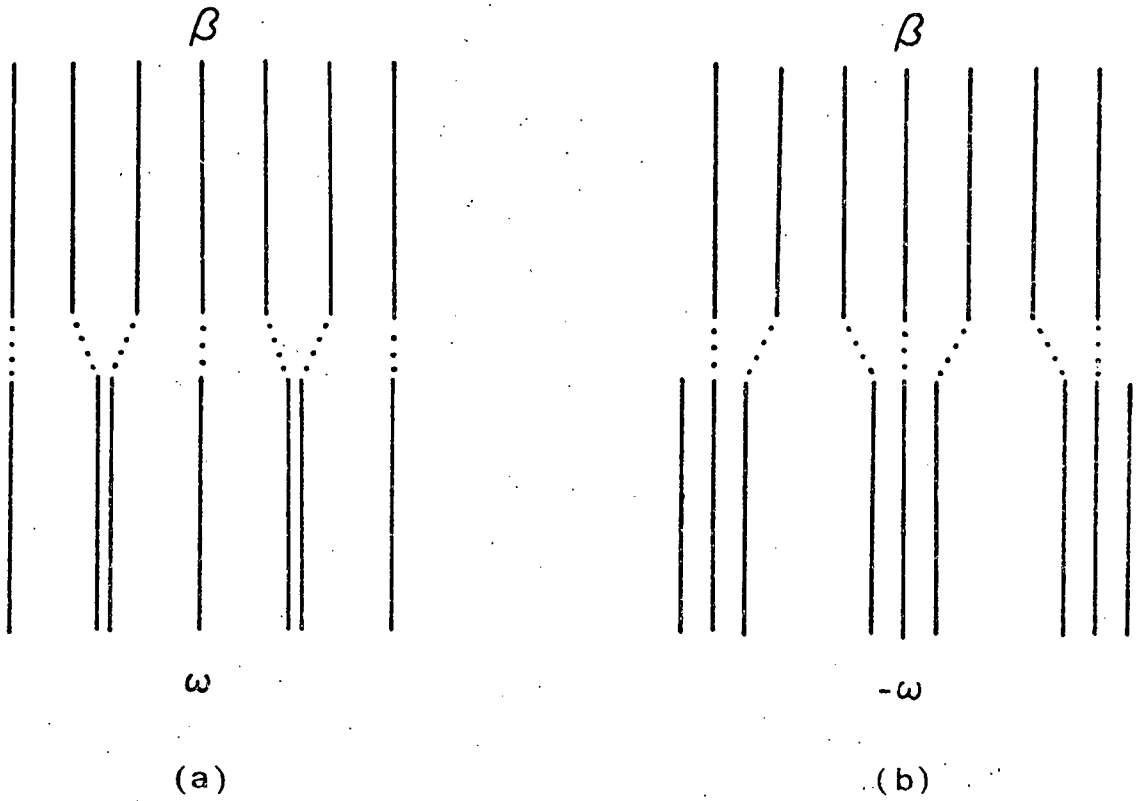

Fig. 11. Formation of ω (a) and Anti-ω (b) Regions Illustrating the First-Order Nature of the ω Transformation.

which describe the response of the system to this displacement. Since deFontaine's model already specifies the displacement field, it remains only to determine the values of the coupling parameters in order to calculate the relative stability of a given configuration.

Values of the ϕ_{ij}'s are obtained indirectly usually by fitting theoretical calculations of the response of harmonic or anharmonic crystals to a vibrational wave (i.e., phonon dispersion curves). The results[27] obtained by fitting the Fourier transform Φ (k) of the second-order force constants (ϕ_{ij}) to the square of the longitudinal phonon dispersion curve along a [111] direction in k-space are shown in Fig. 12. As was pointed out by Moss et al.[15] a relative minimum occurs in the Φ (k) curve for the bcc transition metals, at a wave vector k_m which is just greater than the ideal ω forming wave k_ω. Cook was able to show that, as a consequence of this, a displacement wave in the vicinity of T_ω can actually lower its energy by shifting its wave vector to k_m, rather than remain at k_ω (Fig. 13), the ideal ω-forming wave.

This shift of wave vector to k_m has a pronounced effect on the predicted microstructure of ω; no longer is the crystal subject to a displacement function which is in perfect registry with the lattice but rather to a wave which ultimately creates a modulated structure alternating between the β and ω phases. This can be seen by considering the effects of an ω-like wave,

$$u_{<111>} = \eta \frac{a}{6} \sin[k_m \cdot x] = \eta \frac{a}{6} \sin[(k_\omega + \Delta k) \cdot x] \quad . \qquad (1.3)$$

which can be rearranged into

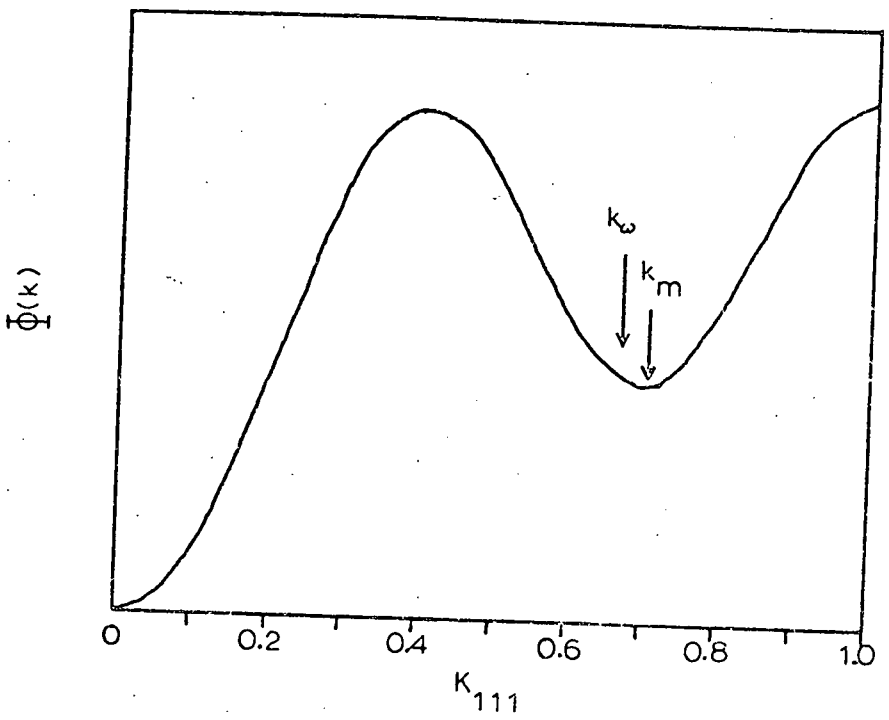

Fig. 12. Fourier Transform $\phi(k)$ of the Second-Order Force Constants after Cook.[27]

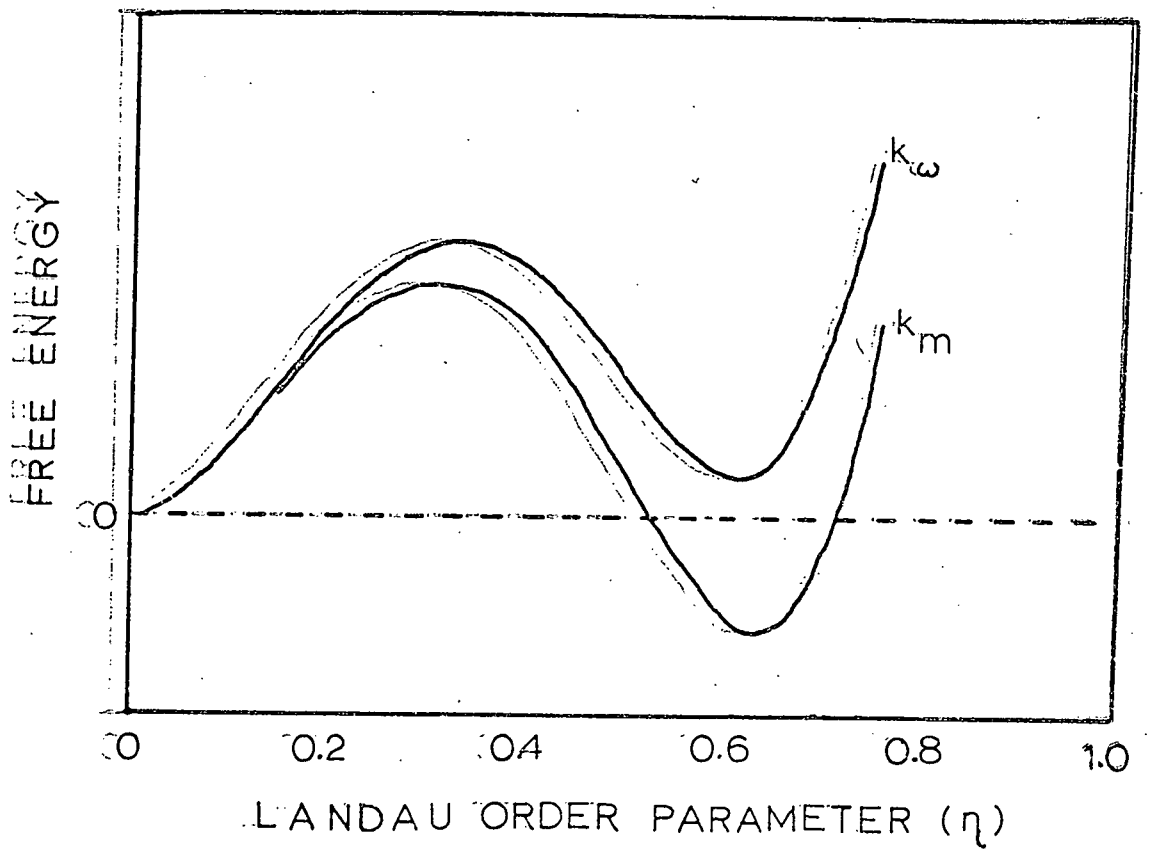

Fig. 13. Calculated Free Energy Curves for the Ideal ω-Forming Wave (k_ω) and a Shifted Wave (k_m) Corresponding to the Minimum in $\phi(k)$ after Cook.[27]

$$u_{<111>} = \eta \frac{a}{6} \{\cos(\Delta k \cdot x) \sin(k_\omega \cdot x) + \sin(\Delta k \cdot x) \sin(k_\omega \cdot x)\} . \qquad (1.4)$$

The first term of this equation yields a cosine modulated standing wave, which creates locally alternate regions of omega and anti-omega (Fig. 14). The second term peaks between the ω and anti-ω regions and represents a transitional structure between the two forms. Using this, Cook was able to outline a possible nucleation process for the β to ω reaction; this is shown graphically in Fig. 15. Above the transition temperature (T_ω) quasi-static fluctuations in the bcc lattice with wave vector k_m create alternate regions of ω and anti-ω. Both these structures are unstable relative to the bcc phase and are continually forming and decaying (Stage 1). As the temperature reaches T_ω this unstable structure splits (Stage 2), the ω-forming part becoming stabilized, and the anti-ω state decaying away rapidly. Interestingly, the formerly anti-ω region, in reverting back to the bcc state, now becomes eligible for the formation of ω as the vibrational mode "flips" in sign (Stage 3), allowing it to become ω forming. Interspaced between these regions of ω are areas in which the displacement wave has not reached the critical size for nucleation and therefore remaining, on average, bcc.

This model predicts a long-range periodic structure immediately below T_ω consisting of alternate β and ω regions, where the period of this structure is governed by the initial offset of k_m from k_ω (Δk) or about 25 Å. As the temperature drops well below T_ω, increases of the third-order anharmonic coupling parameter with respect to the harmonic force constants will begin to shift stability toward the ideal k_ω wave and

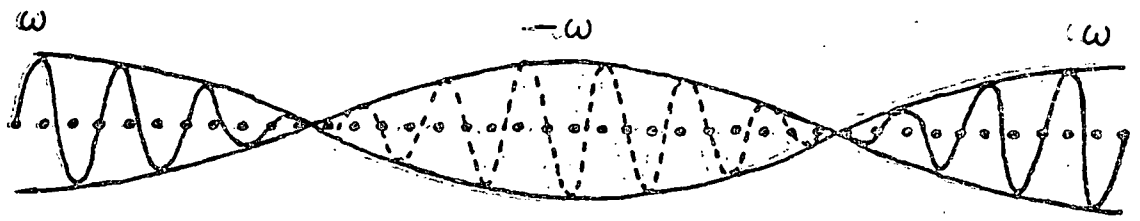

Fig. 14. Cosine-Modulated Standing Wave Creating ω and Anti-ω Regions in the β Lattice.[27]

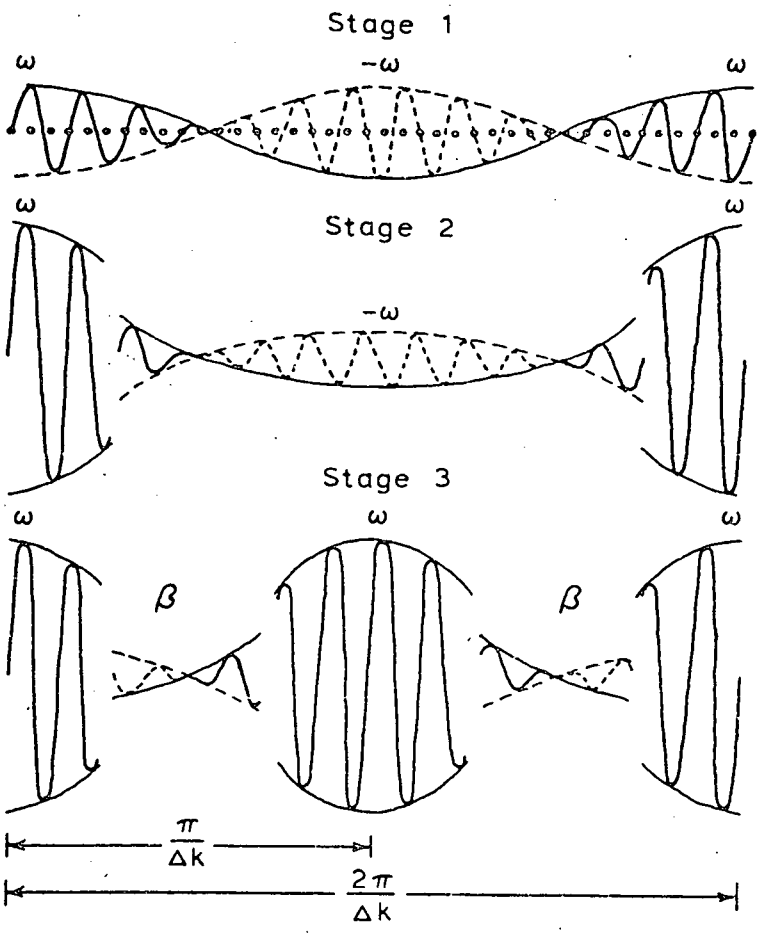

Fig. 15. Nucleation Process for a Long-Period β-ω Structure after Cook.[27]

the pure ω structure will become stable relative to the long period structure.

Using this theory, Cook was able to account for the details of the diffraction experiments discussed previously: namely, (1) the initial offset of scattering (Δk) from the ideal wave vector k_ω, (2) the pronounced diffuse streaking perpendicular to <111> directions in k space, and (3) the subsequent shift of the ω reflections toward k_ω with related increases in intensity and sharpness on cooling. In order to test the applicability of Cook's theories on this transformation, a series of *in-situ* thermal cycling experiments were proposed. If a long-period metastable ω structure develops just below T_ω, then it should be possible to detect an ordering/disordering phenomenon in an ω-forming system through *in-situ* experiments in an electron microscope.

The nature of phase transformations in most materials is usually complex, generally involving changes in structure, composition, and morphology. It is, therefore, extremely important to be able to completely characterize all the details of a particular transformation. As such, analytical electron microscopy plays an essential role, not only with respect to this study but also in essentially all fields of materials research. Thus the details of analytical techniques investigated during this research are presented in Chap. 2 and comprise a substantial portion of this thesis.

CHAPTER 2

2. ANALYTICAL ELECTRON MICROSCOPY

2.1 Introduction

Transmission Electron Microscopy (TEM) has, during the last two decades, proven itself to be an extremely powerful tool for the study of the microstructure of materials. Through the use of electron diffraction experiments it is possible to both observe and characterize a variety of crystalline defects and solid state processes and thus correlate their presence with macroscopic properties. Yet the information obtained about the specimen from such experiments represents only a fraction of that produced by the electron-solid interaction, and the products of inelastic scattering yield additional information concerning the elemental, chemical, and electronic state of the material under investigation. This information is released from the specimen in various forms – for example, the production of secondary, backscattered, and Auger electrons, or in the generation of characteristic and continuum x rays and in fact even within the transmitted electron beam which incurs characteristic energy losses during each of these processes. Analytical Electron Microscopy (AEM) is the term which is now applied to the microcharacterization of materials using as many of these electron-solid interactions as possible.

Although instrumentation has been developed over the years for materials characterization, there has been one common limitation – namely, spatial resolution. Prior to a few years ago, analytical spatial

resolution was limited to the 2 to 5 μm range. Recent advances in electron-optical design in the field of scanning transmission electron microscopy (STEM) coupled with the development of field emission electron sources, provide extremely intense and small electron probes (< 10 Å) and have allowed a quantum jump to occur in analytical sensitivity and spatial resolution. State-of-the-art instrumentation now affords the possibility of analysis of regions down to the 20 Å level depending on material, technique and instrumental factors. At the time at which this research was started AEM was in its infancy and the various analytical techniques showed great potential. This chapter describes the work done in developing, refining, and standardizing several of these techniques. In many cases, contributions (i.e., fundamental physical equations) have been collected from the literature, and these sources are appropriately referenced in the text.

2.2 X-Ray Microchemical Analysis

The interfacing of a solid-state Si(Li) energy dispersive x-ray spectrometer (EDS) to a transmission electron microscope provides a convenient means of measuring the characteristic x-ray emission (for elements of atomic number Z > 12) from microvolumes of material. By measuring the relative integrated peak intensities obtained by irradiating various regions of the sample with the electron probe, it becomes a simple matter to obtain qualitative microchemical information. The interpretation

of these data in terms of quantitative analysis requires, however, careful consideration of both experimental procedure and theoretical corrections, and is the subject of this section.

2.2.1 Theory of Quantitative X-Ray Microanalysis

Several methods of reducing measurements of characteristic x-ray emission into quantitative chemical analysis of thin samples have been developed over the last decade.[30–41] Generally, all of these procedures rely on the validity of Philibert's "thin-film" approximation which states that for a sufficiently thin specimen the effects of energy losses in the incident electron beam, electron backscattering, x-ray fluorescence (both by characteristic and continuum radiation) and x-ray absorption can be ignored. Using this approximation, one can show that for a homogeneous sample composed of the elements A and B the ratio of any two characteristic x-ray peaks $\left(\text{e.g., } I_A^{K_\alpha}/I_B^{K_\alpha}\right)$ is independent of sample thickness; it is directly proportional to the relative concentration ratio of those elements; that is:

$$\frac{I_A^{K_\alpha}}{I_B^{K_\alpha}} = \kappa_{AB} \frac{C_A}{C_B} \quad . \tag{2.1}$$

Here κ_{AB} is a constant for a given binary system, $I_A^{K_\alpha}$ the intensity of the K_α (or M_α, L_α, etc.) characteristic x-ray emission from element A and C_A the composition in weight percent of element A in the compound AB. In the past it has been the accepted procedure to consider an electron transparent specimen to be "thin" in the Philibert sense;[32] however, Jacobs and Baborovoska,[33] Zaluzec and Fraser,[42–44] and Goldstein et al.[45] have shown

that this is not generally valid. These breakdowns of the simpler analytical models range from failures of the thin film approximation, which can be accounted for theoretically, to experimental details which can only be corrected by instrumental modifications.[43,44]

The theory outlined in the following section is concerned with determining the variation with thickness of the relative intensity ratio of two characteristic x-ray lines. Since a ratio of intensities is being calculated, rigorous treatment of several parameters such as electron backscattering, transmission, and beam broadening is not required. This is due to the fact that these processes affect the generation of x rays for all elements equally. They will however be considered at the appropriate times.

The generation and subsequent emission of characteristic x rays from a material depend on the product of three terms commonly referred to in the literature as ZAF corrections. These terms describe the basic processes by which the characteristic x-ray intensity is influenced — namely the atomic number effect (Z), the absorption correction (A), and finally fluorescence (F) emission. The calculation of the atomic number correction is always necessary as it reflects the inherent efficiency of x-ray generation by electrons for various elements. The absorption correction, on the other hand, accounts for decreases in detected intensity due to the fact that x rays are absorbed in leaving the specimen and thus is directly tied to the sample thickness. Lastly, the fluorescence term deals with the probability that on absorption x rays can also simulate

characteristic emission. Clearly, if the sample becomes thin enough such that the absorption correction is small, the fluorescence term must in turn be negligible. However, the converse does not always apply. That is, it is possible to have measurable absorption effects with little or no fluorescence correction. The "thin film" approximation reduces to a calculation of the atomic number effect, which for the majority of TEM specimens becomes the principal correction. The inclusion of absorption and fluorescence becomes a specialized but important case of TEM-based microanalysis. Rigorously, the calculation of these effects should be evaluated along each electron's path within the sample. However, within the present set of experimental errors, a reasonable approximation results from an integration of these factors through the sample thickness.

2.2.2 The Atomic Number Correction

Consider a homogeneous sample of the elements A and B. The total number of K_α characteristic x rays of element A generated within the infinitesimal slab dz by electrons which have traveled a path length z within the specimen can be written as:

$$\phi_A^{K_\alpha}(z)\cdot dz = Q_A^K \cdot \frac{N_0 \bar{\rho} C_A}{w_A} \cdot \eta_{AB}(z) \cdot \omega_A^K \cdot f_A^{K_\alpha} \cdot dz \quad . \tag{2.2}$$

Here Q_A^K is the ionization cross section of the K-shell of element A; $N_0, \bar{\rho}$, C_A, and w_A are, respectively, Avagadro's number, the sample density, the concentration in fractional weight percent, and the atomic weight of A, $\eta_{AB}(z)$ the number of electrons bombarding dz, ω_A^K the K-shell x-ray fluorescence yield of A and $f_A^{K_\alpha}$ and K_α fraction of the total

K-shell emission. For the remainder of this section the discussion will consider the emission of K_α characteristic x rays; the extension of L_α or other shells can be obtained by substituting the corresponding terms for that subshell in the appropriate equations.

Various expressions have been suggested for calculating the parameters in Eq. (2.2). Most of these have resulted from considerations of quantitative x-ray analysis in bulk specimens using electron energies in the 5 to 30 keV range typically found in electron microprobes. Generally these relations were developed to obtain analysis for either the case of infinitely thick (bulk) specimens in which the electron probe stops completely, or infinitesimally thin samples and hence negligible energy loss. Although those analyses are indeed applicable to the cases considered, the question of TEM-based x-ray analysis dictates the consideration of the interaction of fast (i.e., relativistic) electrons with not thin, but rather semi-thick targets.

Several analytic expressions have been proposed in recent years as approximations to the ionization cross section for use in the atomic number correction. Generally all of these equations can be written in the form

$$Q_A^K(E_0) = \frac{\pi e^4 \cdot Z_A^K \cdot a_A^K}{E_0 \cdot E_A^K} \cdot \ell n \left\{ b_A^K \cdot \frac{E_0}{E_A^K} \right\}, \qquad (2.3)$$

which relates the probability of a K-shell ionization event $\left(Q_A^K(E_0)\right)$ to the incident electron energy (E_0), the critical excitation energy of the K-shell E_A^K of A, the number of electrons in that shell Z_A^K, and two

constants a_A^K, b_A^K which are related to the atomic structure of A. Since the calculation of the parameters a_A^K and b_A^K is non-trivial[46,47] for all elements with atomic number greater than 2, considerable discussion over the optimum choices for these constants can be found in the literature.[48–54] The most recent review of this has been given by Powell[52] for electrons in the 1 to 40 keV range.

It has been the general procedure to obtain values for these constants by fitting Eq. (2.3) to experimental measurements of Q_A^K. Although it is perfectly reasonable to obtain the values of a_A^K and b_A^K by this procedure, there is an important limitation to be considered. Thus, the empirical constants obtained using this method are only applicable over a specific energy range and for a specific element. Furthermore, Eq. (2.3) must be reconsidered for application to analytical electron microscopy since relativistic effects become important for electron energies greater than 80 keV. Thus for application to AEM, Eq. (2.3) has been reformulated as follows:

$$Q_A^K(E_0) = \frac{\pi e^4 \cdot Z_A^K \cdot a_n^K}{E_0 \cdot E_A^K} \left\{ \ell n\left(b_A^K \frac{E_0}{E_A^K} \right) - \ell n\left(1 - \beta^2\right) - \beta^2 \right\}, \qquad (2.4)$$

where

$$a_A^K = 0.35$$

$$b_A^K = \frac{0.2}{U_0 \cdot \{1 - \exp(-\gamma)\} \cdot \{1 - \exp(-\delta)\}}$$

$$U_0 = E_0/E_A^K \equiv \text{overvoltage ratio}$$

$$\delta = \frac{1}{2} \cdot E_A^K$$

$$\gamma = \frac{1250.}{\{E_A^K \cdot U_0^2\}}$$

$$\pi e^4 = 6.4924 \times 10^{-20}$$

$$\beta = \frac{v}{c} = \text{relativistic correction factor}$$

when all energies are expressed in keV, the units of $Q_A^K(E_0)$ are cm^2/atom.

The basic equation (2.4) was taken from the relativistic treatment of Mott and Massey,[48] while the functions a_A^K and b_A^K were determined analytically by fitting Eq. (2.4) to a series of measurements of Q_A^K. Figures 16, 17, and 18 compare the predictions of this equation (solid curve labeled #1) with experimental measurements of the K-shell cross section of aluminum,[53] nickel,[54] and silver.[55] Also plotted on this figure for comparison are the calculated values of Q_A^K using suggested parameters for a_A^K and b_A^K using Eq. (2.3).

The broken curve (#4) in these figures is the Mott and Massey non-relativistic Eq. (2.3) with modifications suggested by Worthington and Tomlin[49] and Burhop[50] using $a_A^K = 0.35$ and $b_A^K = \frac{4.0}{1.65 + 2.35 \cdot \exp(1 - U_0)}$ which has been applied fairly extensively for several years. From these figures one can see that this expression substantially underestimates the cross-section values at high overvoltages; however, at lower values ($1 \leq U \leq 4$) where the expression was formulated the fit is reasonable. The dashed curves (#2 and #3) are calculations based on Powell's fit to a linearized version of Eq. (2.3). Curve #2 is plotted using the constants $a_A^K = 0.9$ and $b_A^K = 0.79$ which he obtained by fitting Eq. (2.3) to measurements of aluminum. Curve #3, with coefficients $a_A^K = 1.05$ and

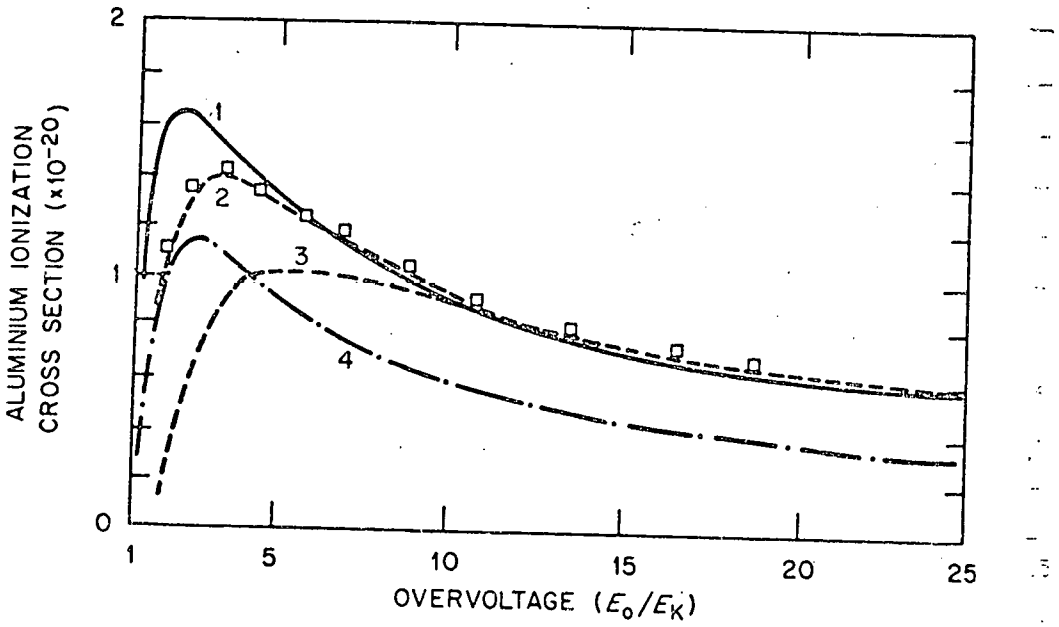

Fig. 16. Comparison of Experimental Ionization Cross Section as a Function of Overvoltage for Aluminum (squares) to Various Calculations. (1) Using Eq. (2.4); (2),(3) due to Powell; and (4) due to Mott and Massey.

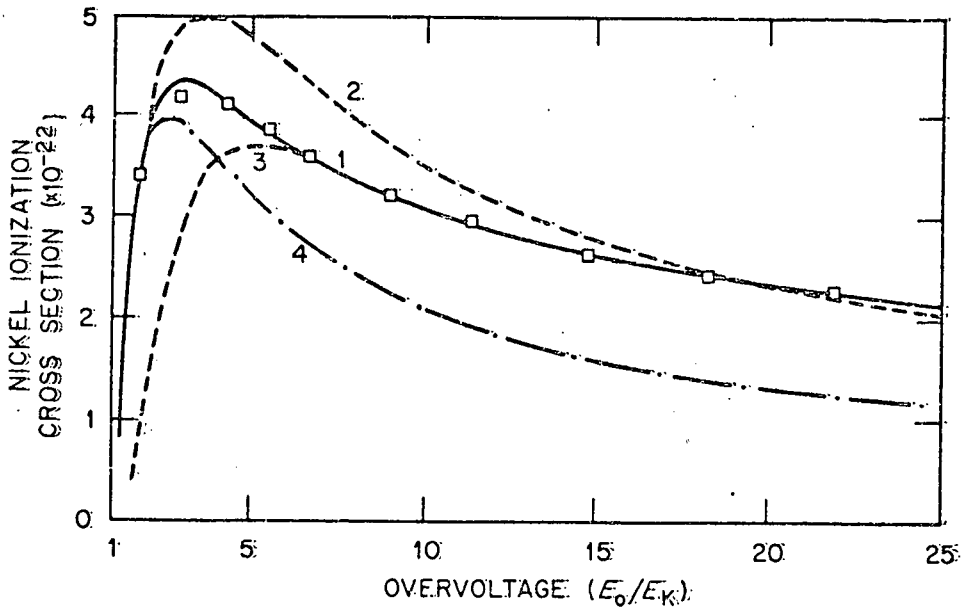

Fig. 17. Comparison of Experimental Ionization Cross Section as a Function of Overvoltage for Nickel (squares) to Various Calculations. (1) Using Eq. (2.4); (2), (3) due to Powell; and (4) due to Mott and Massey.

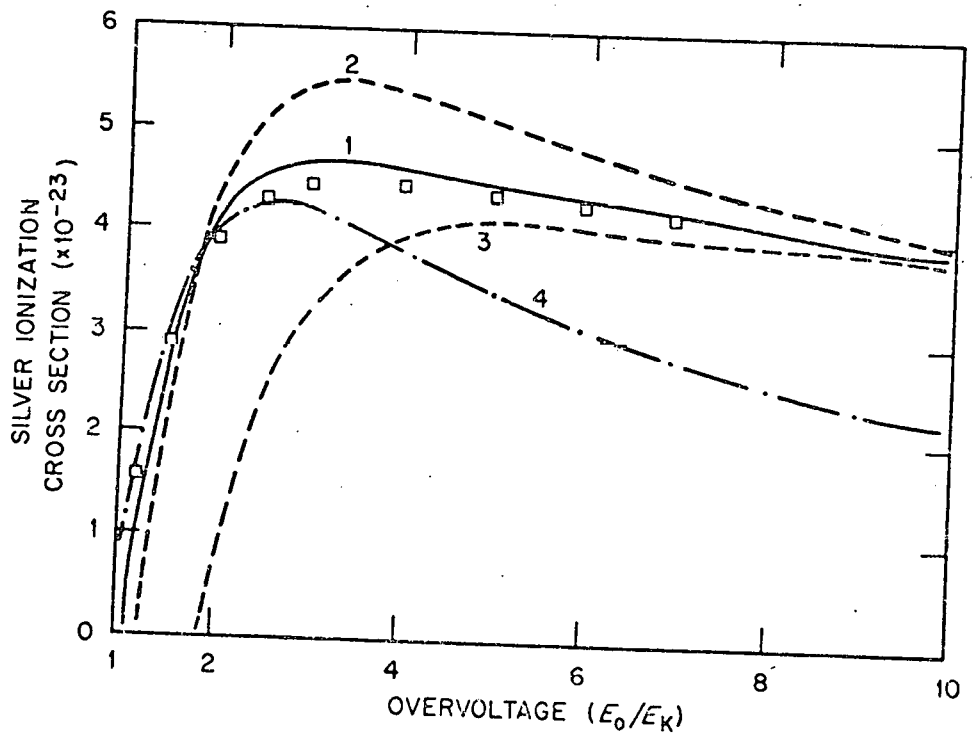

Fig. 18. Comparison of Experimental Ionization Cross Section as a Function of Overvoltage for Silver (squares) to Various Calculations. (1) Using Eq. (2.4); (2), (3) due to Powell; and (4) due to Mott and Massey.

$b_A^K = 0.51$ represents his fits to data of nickel. In these figures one can see that although it is possible to find a set of constants $\left(a_A^K, b_A^K\right)$ which represents the experimental data reasonably well [#2, Fig. 1(b)] for one element, it is not generally valid to extrapolate these same constants for elements of a significantly different atomic number (#2, Fig. 17, #2, Fig. 18). Thus, to use such an approach requires the parameters a_A^K and b_A^K to be determined explicitly for all elements of interest. Unfortunately, there is an insufficient amount of experimental data to use the Powell coefficients confidently over the wide range of atomic numbers and for typical incident beam energies used in analytical microscopy. Thus, the more complex form of Eq. (2.4) is preferred. It should be noted that in the context used here, the form of a_A^K and b_A^K no longer have physical interpretation since they have been used purely as adjustable parameters.

Comparison of these expressions to L shell data for atomic numbers greater than 30 is difficult owing to the lack of measurements in the appropriate energy ranges. Hence, it is assumed that the variation of the L shell cross sections with energy is similar to the K shell. Thus, application of Eq. (2.4) is obtained by changing all superscripts to their respective L shell equivalents, and the constant a_A^L set equal to 0.25.[50]

In order to express the ionization cross section as a function of path length it becomes necessary next to consider the rate of electron energy loss with path length (dE/dz).[56–59] In the context to be used here, it becomes most convenient to use the integral rather than the differential form, which can be written to a good approximation as:

$$\left(E_0\right)^m - \left(E_{AB}\right)^m = k\bar{\rho}z \quad , \tag{2.5}$$

where E_0 is the incident electron energy, k a constant and $E_{AB}(z)$ the electron energy after traveling a path length z in AB. As this equation is only an approximation, the coefficient m varies with the energy; experimental measurements show that it changes from values of 2 at 10 keV[58] to nearly 1 at 1 MeV.[59] Rearranging this equation, one obtains the expression for the mean electron energy with path length as

$$E_{AB}(z) = E_0 \left(1 - \frac{z}{z_R}\right)^{1/m} \quad , \tag{2.6}$$

where z_R can now be interpreted as an effective range (evaluated along the electron's path). Archard and Mulvey[60] have derived the following expression for this range

$$z_R = 1.44 \times 10^{-5} \cdot \left(\frac{\bar{w}_A}{\bar{\rho}\bar{Z}}\right) \cdot \frac{E_0^2}{2\ln\left[\frac{(101.0)\cdot E_0}{\bar{Z}}\right]} \quad , \tag{2.7}$$

where $\bar{w}_A$, $\bar{\rho}$, and $\bar{Z}$ are the average atomic weight, density and number of the compound. Expressing E_0 in units of keV, the units of z_R become centimeters. Calculations of x-ray generation have been performed using various values of the coefficient m in Eq. (2.6) between the values 1 and 2 and as long as the path length z is less than 0.5 z_R the choice of m has little effect. This again is due in part to the fact that ratios of intensities as well as high incident beam energies are being considered. A value of 1.5 has been adopted for TEM work.

The x-ray fluorescence yield from most elements can be obtained with reasonable accuracy from the expression first proposed by Wentzel[61]

$$\omega_A^K = \frac{Z^4}{c^K + Z^4} \qquad (2.8)$$

where Z is the atomic number and c^K a constant for the shell in question $\left(c^K = 1.12 \times 10^6;\ c^{L_{III}} \sim 1 \times 10^8\right)$.[62] Another and more accurate representation is the empirical expression[63]

$$\left(\frac{\omega_A^K}{1 - \omega_A^K}\right)^{\frac{1}{4}} = A + BZ + CZ^3, \qquad (2.9)$$

in which the coefficients A, B, and C are fitted to experimental measurements. In this case the periodic table is broken up into segments and a set of constants is used to determine ω_A^K for various ranges of Z. Since it is usually the case that dedicated minicomputers are used for determining quantitative analyses, it is preferred to use Eq. (2.9) (or tabulated values[64,65]) rather than Eq. (2.8). Similarly, as in the case of fluorescence yields, the K_α fraction of the total K-shell emission $f_A^{K_\alpha}$ [defined as $K_\alpha/(K_\alpha + K_\beta)$] can be obtained from polynomial fits to experimental data[66] or in tabulated form.[67–69]

The last term to consider in the atomic number correction is $\eta_{AB}(z)$, the total electron flux bombarding the infinitesimal element dz. This flux is composed of two parts – first, those electrons forward-scattered from the sample volume directly above dz, and second, any electrons which have been backscattered from deeper levels.

The forward-scattered flux at a depth t emitted into a cone of semi-angle, $\pi/2$, centered about the incident beam direction, can be obtained from Bothe's multiple scattering theory

$$f\left(t, \theta = \frac{\pi}{2}\right) = f_0 \cdot \left\{1 - \exp\left(\frac{-\left(\frac{\pi}{2}\right)^2}{2\lambda_B^2}\right)\right\} \tag{2.10}$$

where f_0 is the incident flux and λ_B is given by Bothe as

$$\lambda_B^2 = 1.6 \times 10^5 \cdot \left(\frac{Z}{E_0}\right)^2 \cdot \frac{\bar{\rho} \cdot t}{w_A} \quad ; \tag{2.11}$$

here Z, E_0, w_A are as previously defined, and λ_B was obtained by an analytical fit to the experimental measurements of Crowther[70] on fast electron ($\sim$600 keV) transmission through various materials. Cosslett and Thomas[58] in a study of electron solid interactions determined that Eq. (2.10) also fits electron transmission at lower energies (5 to 25 keV) with λ modified to:

$$\lambda_{CT}^2 = 1.39 \times 10^5 \left(\frac{Z}{E_0}\right)^{\frac{3}{2}} \cdot \frac{\bar{\rho} \cdot t}{w_A} \quad . \tag{2.12}$$

In both Eqs. (2.11 and 2.12), λ has the units of radians with E_0 expressed in keV. The difference in λ between these two equations is negligible for typical thicknesses (0.05 to 2.0 μm) and accelerating voltages (50 to 200 keV) used in most AEM work; as such, Eq. (2.12), being the more recent, is preferred.

The backscattered flux across dz will in general be a varying fraction of the number of electrons transmitted through that layer. This effect can be represented by a function of depth, $r_{AB}(t)$, which when multiplied by $f_{AB}(t)$, describes the composite flux due to both sources. For large depths within the sample, where the electrons can be considered as fully scattered, $r_{AB}(t)$ is a constant, since as many electrons will be

traveling forward as backward. On the other hand, for an infinitely thin layer suspended *in vacuo* $r_{AB}(t)$ must be equal to unity. Philibert[37] first considered this problem and assumed a simple exponential variation for $r_{AB}(t)$:

$$r_{AB}(t) = R_\infty - (R_\infty - R_0) \exp\left(-k_{AB} \cdot \rho \cdot t\right) \qquad (2.13)$$

where R_∞ is the bulk (or fully scattered) value and R_0 the surface contribution. Assuming a cosine-like angular distribution of electron scattering he obtained a value for R_∞ as 4. Later, based on the measurements of Cosslett and Thomas, which showed the distribution to vary as cosine squared, Reuter determined that R_∞ should in fact be equal to 3. For R_0, Philibert assumed the simple form

$$R_0 = 1 + \varepsilon \qquad (2.14)$$

with ε being chosen to match experimental measurements of the depth distribution of characteristic x rays. Reuter[40] succeeded in expressing R_0 as:

$$R_0 = 1 + 2.8 \left(1 + \frac{0.9}{U_0}\right) \cdot \eta \quad , \qquad (2.15)$$

based on experimental measurements of x-ray emission from thin films on bulk substrates. In Eq. (2.15) U_0 is the overvoltage ratio and η the bulk backscattering coefficient. For the case of self-supporting thin films, such as TEM specimens, R_0 should be further modified to account for the fact that η is now a function of sample thickness.[58]

Thus η in Eq. (2.15) should be replaced by the function $\eta(t_0)$:

$$\eta(t_0) = \eta \left\{ 1 - \exp \left[-\mu^*_{AB} \cdot t_0 \right] \right\} \tag{2.16}$$

where t_0 is the total sample thickness in the direction of the incident beam. η, the bulk backscattering coefficient, can be calculated from the polynomial equation;[40]

$$\eta = -0.0254 + 0.0167 - 1.86 \times 10^{-4} \cdot Z^2 + 8.3 \times 10^{-7} Z^3 \quad . \tag{2.17}$$

The coefficient μ^*_{AB} can be obtained from the results of Cosslett and Thomas. In their measurements they noted that after a sample thickness corresponding to 20 to 30% of the mean electron range η attains bulk specimen values. Setting t_0 equal to 25% of the mean electron range (R_m) and requiring that at this point $\eta(t_0) \gtrsim 0.95\ \eta$ one then obtains the following:

$$\mu^*_{AB} \approx \frac{12.0}{R_m} \quad . \tag{2.18}$$

Cosslett and Thomas have also shown that R_m is always less than the Bethe range (z_R) defined in Eq. (2.7). Thus upon substitution of z_R instead of R_m into 2.18 one obtains a reasonable approximation for μ^*_{AB} as:

$$\mu^*_{AB} \approx 1.66 \times 10^{-16} \left(\frac{\bar{\rho} \cdot Z}{W_A} \right) \cdot \frac{\ell n \left\{ \frac{101 \cdot E_0}{Z} \right\}}{E_0^2} \quad . \tag{2.19}$$

The use of z_R instead of R_m is not a serious discrepancy since it effectively resets the defining criterion for the point at which $\eta(t_0)$ is considered a bulk value.

The last parameter needed to complete the expression for $\eta_{AB}(z)$ is k_{AB} from Eq. (2.13). It is noted that this coefficient determines the depth at which the total scattering in any direction becomes constant (i.e., the diffusion depth). Philibert and Reuter differ somewhat on this point, basically due to their respective sources of information. Philibert's criterion requires that the most probable scattering angle becomes $\pi/4$. Reuter, on the other hand, chooses 38° to be consistent with the data of Cosslett and Thomas. Furthermore, Philibert solves for the diffusion depth using Bothe's equation for the most probable scattering angle θ_ρ

$$\theta_\rho^B = \frac{400}{E_0}\left(\frac{Z^2 \cdot \rho t}{A}\right)^{\frac{1}{2}} \tag{2.20}$$

while Reuter uses the analytic fit proposed by Cosslett and Thomas

$$\theta_\rho^{CT} = 109.5\left(\frac{Z^{\frac{3}{2}} \cdot \rho t}{A \cdot E_0}\right)^{\frac{1}{2}} . \tag{2.21}$$

Unfortunately, there has been no experimental work to date done on this question in the 50 to 200 keV range, which straddles these two extremes. Thus for low voltage work ($\lesssim$ 100 keV), Eq. (2.21) is used, while for high voltage measurement ($\gtrsim$ 200 keV) Eq. (2.20) becomes more appealing. In both cases, however, the Philibert choice of most probable scattering angle $\pi/4$ is chosen, since it represents the condition of equal scattering in both the horizontal and forward directions. Upon rearranging, one obtains the following equations for the onset of the diffusion depth for high and low energies, respectively, as:

$$t_{diff}^{\text{high E}} = \frac{w_A}{\bar{\rho}\cdot\bar{Z}^2}\cdot\left(\frac{\pi E_0}{1600}\right)^2 \tag{2.22}$$

$$t_{diff}^{\text{low E}} = \frac{w_A\cdot E_0}{\bar{\rho}\cdot\bar{Z}^{3/2}}\cdot\left(\frac{\pi}{438}\right)^2 \tag{2.23}$$

As with the backscatter coefficient, k_{AB} is then determined by setting $r_{AB}(t)$ equal to 95% of the bulk value. Substituting into Eq. (2.13) and rearranging terms, one can show:

$$k_{AB} = \frac{1}{\bar{\rho}\, t_{diff}}\cdot \ell n\left(\frac{0.05}{1-\frac{R_0}{R_\infty}}\right) \tag{2.24}$$

where t_{diff} is determined from either 2.22 or 2.23, whichever becomes most appropriate.

Combining Eqs. (2.2) through (2.24) one can begin the calculation of x-ray generation for a thin sample. Consider first the case of infinitely thin slab, dz, from Eq. (2.2); the generated intensity ratio of element A to B is:

$$\frac{I_A^{K\alpha}}{I_B^{K\alpha}} = \frac{\phi_A^{K\alpha}(z)dz}{\phi_B^{K\alpha}(z)dz} = \frac{\dfrac{Q_A^K N_0 \bar{\rho} C_A\ \omega_A^K f_A^{K\alpha}\ \eta_{AB}(z)dz}{w_A}}{\dfrac{Q_B^K N_0 \bar{\rho} C_B\ \omega_B^K f_B^{K\alpha}\ \eta_{AB}(z)dz}{w_B}} \tag{2.25}$$

which simplifies to

$$\frac{I_A^{K\alpha}}{I_B^{K\alpha}} = \frac{Q_A^K}{Q_B^K} \cdot \frac{w_B}{w_A} \cdot \frac{\omega_A^K f_A^{K\alpha}}{\omega_B^K f_B^{K\alpha}} \cdot \frac{C_A}{C_B}, \tag{2.26}$$

resulting in the simple relation that for an infinitely thin film the relative intensity ratio is directly proportional to the concentration ratio. The constant of proportionality here is a function of the ionization cross sections, the atomic weights, and the x-ray yields of the elements under excitation.

For a sample of finite thickness t_0 the intensity ratio can be written as a ratio of integrals of Eq. (2.2)

$$\frac{I_A^{K\alpha}(t_0)}{I_B^{K\alpha}(t_0)} = \frac{\int_0^{t_0} \phi^{K\alpha}(z)\, dz}{\int_0^{t_0} \phi^{K\alpha}(z)\, dz}, \tag{2.27}$$

both of which must be evaluated along each electron's path within the sample. It is important at this point to recall that $\phi_A^{K\alpha}(z)$ has been formulated as several constants multiplied by two functions $Q_A^K(z)$ and $\eta_{AB}(z)$. $Q_A^K(z)$ is a function of path length; however $\eta_{AB}(z)$ has been expressed as a function of depth (t). The two quantities are in general not equal (path length $\geq$ thickness); however, for the special case of thin films and high incident beam energies the difference will be small. Thus to a good first approximation (for TEM specimens) one can equate the two variables and proceed with the integration.

The results of such an integration are shown in Fig. 19, which was evaluated by numerically integrating Eq. (2.27) for a 50/50 atomic

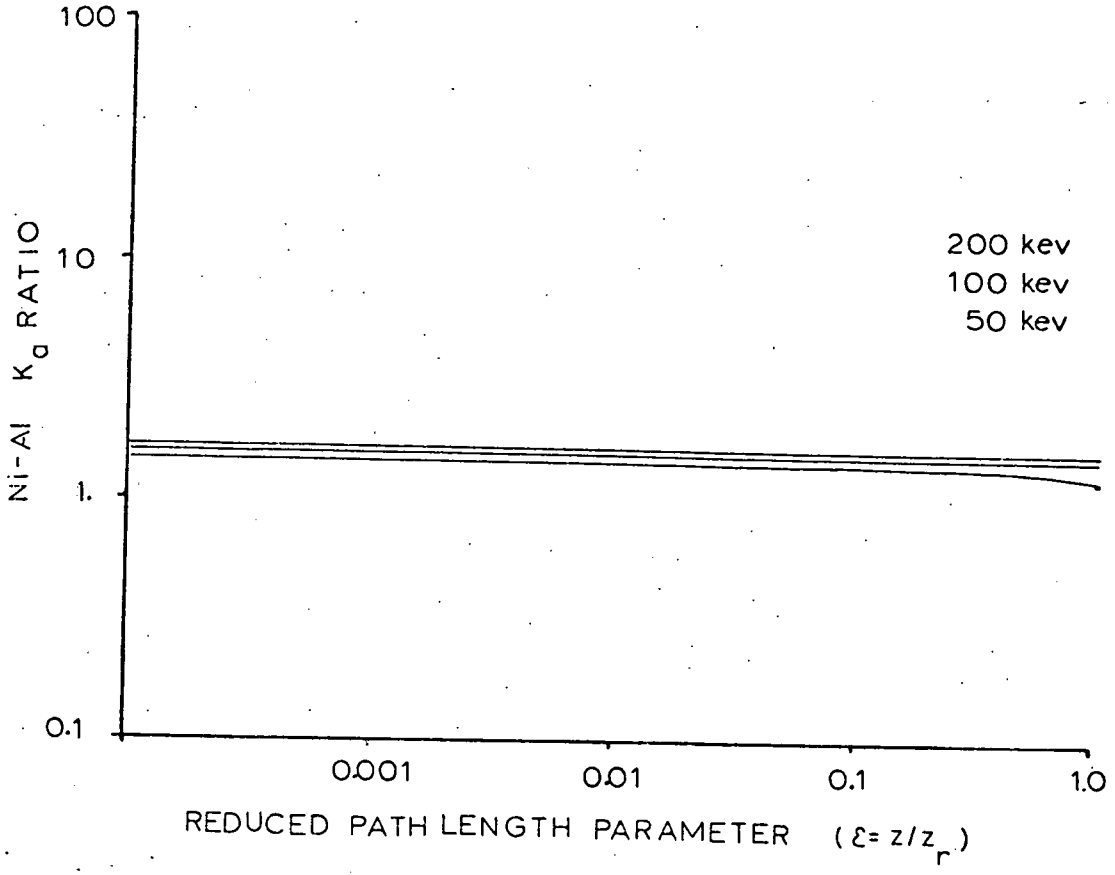

Fig. 19. Results of Calculation of Ni/Al Ratio by Numerical Integration of Eq. (2.27) for Incident Electron Energies of 200, 100, and 50 keV (top, middle, and bottom curves, respectively).

percent alloy of NiAl. The ordinate ζ is a reduced path-length parameter ($\zeta = z/z_R$) and is defined such that when its value becomes unity the mean electron energy has dropped below the x-ray critical excitation edge. At this point the electrons have reached their maximum usable range in the material. Obviously these calculations have been extrapolated significantly beyond the point where the path length/thickness approximation breaks down. Furthermore, once the electron diffusion depth is reached, the forward scattered flux $f(t,\pi/2)$ in Eq. (2.10) should in reality be replaced by Lenard's law of electron transmission

$$f(t,\pi/2) = f_0 \exp(-\sigma t) \tag{2.28}$$

rather than Bothe's multiple scattering theory for the sample (here σ is the electron attenuation coefficient). Although both of these effects should be included in order to accurately describe the generation process, their emission at this point will not alter the calculated ratio. The simple reason for this is that the inclusion of these terms merely changes the net electron flux crossing a given layer and therefore affects the generation process equally for both elements. Thus there will be no net change in the calculated ratio.

The theory up to this point has yielded a useful result – namely that the generated x-ray ratio is nearly independent of path length (hence also thickness) for a wide range of incident energies (50 to 200 keV). The slow decrease in the calculated ratio predicted in the 50 keV calculations of Fig. 19 reflects the fact that as the electrons approach their respective maximum ranges ($\zeta \equiv 1$) changes in the ionization cross section begin to favor the element with the lowest critical

excitation energy (E_A^K). Similar results are also predicted in the 100 and 200 keV calculations; however, scale factors prohibit their observation. Thus it would appear that for samples whose thickness is such that the total path length traveled is less than 0.25 z_R, Eq. (2.26) is ideally suited for quantitative analysis. Unfortunately, the effects of x-ray absorption must frequently be included in order to correctly interpret results from many TEM-based analyses.

2.2.3 The Absorption Correction

The inclusion of x-ray absorption effects to the calculation of x-ray emission is fundamentally a simple concept. The generated intensity, at each point within the specimen, must travel through a finite amount of material in order to be detected and, as such, suffers a reduction in intensity due to absorption. This can be expressed as

$$\phi_A^{K_\alpha}(d,t) = \phi_A^{K_\alpha}(t)\cdot\exp\left\{-\left(\frac{\mu}{\rho}\right)_{AB}^{K_\alpha,A}\cdot\bar{\rho}\cdot d\right\} \qquad (2.29)$$

where $\phi_A^{K_\alpha}(d,t)$ is the number of K_α photons of A generated at depth t leaving the specimen after having traveled a distance d within a medium of mass absorption coefficient $\left(\frac{\mu}{\rho}\right)_{AB}^{K_\alpha,A}$, and $\phi_A^{K_\alpha}(t)$ is the initial generated intensity at that depth. The task at hand is clearly to determine the relationship between t, the depth of production, and d, the exiting path length, which is solely dictated by the system/sample geometry.

The geometry found in most electron microprobes is relatively simple. The electron probe strikes a plane surface usually at normal

incidence as is shown in Fig. 20. Only those x rays which leave the specimen in the direction of the x-ray detector, which is oriented at an elevation (or takeoff) angle θ_E relative to the sample surface, are recorded by the measuring system. Thus it is an easy exercise to show that the exiting path length d is given by the following equation:

$$d = t \operatorname{cosec} \left(\theta_E\right) , \tag{2.30}$$

where t is the depth of production. Unfortunately, due to the constraints on detector size and position imposed by a transmission electron microscope objective lens pole piece, the geometry found in TEM is not as simple as this. In most TEM instruments the detector axis lies in the same plane as the specimen $\left(\text{hence } \theta_E \approx 0°\right)$ and it therefore becomes necessary to tilt the sample through some angle in order that characteristic x rays generated by the electron probe can leave the sample and reach the detector system. This angle can be as much as 20 to 30° owing to the added complications that the specimen stage and supporting mechanisms also tend to block the line of sight of the detector to the specimen. In some of the newer designs, AEM systems (both CTEM/STEM and DSTEM) have been modified such that the elevation angle, θ_E, is nonzero ($\sim$15°); however, one must still tilt the sample in order to optimize experimental conditions. Therefore, the x-ray geometry found on most analytical electron microscope is shown in Fig. 21, which represents a plane section through the sample containing the incident beam direction and the detector axis. The elevation angle, θ_E, is defined relative to an imaginary plane perpendicular to the incident beam direction and is nominally located at

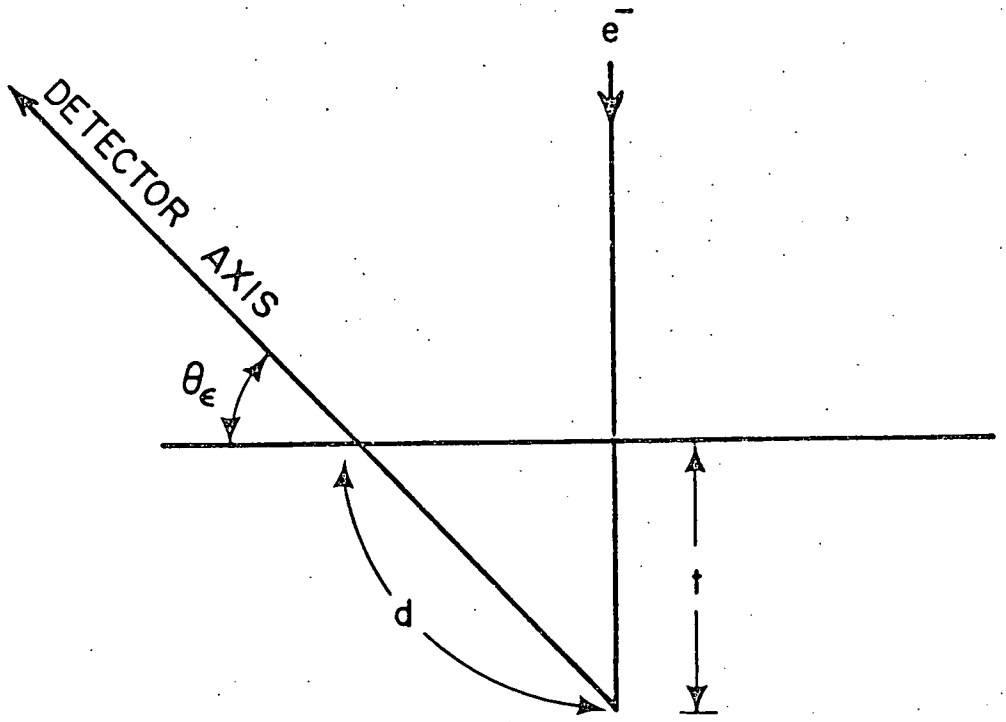

Fig. 20. Geometry of the Absorption Correction Commonly Found in Electron Microprobes.

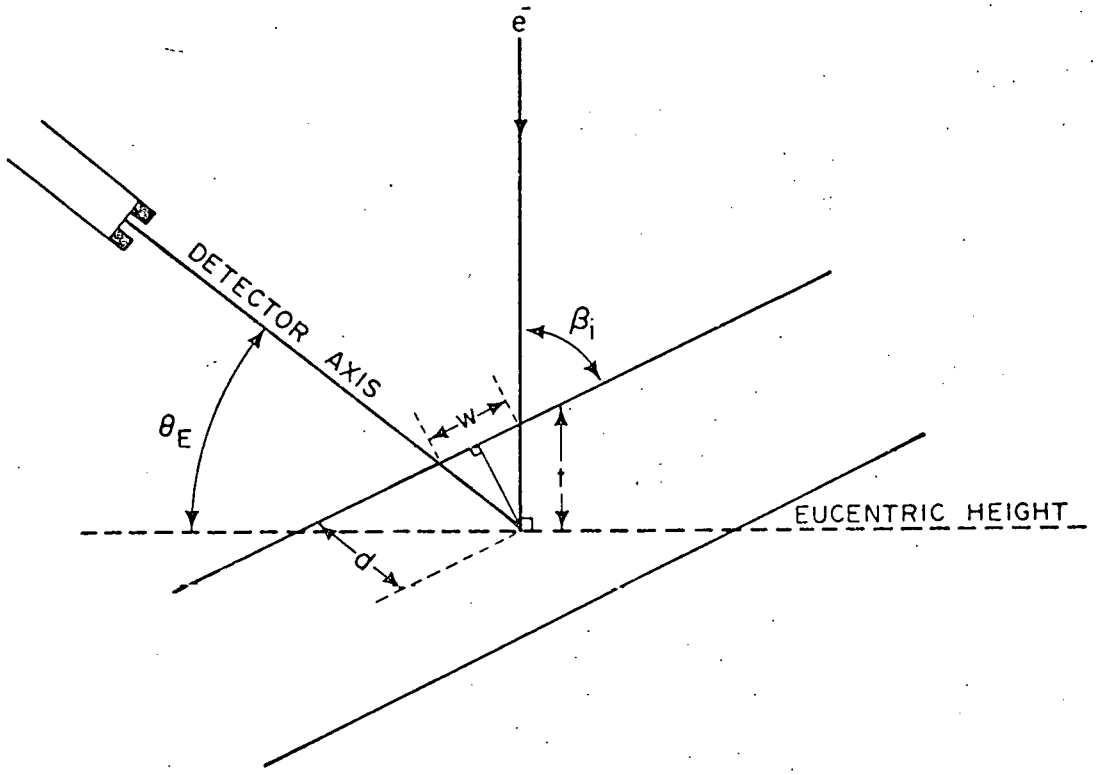

$$d = t \cdot \frac{\sin(\beta_i)}{\cos(\beta_i - \theta_E)}$$

Fig. 21. Detector/Specimen Geometry for an AEM Instrument.

the height of the midplane of the untilted specimen position. The inaccuracies involved with this definition of θ_E are obvious since for a tilted specimen θ_E actually is a function of t; however, for typical detector-specimen distances (~2 cm) and sample thicknesses (0.1 to 1.0 μm) this error is insignificant. The electron incidence angle β_i is also defined in Fig. 21, as the angle between the electron probe and the sample surface. From this figure one can show that the relationship between depth of production and exiting path length is given by:

$$d = t \cdot \frac{\sin\ (\beta_i)}{\cos\left[\beta_i - \theta_E\right]} \quad . \tag{2.31}$$

It can be seen that for the special case of normal incidence ($\beta_i = \pi/2$) Eq. (2.31) reduces to (2.30). Implicit in this equation is the assumption that the sample can be considered to be a plane slab of uniform thickness. Obviously on a macroscopic scale most TEM specimens do not satisfy this criterion; however, again considering the scale on which most analytical work is done (< 1000 Å) the approximation is reasonable. Care must, however, be taken in using Eq. (2.31) on samples which are severely bent or having significant thickness changes over distances whose dimensions are on the order of ω_0:

$$\omega_0 = t_0 \left[\sin\beta_i \tan(\beta_i - \theta_E) + \cos\ \beta_i\right] \tag{2.32}$$

where ω_0 is the distance between the point at which the incident probe strikes the sample and the exit point for x rays emitted from the maximum

depth (t_0) of production measured parallel to the incident beam direction (see Fig. 21).

The angle of electron incidence, β_i, is similarly a function of the detector/specimen geometry. Although it is possible to determine β_i using solid geometry it is more convenient to plot the various parameters on a stereographic projection from which the value of β_i can be easily read. In order to proceed it is necessary to first define a cartesian coordinate system within the microscope. The logical choice for such a system is the set of vectors defined by the two specimen translate directions and the electron-optical axis, labeled x, y, and z, respectively, in Fig. 22. Relative to this coordinate system, one can uniquely specify the position of the x-ray detector using two angles. The azimuthal angle (θ_A) describes the relative position of the detector plane (i.e., the plane containing the detector axis and the electron-optical axis), and is defined as the rotation in the x-y plane about the z axis of this plane relative to either the x or y direction. The elevation angle, θ_E, was introduced previously and in this coordinate system is defined as the angle between the detector axis and the x-y plane (measured in the detector plane). Figure 22 illustrates these relationships using a standard cartesian coordinate system, and Fig. 23(a) shows the same relationships on a stereographic projection.

In the initial nontilted position the sample normal is oriented parallel to the electron optical axis. Knowing the amount of tilt and the relationship of the respective tilt axes to the reference coordinate

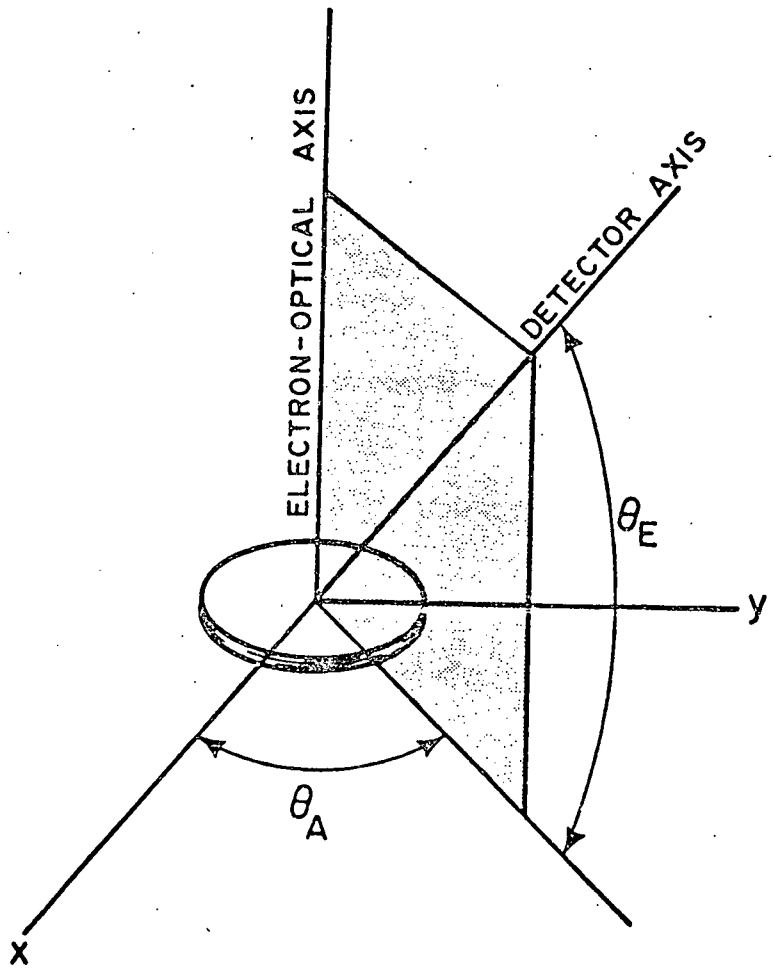

Fig. 22. Coordinate System Used in the Absorption Correction for AEM X-Ray Work.

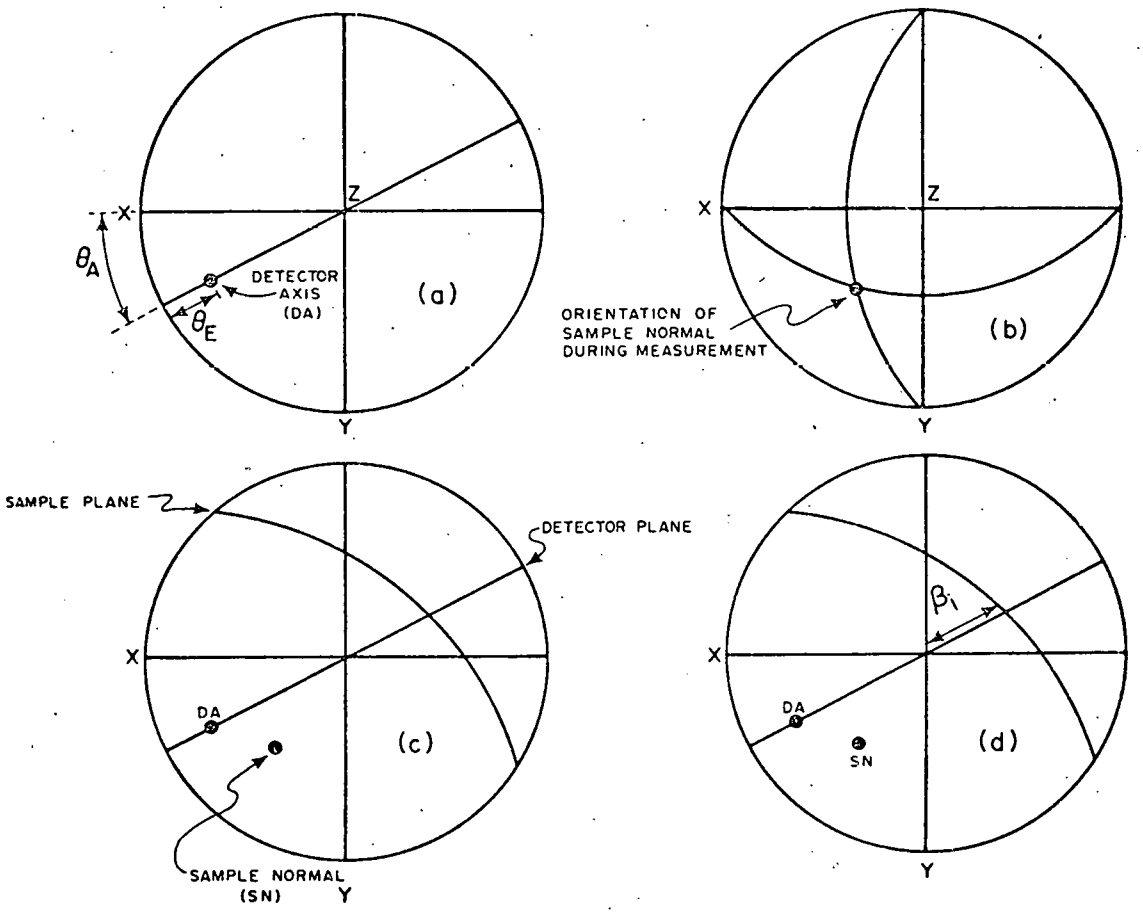

Fig. 23. Stereographic Projection Indicating the Absorption Correction Geometry.

system it is possible to plot the position of the sample normal on the stereographic projection [Fig. 23(b)]. Care must be taken in plotting the normal, particularly in determining the position of the tilt axes. This is due to the fact that in most double-tilt stages, the secondary tilt axis is usually not independent of the primary axis. This is an important point to remember when determining β_i, and is readily accounted for using the standard rules of stereographic projection.[71] Having plotted the sample normal, one proceeds to draw in the detector plane and sample plane [Fig. 23(c)]. The angle of incidence, β_i, is then determined as the angle between the sample plane and z axis measured in the detector plane [Fig. 23(d)].

The total characteristic intensity emitted in the direction of the detector system, including absorption effects, is given by:

$$I_A^{\kappa\alpha} = \int_0^{t_0} \phi^{\kappa\alpha}(z) \cdot \exp\left\{ - \left(\frac{\mu}{\rho}\right)_{AB}^{\kappa\alpha,A} \cdot \bar{\rho} \cdot d \right\} dz \quad , \tag{2.33}$$

and the intensity ratio is, upon substitution,

$$\frac{I_A^{\kappa\alpha}}{I_B^{\kappa\alpha}} = \left(\frac{C_A}{C_B}\right) \cdot \left(\kappa_{AB}\right) \cdot \left\{ \frac{\int_0^{t_0} Q_A^{\kappa}(Z) \cdot n_{AB}(Z) \cdot \exp\left\{ - \left(\frac{\mu}{\rho}\right)_{AB}^{\kappa\alpha,A} \cdot \bar{\rho} \cdot t \cdot \frac{\sin(\beta_i)}{\cos(\beta_i - \theta_E)} \right\} \cdot dZ}{\int_0^{t_0} Q_B^{\kappa}(Z) \cdot n_{AB}(Z) \cdot \exp\left\{ - \left(\frac{\mu}{\rho}\right)_{AB}^{\kappa\alpha,B} \cdot \bar{\rho} \cdot t \cdot \frac{\sin(\beta_i)}{\cos(\beta_i - \theta_E)} \right\} \cdot dZ} \right\} \tag{2.34}$$

where

$$\kappa_{AB} = \frac{w_B \cdot \omega_A^{\kappa} \cdot f_A^{\kappa\alpha}}{w_A \cdot \omega_B^{\kappa} \cdot f_B^{\kappa\alpha}} \quad .$$

The mass absorption coefficient $\left(\frac{\mu}{\rho}\right)_{AB}^{K_\alpha,A}$ for K_α x-ray photons of element A of the alloy AB is defined as:

$$\left(\frac{\mu}{\rho}\right)_{AB}^{K_\alpha,A} = \sum_{i=1}^{N} \left(\frac{\mu}{\rho}\right)_{i}^{K_\alpha,A} C_i \quad , \tag{2.35}$$

which is clearly a function of the composition of the compound under investigation. C_i is the composition in weight percent of the i^{th} element in the sample and $\left(\frac{\mu}{\rho}\right)_{i}^{K_\alpha,A}$ is the absorption coefficient for the K_α x ray of A in the pure element i. Obviously the composition of the alloy is initially an unknown quantity; however, it is possible to determine $\left(\frac{\mu}{\rho}\right)^{K_\alpha}$ iteratively. As a first approximation the composition of the alloy is determined solely using the atomic number correction. Using these values, a first-order absorption correction is calculated. The new values of composition are then backsubstituted into the absorption term and the procedure is repeated until a converence is obtained.

Figure 24 illustrates the change in the intensity ratio expected from the NiAl compound previously described with the inclusion of absorption [Eq. (2.34)]. This figure can be directly compared with 19, which represents a calculation of only the atomic number effect. In order to perform these computations the same approximations used in obtaining Fig. 19 were applied here. Of these, the most important is the path length/thickness approximation and, as in the case of the atomic number calculation, the computations have been extended well beyond their valid ranges. Because of this the results presented for thick films ($\zeta \gtrsim 0.1$)

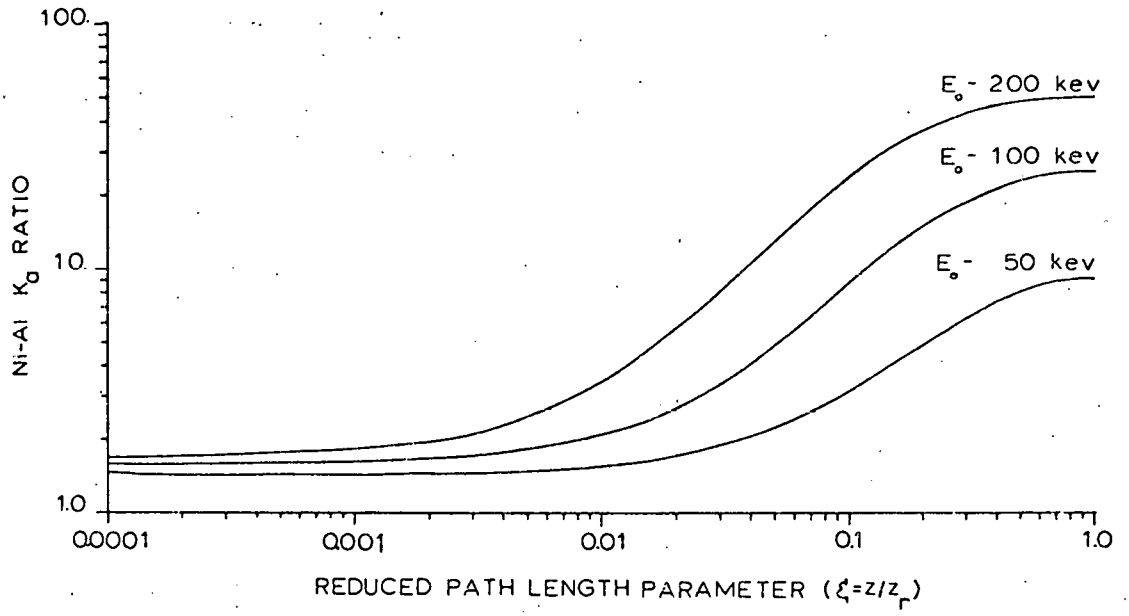

Fig. 24. Calculated Variation in Ni/Al K_α Ratio Including Absorption Effects for Various Incident Beam Energies.

should be considered only as a qualitative illustration of absorption. In this range the intensity ratio initially increases due to the preferential absorption of the lower energy aluminum K_α x rays (1.48 keV) while the higher energy nickel K_α line (7.45 keV) is easily transmitted. Ultimately, however, the ratio levels out as the sample thickness becomes sufficient to absorb a substantial portion of the nickel intensity. The variation below $\zeta = 0.1$, the region of interest in most transmission work, however, merits further consideration particularly with respect to path length/thickness assumptions.

This approximation was initially invoked because the ionization cross section was formulated as a function of path length through the use of the rate of energy loss equations. On the other hand, the net electron flux across a given layer dz was expressed as a function of the depth, t, below the electron entrance surface. Obviously these two variables are in general not equivalent; however, because of the relatively slow variation in the values of the cross section for the energy ranges typically encountered in AEM, the discrepancy between these parameters can be ignored. This can be seen by considering the change in cross section (Q_k) predicted by Eq. (2.4) for moderate ($\sim$10%) changes in energy in the vicinity of 100 keV. Reference to curve 1 of Figs. 16, 17, and 18 shows that only minor changes are observed in the value of Q_k in the region of 100 keV (U = 64, 12, and 4 for aluminum, nickel, and silver, respectively). Thus, the inaccuracies involved in the calculations for $\zeta \leq 0.1$ obtained by equating path length and thickness are

small. Furthermore, these inaccuracies decrease as the incident energy increases.

2.2.4 The X-Ray Fluorescence Correction

Up to this point we have been concerned with calculating the contributions to characteristic x-ray emission resulting solely from electron excitation of the sample. It is, however, equally possible to induce characteristic emission through an x-ray fluorescence process. Thus whenever an x-ray quantum of sufficient energy is absorbed by the sample there is a finite probability that it will ionize an inner core level and a certain fraction of these events will result in the emission of characteristic x rays from that shell. There are a variety of sources of x-ray radiation which bombard the sample in a conventional TEM, all of which are nonlocalized and are thus detrimental to microanalysis. Most of these sources can be eliminated or reduced to negligible intensities by suitable modifications to the microscope column. However, those x rays generated within the sample itself cannot be eliminated; hence, the calculations outlined in the following section are presented in order to estimate their influence on characteristic emission.

Figure 25 illustrates a schematic x-ray spectrum from a multielement sample composed of the elements A, B, and C. For simplicity, only the K lines of each element along with their respective absorption edges are indicated. In order to induce x-ray fluorescence of element A the fluorescing radiation must have an energy greater than the critical excitation edge (E_A^K); thus all x-ray photons in Fig. 25, both

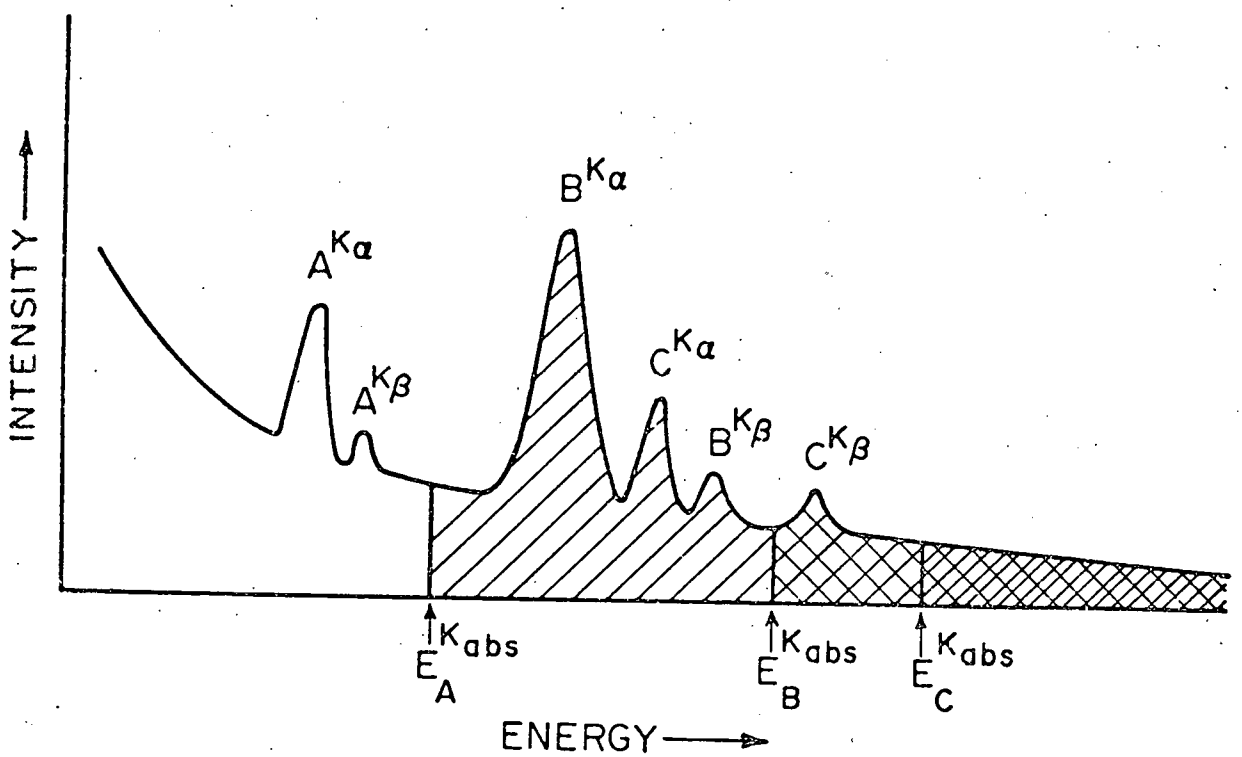

Fig. 25. Schematic X-Ray Spectrum Indicating Relative Absorption Edge Positions for Use in the X-Ray Fluorescence Correction.

characteristic and continuum, whose energy is greater than E_A^K are eligible to excite A. Element B represents a slightly different case of fluorescence. Here the K_α line of element C lies just below the K edge of B; hence only the K_β line of C together with the remaining continuum spectrum can excite B. Finally, element C cannot be fluoresced by any characteristic lines of A or B and thus can only be enhanced via continuum fluorescence. For an electron microscope, correctly aligned and modified for x-ray microanalysis, the continuum intensity generated by electron excitation of TEM specimens is small and fluorescence due to this source can generally be neglected. The following calculations are presented, therefore, to estimate the influence of only characteristic fluorescence.

The total K_α x-ray intensity of A emitted by samples can be written as:

$$I_A^{Total} = I_A^{el} + I_A^{fl} , \tag{2.36}$$

where I_A^{el} is the contribution due to electron excitation and I_A^{fl} the fluorescence contribution. Since the relative intensity due only to electron excitation is the parameter of interest for quantitative analysis the fluorescence correction can be written as:

$$I_A^{el} = \frac{I_A^{Total}}{\left(1. + I_A^{fl}/I_A^{el}\right)} , \tag{2.37}$$

and thus it is necessary to calculate the ratio I_A^{fl}/I_A^{el}. In order to reduce the complexity of the formulae which follow we shall consider the case of fluorescence of element A only by a single characteristic line

(K_α) of element B. The extension to the K_β line or other lines as well as the addition of multiple elements is straightforward.

Let us assume that I_B^{ab} is the total amount of B K_α radiation absorbed within the multi-element sample. Of this absorbed intensity the fraction

$$C_A \cdot \left\{ \frac{(\mu/\rho)_A^{K\alpha,B}}{(\mu/\rho)_B^{K\alpha,B}} \right\} \tag{2.38}$$

will be absorbed by atoms of element A, where C_A is the concentration of A in fractional weight percent and $(\mu/\rho)_C^{K\alpha,D}$ is the mass absorption coefficient for K_α x rays of element D in the pure element C. Furthermore the fraction

$$\left(r_K^A - 1\right) \Big/ r_K^A \tag{2.39}$$

of this intensity will be absorbed by the K shell of A, and hence the total number of ionization events of the K shell of A due to x-ray fluorescence $\left(Q_A^{K,Ab}\right)$ is given by:

$$Q_A^{K,Ab} = C_A \cdot \left\{ \frac{(\mu/\rho)_A^{K\alpha,B}}{(\mu/\rho)_B^{K\alpha,B}} \right\} \cdot \left\{ \frac{r_K^A - 1}{r_K^A} \right\} \cdot I_B^{ab} \tag{2.40}$$

with the quantity r_K^A defined as the K absorption edge jump ratio of element A.

The total yield of K_α x rays from element A due to this ionization is given by the product of $Q_A^{K,Ab}$ and the relative yield of K_α x rays from the K shell $(\omega_A^K \cdot f_A^{K\alpha})$

$$I_A^{fl} = C_A \cdot \left\{ \frac{\left(\frac{\mu}{\rho}\right)_A^{K_{\alpha},B}}{\left(\frac{\mu}{\rho}\right)_B^{K_{\alpha},B}} \right\} \cdot \left\{ \frac{r_K^A - 1}{r_K^A} \right\} \cdot \omega_A^K \cdot f_A^{K_{\alpha}} \cdot I_B^{ab} \qquad (2.41)$$

An exact calculation of I^{fl} actually requires that I_B^{ab} be calculated at each point in the sample. The fluorescence intensity at each point having been determined, an absorption correction to the intensity emitted in the direction of the detector system is then calculated using the procedure outlined previously. Realistically the fluorescence correction is small; hence it becomes reasonable to make certain simplifying approximations. Firstly the total absorbed intensity of the characteristic line of B can be approximated by:

$$I_B^{ab} = \frac{1}{2} \cdot I_B^{K_{\alpha}} \cdot \exp\left\{ \left(-\frac{\mu}{\rho} \right)^{K_{\alpha},B} \cdot \bar{\rho} \cdot t_0 \right\} \qquad (2.42)$$

where $I_B^{K_{\alpha}}$ is the total characteristic emission generated in the sample of thickness to purely by electron excitation, and $\left(\mu/\rho\right)_{AB}^{K_{\alpha},B}$ the mass absorption coefficient of the compound for B K_{α} radiation as previously defined in Eq. (2.35). Secondly, let us further assume that all the fluorescence intensity is emitted in the direction of the detector system from the midpoint of the sample thickness which results in the following expression for I_A^{fl}

$$I_A^{fl} = \frac{1}{2} \cdot C_A \cdot \left\{ \frac{\left(\frac{\mu}{\rho}\right)_A^{K_{\alpha},B}}{\left(\frac{\mu}{\rho}\right)_B^{K_{\alpha},B}} \right\} \cdot \left\{ \frac{r_K^A - 1}{r_K^A} \right\} \cdot \omega_A^K \cdot f_A^{K_{\alpha}} \cdot \exp\left\{ -\frac{3}{2} \cdot \left(\frac{\mu}{\rho}\right)_{AB}^{K_{\alpha},B} \cdot \bar{\rho} \cdot t_0 \left[1 + \frac{\sin\beta_i}{\cos\left(\beta_i - \theta_E\right)} \right] \right\} \cdot I_B^{K_{\alpha}} \qquad (2.43)$$

Finally, dividing by $I_A^{K\alpha}$ we obtain the following approximate expression for I_A^{fl}/I_A^{el} for a TEM specimen as:

$$\frac{I_A^{fl}}{I_A^{el}} = \frac{C_A}{2} \cdot \left\{ \frac{\left(\frac{\mu}{\rho}\right)_A^{K\alpha,B}}{\left(\frac{\mu}{\rho}\right)_B^{K\alpha,B}} \right\} \cdot \left\{ \frac{r_K^A - 1}{r_K^A} \right\} \cdot \omega_A^K \cdot f_A^{K\alpha} \cdot \exp\left\{ - \chi_{AB}^{K\alpha,B} \right\} \cdot \frac{I_B^{K\alpha}}{I_A^{K\alpha}} \qquad (2.44)$$

with

$$\chi_{AB}^{K\alpha,B} = \frac{3}{2} \cdot \left(\frac{\mu}{\rho}\right)_{AB}^{K\alpha,B} \cdot \bar{\rho} \cdot \left\{ 1 + \frac{\sin\beta_i}{\cos(\beta_i - \theta_E)} \right\} \cdot t_0 \cdot \qquad (2.45)$$

All quantities have been previously defined. Clearly from Eq. (2.41) if absorption effects within the sample are small the fluorescence intensity will be minimal. It is seldom the case that this correction amounts to more than a few percent change and is usually negligible for atomic numbers less than 20. For a given element A, the magnitude of I_A^{fl}/I_A^{el} decreases with increasing separation of the atomic number B. The most important range for this correction is the transition metals titanium through zirconium, particularly combinations such as Ni-Fe.

2.2.5 Detector Efficiency

After being emitted from the sample, the x-ray intensity must be measured by some type of detector system. Usually in AEM systems solid state Si(Li) x-ray detectors are used because of their compact size. These detectors have an inherent efficiency in their response to x-ray events, the most important of which is due to absorption effects in the window material limiting the detector sensitivity to low-energy x rays.

This absorption must be accounted for in order to correctly convert intensity measurements to quantitative results. The reduction in intensity can be calculated from the expression:

$$I^{\text{Measured}} = I(E)^{\text{Actual}} \cdot \prod_{i=1}^{N} \exp\left[-\left(\frac{\mu}{\rho}\right)_i^E \cdot \rho_i \cdot \frac{t_i}{\cos\alpha}\right] \qquad (2.46)$$

where π is the usual notation for the product of i terms, $(\mu/\rho)^E$ is the mass absorption coefficient of element i for x rays of energy E, ρ the density of i, and t_i the thickness of the respective absorbing medium along the detector axis. The factor $\cos\alpha$ accounts for increases in path length which will be experienced if the x rays do not enter the detector parallel to its axis. The angle α is defined in Fig. 26. Figure 27 plots the calculated efficiency for a typical solid state Si(Li) detector as a function of incident x-ray energy using the following typical detector parameters:

Window thickness Be	= 0.008 mm
Window thickness Au	= 0.02 μm
Si dead layer	= 0.1 μm
α	= 0°

The steps in the curve correspond to absorption edges of Au and Si. Above 20 keV the efficiency of the detector begins to fall again due to transmission of the high-energy x rays through the silicon crystal (nominally 4 mm thick); however, it is usually the case that for these elements one changes to the L lines rather than the higher energy K series.

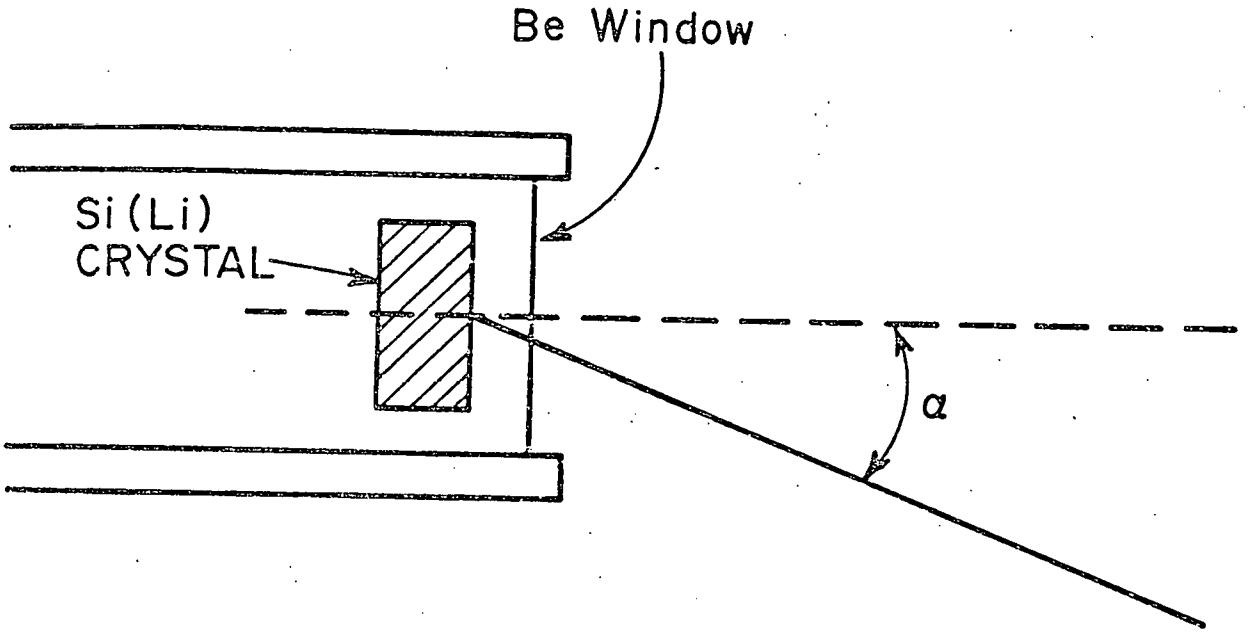

Fig. 26. The Definition of the X-Ray Entrance Angle (α) Relative to Detector Axis.

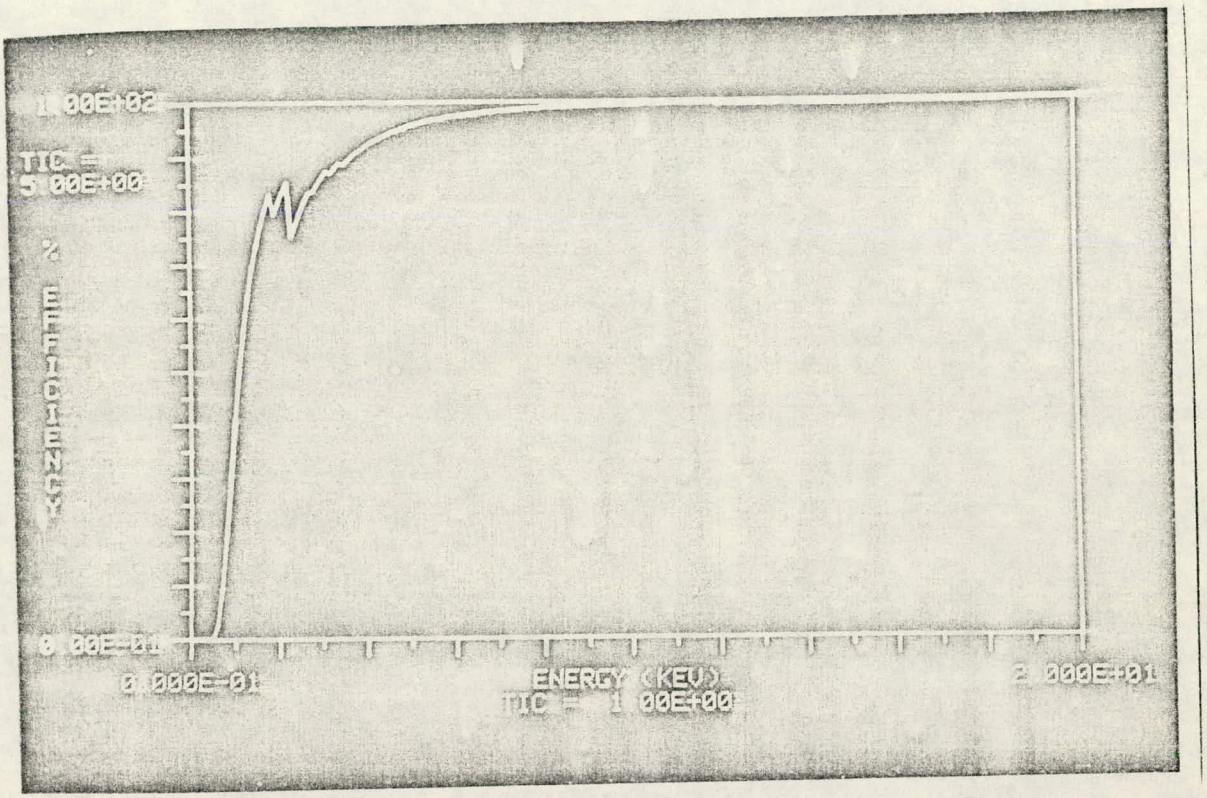

Fig. 27. Calculated Detector Efficiency for a Si(Li) Detector Due to Absorption Effects in the Be Window Au and Si Dead Layers.

2.2.6 Optimum Experimental Conditions for X-Ray Analysis

The ultimate sensitivity of x-ray microchemical analysis in an electron microscope is a function of the specific operating conditions which exist during the experimental measurements. In general one wants to maximize the characteristic information measured from the specimen and minimize all other emission. The parameter which is used to express the sensitivity of x-ray analysis is then the ratio of characteristic (peak) to continuum (background) intensities. Several factors influence this ratio and the calculations outlined in this section are specifically formulated to assess the effects of incident beam energy, specimen/detector geometry and sample composition on the peak-to-background (P/B) ratio. These computations will assume that the sample is thin enough so that complications resulting from electron scattering, x-ray absorption and x-ray fluorescence can be neglected. Furthermore, instrumental factors associated with systems peaks, bremsstrahlung fluorescence, electron tails, and sample contamination are not considered since such artifacts must be eliminated in order to obtain meaningful x-ray results in all cases. A discussion of these artifacts and their minimization can be found in Sect. 2.2.7.

Let us consider an infinitely thin sample of thickness, dt. The number of characteristic x-ray photons emitted into the solid angle $d\Omega$ can from the previously described formalism be written as:

$$I_p^A = \frac{Q_A^K \cdot N_0 \cdot \bar{\rho} \cdot C_A \cdot \omega_A^K \cdot f_A^{K_\alpha} \cdot \eta_{AB}(t) \cdot dt \cdot d\Omega}{W_A \cdot 4\pi} \quad , \qquad (2.47)$$

where all parameters in Eq. (2.47) have been previously defined, the emission being isotropic over 4π steradians. The continuum intensity is, on the other hand, highly anisotropic and is strongly influenced by relativistic effects. The number of continuum photons within the energy window E_B to $E_B + dE_B$ emitted at an angle Ω with respect to the forward scattering direction is given by:

$$I_B = I_\Omega \cdot \frac{N_0 \cdot \bar{\rho} \cdot \eta_{AB}(t) \cdot dE_B \cdot dt \cdot d\Omega}{w_A \cdot E_B} , \qquad (2.48)$$

with

$$I_\Omega = I_\chi \left\{ \frac{\sin^2\Omega}{\left(1 - \beta\cos\Omega\right)^4} \right\} + I_y \left\{ 1 + \frac{\cos^2\Omega}{\left(1 - \beta\cos\Omega\right)^4} \right\} \qquad (2.49)$$

$\beta = v/c$ = relativistic correction factor.

I_χ and I_y in Eq. (2.47) are the continuum radiation components resulting from the slowing down of the electrons in the sample. The calculation of these components has been determined from the theory of Sommerfeld[72] by Weinstock;[73] however, the routine evaluation of his expressions is non-trivial. Kirkpatrick and Weidmann[74] have succeeded in obtaining the following analytic expressions for I_χ and I_y which are accurate to 2% relative to the more complex computations.

$$I_\chi = \left\{ \frac{0.252 + a_2(d_1 - 0.135) - b_2(d_1 - 0.135)^2}{c_1} \right\} \cdot 1.51 \times 10^{-28} \qquad (2.50)$$

$$a_2 = 1.47\ b_1 - 0.507\ a_1 - 0.833$$

$$b_2 = 1.70\ b_1 - 1.09\ \ a_1 - 0.627$$

$$a_1 = \exp\ (-\ 0.223\ c_1) - \exp(-57\ c_1)$$

$$b_1 = \exp(-0.0828\ c_1) - \exp(-84.9\ c_1)$$

$$c_1 = \frac{E_0}{300\ Z^2}$$

$$d_1 = \frac{E_B}{E_0}$$

$$I_y = \left\{-j_1 + \frac{k_1}{(d_1 + h_1)}\right\}\left\{\frac{1.51 \times 10^{-28}}{c_1}\right\} \qquad (2.51)$$

$$k_1 = \frac{-0.214\ e_1 + 1.21\ f_1 - g_1}{1.43\ e_1 - 2.43\ f_1 + g_1}$$

$$j_1 = (1 + 2h_1)f_1 - 2(1 + h_1)\ g_1$$

$$k_1 = (1 + h_1)(g_1 + j_1)$$

$$e_1 = 0.220\ [1 - 0.39\ \exp(-26.9\ c_1)]$$

$$f_1 = 0.067 + \frac{0.023}{(c_1 + 0.75)}$$

$$g_1 = -0.00259 + \frac{0.00776}{(c_1 + 0.116)}$$

Z = atomic number of specimen.

It should be noted that the preceding equations (2.48, 2.49, 2.50, and 2.51) have been rewritten using the MKS system of units rather than the Gaussian units found in the original work. The units of I_Ω become m^2/steradian/atom/electron when all energies are entered in electron volts.

A polar plot of the angular distribution of continuum x-ray radiation generated by 10 and 100 keV electrons incident on a pure nickel specimen ($Z = 28$) is shown in Figs. 28 and 29, respectively. The intensity in these figures has been normalized to $I(\Omega)/I_{max}$; thus in all

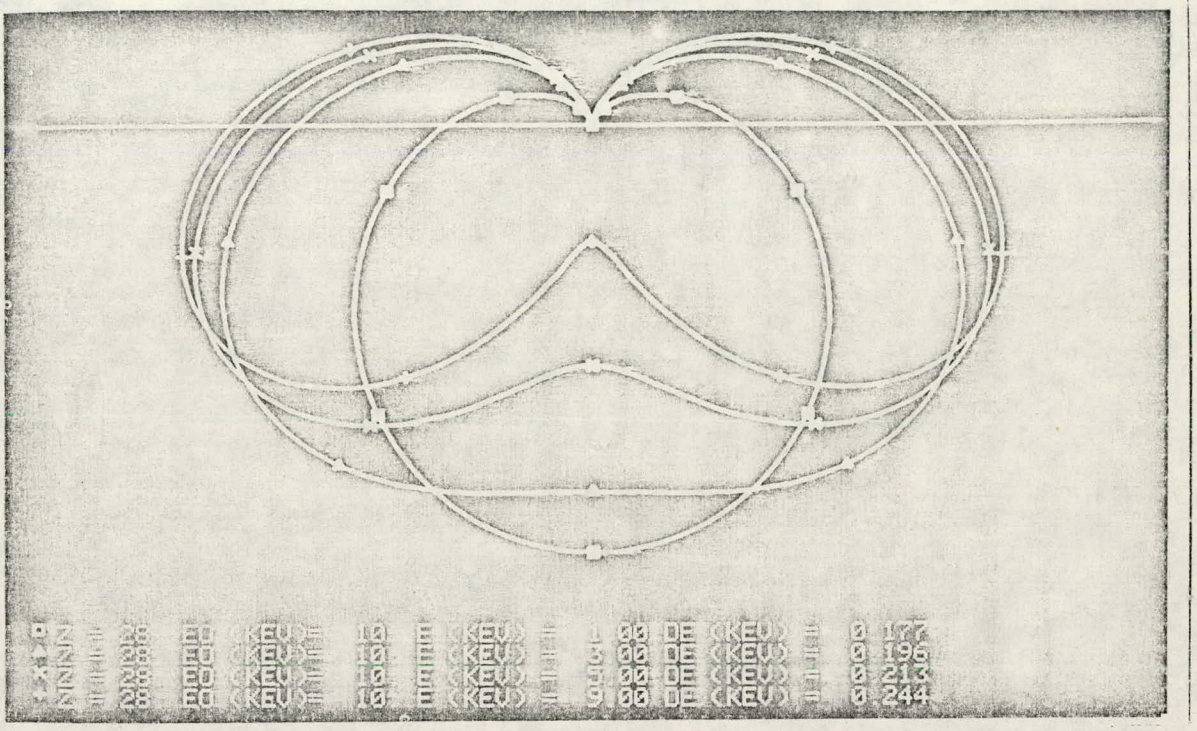

Fig. 28. Polar Plot of the Continuum Intensity Generated by a 10 keV Incident Energy Electron Beam on a Thin Foil at Various Values of Continuum Energy (E).

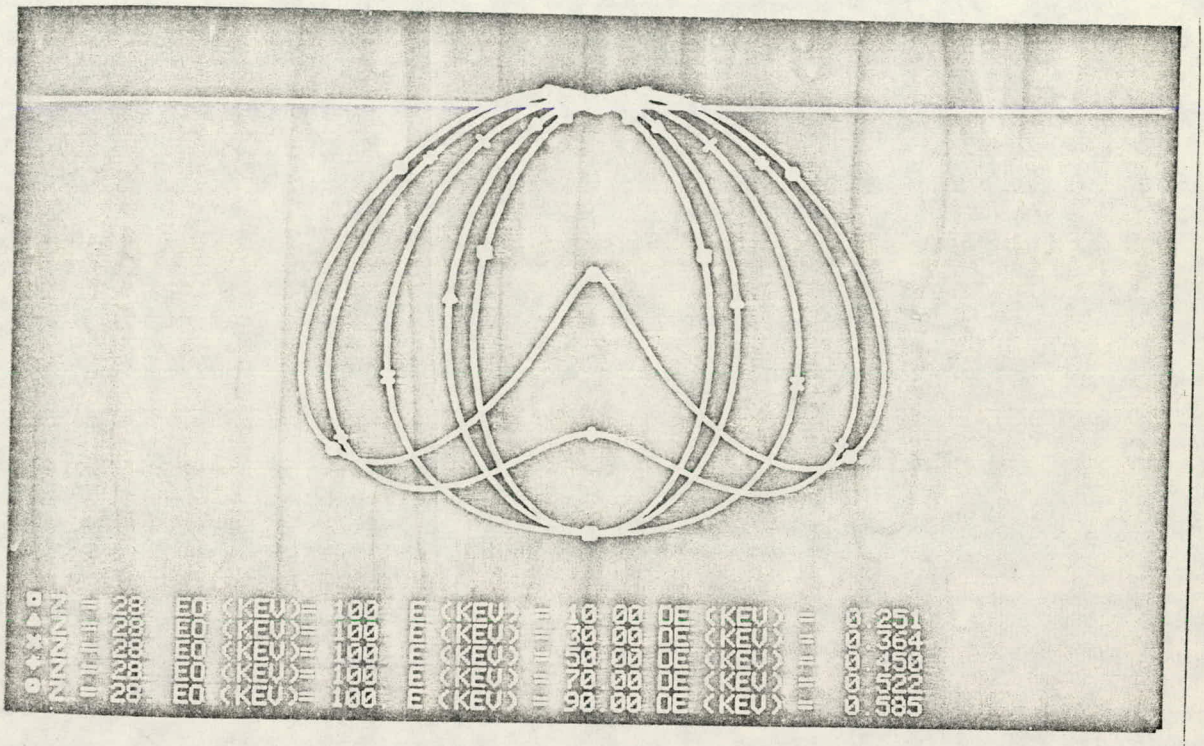

Fig. 29. Polar Plot of the Continuum Intensity by Electron Beam of Incident Energy of 100 keV on a Thin Foil for Various Values of Continuum Energy (E).

curves the maximum intensity plotted is unity. This is done in order that relative changes in the distribution can be easily observed. The intensity distribution is rotationally symmetric about the electron beam axis and is proportional to the radial distance from the point of incidence. These figures show that the continuum intensity on the electron entrance surface of the specimen ($\Omega \geq 90°$) is in general less than the exit surface, and also that relativistic effects (100 keV results) clearly shift the emission in the forward scattered direction. This is illustrated in more detail in Fig. 30. This figure shows the normalized continuum distribution of x rays in the vicinity of the nickel K_α peak ($\sim$7.5 keV) as a function of incident electron energy (E_0) over an energy window dE roughly corresponding to the full-width half maximum (FWHM) of the nickel K_α line. The relative intensity in any direction on the electron entrance surface clearly decreases with increasing E_0. Figure 31 reproduces the same calculations on an absolute scale; hence a direct comparison of the various intensities can be made. Note that in plotting this figure the 200 and 100 keV calculations have been truncated in the forward scattering direction for clarity. From these calculations it is apparent that the placement of the detector relative to the electron entrance surface is an important consideration.

The optimum position of the detector can now be evaluated by calculating the characteristic peak-to-background (P/B) ratio as a function of Ω using Eqs. (2.47) through (2.51). This is plotted in Fig. 32 for the same pure nickel sample as a function of observation angle (Ω) at various values of incident beam energy. We recall that the forward

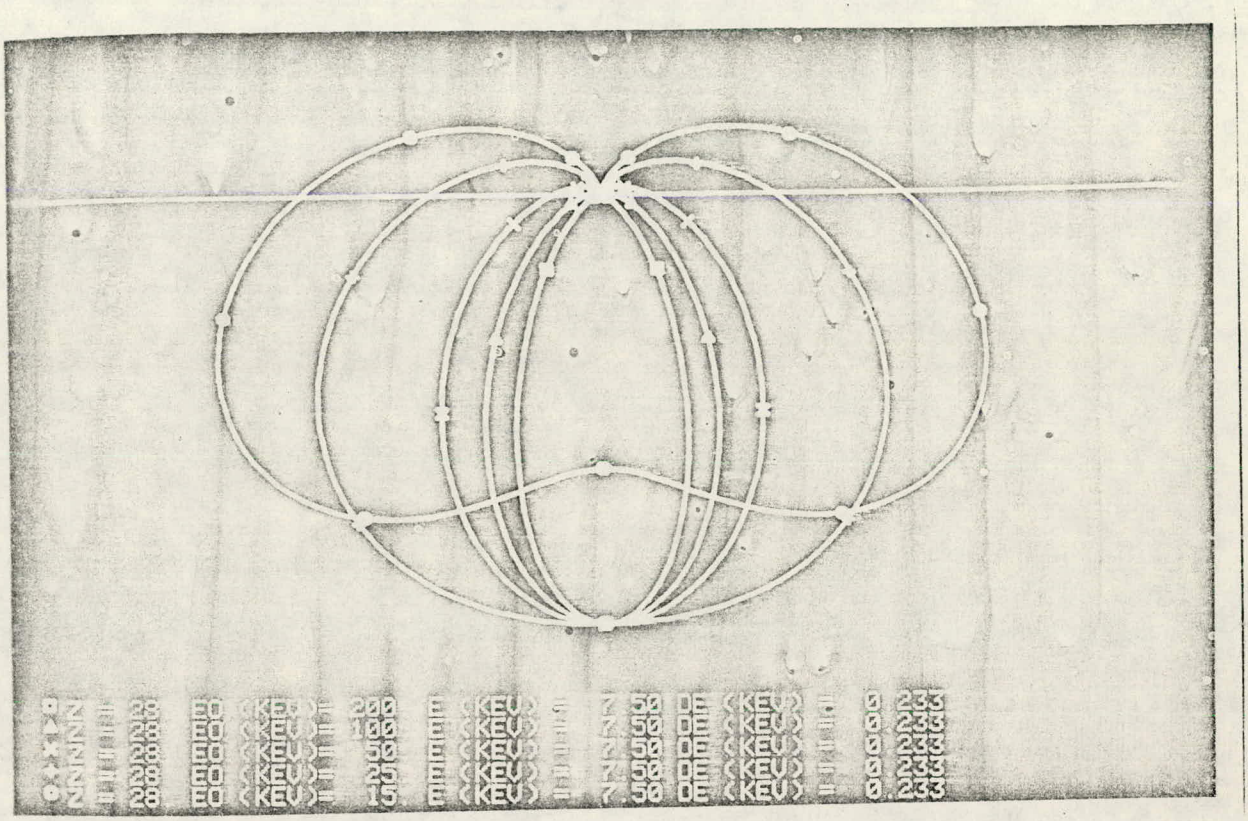

Fig. 30. The Angular Distribution of Continuum Intensity Generated (at 7.5 keV) by Various Energy Electron Beams. (All curves normalized to unity maximum intensity.)

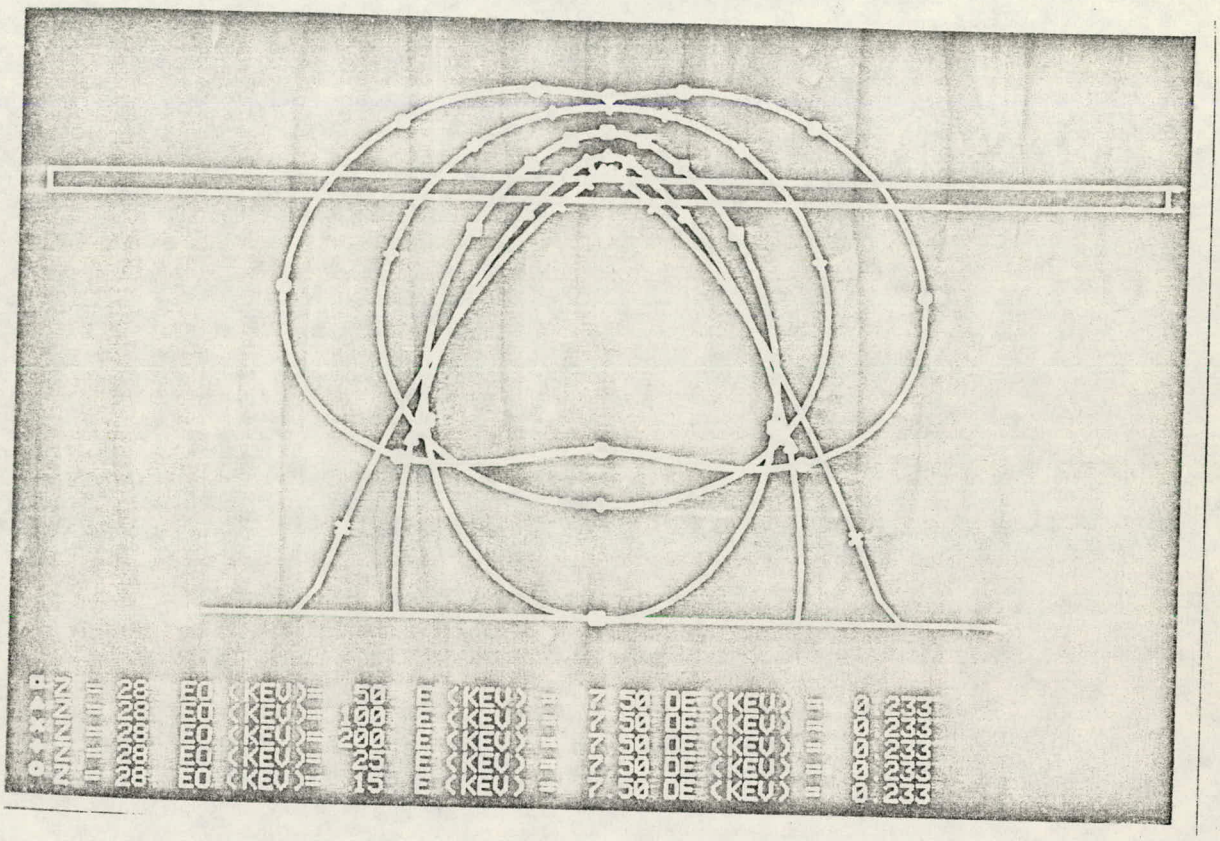

Fig. 31. The Angular Distribution of Continuum Intensity Generated (at 7.5 keV) by Various Energy Electron Beams.

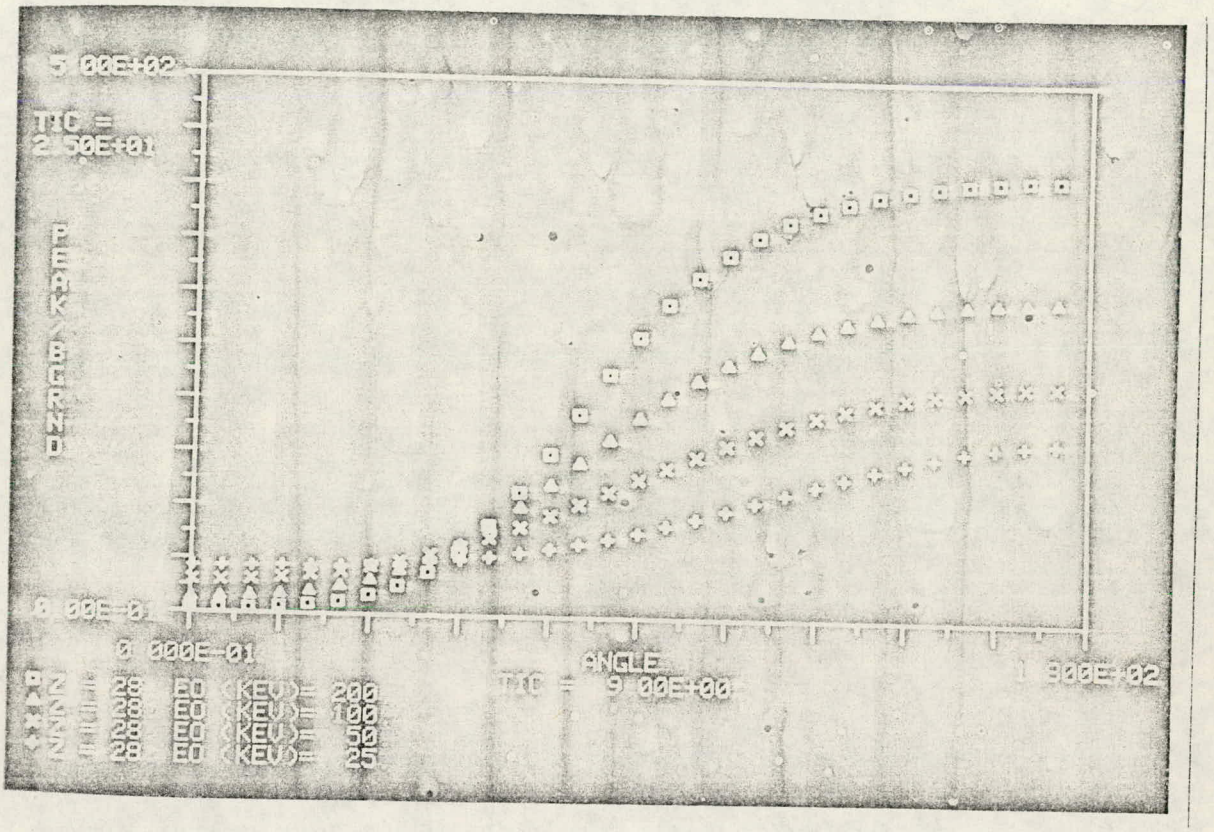

Fig. 32. Calculated P/B Ratio as a Function of Detector Observation Angle Ω at Various Values of Incident Electron Beam Energy.

scattering direction corresponds to an observation angle of 0° and in this position the detector axis is perpendicular to the electron exit surface. Similarly, $\Omega = 180°$ corresponds to the detector axis being colinear with the incident beam direction. Referring to Fig. 32 one can see that in all cases the P/B ratio is maximized when the x-ray detector is positioned on the electron entrance surface ($\Omega \geq \pi/2$). It is, however, interesting to note that the variation in P/B begins to level out at angles above 125° (at 100 keV). Thus, several of the new AEM instruments commercially available, such as the Vacuum Generators HB5, Hitachi H-500, and Philips EM-400 microscopes whose detector observation angles are $\geq 105°$, are approaching the optimum geometry for x-ray analysis.

Using the equations presented in this section, it is also possible to calculate the variation in P/B as a function of several other parameters. Figure 33 plots the change in the P/B ratio for the K_α line of pure elements (atomic number Z) at various values of incident energy. In computing these curves a detector observation angle of $\pi/2$, the geometry found in most CTEM/STEM instruments, was used. These results show a monotonic increase in P/B with increasing E_0 for all elements. The sharp drop at Z = 45 corresponds to a change in the calculation from K_α to the L_α line. Extended calculations for incident energies greater than 1 MeV indicate a continuous increase in P/B to nearly 2.5 times the 100 keV values (see Fig. 34). However, the extrapolation of these equations to such energies is questionable; thus only the trends should be considered.

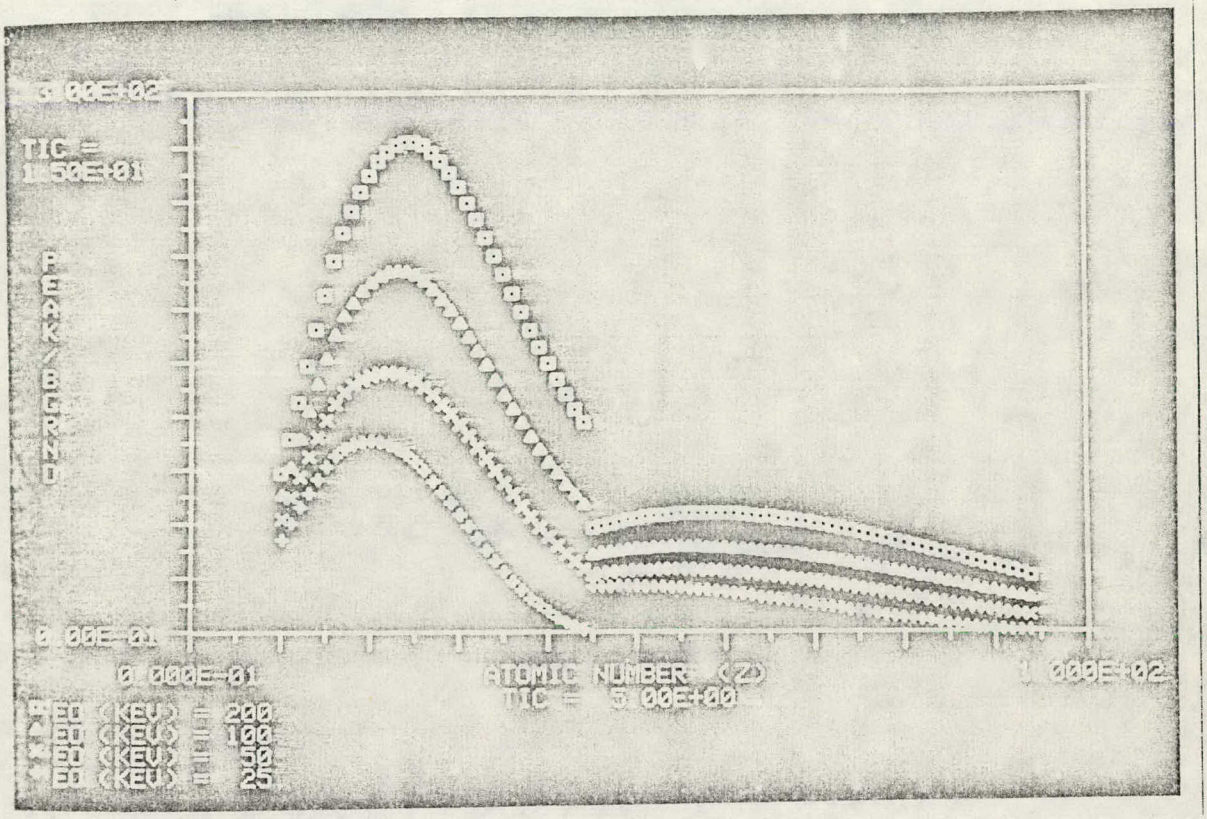

Fig. 33. Calculated P/B Ratio for Pure Element Samples as a Function of Incident Beam Energy.

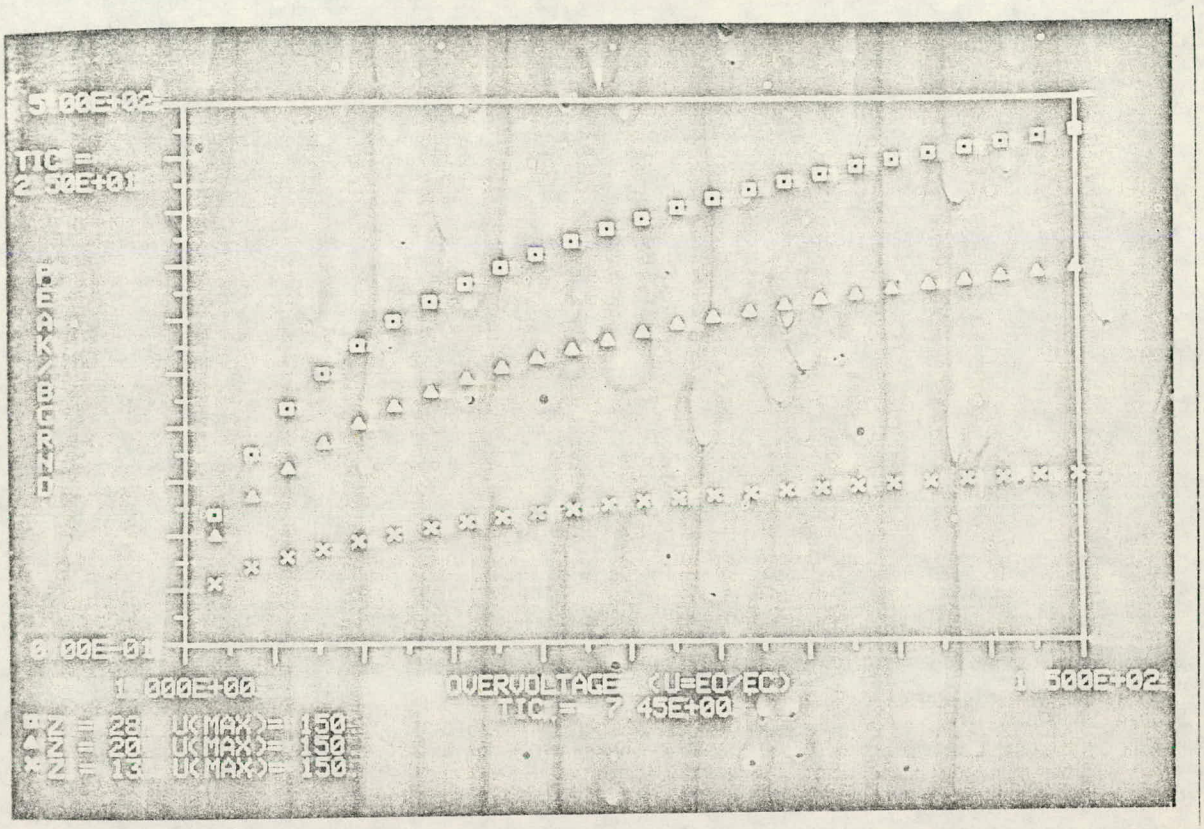

Fig. 34. Calculated P/B Ratio as a Function of Overvoltage for Various Elements.

Finally by substituting different values of Z, W, and $\bar{\rho}$ into the characteristic and continuum equations, respectively, it is possible to evaluate the P/B ratio for one element in a matrix of different (or average) atomic number (Z_{av}). Such a calculation is presented in Fig. 35 which shows, as would be expected, a monotonic decrease in the P/B ratio with increasing matrix atomic number (Z_{av}) at constant electron energy. Similarly, Fig. 36 shows a monotonic decrease in the P/B ratio with decreasing E_0 for a constant matrix composition. In calculating both these figures, C_A in Eq. (2.47) was set to unity; thus, in any comparison with experimental data the value of P/B predicted should be multiplied by the composition in weight percent.

In summary, these calculations have demonstrated that the maximum theoretical sensitivity is obtained by placing the x-ray detector with an observation angle $\Omega \geq \pi/2$, using the highest value of incident beam energy, and minimizing (when possible) the average atomic number of the matrix.

2.2.7 Instrumental Factors Influencing X-Ray Analysis

Although the coupling of a solid state Si(Li) x-ray detector to a transmission electron microscope affords the possibility of performing microchemical analysis of thin specimens on a scale of several hundred angstroms or less, there are several experimental aspects of this technique which limit its applicability. Furtunately, these factors are purely instrumental in nature and can be reduced or eliminated by judiciously modifying the analytical system. Three topics will be considered in this

ORNL PHOTO 5790-78

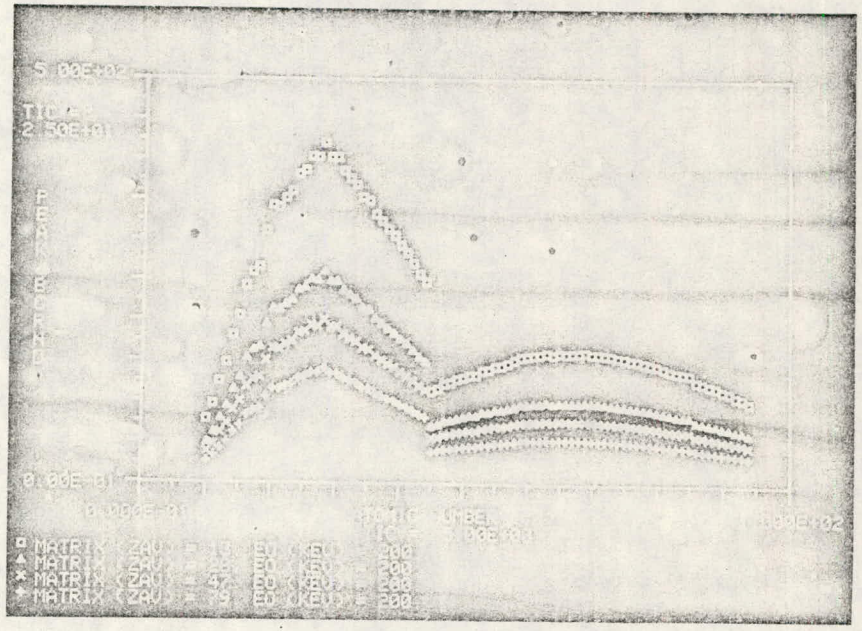

ORNL PHOTO 5793-78

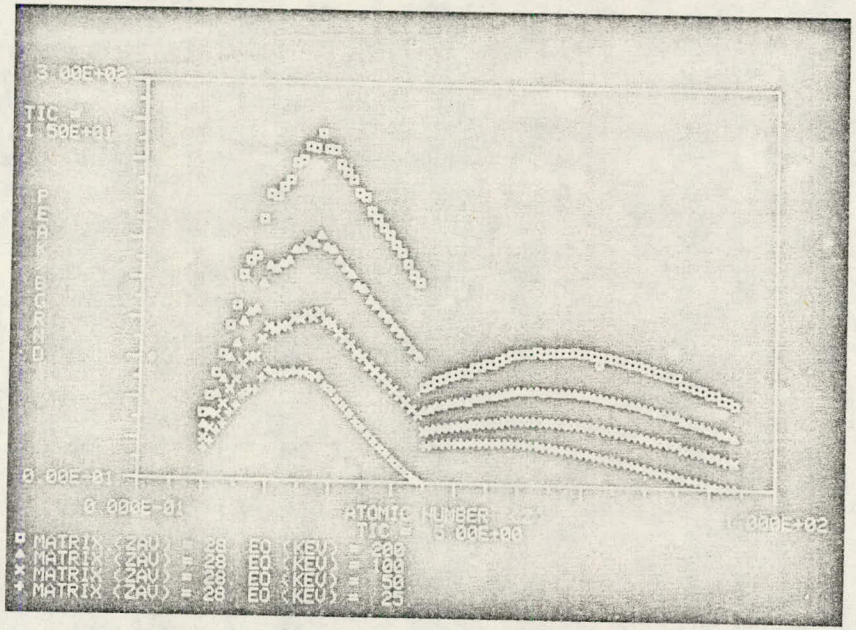

section – namely: systems peaks; fluorescence by uncollimated radiation; and specimen contamination effects. These problems are found in all electron microscopes; however, their relative magnitude changes from one instrument to another. In all cases, it is important that these artifacts be identified and eliminated since they affect the qualitative as well as quantitative analysis detrimentally.

System Peaks: When a solid state Si(Li) x-ray detector is used to measure the x-ray emission produced in an electron microscope, a spectrum consisting of several characteristic peaks superimposed on a continuum or background intensity distribution is observed. Ideally, this spectrum is a result of electron-induced excitation of the sample; unfortunately, x rays are also produced in the material immediately surrounding the sample (i.e., the sample stage, aperture drives, cold finger, etc.) by mechanisms other than direct electron excitation, and hence are recorded simultaneously with the sample spectrum. Although it is usually possible to identify these "systems peaks" it is important to eliminate them rather than simply account for their presence.

The reduction of system peak intensity is accomplished by replacing the material surrounding the specimen by an element which does not produce detectable x rays. Several stages have been designed for this purpose; they were constructed from graphite[75] or plastic (PMMA).[76] However, they are severely limited in their in-situ tilting capabilities making them unsuitable for analytical microscopy. Thus, a modified design of gimbal cup was developed for use in the double-tilt stage supplied with the JEOL JSEM 200 keV CTEM/STEM.[77] Machined totally out

of graphite this cup provides full two-axis-tilting capabilities along with the reduction of systems peaks. Since this time, several researchers have developed total specimen stages machined from beryllium[78,79] and graphite[80] which provide equivalent capabilities as well as high mechanical stability. A brief description of the modified gimbal cup for the JEOL double-tilt stage developed in this research follows.

Shown in Fig. 37 is a schematic diagram of the x-ray geometry in the JEOL JSEM 200 with the incident electron beam being normal to the plane of the page. Optimization of the x-ray count rate is accomplished through the use of a double-tilt stage, which allows tilting of the specimen about two mutually perpendicular axes. The primary axis (A-A′ in Fig. 37) can be tilted by ±55° and the secondary axis (B-B′ in Fig. 37) by ±45°. An ORTEC Minitec Si(Li) x-ray detector is mounted on the microscope column normal to the incident electron beam (i.e., a detector observation angle $\Omega = \pi/2$ defined in Sect. 2.2.6) and at an azimuthal angle of 45° to the primary tilt axis. The front of the detector is protected by a 7.5-μm-thick beryllium window and the specimen-to-window distance is approximately 2 cm. Through the use of a graphite collimator the x-ray acceptance angle (θ in Fig. 37) is $\sim$15°; i.e., the detector accepts radiation from roughly a 0.5-cm-dia disk at the specimen surface.

There were two purposes in redesigning the specimen holder. The first was to remove the interference in the recorded x-ray spectrum due to the "system peaks" generated in the specimen cup. The original cup is machined from a Cu-Be alloy and removal of the "system peaks" from it

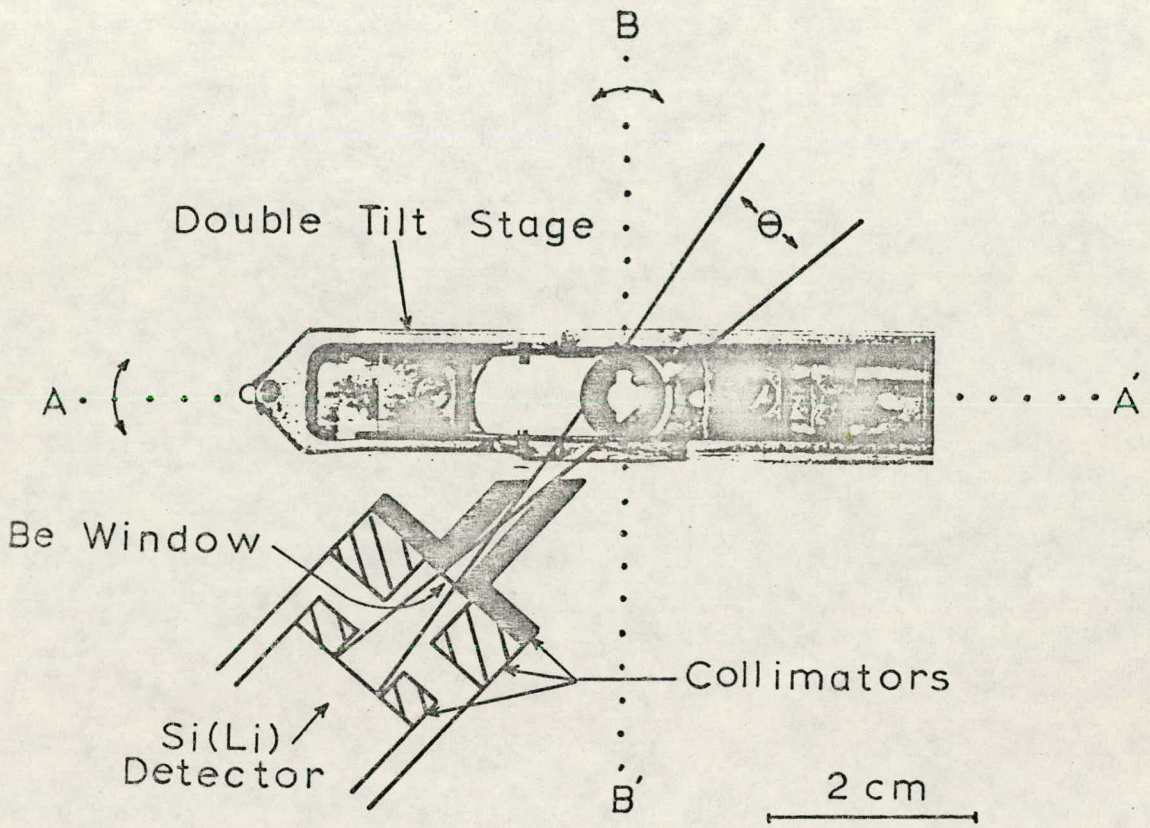

Fig. 37. Schematic Diagram of the X-Ray Geometry in the JEOL JSEM 200.

is accomplished by replacing this alloy by an alternate material. Beryllium would be the best choice; however, due to the hazards involved in its machining, graphite was chosen as an alternative. The second purpose was to increase the range of take-off angles in which usable x-ray information can be obtained. In the original design [Fig. 38(a)], the sample is held in position by a copper retaining spring on the underside of a ledge. This serves to severely restrict the angular range from which x rays generated in the sample can be seen by the detector. Figure 38(b) shows the changes which have been made to the specimen cup geometry. First the interior design of the cup has been inverted so that the sample now rests on top of a small ledge and is no longer overshadowed by a large mass of material. Secondly the excess material around the top of the cup, which served as a further restriction to the x-ray take-off angle, has been machined away as much as possible. The only restrictions on this last change are that sufficient material be left perpendicular to axis B-B′ so that the friction drives for the tilt mechanism can still operate normally. It also becomes important to replace the copper retaining spring used to hold the sample rigidly in position. Since no suitable spring substitute is available, the sample is now held in place by the judicious application of a colloidian of graphite along the specimen's edges, or on a thin graphite washer used to hold the sample in position.

A homogeneous alloy of β-NiAl was used as a test specimen to evaluate the characteristics of the two types of specimen cups (Cu-Be versus graphite). When determining the characteristics of both cups,

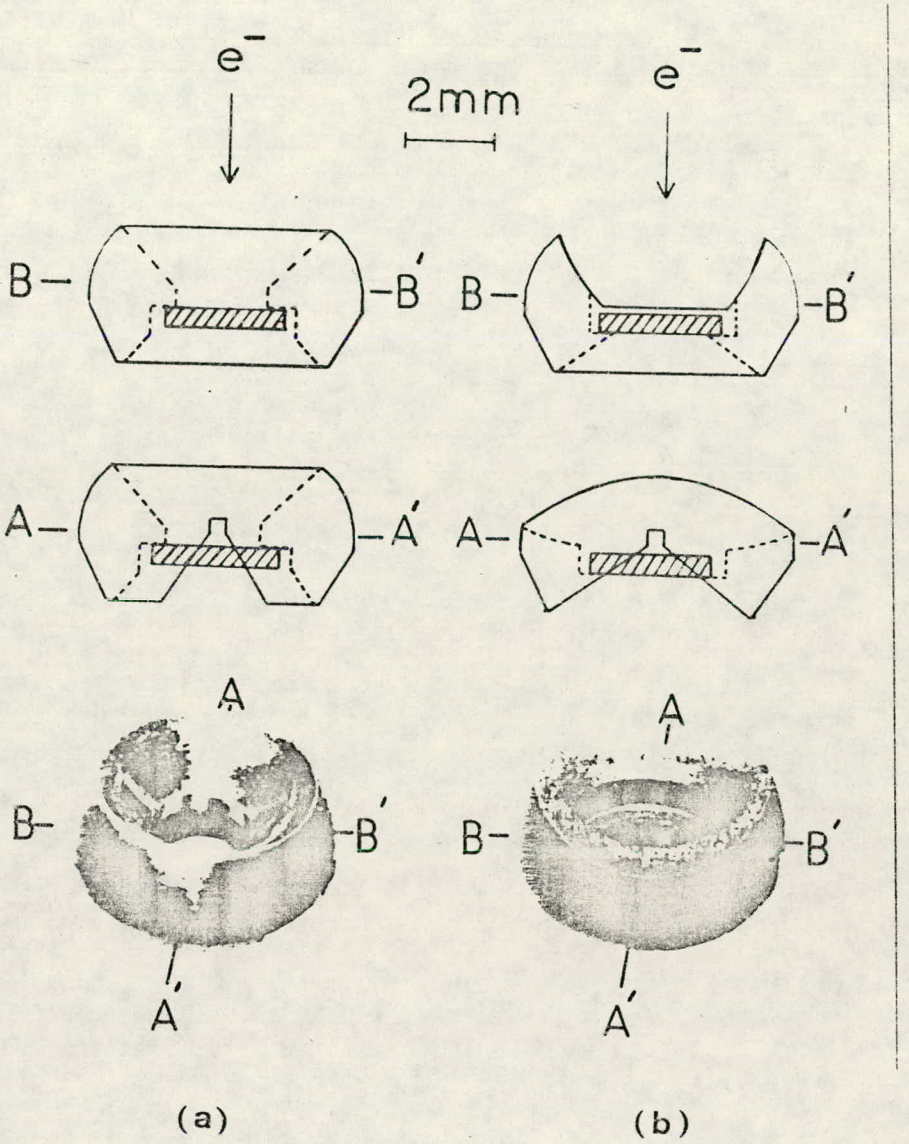

Fig. 38. Modified Design of Specimen Cup to Reduce System Peaks.

care was taken so that the sample was imaged under identical operating conditions and orientations. The microscope was operated with an accelerating voltage of 200 keV and in the STEM mode, so that electron probe diameters of approximately 50 Å could be realized. All x-ray spectra were recorded under these conditions.

Typical spectra obtained using both cups are shown in Fig. 39. It is evident that the removal of the Cu-Be from the immediate vicinity of the sample has substantially reduced the interference from "system peaks." The effect is most pronounced when one considers the CuK_α and NiK_β lines in the emission spectrum. The NiK_β line in Fig. 38(a) has been completely masked by the CuK_α peak. However, when a graphite cup is used, the NiK_β line becomes clearly resolved and the interference due to the CuK_α line is substantially reduced [Fig. 39(b)]. Using a computational technique for profile fitting,[60] it is possible to analyze the extent of overlap of these two peaks. The measured CuK_α/NiK_β ratio is 2.27 ± 0.28 and 0.19 ± 0.03 for the Cu-Be and graphite gimbals, respectively. Thus, a net reduction by a factor of 12 of the CuK_α intensity is achieved. Such reductions are typical; however, "system peaks" from the Cu-Be cup are dependent on the orientation of that cup with respect to the incident electron beam and detector system and changes in this ratio can be expected.

It should be noted that even after removal of one of the most important sources of "system peaks" it is still possible to detect interference. This indicates that the scattered radiation (elastic and inelastically scattered electrons and bremsstrahlung) in the microscope

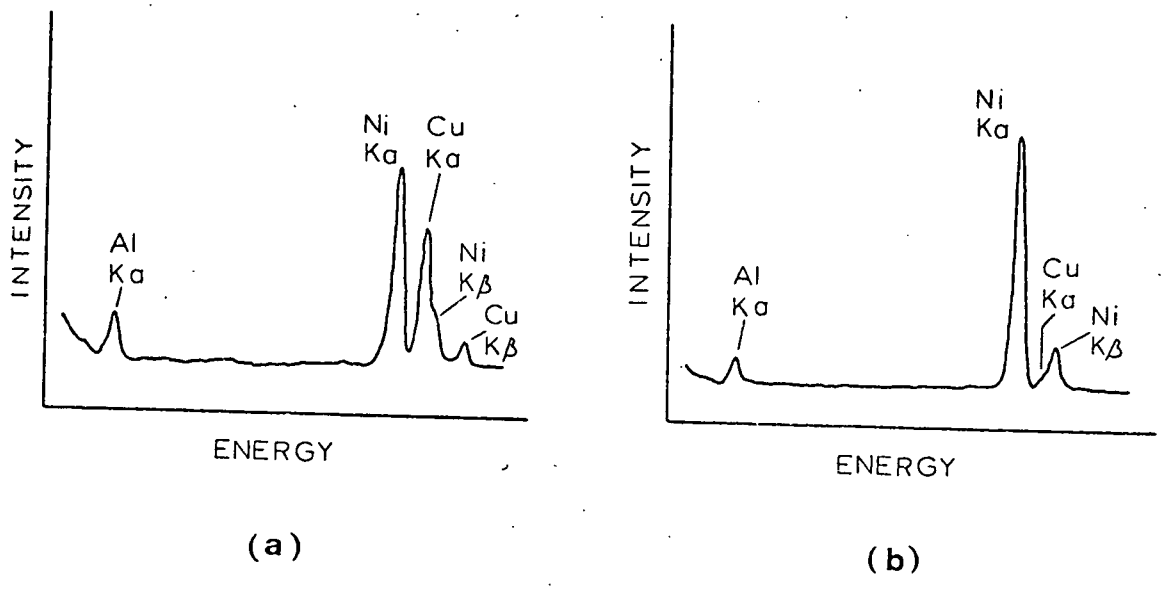

Fig. 39. Comparison of Systems Peak Intensity (a) Before, and (b) after Modified Specimen Cup Design was Introduced into JSEM 200.

is a significant source of x-ray excitation as seen by the detector, and, in addition, it shows that large areas in the specimen region are still being excited.

The importance of eliminating system peaks can be seen by reference to Fig. 40. Shown is a micrograph of a region of a silicon sample containing impurity precipitates. These defects have two distinct morphologies – one rod-like, and the second in the form of spherical precipitates arranged roughly in rows. Surrounding this micrograph are x-ray spectra recorded from the various regions indicated, showing that these precipitates are nickel- and copper-rich, respectively. Furthermore, the matrix spectrum shows only the presence of a SiK_{α} peak; hence the elemental nature of these impurities is indeed confirmed. Had the copper system peaks not been eliminated in this experiment, it would not have been possible to uniquely identify the copper-rich impurity because of the minute amount present. In addition, due to the similarly weak intensity of the nickel line analysis in the presence of a large copper systems peak would have been difficult if not impossible. Thus, for the case of low concentration or small volume fraction precipitates, it is essential to remove all systems peaks.

Fluorescence by Uncollimated Radiation: One of the serious instrumental problems associated with TEM-based microanalysis arises due to nonlocalized excitation of characteristic x rays from the sample. Referring to Fig. 39, it can be noticed that even though a 50 Å electron probe was used to generate x rays in the sample a significant volume of material must have been irradiated in order to produce the magnitude of

ORNL PHOTO 5806-78

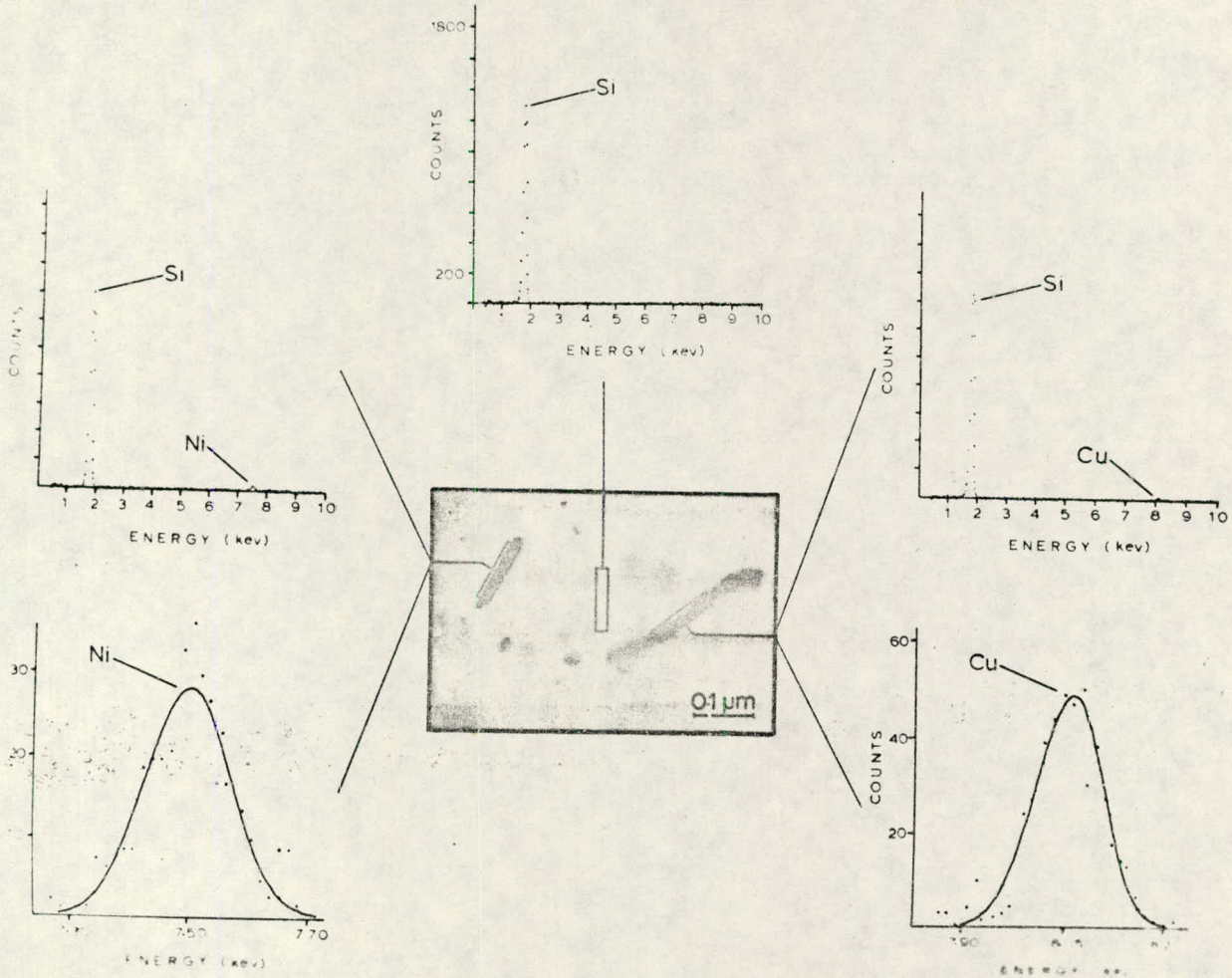

systems peaks which were detected. The removal of medium to high atomic number material from the immediate vicinity of the sample clearly reduces the intensity of systems peaks; however, it is only a cosmetic solution since the effective irradiated volume has not been significantly altered. This poses the following questions. What is the source of the uncollimated radiation, and how does it affect microanalysis?

There are essentially three potential sources of radiation which can induce emission from the specimen. They are:

1. the incident electron probe,
2. uncollimated electrons and x rays produced by the sample,
3. uncollimated electrons and x rays produced by the electron microscope hardware.

The first two sources are basic to the generation process and thus cannot be eliminated. The last term, however, can be further subdivided into two sections – those uncollimated x rays and electrons related to the hardware immediately surrounding the sample (pole pieces, apertures, cold fingers, etc.) and that which is produced elsewhere in the electron-optical column. This first factor is effectively minimized by constructing suitable low atomic number substitutes for various parts of the microscope,[75–81] and amounts to the systems peak correction discussed in *Systems Peaks*. The second term is extremely important and has been shown to be one of the most significant sources of nonlocalized radiation.[43] When present, it can become the limiting factor in both spatial resolution and quantitative analysis. This effect can become so great in some instruments that errors in excess of several hundred

percent can easily develop. The remainder of this discussion will center upon the identification of this radiation and its effects on micro-analysis. The examples given were obtained using a JEOL JSEM 200 CTEM/STEM instrument, but can also be observed in other electron microscopes with varying magnitude.

When an electron beam is positioned on a specimen, it is generally assumed that all characteristic x rays emitted from the sample are generated in the volume defined by that probe. If this is the case, then, when the probe is translated off the sample all x-ray emission should cease (assuming, of course, that the electron column is properly aligned). More often than not an x-ray spectrum from the sample will still be detected and the magnitude of this emission can be substantial. This is illustrated in Figs. 41, 42, and 43, which are typical spectra obtained when the probe is incident on the sample (a) and then allowed to pass through the perforation formed during the sample preparation (b) for incident electron energies of 200, 100, and 50 keV, respectively.

These spectra were accumulated using the experimental geometry described in *Systems Peaks*. The sample used was a three millimeter single-crystal disc of β-NiAl of the 50/50 at. % composition. The specimen was electropolished to TEM quality using standard techniques[82] and had a small perforation approximately 40 μm in diameter near the center of the foil. All spectra were recorded for 200 s with the microscope operating in the STEM mode and using electron probe diameters of approximately 50 Å. Measurements were made by positioning the probe

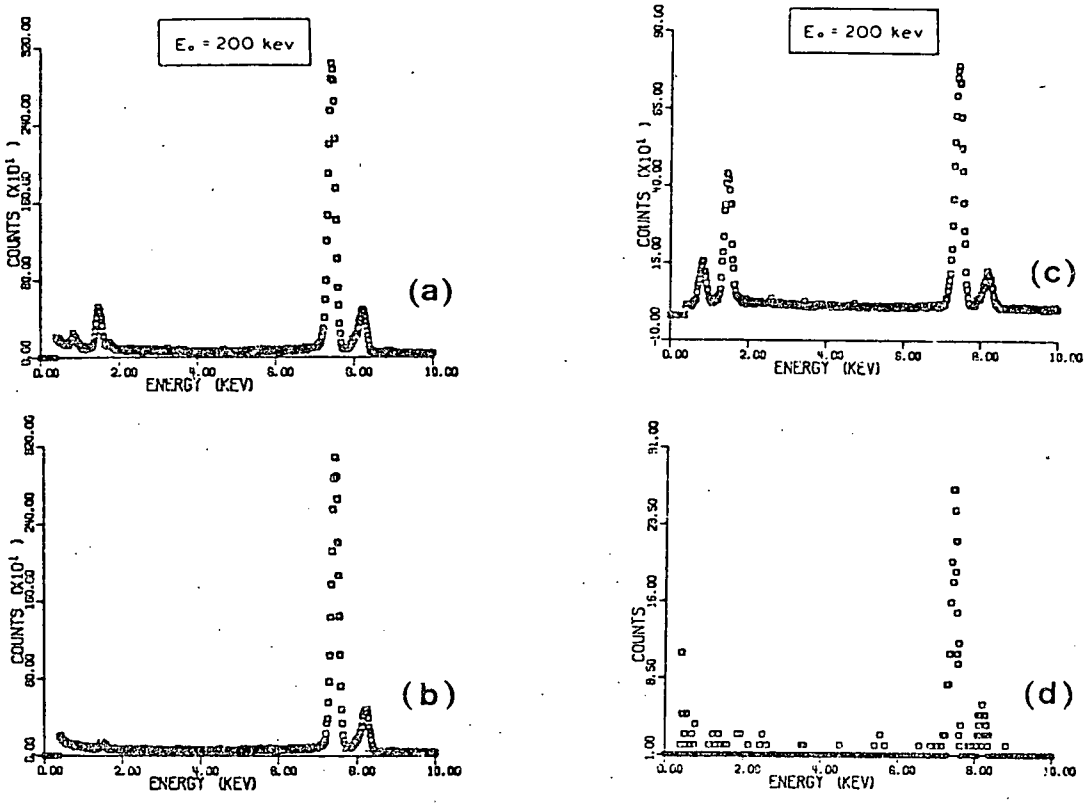

Fig. 41. Sample (a) and In-Hole Spectra (b) before Installation of Bremsstrahlung Aperture. Sample (c) and in-hole spectra (d) after installation of bremsstrahlung aperture. E_0 = 200 keV.

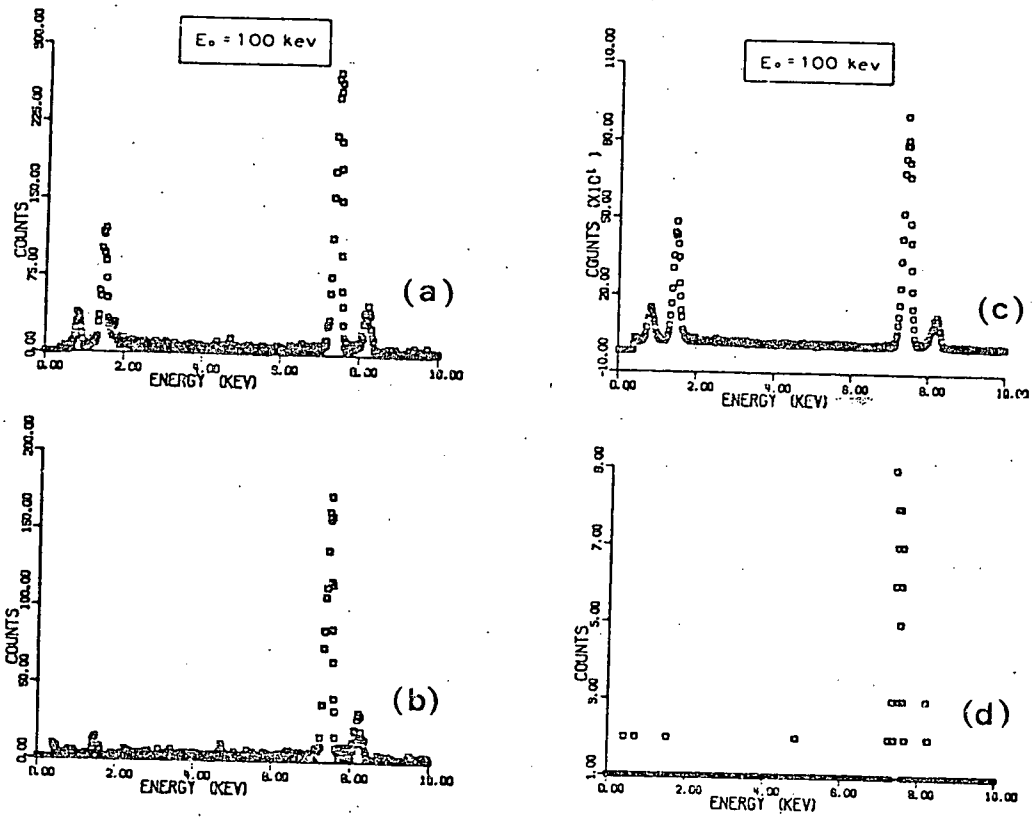

Fig. 42. Sample (a) and In-Hole Spectra (b) before Installation of Bremsstrahlung Aperture. Sample (c) and in-hole spectra (d) after installation of bremsstrahlung aperture. E_0 = 100 keV.

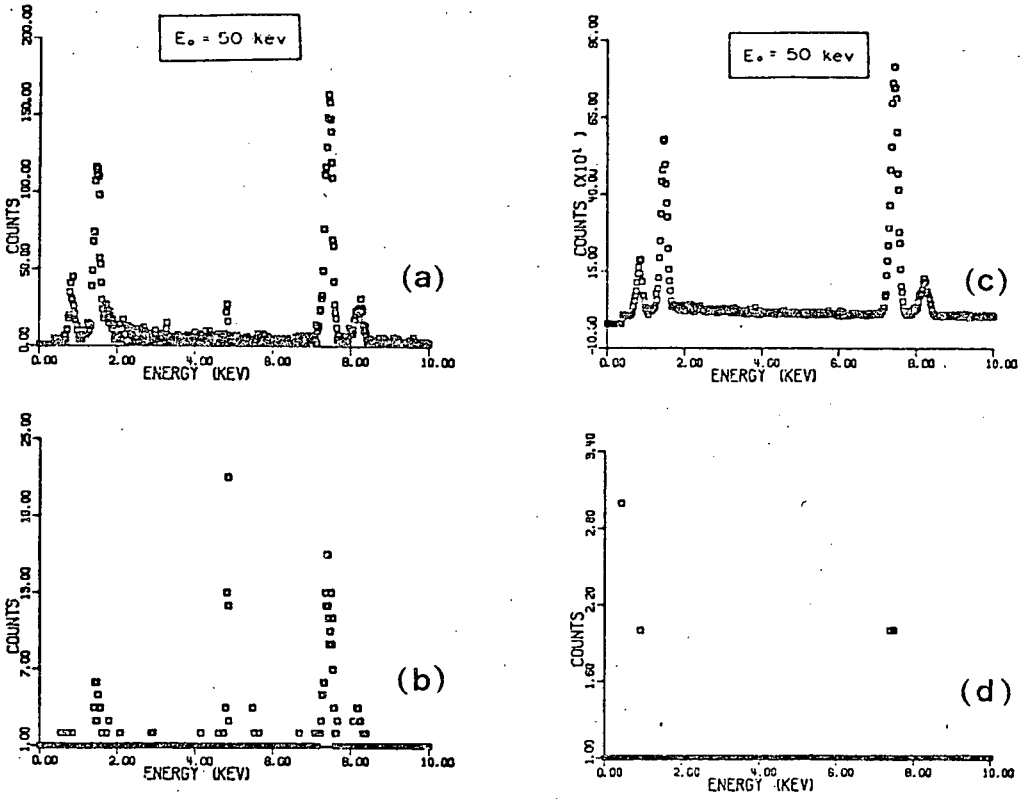

Fig. 43. Sample (a) and In-Hole Spectra (b) before Installation of Bremsstrahlung Aperture. Sample (c) and in-hole spectra (d) after installation of bremsstrahlung aperture. E_0 = 50 keV.

on an electron transparent region near the edge of the foil (position A, Fig. 44) while "in-hole" counts were obtained by translating the probe into the perforation at least 2 μm from the foil edge (indicated as B, Fig. 44).

Examining these spectra one can see that under certain operating conditions the "in-hole" spectrum can exceed 90% of the total emission measured from the sample. Furthermore, one can detect an appreciable atomic number effect in the excitation of characteristic x rays by this uncollimated radiation. The excitation of the nickel K lines is several orders of magnitude greater than aluminum. The effects of this radiation on microanalysis are even more pronounced and are shown in Fig. 45. Plotted is the experimental variation in the Ni/Al K_α intensity ratio as a function of sample thickness for various electron energies. The broken curves under each set of experimental measurements represent the theoretical calculations based on the formalism previously described. One would expect the intensity ratio to be constant initially until a sample thickness is reached when absorption effects become appreciable. At this point, absorption of the lower energy aluminum K_α x rays should cause the ratio to increase monotonically. Experimentally this is not observed. Initially one measures a decrease in the Ni/Al ratio with increasing thickness followed by an inflection point and then a gradual increase in the ratio. This monotonically increasing region interestingly roughly parallels the calculated variation corresponding to the region of high aluminum absorption. Furthermore, a systematic shift in the inflection point toward thinner regions occurs with decreasing

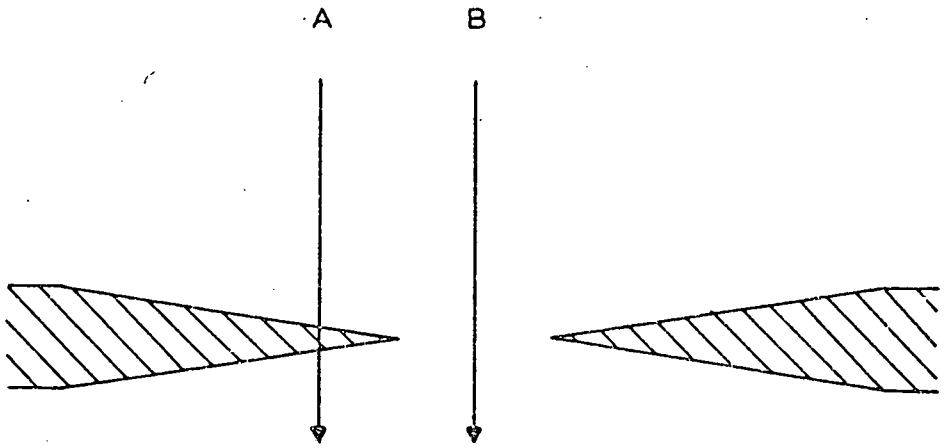

Fig. 44. Schematic Illustration of Electron Probe Position during Sample Measurement (A) and In-Hole Measurement (B).

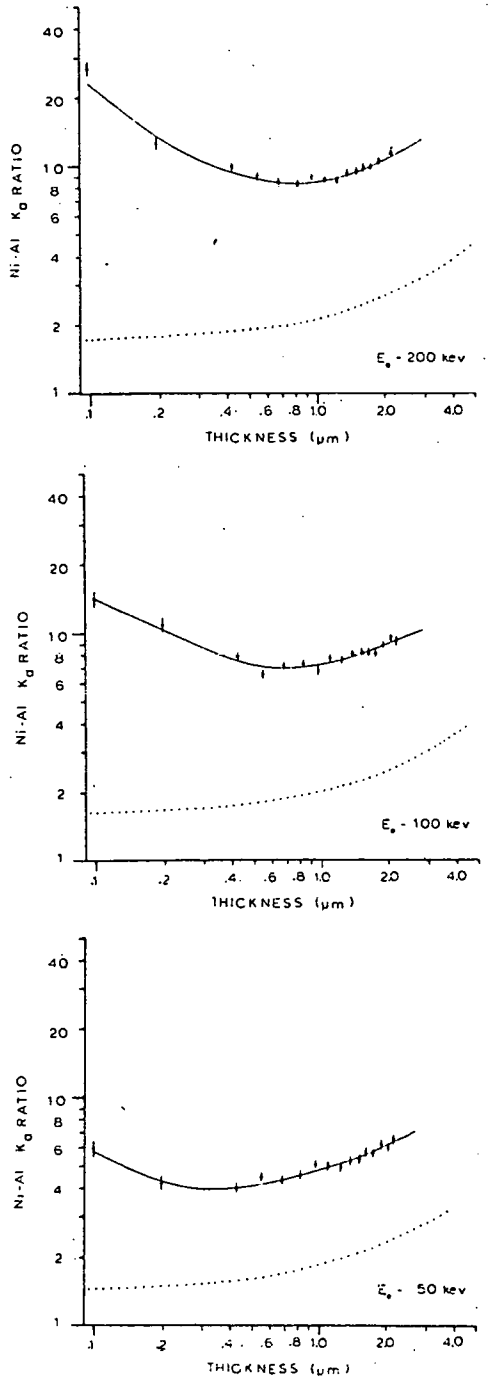

Fig. 45. Plot of Measured Ni/Al Ratio as a Function of Sample Thickness at Various Incident Beam Energies. Broken curve indicates calculated variation.

incident energy. It should be noted that at 200 keV the sample was just barely transparent to electrons at the last data point plotted ($\sim$2 μm). Thus, to measure the intensity ratio at these last few points using lower accelerating voltages it was necessary to operate the STEM unit in the SEM mode, the electron probe being positioned by observing the contamination marks on the sample surface produced during the 200 keV measurements. It is apparent from these data that serious discrepancies exist between experimental and calculated intensities, and it would seem that quantitative analysis under such conditions is impossible.

The breakdown of the theory of quantitative analysis in this case can be traced directly back to the first assumption made in the calculations. That is, it was assumed that all x-ray emission from the sample is a direct result of electron excitation of a microvolume of material. Should there be any additional sources of x-ray excitation they must either be eliminated from the instrument or included in the calculations. The question then still remains as to the nature and the source of this anomalous excitation. Considering closely the characteristics of the "in-hole" spectra as well as their variation with accelerating voltage it was postulated that high energy bremsstrahlung radiation generated in the condenser-aperture system of the electron microscope could account for these experimental results. The following experiment was then devised to test the feasibility of this hypothesis.[83]

The microscope was aligned in the usual manner and an in-hole spectrum from β-NiAl was confirmed. The variable condenser-aperture drive was then removed and the aperture assembly, which was originally

constructed from a Cu-Be alloy, was replaced by a 3-mm-thick lead substitute having a single 200-μm aperture. This lead aperture was replaced in the column and the in-hole effect reproduced. The next step was to cover the 200 μm aperture by a thin lead foil approximately 15 μm thick and replace the entire assembly. This foil is of sufficient thickness that all electrons bombarding the condenser aperture are stopped; however high energy bremsstrahlung radiation generated by the electrons slowing down in this foil can still be transmitted. When this modified aperture was inserted and the instrument returned to normal operating conditions it was still possible to measure an x-ray emission spectrum of NiAl even though all electrons were prevented from striking the sample. From this result one can suggest an explanation of the anomalous results obtained previously as well as propose an effective solution.

Bremsstrahlung radiation, created principally in the thin regions of the condenser apertures, is continuously bombarding the sample area. This radiation is highly peaked in the forward scattering direction and is limited spatially only by the bore of the microscope column. It is then entirely likely that characteristic emission from the sample and surrounding material is induced by an x-ray fluorescence mechanism. This emission will be recorded simultaneously with that produced by electron irradiation of the specimen and is independent of electron probe position on the sample. It is also probable that this fluorescence emission will exceed that produced by direct electron excitation since the fluorescence is of essentially a bulk specimen while the electron-induced fraction results only from the microvolume of material defined by a 100 Å electron

probe. It would also be expected that the intensity ratio of Ni/Al will be relatively high, when compared to electron excitation, since the efficiency of x-ray fluorescence of low atomic number material ($Z < 20$) is poor.

One can then postulate the following sequence of events. In the thinnest region of the foil the measured ratio is dominated by the bulk x-ray fluorescence effects. As the electron probe begins to sample thicker and thicker regions the relative contribution of the electron excitation will increase and eventually exceed the bremsstrahlung contribution. Initially, one would expect a decrease in the measured ratio of Ni/Al to a point at which electron excitation begins to dominate and then it would be expected that the variation in the ratio would begin to follow the theoretically predicted curves. Furthermore, if the relative contribution of the bremsstrahlung radiation is decreased – for example, by lowering the accelerating voltage – then the crossover point of dominance of bremsstrahlung versus electron excitation should shift to thinner regions. All of these effects are clearly demonstrated in Figs. 41, 42, 43, and 45, and when combined with the results of the lead aperture experiment suggest stongly that the source of anomalous emission is x-ray fluorescence.

To attempt a theoretical calculation of a correction to this phenomenon is difficult due to a lack of sufficient information concerning the precise source and magnitude of this radiation. Thus, one must attempt to modify the electron-optical column in such a way as to minimize

or eliminate this radiation from reaching the specimen. The ideal solution to such a problem is to deflect the incident electron probe around a thick x-ray stop, much as is used in high voltage electron microscopes (HVEM) to prevent ion bombardment of the sample. Realistically this requires significant modifications of the electron-optical column, and furthermore would probably result in significant aberrations, and so a simpler solution is necessary. An alternate solution would be to reduce the total x-ray flux bombarding the sample by special collimators;[83] it is by far the easier method, as illustrated in Fig. 46.

This has been accomplished successfully on the JSEM 200 using two different designs of collimators. The first and simplest design is to insert a thick (>2 cm) aperture in the column below the condenser aperture, which reduces the bore of the column from 1 cm to 0.5 mm. This does not interfere with the electron optics, yet substantially reduces fluorescence effects. Two eccentric cylinders are used in this case as shown in Fig. 47. The center and innermost cylinder is aligned with the electron-optical axis by rotating the two cylinders with respect to each other and the column. Such an arrangement was necessary because in this instrument the mechanical axis and the electron-optical axis were not precisely aligned. Later, a more elaborate aperture system was installed and is shown in Fig. 48. Externally adjustable, this bremsstrahlung aperture is mounted on the column in the vacant region normally occupied by a top-entry stage insertion mechanism (Fig. 49). The housing is composed of lead, while the actual aperture (0.5 mm × 2 cm) was machined from brass to facilitate removal and cleaning when necessary. Also mounted on the aperture mechanism is a Faraday cage to monitor the incident probe current.

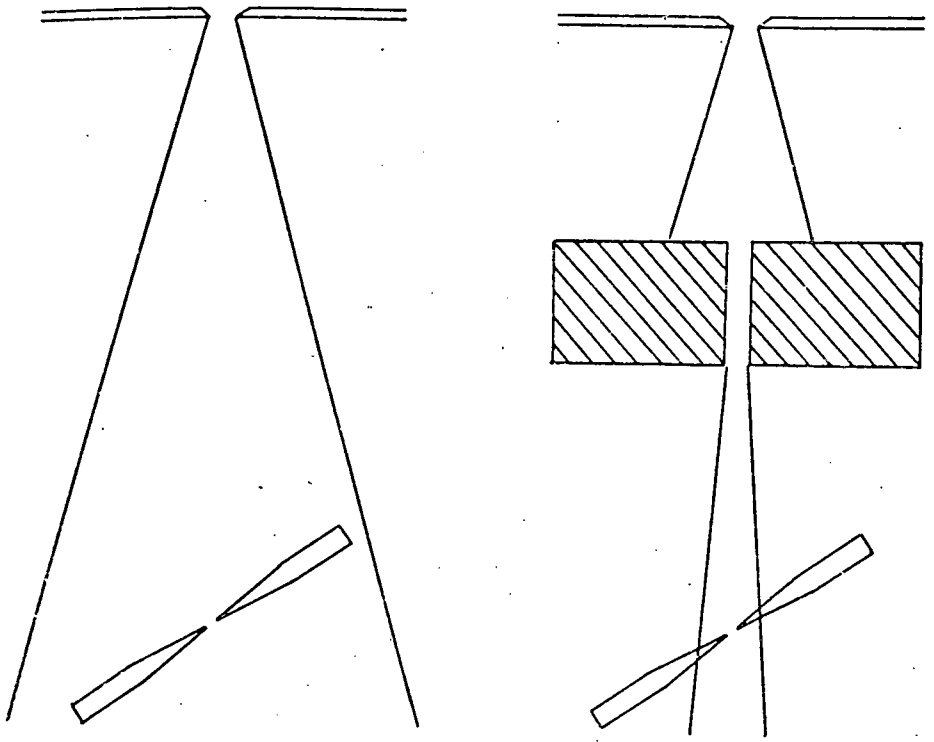

Fig. 46. Schematic Diagram Illustrating Reduction of Fluorescence [illegible] Radiation Using Thick Collimators.

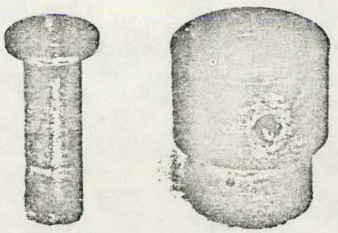

Fig. 47. Eccentric Cylinders Used as Collimators in JEOL JEM 200.

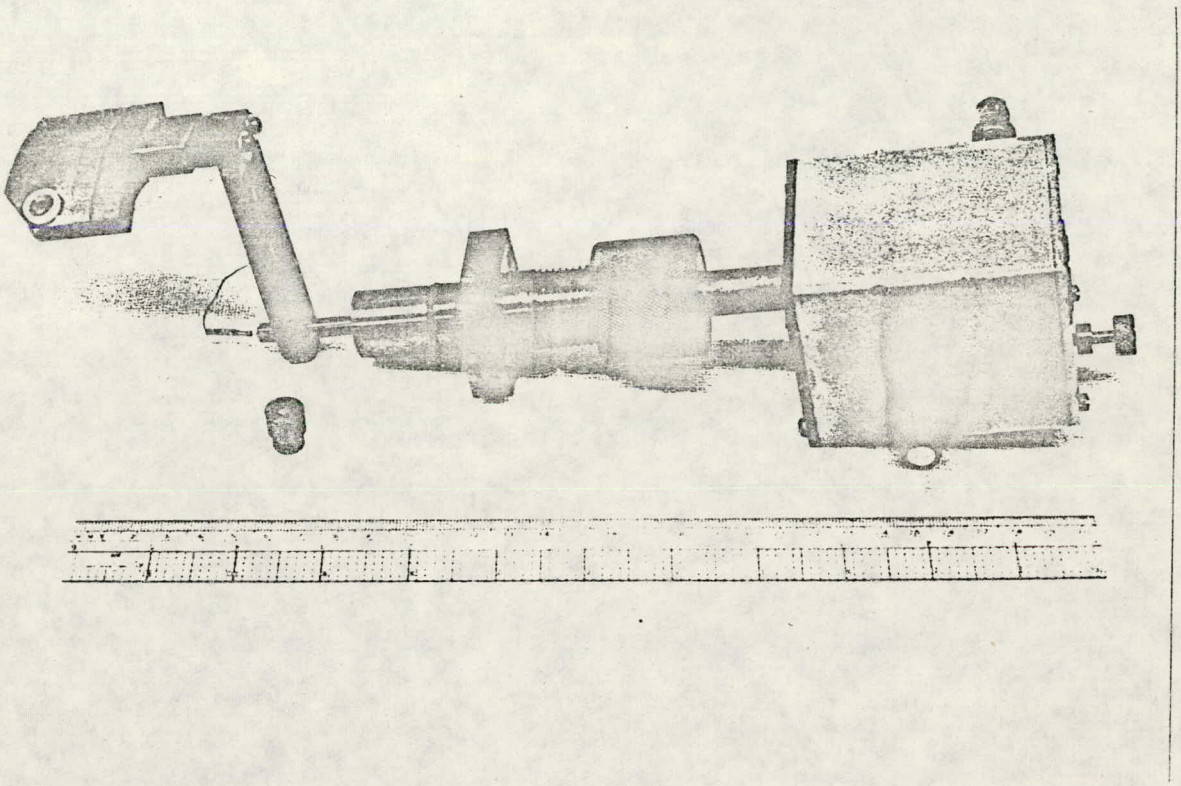

Fig. 48. Adjustable Bremsstrahlung Aperture Drive for JEOL JSEM 200.

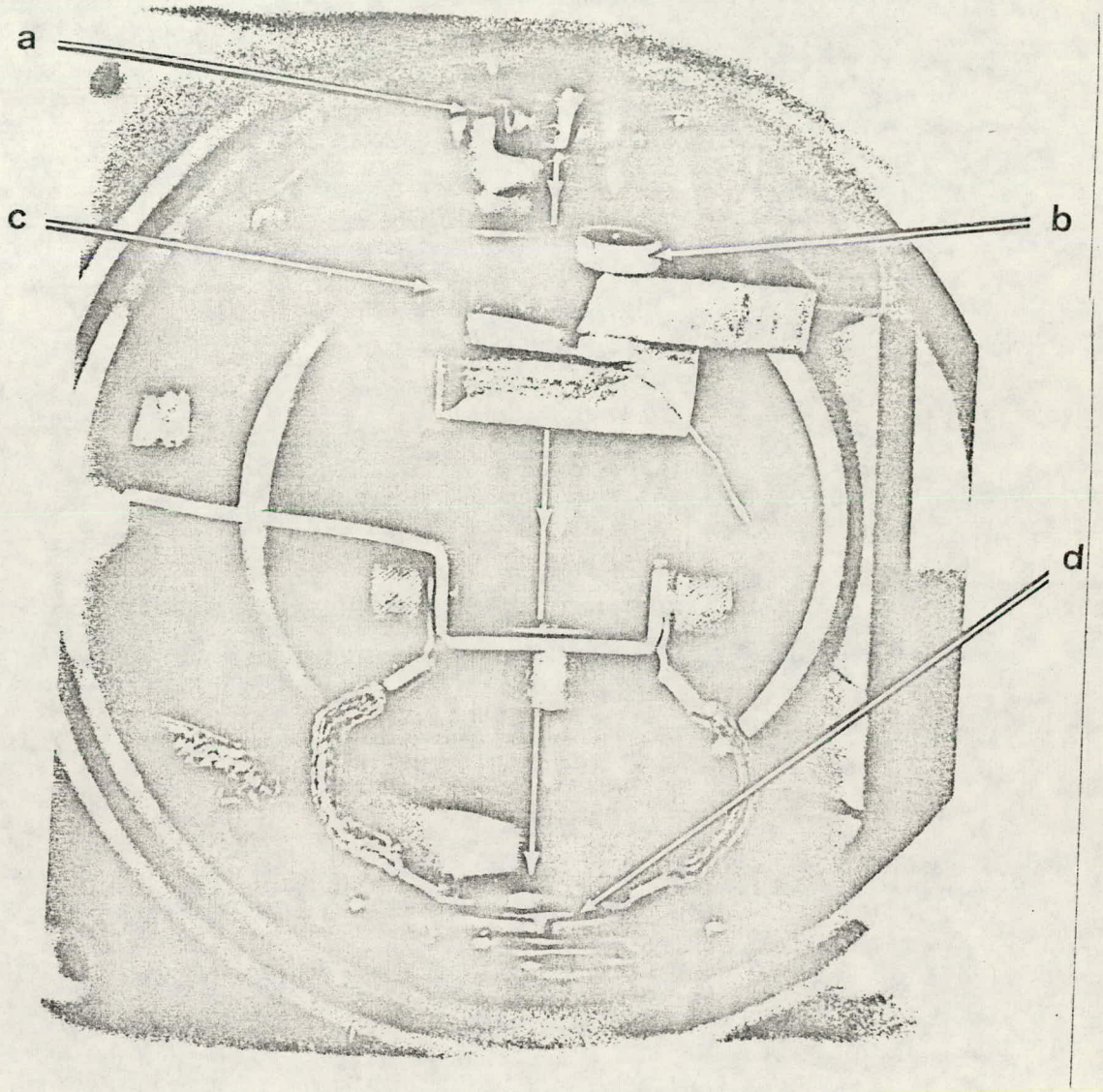

Fig. 49. Adjustable Bremsstrahlung Aperture System Mounted on Microscope Column. (Vertical arrow indicates electron-optical axis.) (a) Eccentric aperture system (see Fig. 47), (b) Faraday cup, (c) adjustable Bremsstrahlung aperture system (Fig. 48), (d) anti-contamination cold trap.

The resulting changes produced by using such a system are shown in Figs. 41, 42, and 43 for the sample (c) and in-hole (d) spectra, respectively. In the worst case (200 keV) the in-hole spectrum has been reduced to less than 2% of the total sample emission. The 100 and 50 keV results show even greater improvements. Figure 50 compares the bremsstrahlung corrected results for the variation in the Ni/Al ratio with thickness to the theoretical calculations. Agreement between the experimental data and calculations is now substantially better. The variation in the intensity ratio with increasing thickness is reproduced well in terms of the general analytical shape of the curve. There is still, however, a discrepancy in absolute value between the two curves which appears to be roughly constant at a given energy. This can, in part, be attributed to contamination of the sample and will be discussed further in the next section.

The procedure now adopted for x-ray measurements in the microscope is to record two spectra for each data point – the first from the region of interest in the sample, and the second the bremsstrahlung (or in-hole) spectrum. The bremsstrahlung spectrum is then subtracted from the sample spectrum before any further analysis is performed. It is important that the uncollimated radiation first be reduced to a low intensity before subtraction. This is simply due to the likelihood of large errors being introduced from the subtraction of two spectra of similar intensity. The effects of this are illustrated in Figs. 51 and 52. In Fig. 51 the upper curve represents the experimental variation in the Ni/Al ratio measured

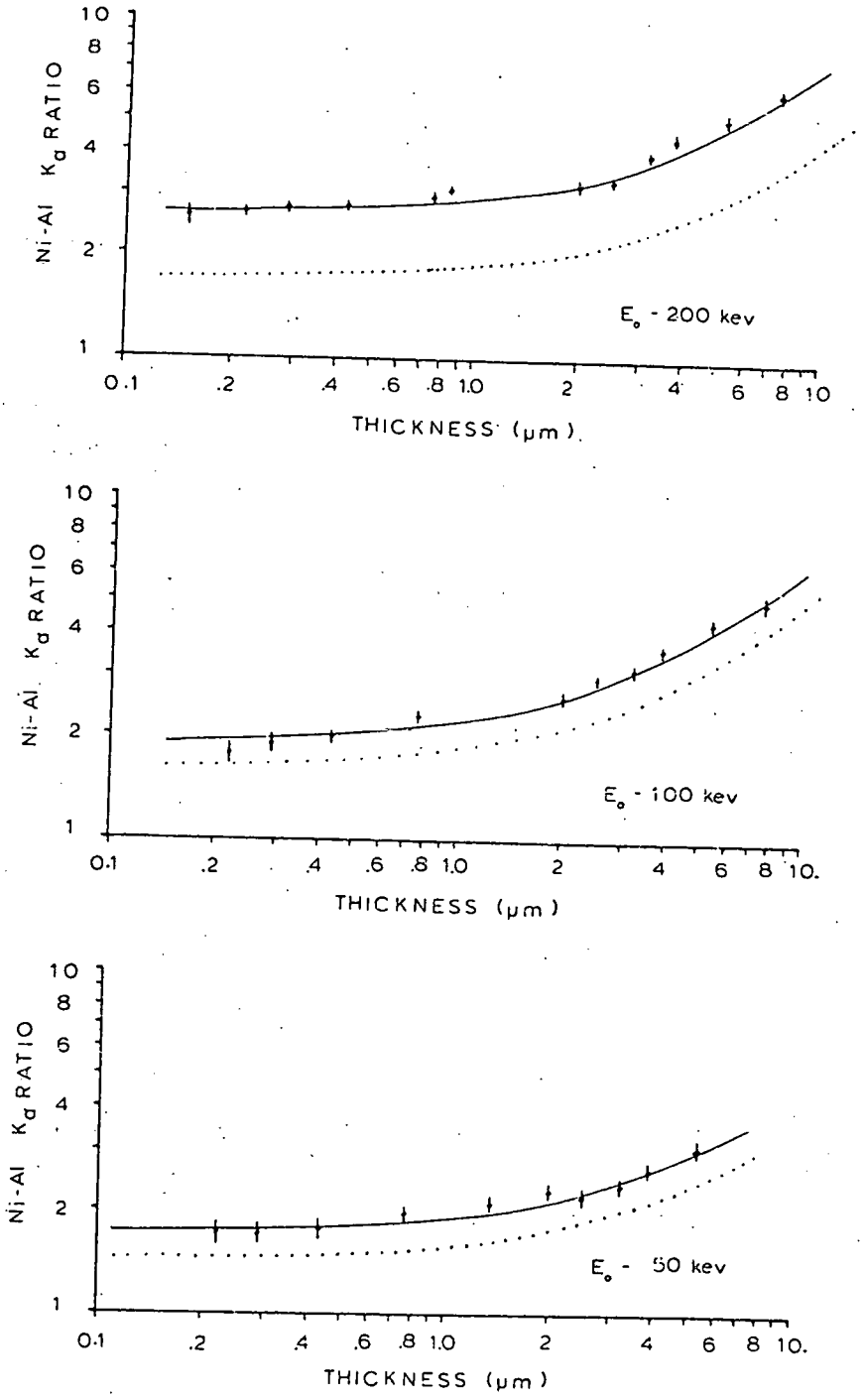

Fig. 50. Corrected Results for the Ni/Al Ratio as a Function of Thickness after Installation of Bremsstrahlung Aperture System. Broken curves indicated calculated variation.

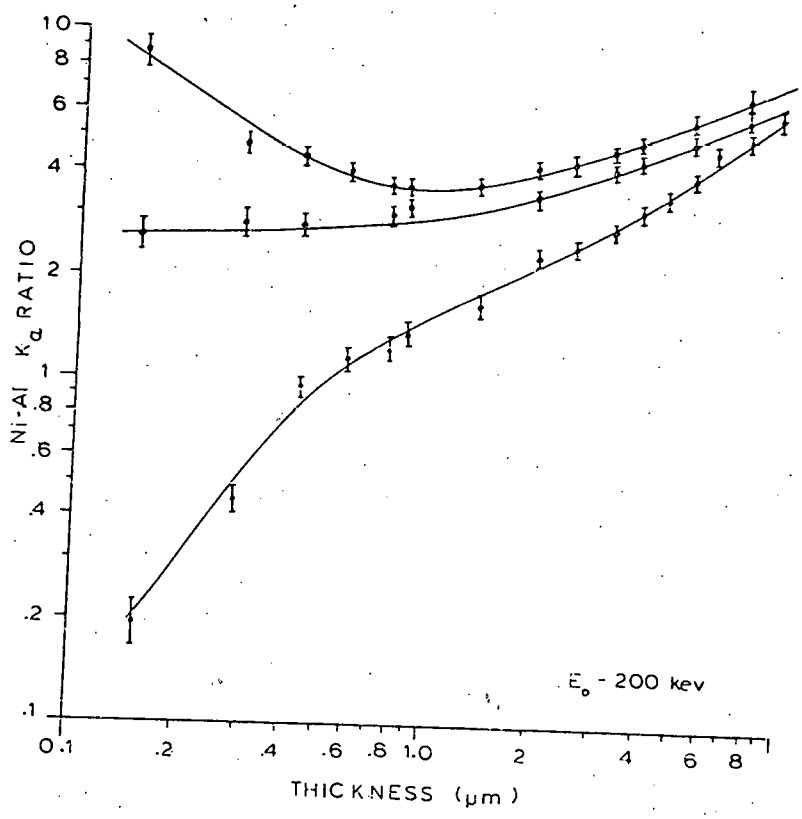

Fig. 51. Errors Resulting from Improper Correction of Bremsstrahlung Fluorescence Problem at 200 keV.

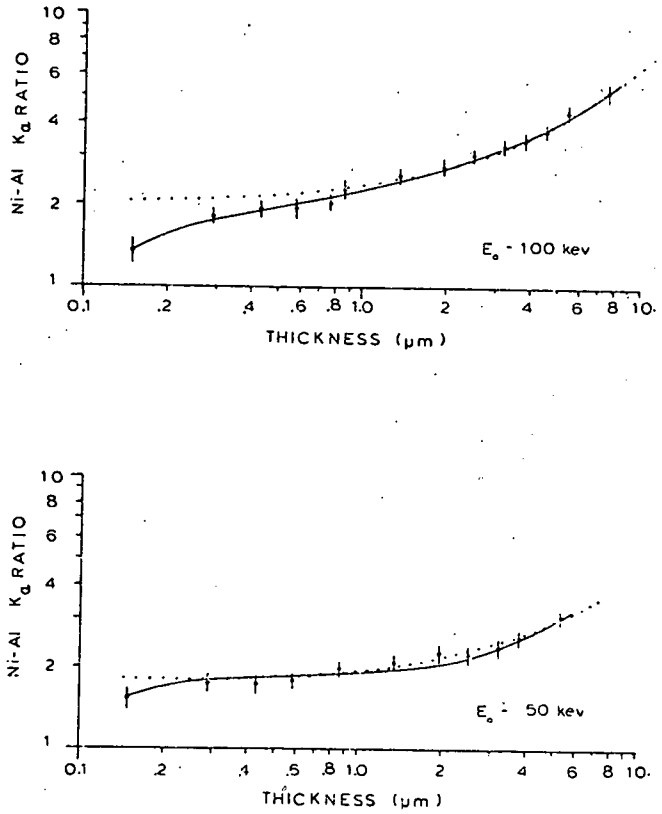

Fig. 52. Errors Resulting from Improper Correction of Brems-strahlung Fluorescence Problem at 100 and 50 keV.

at 200 keV with no bremsstrahlung correction. The lower curve shows the effect of simply subtracting the in-hole count without first reducing the bremsstrahlung flux. Finally, the middle curve was obtained with the x-ray aperture correctly inserted and the reduced in-hole spectrum subtracted from all measurements. Figure 52 plots the similar results for 100 and 50 keV where the broken curve represents the data after being corrected in the prescribed manner, and the solid curve by simply subtracting the in-hole count. The raw data has not been plotted in this figure for clarity. In all cases the in-hole spectrum must, of course, be accumulated for the same period of time as the sample spectrum.

Contamination Effects: Specimen contamination during electron microscope investigations is not a new phenomenon; however, with the advent of STEM and its high current density electron probes, the problems generated have become more pronounced. When the probe is stationary and focused to diameters less than 100 Å, the contamination rates under certain operating conditions can be many orders of magnitude greater than observed in conventional TEM imaging experiments. Two mechanisms of contamination have been identified during the last few years;[84,85] volume diffusion of hydrocarbons from the microscope vacuum system, and surface diffusion of adsorbed material on the sample surface. The volume diffusion component can be reduced by improvements to the microscope vacuum system such as those found in the newer UHV-STEM instruments where the vacuum levels at the specimen are $\leq 2 \times 10^{-9}$ torr (versus $\sim 2 \times 10^{-7}$ torr typical of most new CTEM instruments). The surface

diffusion component is harder to identify and control, being a function of specimen preparation and handling before and during insertion into the microscope environment.

Fourie[85] has studied the formation and shape of contamination in cryopumped TEM and UHV STEM systems. In this work he found that for large probe diameters (0.6 to 3.0 μm) the contamination forms in the shape of a disc of material, the exact profile of which varies with incident electron flux, sample composition, and thickness. In general, the contamination layer was least at the center of the irradiated area, while at the edges the accumulation of material was greatest as shown in Fig. 53. For the probe sizes used in this work ($\leqslant 200$ Å) the shape of the contamination was different, taking on the form of small spiraling cones. This is illustrated in the micrographs of Figs. 53 and 54. Figure 54 is a TEM micrograph showing a region of β-NiAl after an x-ray experiment performed in the STEM mode. The dark spots on the foil (both on the electron entrance and exit surfaces) are the contaminated regions formed during a 200-s analysis with a 100 Å stationary STEM probe. The micrographs in Fig. 55 show the spiral nature of these contamination cones in more detail. This micrograph was taken in the SEM mode of operation in the JSEM 200. Figure 55(a) views the cone end in the orientation in which it was formed, while in Fig. 55(b) the sample was tilted through $\sim 20°$. The spiral shape is most likely due to the electron probe wandering due to charging effects caused by the poor conductivity of the contamination layer.

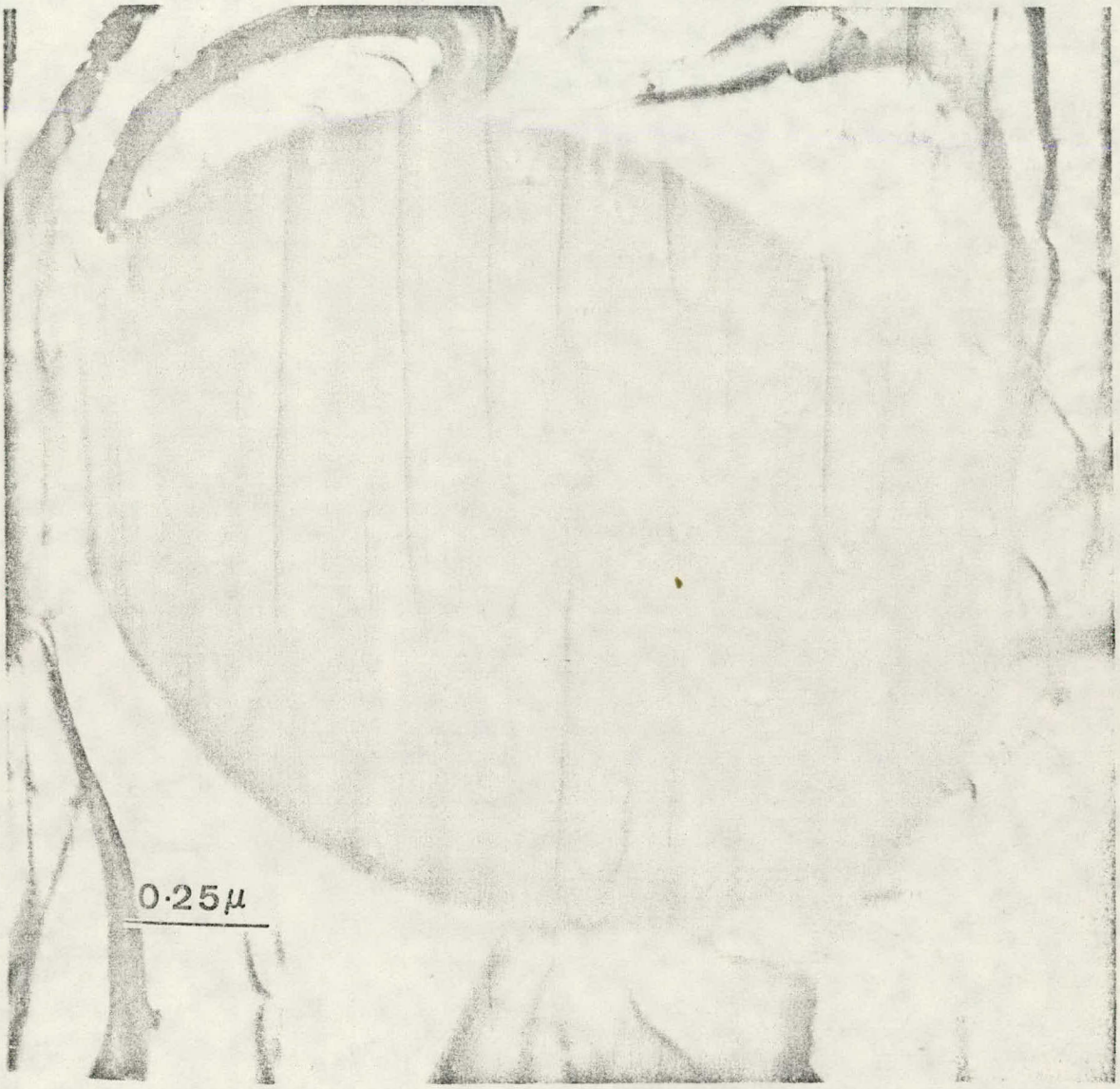
0·25μ

ORNL PHOTO 5794-78

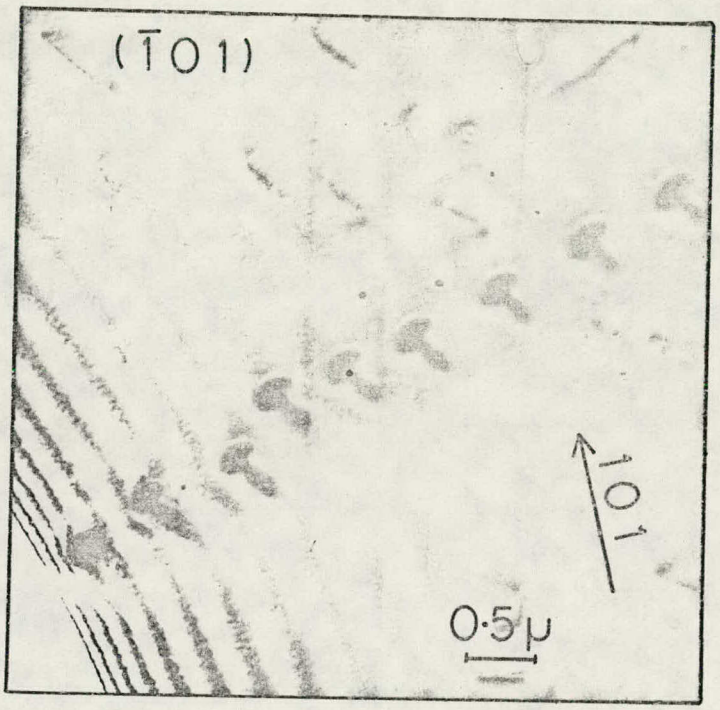

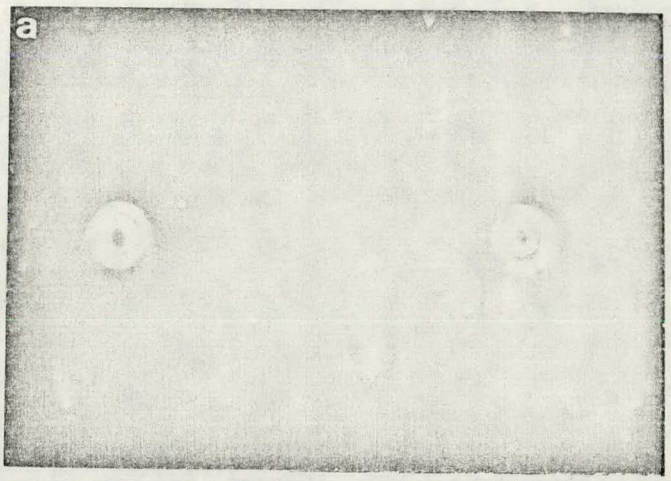
a

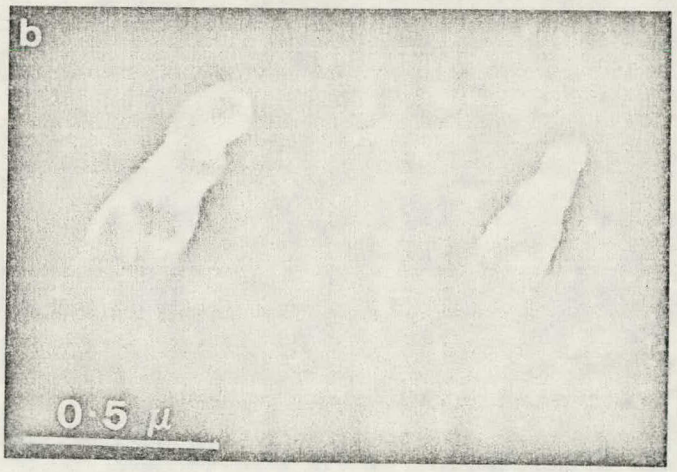
b
0·5 μ

At least three detrimental aspects are immediately apparent from these micrographs. First, there is the obvious result that once the contamination forms it is no longer possible to image the particular region of the sample. Second, the wandering of the electron probe as well as scattering effects in the contamination layer effectively broadens the probe size before it interacts with the specimen, thus decreasing the x-ray spatial resolution provided by the small probe diameter. Finally, the volume of material deposited on the sample provides yet another source of scattering and absorption which will ultimately decrease the sensitivity of analytical information released from the sample. The remaining part of this discussion will focus on this last point in greater detail.

The first problem to consider is related to the generation of systems peaks by the contamination layer. If the deposited material were purely hydrocarbon, then for the case of x-ray detection using standard Si(Li) detectors no additional characteristic emission will be recorded. However, some instruments use a silicon-based diffusion pump oil and O-ring greases which can lead to the accumulation of silicon as well as hydrocarbons on the sample. This is shown in Fig. 56 which is an expanded region of the x-ray emission spectrum from β-NiAl from 0.5 to 2.0 keV. Three peaks are clearly resolved: Ni L_α (∿0.85 keV), Al K_α (∿1.49 keV) and Si K_α (∿1.74 keV). The presence of the silicon peak correlates with the degree of contamination observed to exist in the local region being analyzed. When the diffusion pump oil was changed from a silicon-based system to one using fluorinated hydrocarbons the Si K_α peak was eliminated, until outgassing from "O-ring" greases and roughing pump lines resaturated the diffusion pump oil with silicon contaminants.

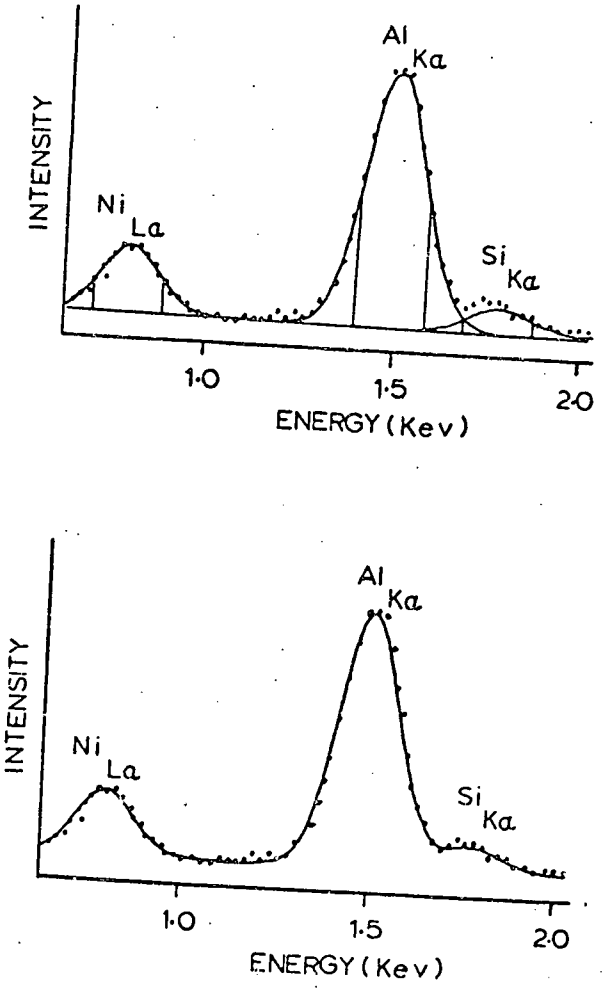

Fig. 56. Silicon Contamination Peak Recorded on a Pure Ni/Al Specimen.

The accumulation of considerable amounts of foreign material on the sample surface also raises the question of x-ray absorption of x rays within this deposited layer. Figure 57(a) once again compares the measured Ni/Al K_α ratio to calculations at 200 keV. There is clearly a moderate discrepancy between the two curves. Since all measurements in this figure were obtained under the same operating conditions and measurement times (200 s), the amount of contamination deposited on the sample will be constant to a first approximation. This would then lead to a constant discrepancy between the experimental and calculated results due to absorption of the lower energy Al K_α x rays. To test this hypothesis the Ni/Al K_α ratio was measured as a function of time (hence also contamination) at constant thickness and incident energy. The results of this experiment, Fig. 57(b), confirm that absorption effects can be appreciable. To account for most of the discrepancy in Fig. 57(a), the amount of absorption at 200 s seems to be about the correct order of magnitude, when comparing Fig. 57(b) to the appropriate point of 57(a).

One further aspect of sample contamination is left to consider — namely, the effects on mass sensitivity. In an early study of TEM-based microanalysis, Russ[86,87] presented results which seemed to indicate that the optimum accelerating voltage for x-ray work was in the vicinity of 100 keV. This conclusion was based on experimental measurements of the peak-to-background (P/B) ratio for various elements which exhibited a broad maximum in this incident energy range and then a decrease in P/B at higher energies. This is in sharp contrast with the theoretical calculations presented in Sect. 2.2.6 which predict a continuous increase

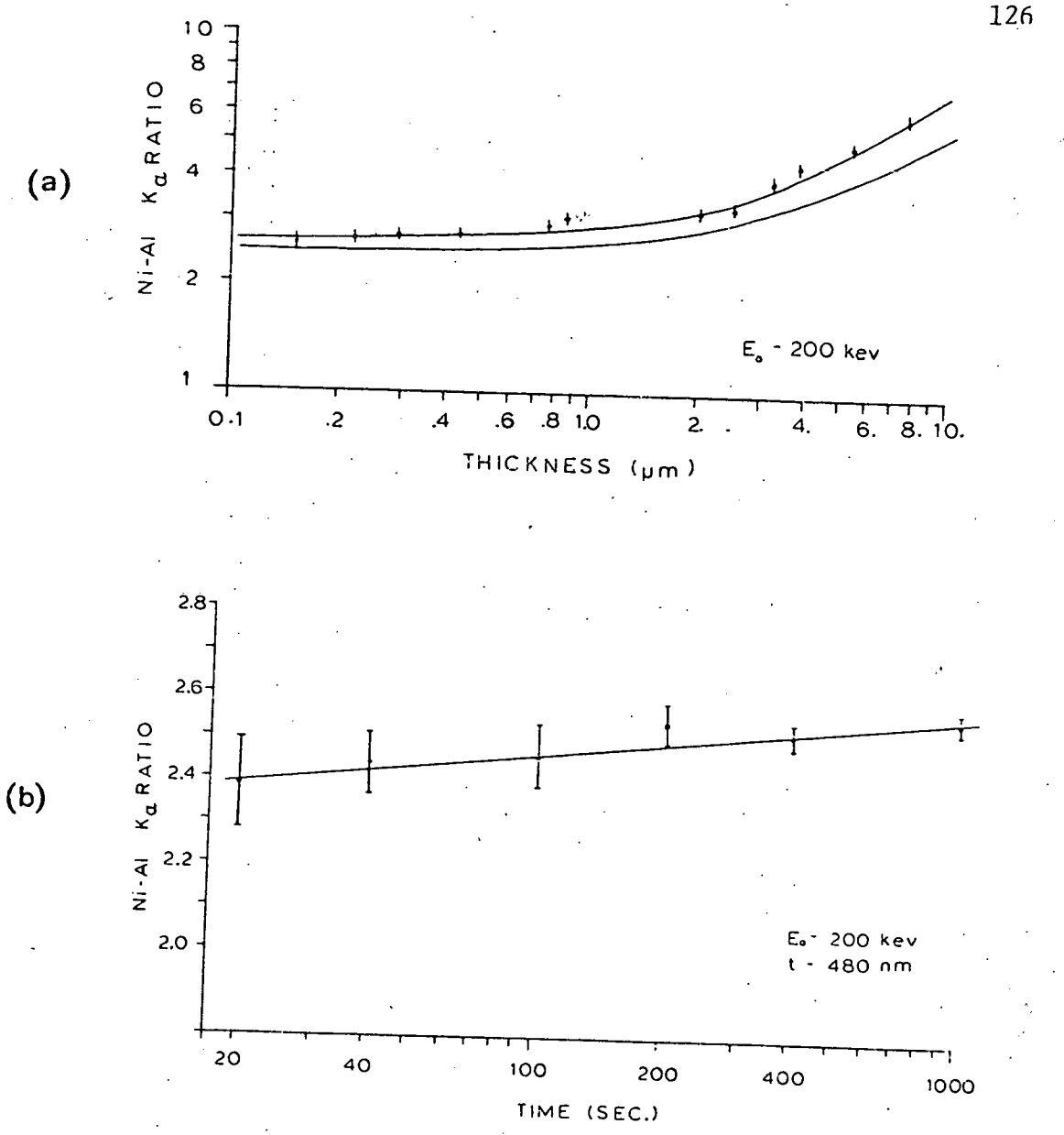

Fig. 57. Comparison of Experimental and Calculated Ni/Al Ratio (a). Effects of contamination accumulation on experimental Ni/Al ratio (b).

in the P/B ratio with electron energy. Further experimental work by Zaluzec and Fraser[44] has shown that these discrepancies may be attributed to a combination of x-ray fluorescence and sample contamination effects.

The effects of x-ray (bremsstrahlung) fluorescence on quantitative analysis has been discussed at length previously; however, the effects on mass sensitivity have been postponed until this time. Referring to Sect. 2.2.6, theoretical calculations indicate that for thin foils of all elements the characteristic P/B ratio should increase with accelerating voltage monotonically. This result assumes that all x-ray emission from the sample was derived from purely electron excitation. The effects of bremsstrahlung fluorescence on the experimentally determined P/B ratio are demonstrated in Fig. 58. Figures 58(a) and 58(b) plot the results of measurement of the NiK_α and Al K_α P/B ratio in β-NiAl as a function of incident beam energy without the correction for bremsstrahlung fluorescence. These data are similar to those obtained by Russ in an earlier study. When the appropriate modifications are made to the electron-optical column the results shown in Figs. 58(c) and 58(c) are obtained.

The effects of contamination on the recorded P/B ratio are complex and difficult to control. In all cases the amount of material accumulated on the sample is a function of the total electron flux irradiating the area. Hence it will be assumed in the following discussion that contamination increases monotonically with time at constant probe current. In addition, it will be also assumed that approximately equivalent results can be obtained by holding the product of beam current and irradiation time constant. The trends presented in this section should

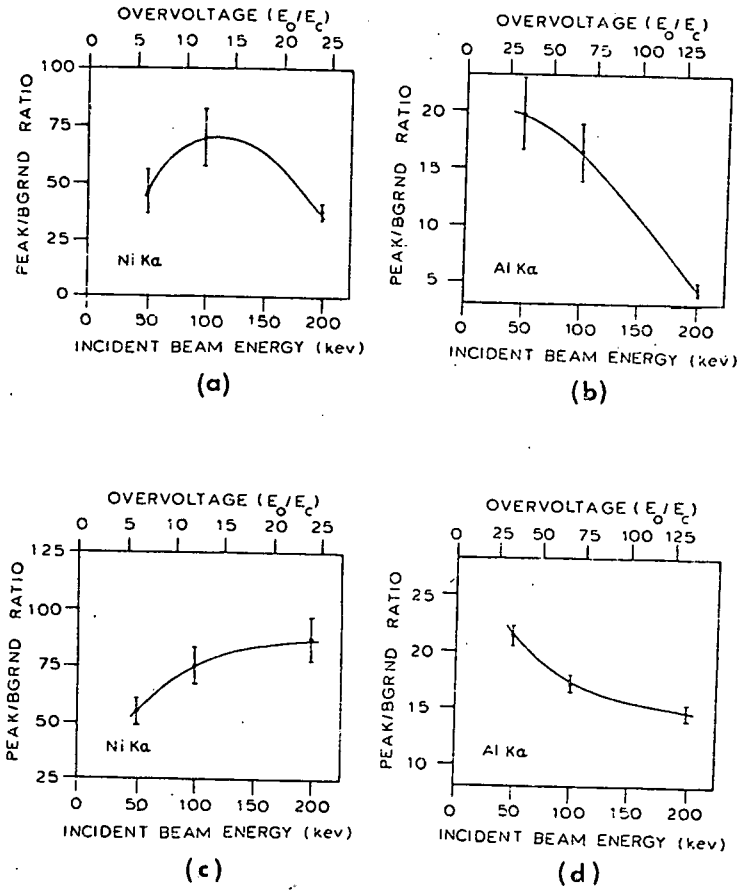

Fig. 58. P/B Ratios for Ni and Al in Ni/Al (a,b) Without Correction for Bremsstrahlung Fluorescence; (c,d) with Correction for Bremsstrahlung Fluorescence.

be considered only as qualitative indications of the effects of contamination since quantitative measurements of the contamination are presently impossible to obtain. Lastly, in order to minimize the complications which result from the effects of absorption of low-energy x rays in the contamination layer the results shown in the following figures will center mainly on the Ni K_α P/B ratio.

Ideally, from the theoretical calculations presented in Sect. 2.2.6, the P/B ratio should to a first approximation remain constant as a function of both sample thickness and time, and in the absence of fluorescence effects should increase monotonically with incident beam energy. Experimental measurements, unfortunately, do not exhibit such a simple behavior; they are summarized in Figs. 59(a) and 59(b). The discrepancies are, however, systematic in nature and can be related to the nonlinear variation in the continuum intensity generated as a function of time. This can be seen in Figs. 60(a) and 60(b). The intensity of the Ni K_α peak in this figure varies linearly with both sample thickness and irradiation time. The continuum intensity, which in this case is the intensity measured in the region from 9.5 to 10.0 keV (i.e., a region isolated from all characteristic peaks), shows a highly nonlinear response. The most important parameter which influences this intensity is the total sample thickness, all other parameters being roughly constant [see Eq. (2.2)]. Thus, the changes in continuum intensity can be directly correlated with the accumulation of contamination on the sample. With this in mind, the systematic changes in Figs. 59(a) and 59(b) can be qualitatively explained.

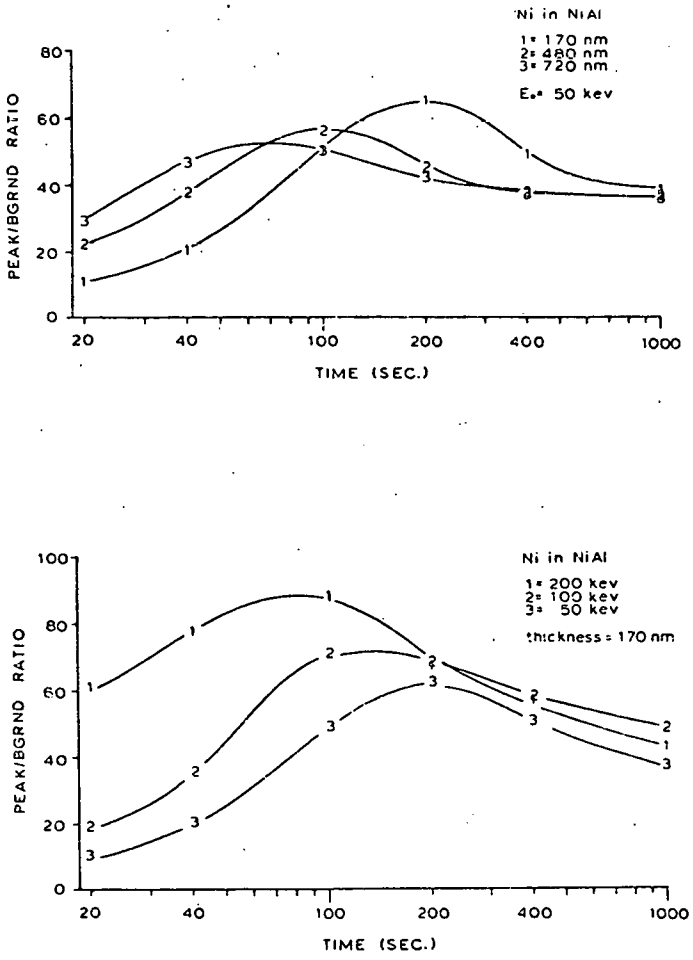

Fig. 59. Variation in Experimental P/B Ratio as a Function of Contamination and Operating Conditions.

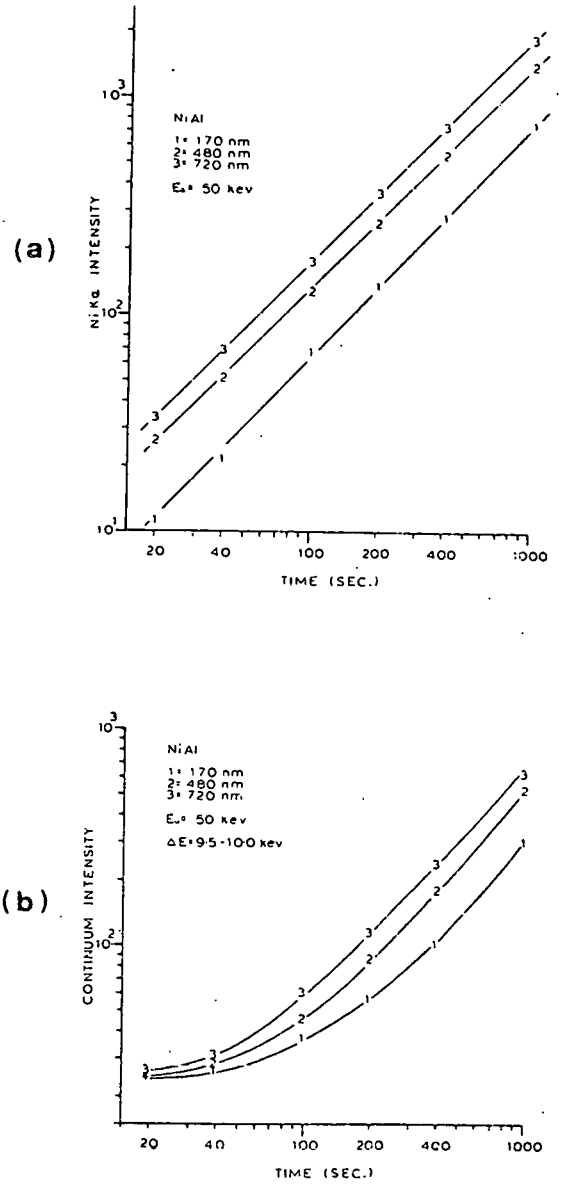

Fig. 60. Variation in Ni K_α Intensity with Time and Thickness (a). Variation in continuum intensity with time and thickness (b).

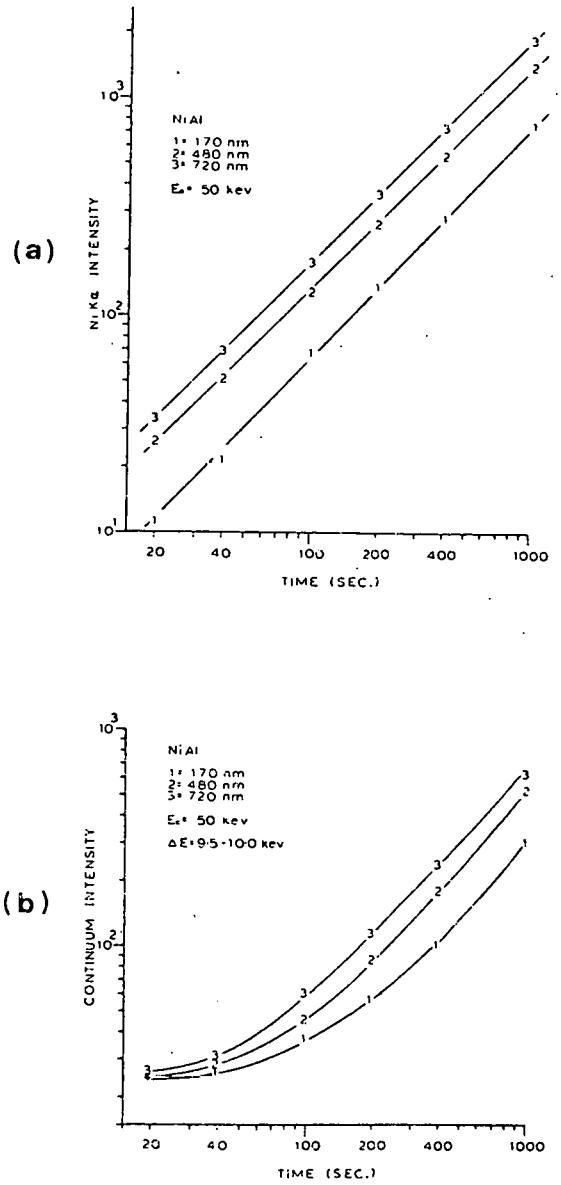

Fig. 60. Variation in Ni K_α Intensity with Time and Thickness (a). Variation in continuum intensity with time and thickness (b).

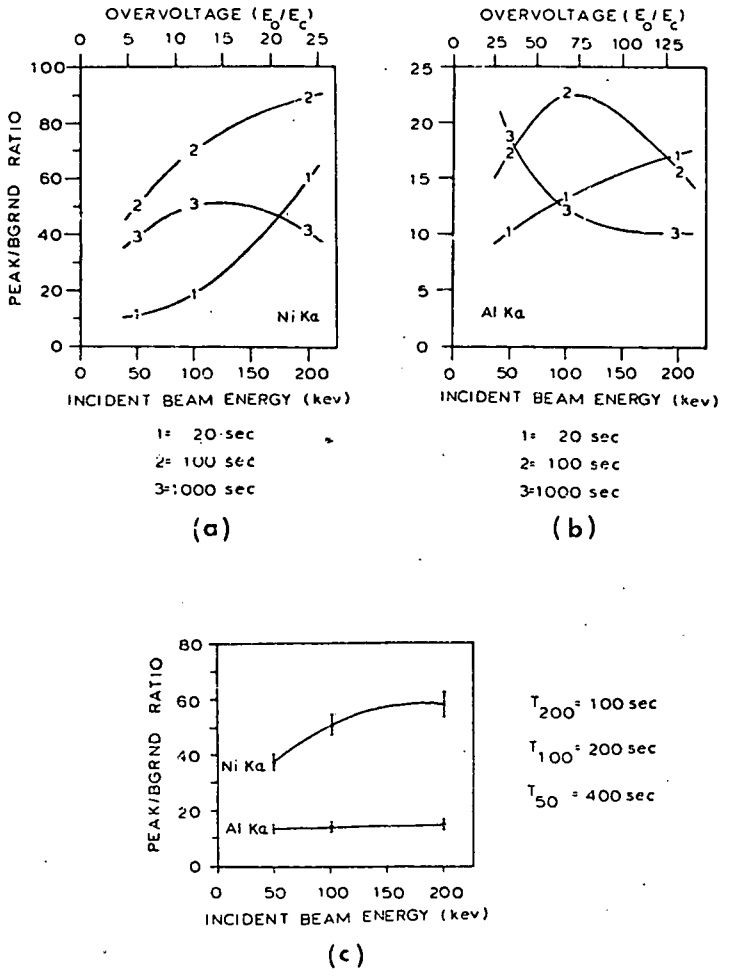

Fig. 61. Variation in P/B Ratio as a Function of Time for Ni (a) and Al (b). Comparison of experimental results at approximately constant contamination (c).

information obscured by peak overlaps. Clearly, as the level of sophistication of analysis increases, there arises a need for corresponding increases in computational facilities, versatility and speed necessary to perform these tasks.

Consequently, a microcomputer system consisting of a DEC LSI-II microprocessor, with 32K words of MOS memory, an AED 5100 dual-density floppy disc mass storage device, an ASR-33 Teletype terminal, and a 4010-1 Tektronics graphics terminal was assembled and interfaced to an ORTEC 6200 multichannel analyzer (MCA). In addition to this hardware expansion a series of operator interactive computer programs have been developed to facilitate simple on-line analysis of x-ray spectra. The software developed during this research has undergone a continuous process of updating and revision in order to keep up with changes in experimental techniques and is documented in Appendices A through F. Included in these listings are subroutine libraries (NXRYL, NGRAPH) which serve as building blocks for the general-use programs (NEDS, NXRYRT, NMCS) directed toward specific applications of data reduction and analysis of EDS, ELS, and TSED data. The software has been written in FORTRAN IV to optimize access in a multi-program/user environment and furthermore to facilitate modifications to existing programs as future developments occur. It is appropriate to note at this point that several subroutines found in the x-ray library (NXRYL) have been adapted in whole or in part from the MAGIC series of x-ray analysis programs developed by Colby[63] for quantitative analysis of bulk specimens using electron microprobes.

Three programs documented in the appendices are specifically devoted to x-ray analysis – namely, MCA, NEDS, and NXRYRT. The program MCA is used to read data from the multichannel analyzer and creates a semi-permanent record onto a floppy disc file. NEDS is subsequently used to process recorded spectra, extracting characteristic intensities from the raw data. Finally NXRYRT is used to convert relative intensity ratios into composition measurements using a standardless approach. An outline of a procedure for x-ray analysis using the "thin-film" standardless technique is given next, and this can be used for the majority of x-ray work done on the current breed of TEM/STEM/AEM instruments. This will be subsequently followed by a discussion of the application of the absorption correction and finally on quantitative analysis using thin-film standards.

Standardless Analysis: Having optimized the various geometrical and instrumental factors outlined in Sect. 2.2.6, one proceeds to record a spectrum from the specimen, which should be measured over a sufficient period of time to ensure statistical significance of all characteristic peaks under investigation. In addition to these considerations, one should ensure that the sample is appropriately oriented so that anomalous emission due to electron channeling is minimized.[88–90] Once the sample spectrum has been recorded and stored, then a second spectrum which is due to the effects of uncollimated radiation must be measured. This can be simply obtained by translating the electron probe off the specimen (for example, by moving the probe into a hole in the TEM disc) and

accumulating the resulting spectrum under identical operating conditions. This "in-hole" spectrum should not exceed ∿5% of that obtained when the electron probe is positioned on the thinnest region of the sample to be analyzed, since the form of these two spectra may be quite different because of differences in the mechanism of x-ray generation. Thus, subsequent subtraction of spectra may result in substantial errors if they are of comparable intensities.

The correction to the sample spectrum for uncollimated radiation is straightforward – namely, a simple channel-by-channel subtraction. In order for this subtraction technique to be considered valid, two criteria must be satisfied. First the in-hole spectrum must be small with respect to the sample spectrum; otherwise, large systematic errors can develop. Secondly the in-hole spectrum which is subtracted must reflect the identical electron dose relative to the corresponding sample spectrum. For the case of CTEM/STEM instruments with conventional thermionic emission or LaB_6 filaments the emission current has sufficient long-term stability that measurements at constant detector live time will to a good approximation be equivalent to constant electron dose. This is not generally valid for field emission sources where the emission current can vary substantially with time and hence some appropriate beam current monitoring system must be developed to compensate.[91]

Once the sample spectrum is corrected for fluorescence by uncollimated radiation then standard techniques for spectral deconvolution can be employed.[92] In order to facilitate this procedure the program NEDS

was developed for routine analysis. The program inputs from a floppy disc file both a sample and in-hole spectrum, then performs a channel-by-channel subtraction. Next all characteristic lines are identified by the operator through the use of KLM markers. In this context, KLM markers refer to lines superimposed on a sample spectrum (displayed on a graphics terminal) which indicate the positions of characteristic x-ray emission lines (K_α, K_β, L_α, L_β, M_α, M_β, etc.) for a particular atomic species. Once all characteristic lines have been identified a background curve is calculated by fitting a polynomial expression of the form:

$$N(E)_i = \left\{ A \cdot \left[\frac{E_0 - E_i}{E_i} \right]^2 + B \cdot \left[\frac{E_0 - E_i}{E_i} \right] + C \right\} \cdot \left\{ \prod_{j=1}^{3} \exp\left[- \left(\frac{\mu}{\rho} \right)_j \cdot \frac{\rho_j \cdot t_j}{\cos\alpha} \right] \right\} \quad (2.52)$$

to regions of the spectrum selected by the operator. Here $N(E)_i$ is the number of continuum photons of energy, E_i, E_0 the incident electron energy, A, B, and C fitting constants, and the last term is the detector efficiency factor previously discussed. After background subtraction the program proceeds to fit Gaussian profiles to all characteristic lines identified by the operator using a chi-squared minimization criterion. For the case of overlapped peaks the program systematically searches parameter space for those combinations of Gaussian peak shapes whose values most closely duplicate the profile of the convoluted spectrum (constrained to the response function of the detector system). Because of this multipeak overlap analysis is not necessarily unique. When finished the program produces an output listing of all analyzed lines

in a format suitable for processing using the NXRYRT program. A flow diagram together with an example of a fitted spectrum can be found in Appendix A for the program NEDS.

Following data reduction using NEDS or a similar program the next step in quantitative analysis involves the reduction of measured intensities into composition values. Currently the most popular procedure employs the thin-film standardless approach using relative intensity ratios. Here the intensity ratio of all characteristic lines in a given spectrum is calculated relative to the most prominent peak. These intensity ratios are then converted into composition ratios (using Eq. 2.26) and the sample composition determined assuming that

$$\sum_i C_i \equiv 1 \quad . \tag{2.53}$$

A flow diagram for the program NXRYRT which converts intensity ratios into composition ratios can be found in Appendix D.

Three examples of standardless analysis using NXRYRT for samples of β-NiAl, β-ZrNb and Ni_4Mo are given in Table 1. As can be seen the calculated compositions for both the β-NiAl and β-ZrNb alloys are in good agreement with the compositions obtained from bulk analyses. The last example Ni_4Mo compares quantitative analysis of the sample using several of the characteristic emission lines which can be simultaneously recorded in a single x-ray spectrum. In this case the most intense lines were NiK_α (7.48 keV) and MoL_α (2.29 keV); however, it was also possible to measure the MoK_α (17.4 keV) as well as the NiL_α (0.85 keV) lines and

Table 1. Comparison of Thin-Film X-Ray Microanalysis of TEM Specimens to Chemical Analysis Starting Material

Sample	Incident Energy	Intensity Ratio	Composition		
			Calculated Ratio	Calculated (wt %)	Bulk (wt %)
β-NiAl	200 keV	$\frac{NiK_\alpha}{AlK_\alpha}$ = 2.05 ±0.02	$\frac{Ni}{Al}$ = 2.28 ±0.02	Ni = 69.5 Al = 30.5	Ni = 68.5 Al = 31.5
	100 keV	$\frac{NiK_\alpha}{AlK_\alpha}$ = 1.79 ±0.02	$\frac{Ni}{Al}$ = 2.33 ±0.02	Ni = 69.9 Al = 30.1	Ni = 68.5 Al = 31.5
β-ZrNb	200 keV	$\frac{NbK_\alpha}{ZrK_\alpha}$ = 0.163 ±0.003	$\frac{Nb}{Zr}$ = 0.176 ±0.003	Nb = 15.0 Zr = 85.0	Nb*,† = 15.4 Zr = 84.6 ±3%
Ni_4Mo	120 keV	$\frac{MoK_\alpha}{NiK_\alpha}$ = 0.142 ±0.003	$\frac{Mo}{Ni}$ = 0.489 ±0.01	Mo = 32.8 Ni = 67.2	Mo* = 29.0 Ni = 71.0 ±1%
		$\frac{MoL_\alpha}{NiK_\alpha}$ = 0.227 ±0.003	$\frac{Mo}{Ni}$ = 0.416 ±0.005	Mo = 29.4 Ni = 70.6	Mo = 29.0 Ni = 71.0 ±1%
		$\frac{MoL_\alpha}{NiL_\alpha}$‡ = 2.73 ±0.04	$\frac{Mo}{Ni}$‡ = 0.658 ±0.010	Mo‡ = 39.7 Ni = 60.3	Mo* = 29.0 Ni = 71.0 ±1%

*Wet chemical analysis of bulk specimen.

†Electron microprobe x-ray analysis of bulk specimen.

‡Significant contamination of sample during analysis will affect this result.

thus quantitative analysis using each of these lines was attempted. Analysis using the NiLα is clearly extremely poor when compared to the other two determinations. This can be attributed directly to absorption effects of the NiL_α line in the contamination layer which formed during the time of data accumulation. The results have been included for comparison. Considering the accuracies to which standardless analysis is valid ($\sim$5% for K-K and K-L lines, $\sim$10% for L-L lines), these results are in good agreement with bulk composition measurements.

Absorption Correction for Standardless Analysis: An extended discussion on the inclusion of absorption effects was presented earlier in Sect. 2.2.3. Unfortunately there is no simple analytic solution that can be used to include all the aspects which were considered therein and hence numerical integration becomes the only viable alternative. If, however, one assumes that the generation function $\phi_A^{K\alpha}(z)$ is nearly constant, then Eq. (2.33) can be solved analytically as follows:

$$I_A^{K\alpha} = \phi_A^{K\alpha}(0) \cdot \int_0^{t_0} \exp\left[- \left(\frac{\mu}{\rho}\right)_{AB}^{K\alpha,A} \cdot \bar{\rho} \cdot \frac{\sin(\beta_i)}{\cos(\beta_i - \theta_E)} \cdot t \right] dt$$

$$= \phi_A^{K\alpha}(0) \cdot \left\{ \frac{1 - \exp\left[- \left(\frac{\mu}{\rho}\right)_{AB}^{K\alpha,A} \cdot \bar{\rho} \cdot \frac{\sin(\beta_i)}{\cos(\beta_i - \theta_E)} \cdot t_0 \right]}{\left(\frac{\mu}{\rho}\right)_{AB}^{K\alpha,A} \cdot \bar{\rho} \cdot \frac{\sin(\beta_i)}{\cos(\beta_i - \theta_E)}} \right\} \quad (2.54)$$

where in this equation $\phi_A^{K\alpha}(0)$ is the generation function evaluated at zero thickness (i.e., zero energy loss).

Using this equation one can then write that the generated intensite ratio with correction for absorption is:

$$\frac{\phi_A^{K_\alpha}(0)}{\phi_B^{K_\alpha}(0)} = \frac{I_A^{K_\alpha}}{I_B^{K_\alpha}} \cdot \left\{ \frac{\left(\frac{\mu}{\rho}\right)_{AB}^{K_\alpha,A}}{\left(\frac{\mu}{\rho}\right)_{AB}^{K_\alpha,B}} \right\} \cdot \left\{ \frac{1 - \exp\left[-\left(\frac{\mu}{\rho}\right)_{AB}^{K_\alpha,B} \cdot \bar{\rho} \cdot \frac{\sin(\beta_i)}{\cos(\beta_i - \theta_E)} \cdot t_0 \right]}{1 - \exp\left[-\left(\frac{\mu}{\rho}\right)_{AB}^{K_\alpha,A} \cdot \bar{\rho} \cdot \frac{\sin(\beta_i)}{\cos(\beta_i - \theta_E)} \cdot t_0 \right]} \right\} \quad (2.55)$$

This equation is of course only valid for a homogeneous sample of thickness t_0. The application of an absorption correction to an inhomogeneous sample is nearly impossible without some prior knowledge as to the relative composition and thickness of each phase in the excited volume. Thus, one usually resorts to analysis of thinner regions of the sample which can be then considered locally homogeneous.

Once the intensity ratio has been corrected for absorption effects, then the data can be converted into relative composition ratios using the standardless analysis approach previously discussed. If, however, the application of Eq. (2.55) yields corrections in excess of 10%, then serious consideration should be given to either extended calculations of the variation of $\phi_A^{K\alpha}$ with thickness (Sect. 2.2.3) or to repeating the measurements in a thinner region of the sample. Since a 10% criterion is used as the maximum acceptable absorption correction, the correction due to characteristic x-ray fluorescence can be ignored.

Quantitative Analysis Using Thin Standards: Up to this point quantitative analysis has been approached on the basis of calculating correction factors for the generation efficiency of various x-ray lines. At best these factors are accurate to ±5% and therefore it becomes

appropriate to examine quantification using thin standards in an attempt to improve the accuracy of an analysis. Consider the intensity ratio of the K_α line of element A $\left(I_A^{K_\alpha}\right)$ from an unknown sample (AB) relative to the intensity of the same line in a standard $\left(I_{STD}^{K_\alpha}\right)$. This can be written in the thin-film approximation as:

$$\frac{I_A^{K_\alpha}}{I_{STD}^{K_\alpha}} = \frac{Q_A^K \cdot \frac{N_0 \cdot \bar{\rho}}{W_A} \cdot C_A \cdot \omega_A^K \cdot f_A^{K_\alpha} \cdot \eta_{AB} \cdot dz_{AB}}{Q_A^K \cdot \frac{N_0 \cdot \bar{\rho}_{STD}}{W_A} \cdot C_{STD} \cdot \omega_A^K \cdot f_A^{K_\alpha} \cdot \eta_{STD} \cdot dz_{STD}} \quad . \tag{2.56}$$

Assuming both the standard and the unknown sample are analyzed at the same incident beam energy and experimental geometry, then Eq. (2.56) can be simplified into

$$\frac{I_A^{K_\alpha}}{I_{STD}^{K_\alpha}} = \frac{\bar{\rho}}{\bar{\rho}_{STD}} \cdot \frac{\eta_{AB}}{\eta_{STD}} \cdot \frac{dz_{AB}}{dz_{STD}} \cdot \frac{C_A}{C_{STD}} \quad . \tag{2.57}$$

This equation now relates the characteristic intensity ratio to the composition ratio multiplied by three constant terms. These constants — namely the ratios of the relative sample densities $\left(\bar{\rho}/\bar{\rho}_{STD}\right)$, the incident electron flux during each measurement $\left(\eta_{AB}/\eta_{STD}\right)$, and the sample thickness $\left(dz_{AB}/dz_{STD}\right)$ — can each be measured independently. Thus it is possible to improve the accuracy of thin-film x-ray microanalysis assuming one can prepare suitable thin-film standards.

2.3 Electron Diffraction Techniques

Various methods of obtaining structural information about solids using electron diffraction exist; probably the most well known is the selected-area-diffraction technique (SAD). In this method an aperture placed in the image plane of the objective lens of a TEM effectively defines an area on the specimen from which an electron diffraction pattern is obtained. The spatial resolution of this technique is $\sim$5000 Å in diameter with the information being recorded in parallel on a photographic emulsion. The advent of STEM instruments with scan coils located both above and below the specimen as well as modified electron optics providing extremely small electron probes ($\leq$ 50 Å in diameter) has led to the development of complementary techniques to the SAD method. Among these modes are the scanning transmission[93] (STED), transmission scanning[94] (TSED), and stationary diffraction pattern[95] (SDP) techniques. In this section the TSED and SDP techniques will be outlined and the relative advantages and disadvantages discussed.

2.3.1 Stationary Diffraction Pattern Technique

The electron-optical diagram of the stationary diffraction pattern technique in a JEOL JSEM 200 is shown in Fig. 62. A set of scan coils above the specimen deflects the incident electron beam off the optic axis at the back focal plane of the prefield of a highly excited objective lens. This dual-purpose lens acts not only as a final probe forming condensor lens but also serves to deflect the electron beam so

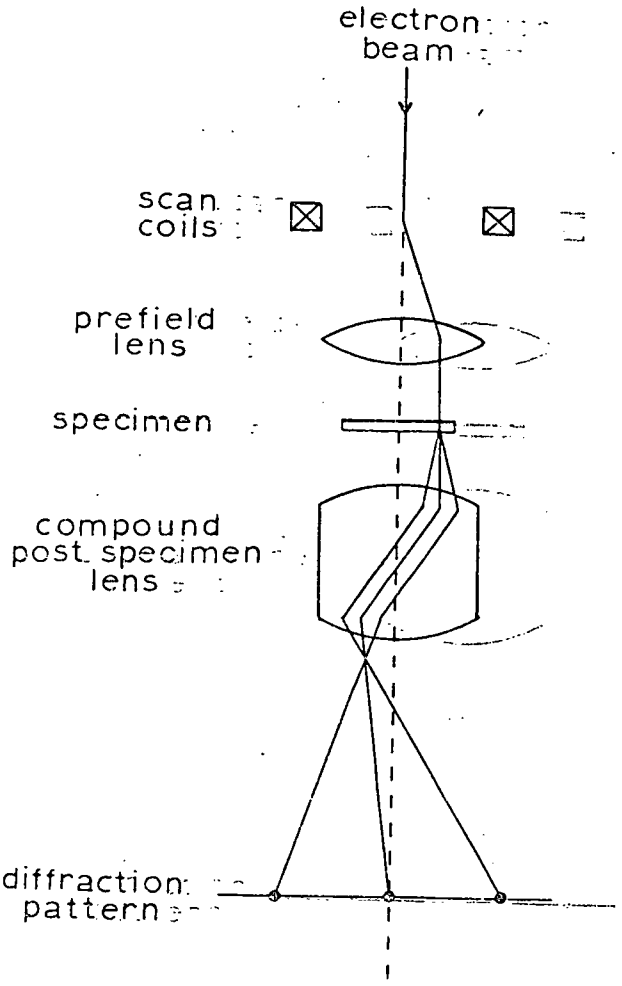

12. Ray Diagram for the Stationary Diffraction Pattern Technique.

that it is once again parallel to the electron-optical axis. The remaining post-specimen field of the compound objective lens system magnifies the resulting electron diffraction pattern so it can be conveniently viewed on a phosphorescent screen at the detector plane. Since the electron probe is incident on the sample plane parallel to the electron-optical axis, a stationary pattern is formed at all times at the final viewing screen.

The principal advantage of this technique is that diffraction patterns from areas as small as 200 Å can be obtained by simply reducing the size of the roster on the specimen. There are, however, two distinct disadvantages of this method. First, the contamination rate usually increases due to the increased current density found in the focused STEM probe. Secondly, the diffraction patterns formed when operating in the highest spatial resolution mode in STEM have poor angular resolution due to the highly convergent beams (10^{-2} to 10^{-3} radians) used to form the small electron probes. This effect is illustrated in the diffraction patterns of Fig. 63 for incident beam convergences varying from nearly parallel illumination ($\sim 6 \times 10^{-4}$ radians, CTEM imaging conditions) to highly convergent illumination ($\sim 2 \times 10^{-2}$, high resolution STEM imaging).

This beam convergence can be changed in either of two ways — by using a smaller condenser aperture, or by decreasing the excitation of the condenser lens current. Decreasing the aperture size is the simplest means by which the angular resolution can be increased;

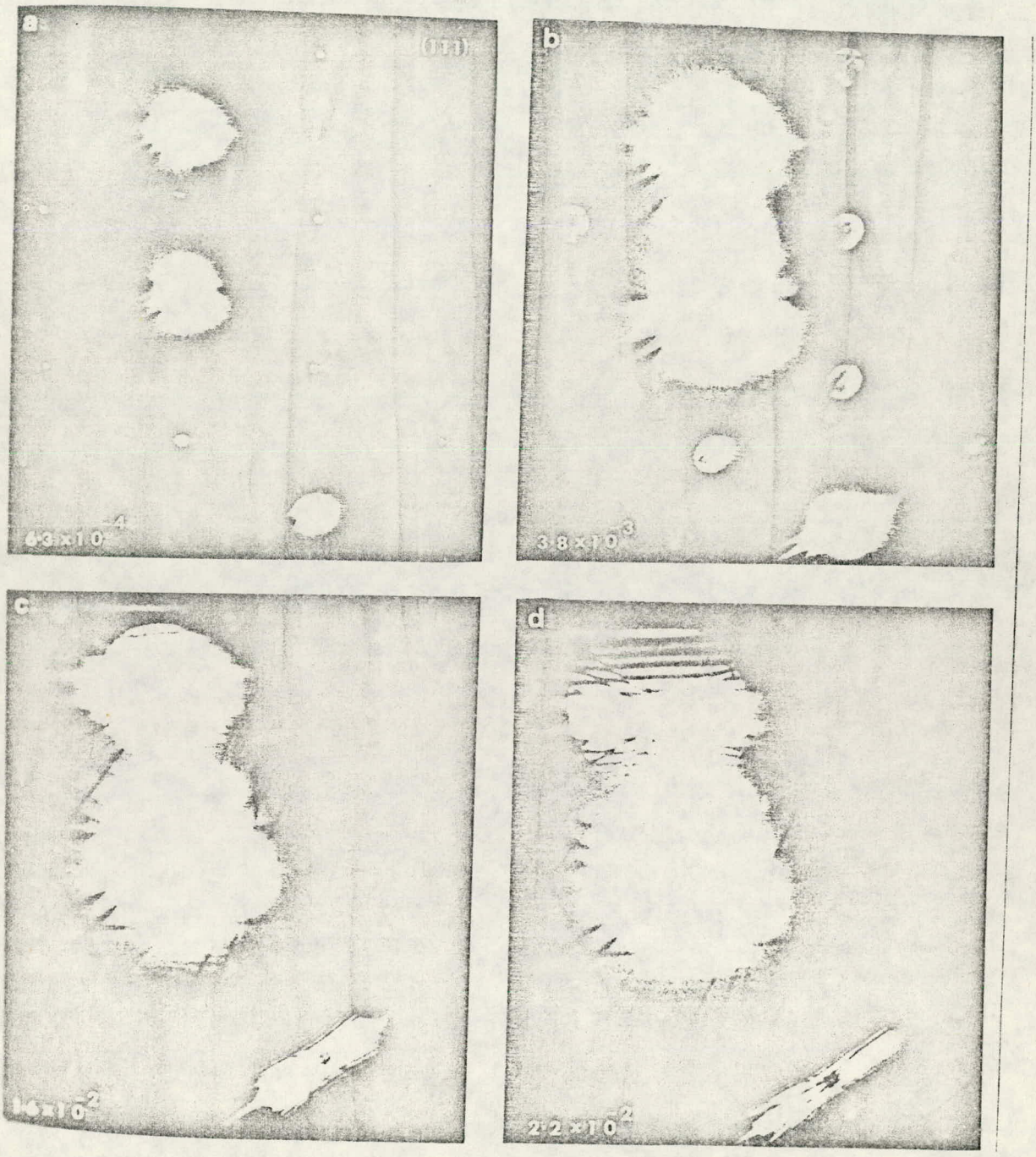

Fig. 63. Comparison of Electron Diffraction Patterns for Various Values of Incident Beam Convergence (as Indicated on Each Figure).

however, this markedly reduces the incident beam current and hence the diffracted intensities. Similar results can also be obtained by changing the excitation of the second condenser lens which has a much smaller effect on the probe current; however, there is a substantial change in the probe diameter as the condenser current is varied. Figure 64 shows the measured variation in probe diameter as a function of second condenser lens current in the JEOL JSEM 200 operating at 200 keV with a condenser aperture of 100 μm. At an excitation of 43 mA the probe diameter was ∿1 μm at a convergence of ∿10^{-4} radians, while at STEM imaging conditions (∿ 52 mA) the probe diameter was ∿100 Å at a convergence of ∿10^{-2} radians. Probe size measurements in Fig. 64 were made by scanning the incident beam perpendicular to a cleavage surface of a crystal of spherolite and simultaneously recording the signal rise profile of the transmitted beam intensity.

Although convergent beam diffraction patterns (CBDP) have poor angular resolution, they contain a substantial amount of information; examples of this can be found in the literature.[83, 89, 96, 97] Furthermore, it is not always necessary to operate a STEM instrument in the highest resolution mode; thus one can judiciously adjust the parameters of probe size, convergence, and current in order to optimize the relevant experimental information obtained during an analysis. Figure 65 illustrates this point, showing a TEM micrograph of a V-Ti-C alloy containing carbide precipitates. With the STEM probe adjusted to ∿ 300 Å in diameter CBDPs were measured from both the carbide precipitate

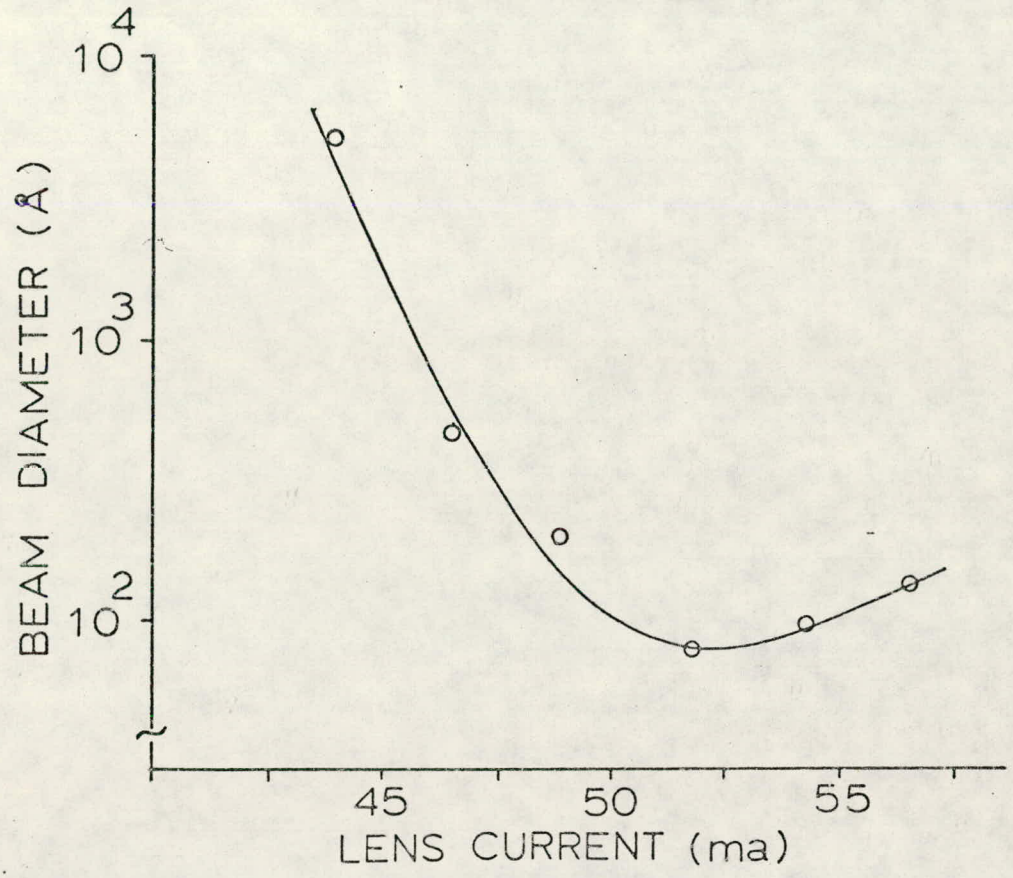

Fig. 64. Variation in Electron Beam Diameter as a Function of Condenser Lens Excitation.

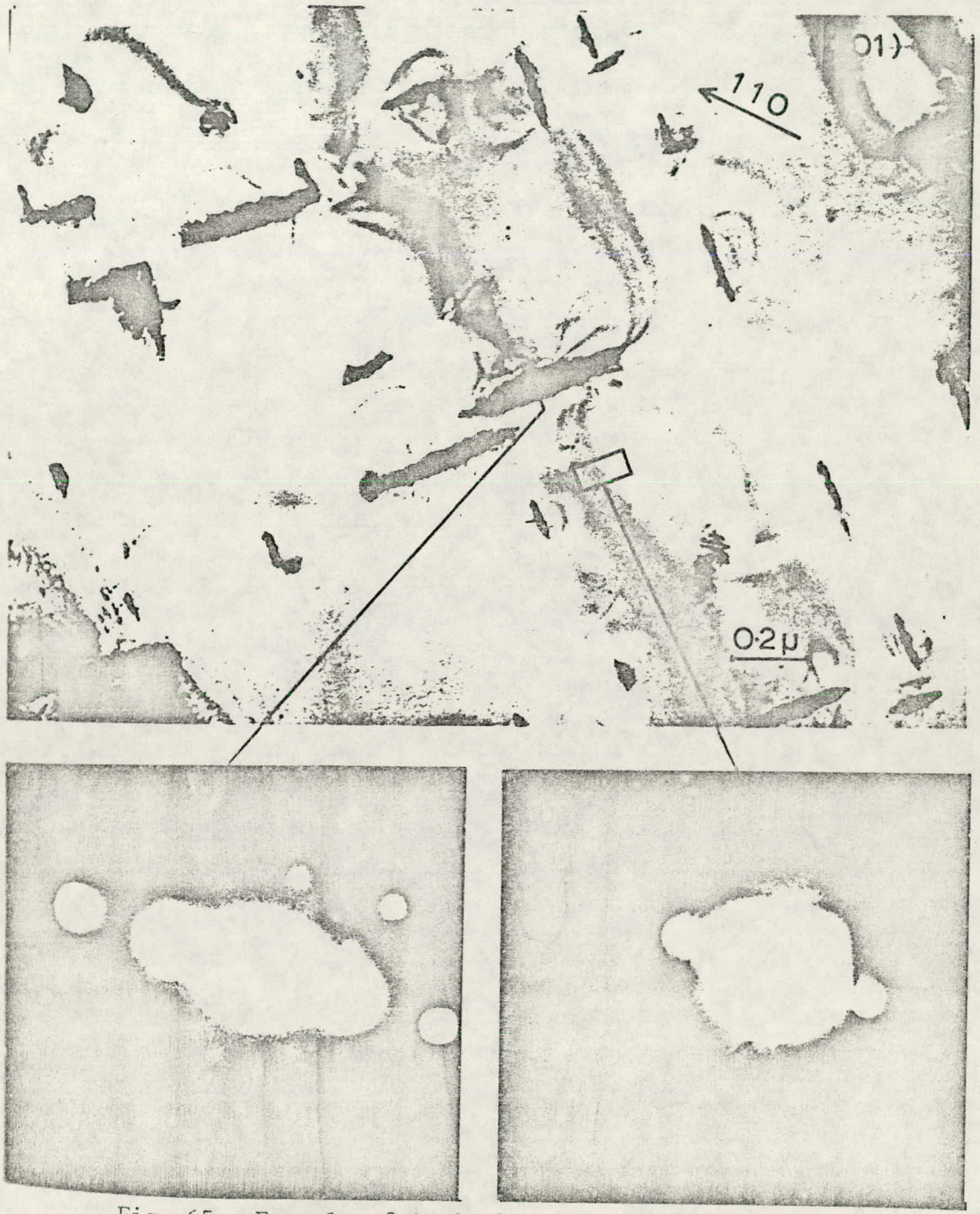

Fig. 65. Example of Analysis of V-Ti-C Precipitate Using Stationary Diffraction Technique.

as well as the matrix regions as indicated. The CBDP obtained from the precipitate reveal a number of extra reflections, which are also easily detected using SAD techniques. However, using SAD it was not possible to determine uniquely whether the extra reflections were a result of faulting and/or twinning in the precipitate or due to an extension of the unit cell. The CBDP obtained from the nearby matrix region clearly shows the presence of Kikuchi lines which are not detected in the precipitate region indicating that faulting and/or twinning is the most likely source of the satellite intensity.

2.3.2 Transmission Scanning Electron Diffraction (TSED)

Transmission scanning electron diffraction (TSED)[94,95,98] refers to the process of post-specimen scanning and the subsequent electronic recording of the intensity distribution of diffraction patterns for static incident electron probes. Since this technique involves post-specimen scanning, any intensity distribution which can be observed in the TEM can be measured; thus when operating in the CTEM imaging mode this technique is referred to as transmission scanning electron microscopy (TSEM).[95,98] The most important aspect of TSED/TSEM is that the intensity distribution is measured electronically rather than photographically yielding a greater sensitivity as well as a wider range of linear response (10^5 versus 10^1) to changes in intensity. The major drawback of the technique is that the information is at present recorded serially. Thus each point must be measured sequentially and hence

scanning rates necessary to accumulate sufficient statistics may be slow. This lengthy recording time may then introduce other errors such as stage drift.

Figure 66 is a schematic diagram of the electron optical system used for TSED/TSEM measurements in the JSEM 200. In this system a set of post-specimen scan coils located between the intermediate and projector lenses is used to translate the intensity distribution of interest across an aperture in the final viewing screen of the microscope. The sweep rate is determined by a time base in the ORTEC 6200 multichannel scaler (MCS) which produces a digital voltage ramp of 1024 points/scan whose dwell time can be adjusted from 1 μs to 10 s per channel. This digital ramp is routed into a control circuit which splits the signal into a ratioed set of x and y scans to which a dc level shift is introduced. Using this signal splitting circuit (Appendix G) digital line scans of continuously variable amplitude, position and orientation can be generated along any desired direction. The detector system consists of the scintillator/photomultiplier unit normally used for STEM imaging. However, in this case the output of the photomultiplier tube (PMT) is routed through a two-stage linear preamplified/amplifier system having a variable gain of 5 to 50 times rather than the STEM electronics. The signal is then digitized using a voltage-to-frequency converter and subsequently stored in the MCS unit. After the data have been accumulated in the MCS memory, software programs can be used to transfer these data to the on-line microcomputer system for storage (using the program MCA) or analysis (using the program NMCS).

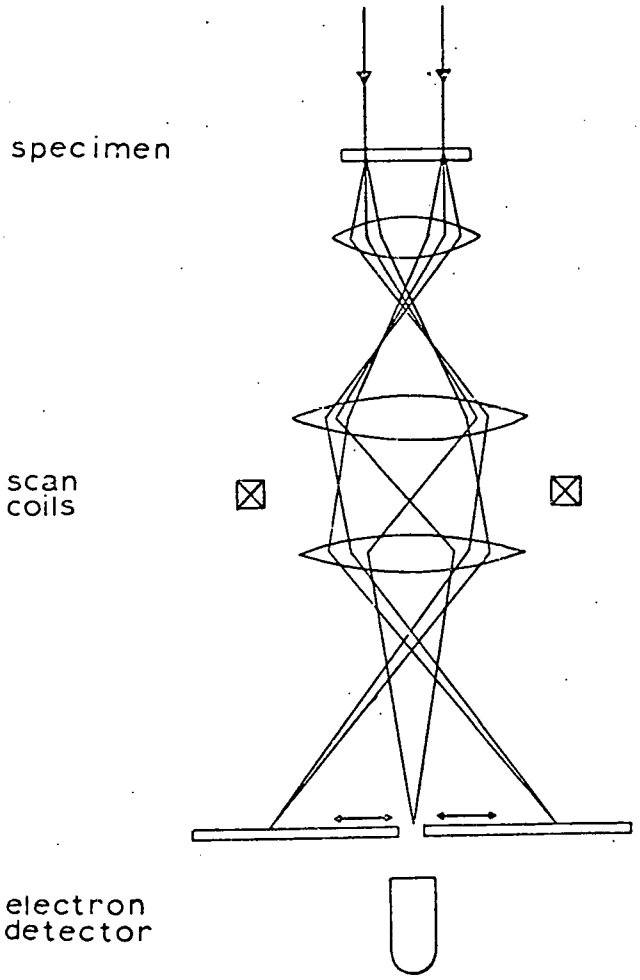

Fig. 66. Ray Diagram for Transmission Scanning Electron Diffraction/Microscopy (TSED/TSEM).

Figures 67 and 68 are examples of TSED and TSEM measurements made on a TEM/STEM instrument equipped with the identical scanning and detection system as described above.[98] Figure 67 shows the measured intensity distribution along a <220> direction in reciprocal space of a single crystal of copper in the (001) orientation having a thin surface oxide layer. Two superimposed traces are shown in Fig. 67(a). Trace A is plotted such that the transmitted beam intensity can be conveniently observed, whereas the second trace B is the same data replotted using a scale factor 100 times greater along the y-axis; in this curve the Bragg intensities as well as the weak oxide reflections are clearly discernible. The ratio of the weakest oxide reflection to that of the transmitted beam intensity is nearly 2000/1. Figure 68 shows an example of a TSEM measurement of the oscillatory fringe contrast from a semicoherent θ′ plate in Al–4% Cu.

2.4 Electron Energy Loss Spectroscopy (ELS)

As electrons pass through TEM specimens they suffer losses in energy due to various inelastic scattering events. These changes in energy have two consequences. First, they are responsible for image distortions due to chromatic aberations which can complicate or obscure image detail. Second, the energy losses, which the transmitted beam incurs, are related to specific inelastic scattering processes and thus contain information concerning the nature of the atomic, electronic, and elemental structure of the sample. Furthermore, electron energy loss spectroscopy (ELS) has the highest yield of information per inelastic

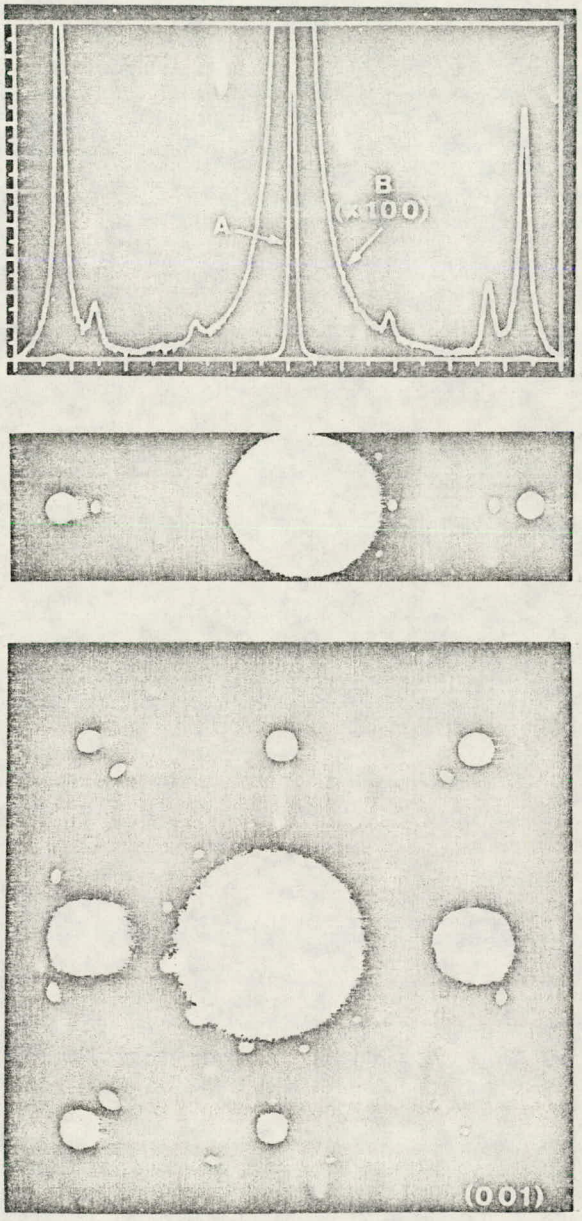

Fig. 67. Example of TSED Measurement along <220> Direction of the (001) Pattern Shown in (c).

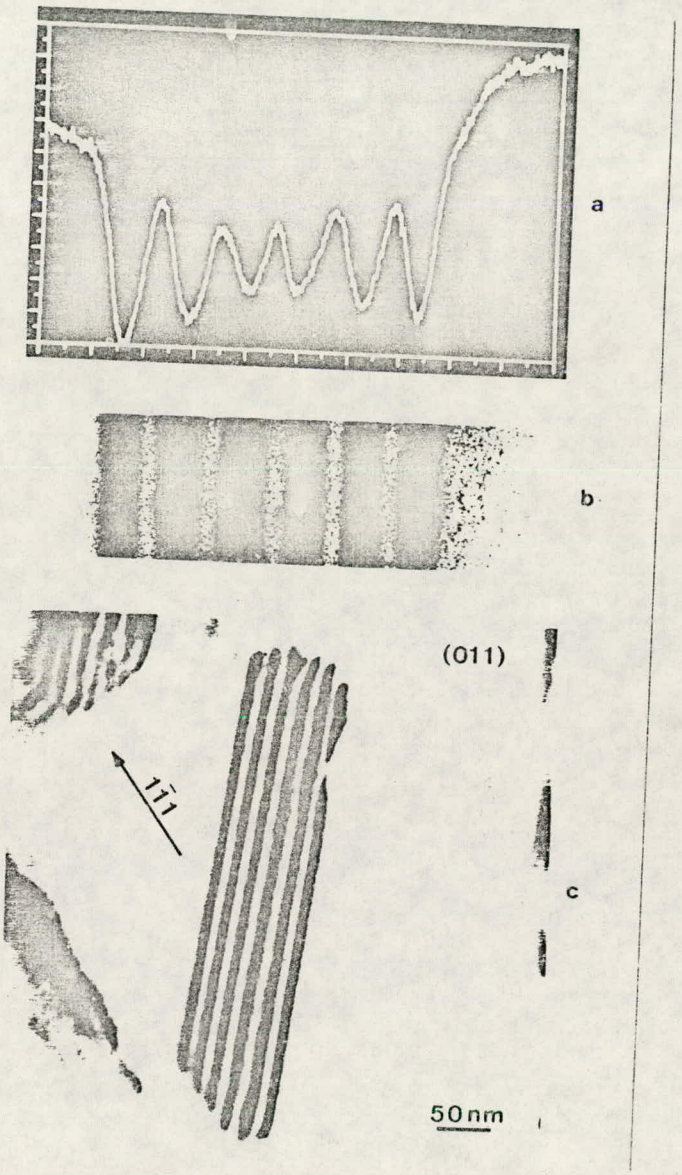

Fig. 68. Example of TSEM Measurement of Fringe Pattern of θ′ Precipitate Shown in (c).

scattering event due to the fact that one is now measuring the primary interaction process rather than a secondary process such as x-ray or Auger emission. For materials related research, one of the most important aspects of ELS is the ability to perform light element analysis such as the detection of the interstitial elements C, N, and O. These measurements cannot realistically be made using conventional x-ray EDS techniques and thus ELS complements the capabilities of an analytical electron microscope system. Spatial resolution of this technique is essentially limited only by beam broadening effects and hence for suitable specimens resolutions less than 5 nm are possible.

Microchemical analysis using energy loss spectroscopy is obtained by measuring the number of electrons which have undergone characteristic energy losses due to the excitation of inner shell levels. These loss electrons exhibit characteristic profiles in an energy loss spectrum, which are similar in shape and meaning to the classical absorption edge profiles in x-ray spectroscopy and are thus similarly labeled. Quantitative analysis using ELS is still in the early stages of development and at the present time the formalism proposed by Egerton and Whelan[99] seems most promising.

During this study ELS was used only as a qualitative tool to detect the presence or absence of oxygen in localized regions of the specimen; however, quantitative analysis using ELS is an interesting and important aspect of AEM.

CHAPTER 3

3. EXPERIMENTAL OBSERVATIONS AND RESULTS

3.1 Instrumentation

A JEOL JSEM 200 transmission electron microscope was the primary instrument used during this investigation. This microscope was equipped with a side-entry goniometer stage allowing specimen tilting so that crystallographic analysis can be performed. In addition, the instrument had facilities for scanning transmission electron microscopy (STEM), secondary electron (SEM) and backscattered electron imaging (BEI). Specimen holders capable of double-tilt, tilt-rotate, single-tilt cooling (-196°C to 25°C) and heating (25°C to 300°C) were also available. The electron source was a standard thermionic tungsten hairpin filament and the microscope was capable of operating at accelerating voltages of 200, 150, 100, and 50 kV. Unless otherwise specified, all micrographs and measurements presented in this section were made at an incident beam energy of 200 keV in conventional TEM imaging and diffraction modes.

Because of the nature of the experiments to be performed in the present work, substantial modifications have been made to the electron-optical column of the JSEM 200 in order to upgrade this CTEM/STEM instrument into an analytical electron microscope (AEM). A solid state Si(Li) x-ray detector was interfaced to the microscope column and an x-ray collimator designed and attached to the detector head. A special bremsstrahlung aperture (see Sect. 2.2.7) was subsequently installed and

a double-tilt stage modified to reduce system peaks (see Sect. 2.2.7). To lessen the number of backscattered electrons from the anti-contamination device, objective aperture blade and pole-piece material from hitting the sample, graphite blocks or coatings were judiciously placed in the specimen chamber. The vacuum system was improved by the addition of a turbo-molecular pump (500 liters/s) to further increase the vacuum in the specimen region and extra liquid-nitrogen cold traps were designed for the sample chamber, high resolution diffraction chamber, and each of the roughing pump lines to reduce backstreaming and contamination. Special isolation valves were fitted to the specimen prepump and column roughing line to further inhibit backstreaming from these sources once the sample was introduced into the column vacuum. Bayard-Albert ionization gauges were attached to the system to monitor the vacuum levels in the specimen chamber and turbopump lines. After these modifications, the column vacuum near the specimen was typically $\sim 8 \times 10^{-6}$ torr and $\sim 2 \times 10^{-7}$ just above the turbopump. In order to improve the diffraction capabilities in STEM, it became necessary to remove and bore out a fixed aperture in the intermediate lens pole piece. The diameter of this fixed aperture was increased from 3 mm to 1 cm yielding nearly a threefold increase in the angle subtended in the STEM diffraction mode. A Faraday cage was designed to fit in the viewing chamber of the column and a ten times preamplifier added to the STEM detector to improve the signal-to-noise performance in the STEM mode. Finally, an on-line computer system was interfaced to the microscope via the multichannel analyzer. The mini-computer was

subsequently connected to the central computer of the Materials Research Laboratory to allow paper tape and/or direct telephone line transfer of data.

A second instrument recently acquired by the Materials Research Laboratory was used for the electron energy loss measurements presented in this study. The microscope was a Vacuum Generators HB5, dedicated scanning transmission electron microscope (DSTEM), operating at accelerating voltages up to 100 kV. The electron source was a cold field emission tungsten single crystal tip and under normal operating conditions the vacuum levels in this UHV instrument were $\sim 2 \times 10^{-11}$ torr in the gun chamber and $\sim 2 \times 10^{-9}$ at the specimen. Electron energy loss measurements were made on a $\pi/2$ magnetic sector energy analyzer having an energy resolution of 1.2 eV at an input divergence of 10^{-4} radian. These data were recorded on an ORTEC multichannel scaler and subsequently analyzed on the mini-computer system previously discussed (Sect. 2.2.8) using the software described in the appendices of this thesis.

3.2 Sample Preparation

The samples used for this study were prepared from an ingot of Zr–15% Nb kindly provided by Drs. Paton and Williams of Rockwell International Science Center, Thousand Oaks, California. The as-received material was homogenized for five days at 1000°C in the β field and then quenched to precipitate the omega phase. The bulk sample was cut into wafers approximately 0.5 mm thick using a high-speed water-cooled diamond slicing wheel and disc shaped specimens 3 mm in diameter

were subsequently prepared using electrodischarge machining. These discs were cleaned in an $HF-HNO_3$ solution[8] to remove contamination from the surface then washed in reagent grade methanol. In order to ensure retention of the omega phase in these discs, all samples were heat treated and quenched a second time. The 3-mm discs were wrapped in zirconium foil and placed in quartz tubes. Large aggregates of sponge titanium were also introduced into the quartz capsules in order to assist the zirconium foils as oxygen getters during heat treatment. The capsules were evacuated to a dynamic pressure of 9×10^{-6} torr and backfilled with high-purity argon gas. The backfilling and evacuation procedure was repeated five times in order to flush as much residual gas out of the tube as possible. The capsules containing a 0.25 atm of argon were then sealed and the samples homogenized for 2 h at 1000°C, followed by quenching into an ice water bath. Following heat treatment, the discs were analyzed using wet chemical, vacuum fusion mass spectrographic and electron microprobe techniques. The results of these analyses are summarized in Table 2.

Initial polishing attempts concentrated on the documented chemical polishing technique of Sass et al.[7–12] in their studies of Zr-Nb alloys. This technique was difficult to use and met with only limited success. Furthermore, when the sample thickness fell below approximately 200 μm, hydride plates were observed to form spontaneously throughout the sample similar to that reported by Flewitt et al.[100] in alloys of 40–85% Nb with Zr. Cooling the solutions to −30°C did not reduce this precipitation and on continued polishing the hydrides were observed to grow, with perforation

Table 2. Chemical Analysis of Zr–15% Nb Samples after Heat Treatment

Element	Concentration (atomic parts per million)
Zr	84.6 (wt %)*,†,‡
Nb	15.4 (wt %)
H	86§
O	235§
Na	5#
Mg	⩽ 3#
Al	70#
Si	50#
Cl	4#
Ca	⩽ 0.3#
Ti	50#
V	⩽ 0.2#
Cr	10#
Fe	50#
Ni	⩽ 2#
Pd	7#
Ag	30#
Cd	⩽ 3#
Sn	⩽ 2#
Hf	20#
Pb	0.3#
Bi	0.3#

*Average of three determinations.

†Wet chemical analysis.

‡Electron microprobe analysis.

§Vacuum fusion analysis.

#Mass spectrographic analysis.

usually occurring at one of these plates presumably due to preferential polishing. Optical and TEM micrographs of this structure are shown in Fig. 69.

In an attempt to reduce this hydride precipitation, a solution developed by Schober and Sorajic,[101] which avoids the introduction of hydrogen into the sample, was used. This electrolyte, 0.05 moles/liter of $Mg(ClO_4)_2$ in CH_3OH, has been successfully used to reduce the hydride formation. Samples were prepared in a dual jet electropolishing unit operating at a potential difference of 100 V drawing a current of 0.05 A. The sample was mounted in a Teflon holder with all electrical connections made using platinum wire; the cathode used was stainless steel and the solution kept at −30°C. Due to the nature of the electrolyte a thick viscous film was observed to form during electropolishing. Schober recommended washing in a dilute H_2SO_4 solution after perforation; however, it was found that by adjusting the flow rate of the polishing solution through the twin jet system to $\sim$10 ml/s/mm^2 it was possible to continuously wash the film from the sample surface. Perforation was monitored by the detection of transmitted light from a He-Ne (100 mW) laser via a photo-resistor/light pipe system. This photo-resistor was electronically coupled so that when light was transmitted through a small hole produced by the electropolishing both the flow of polishing solution as well as all electrical power were disconnected. Samples were immediately washed in reagent grade methanol for approximately 2 min followed by a gentle drying using a forced-air blower. The air flow in this case was always directed parallel to the sample surface

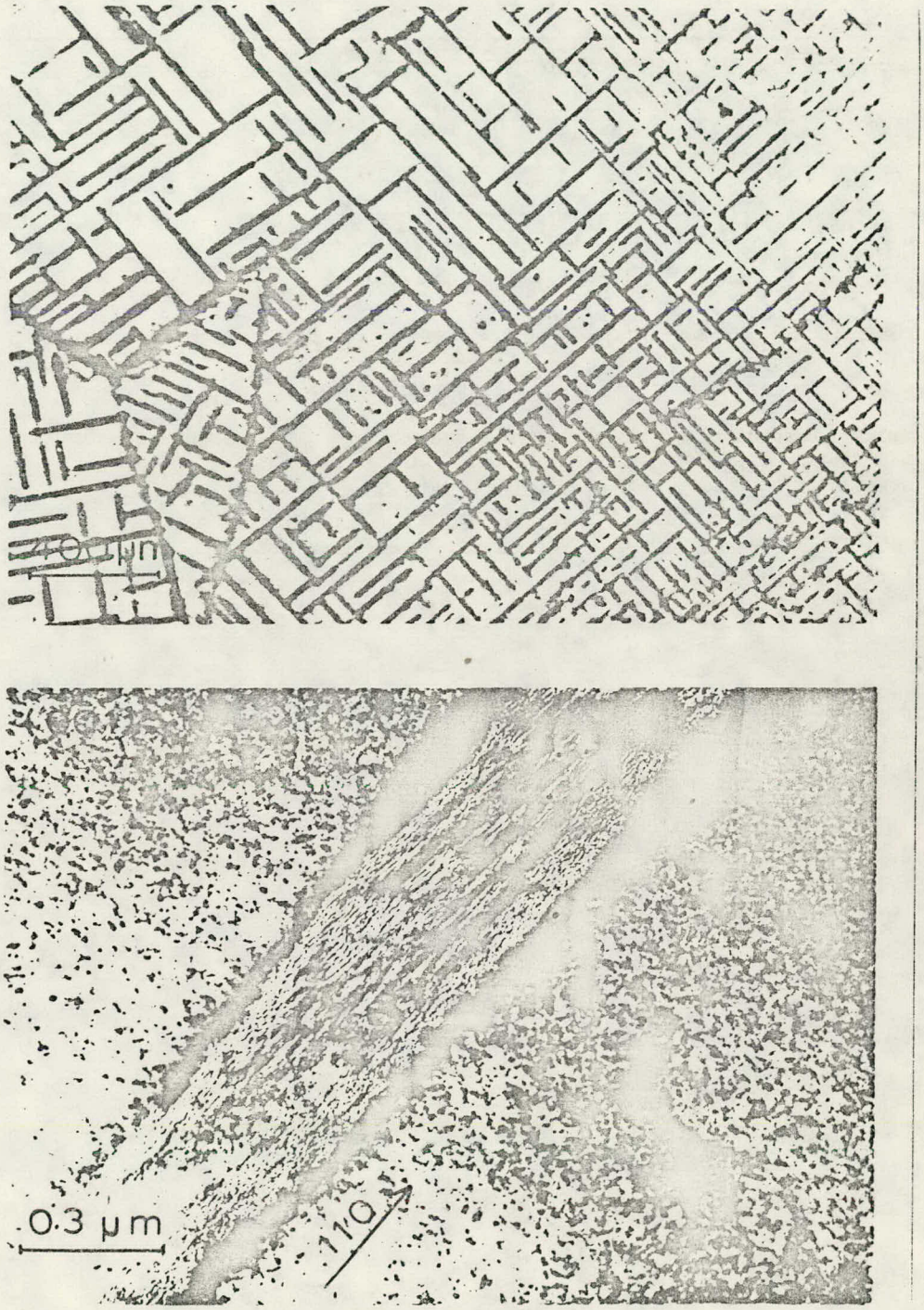

Fig. 69. Optical (a) and CTEM (b) Micrographs of Hydride Precipitates in Zr–15% Nb.

in order to avoid possible damage to the thin specimen area. Typical thin regions usually contained one or two large grains allowing easy manipulation for crystallographic analysis.

3.3 Microstructural Observations

During the course of this study a variety of microstructures in addition to the as-quenched $\omega + \beta$ morphology were noted in the Zr–15% Nb alloy. In at least one case the experimental results were initially misinterpreted as the formation of a long-period ordered structure of the ω phase, and hence a complete characterization of each phase observed became an important part of this research. A summary of these microstructures and their analysis is described in this section.

3.3.1 As-Quenched Morphology of the Omega Phase

The as-quenched microstructure of the Zr–15% Nb alloy containing the omega phase is shown in Fig. 70. Since there are no discernible microstructural features in a bright-field TEM image, the presence of omega must be confirmed through the use of electron diffraction, as is shown in the (011) diffraction pattern of Fig. 70(b). The most striking feature of the microstructure of this alloy is the absence of any observable dislocation structure. This result has been reproduced in some 30 as-quenched samples containing the ω phase indicating an apparent dislocation density of less than $10^5/cm^2$. This low dislocation density correlates with the presences of the omega phase, since for a Zr-Nb alloy which does not contain omega, the dislocation density is on the order of $10^8/cm^2$. This can be seen in Fig. 71 which is the microstructure of a

a

(011)

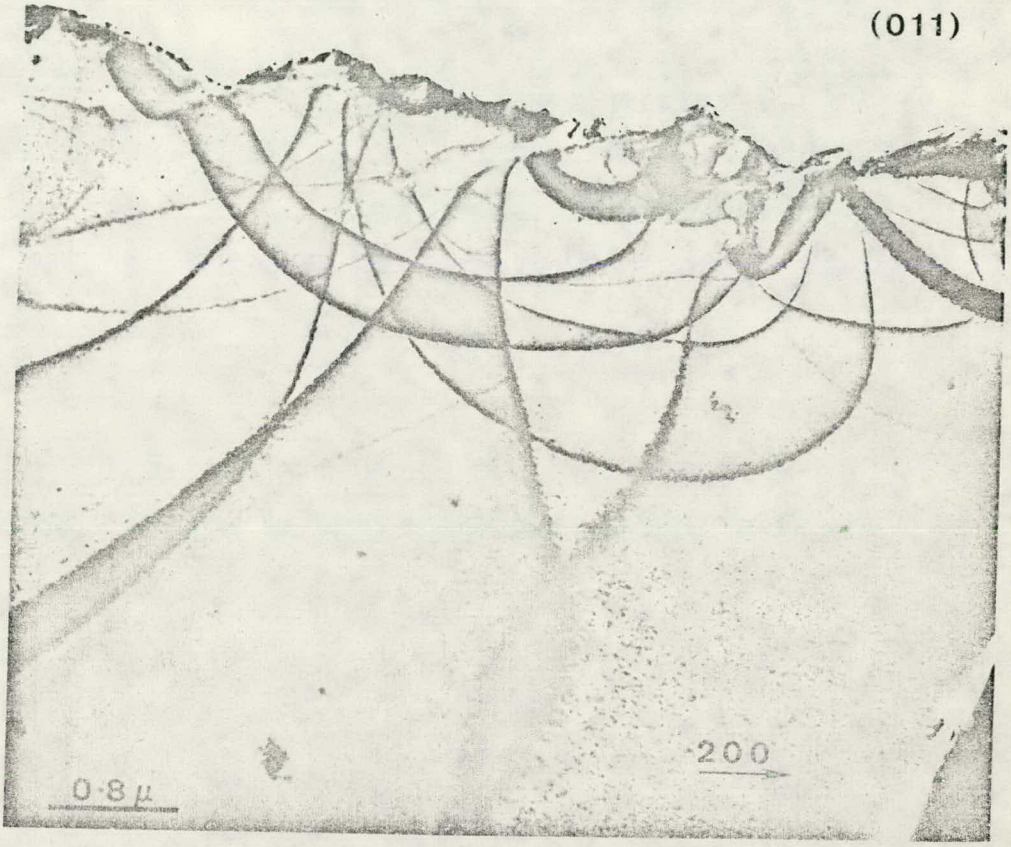

b

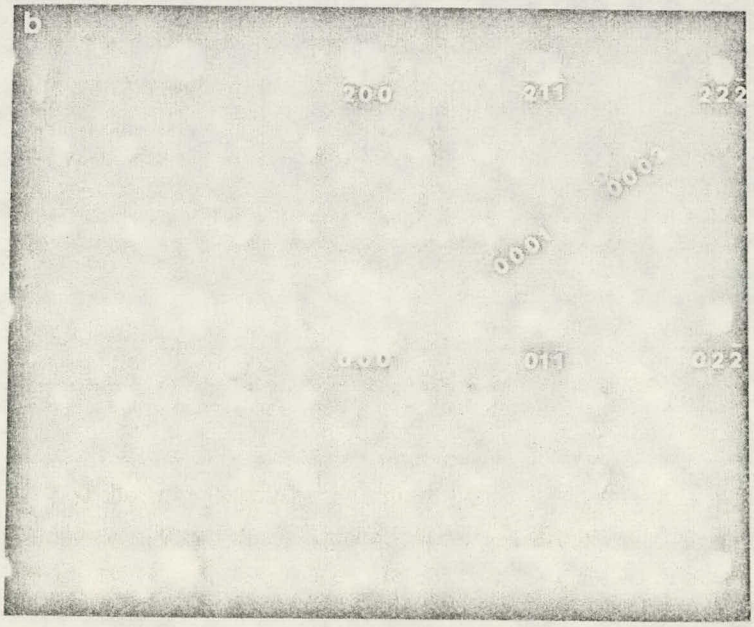

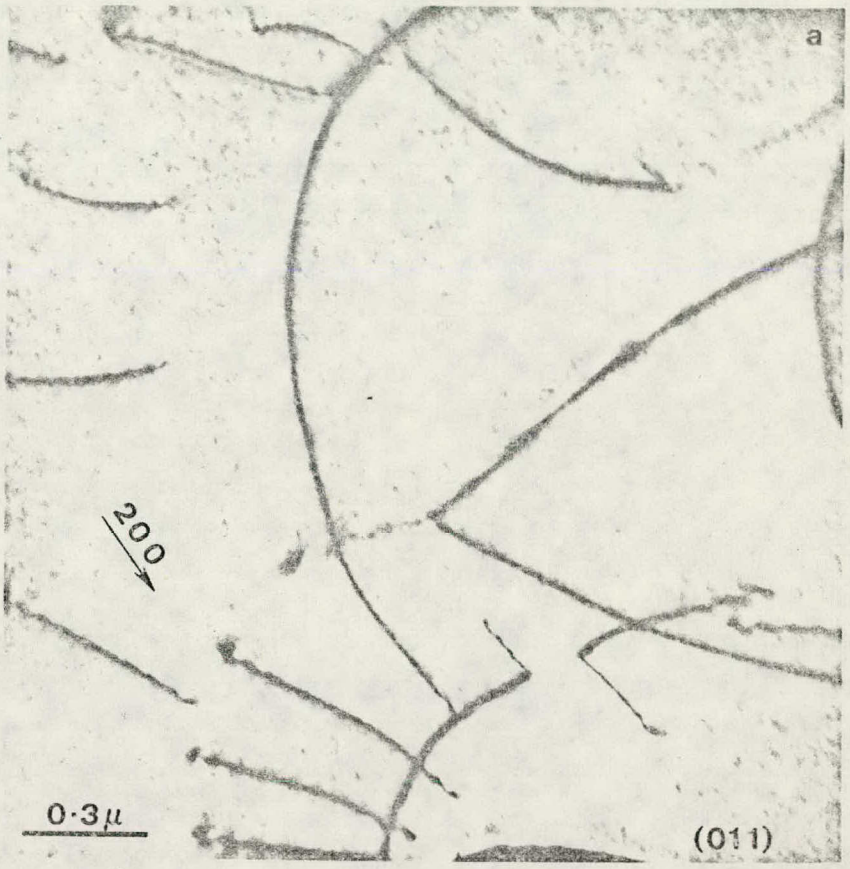
a
200
0·3μ
(011)

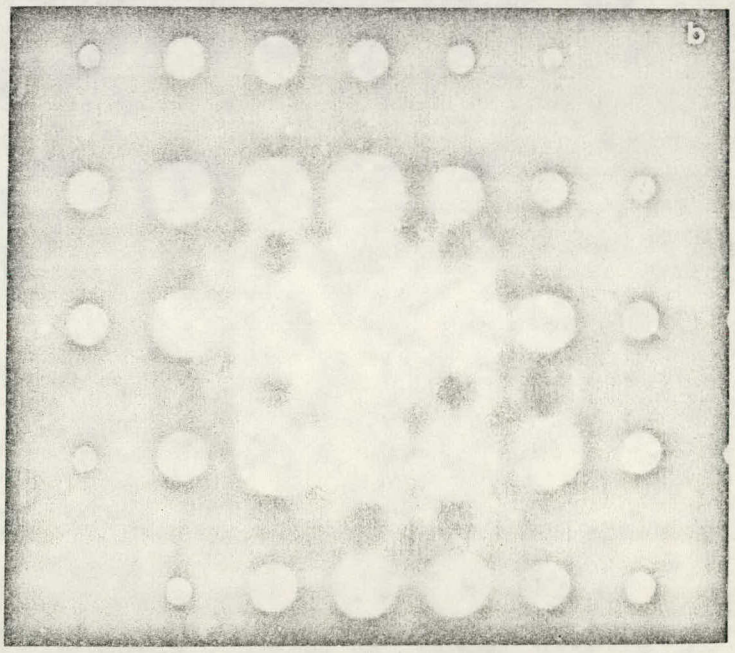
b

Zr–80% Nb alloy having undergone identical sample preparation steps (heat treatment, polishing, etc.) as the 15% Nb alloy. The absence of the omega phase is clearly indicated in the (011) electron diffraction pattern of Fig. 71(b).

Figure 72(a) is a TEM bright-field micrograph of the as-quenched omega structure at higher magnification and as pointed out no distinctive features are present. Dark-field micrographs such as Fig. 72(b) taken using an ω_{0002} reflection [indicated in Fig. 71(b)] show the presence of omega domains less than 30 Å in diameter distributed uniformly in the bcc matrix. Throughout this work no alignment of the omega domains along <111> directions of the bcc lattice has been observed. The fact that in the most recent publication of Kuan et al.[12] it was not possible to duplicate the alignment of omega particles along <111> directions is significant in that there is now no conflict between these results and that of Sass et al.[7–11] A summary of electron diffraction patterns from the 15% Nb alloy over a standard stereographic triangle is given in Fig. 73.

3.3.2 Spontaneous Relaxation Effects

Although the microstructure shown in Fig. 70 is relatively simple, this observation was more the exception rather than the rule for this alloy. The majority of the samples were observed to contain thin foil artifacts which exhibited planar lath-like features. This phenomenon has been termed "spontaneous relaxation"[102–105] and has been attributed to a relaxation of the bulk specimen constraints during thinning due to

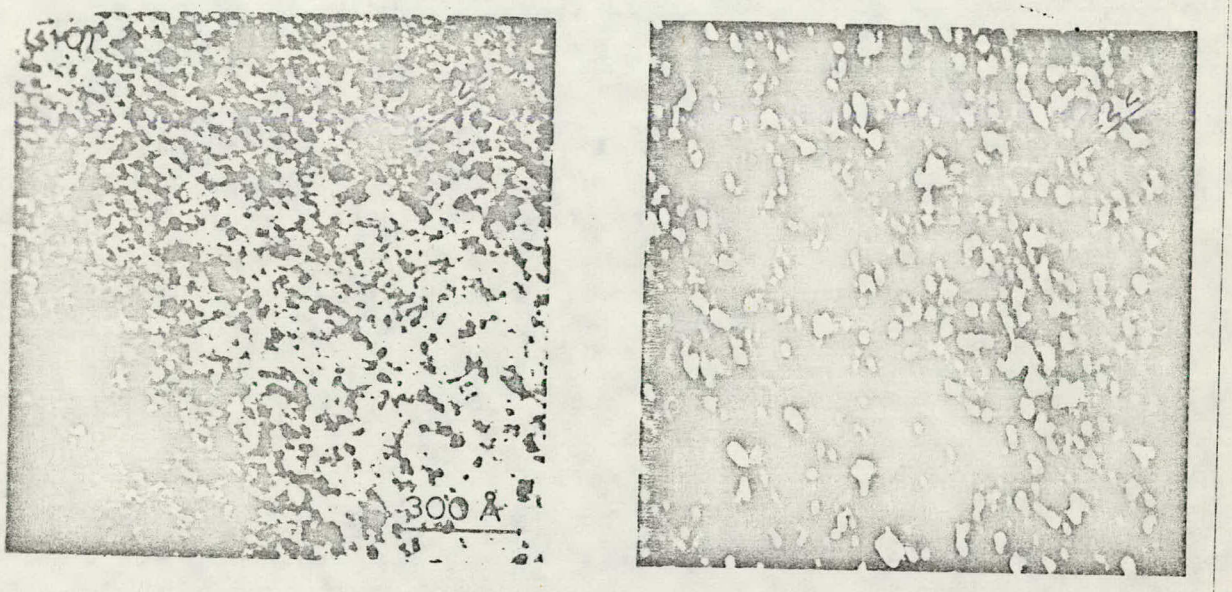

Fig. 72. Bright (a) and Dark-Field (b) CTEM Micrographs of the As-Quenched ω Structure Showing Approximately 30 Å ω Domain Size in the Dark-Field Images.

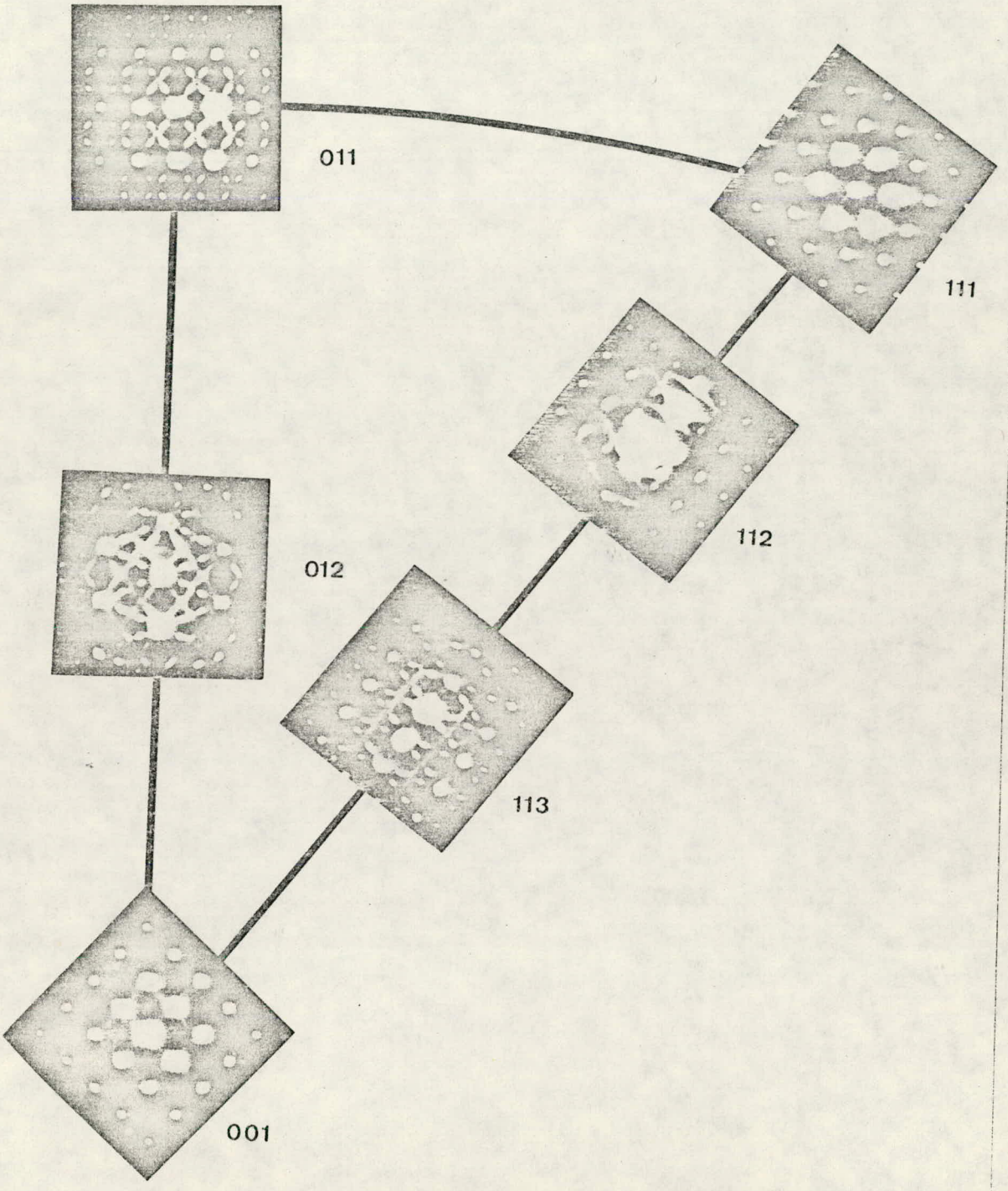

Fig. 73. Summary of Electron Diffraction Patterns from a Zr–15% Nb Sample Containing the As-Quenched ω Phase.

the proximity of the sample surface. An example of this microstructure is shown in Fig. 74. Generally these laths do not occur over the entire specimen region; they do, however, change under the influence of the electron beam. An example of the "dissolution" of these laths with time, and electron irradiation can be seen in Fig. 75. The region in the lower right of Fig. 75(a) shows the presence of the thin foil artifact, while a moving interface in the upper left was caught in the process of transforming the lath-like region. Within approximately 2 min of initial observation (at 200 keV) the region was completely transformed. The diffraction patterns of Figs. 75(b) and (c) show that only a change in the relative crystallographic orientation ($\sim$10°) from approximately $(001)_\beta$ to nearly $(113)_\beta$ has occurred as the interface swept across the field of view. No apparent structural differences were observed between the lath-like and matrix regions. However, it was not possible to verify this observation using a complete crystallographic tilting experiment due to the finite lifetime of these thin foil artifacts.

Spurling et al.[102] has shown that argon ion beam milling techniques can be used to circumvent the relaxation problem in titanium alloys. Using this technique it was possible to eliminate the relaxation phenomenon in the Zr-Nb alloy; however, there are two serious drawbacks of using ion milling with respect to this study. First, considerable radiation damage is introduced into the sample by the ion beam. This produces a "mottled" background superimposed on a coarser undulated

ORNL PHOTO 5804-78

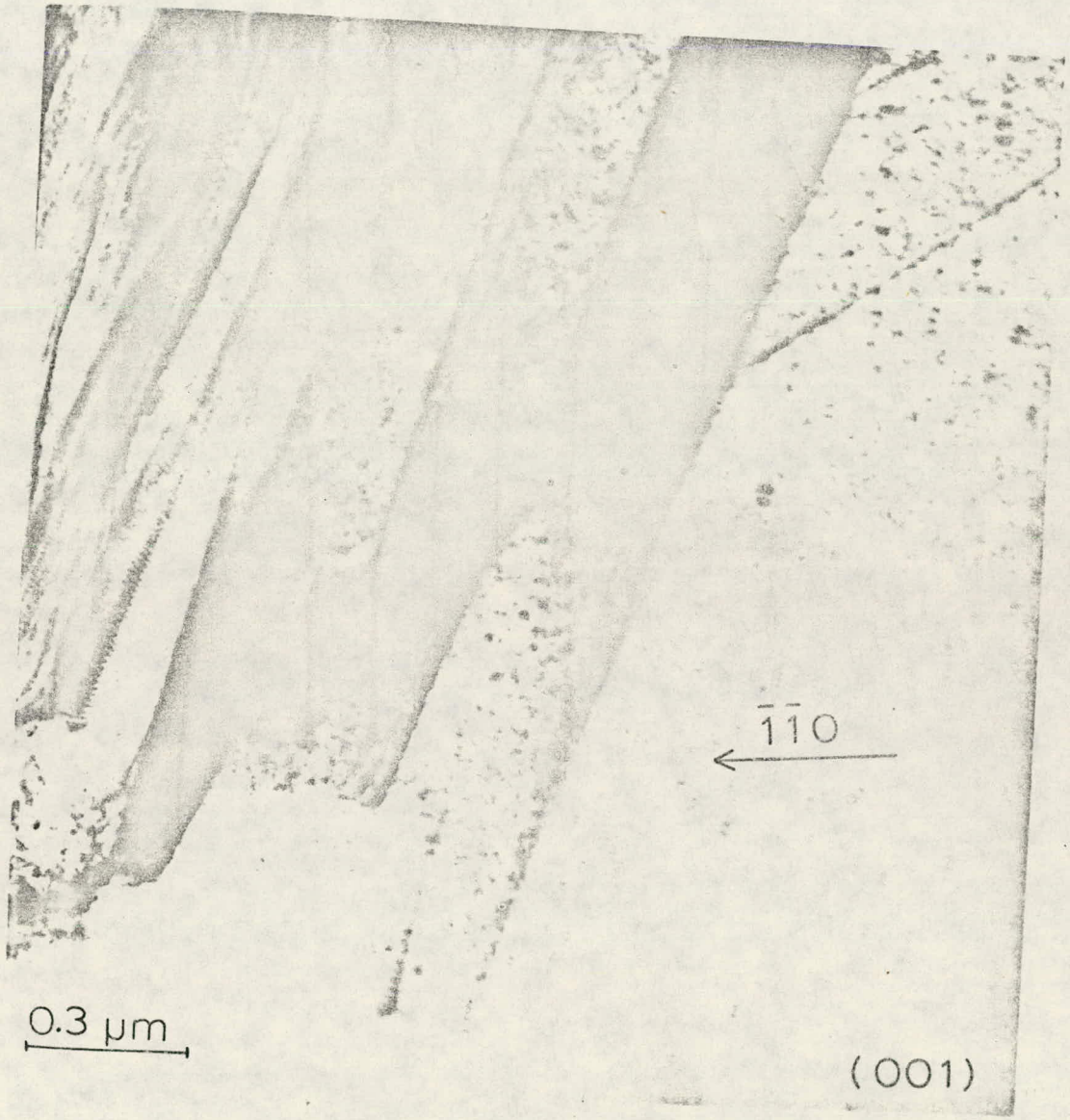

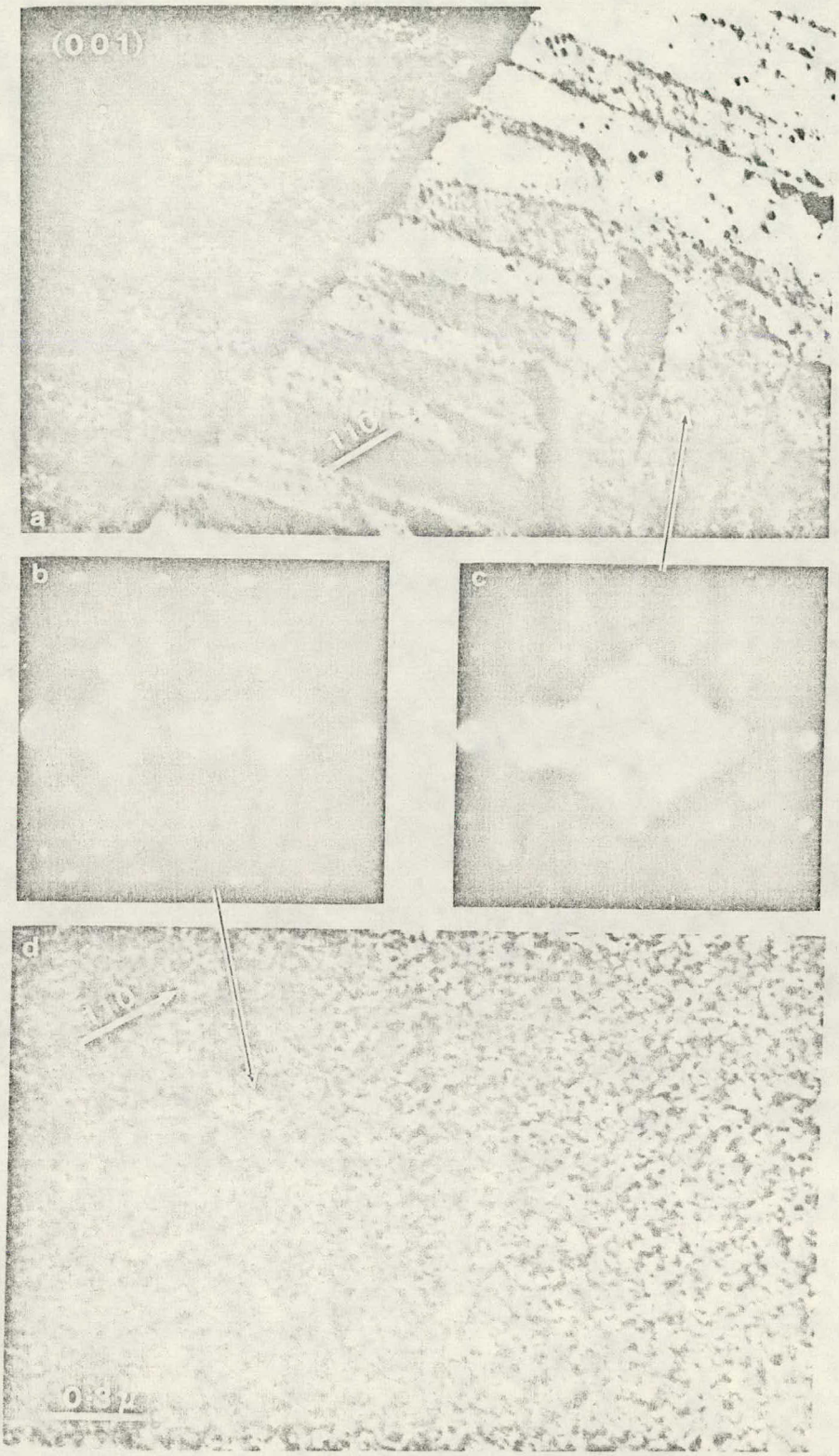
(001)
[110]
a
b
c
d
[110]

structure as shown in the micrograph of Fig. 76. This structure precludes any high resolution studies of the ω phase morphology. The second problem related to ion milling is associated with specimen heating effects. This is due to the fact for typical specimens ∿100 μm thick the ion beam milling times were on the order of 48 h for a dual beam system operating at 5 keV at 30 mA of ion current, and a 20° glancing angle. Under these conditions sample heating effects in excess of 50°C were noted. This has particular importance due to the fact that the omega transformation temperature is in the vicinity of 150°C. Thus, due to these effects, ion beam thinning of TEM specimens was discarded as a viable solution to the spontaneous relaxation problem in this alloy.

3.3.3 Phases Resulting from Compositional Inhomogeneities

It was also observed that occasionally isolated regions of a few specimens contained structures not associated with either the problems previously discussed or the omega phase morphology. One such region is shown in Fig. 77(a) with its (011) diffraction pattern below. Clearly this structure is not characteristic of the 15% Nb alloy, and subsequent x-ray microanalysis measurements showed these regions to be significantly different in composition. The region shown in Fig. 77, for example, was analyzed to contain 50% Nb. All samples found to have such inhomogeneities were discarded from further experimental work.

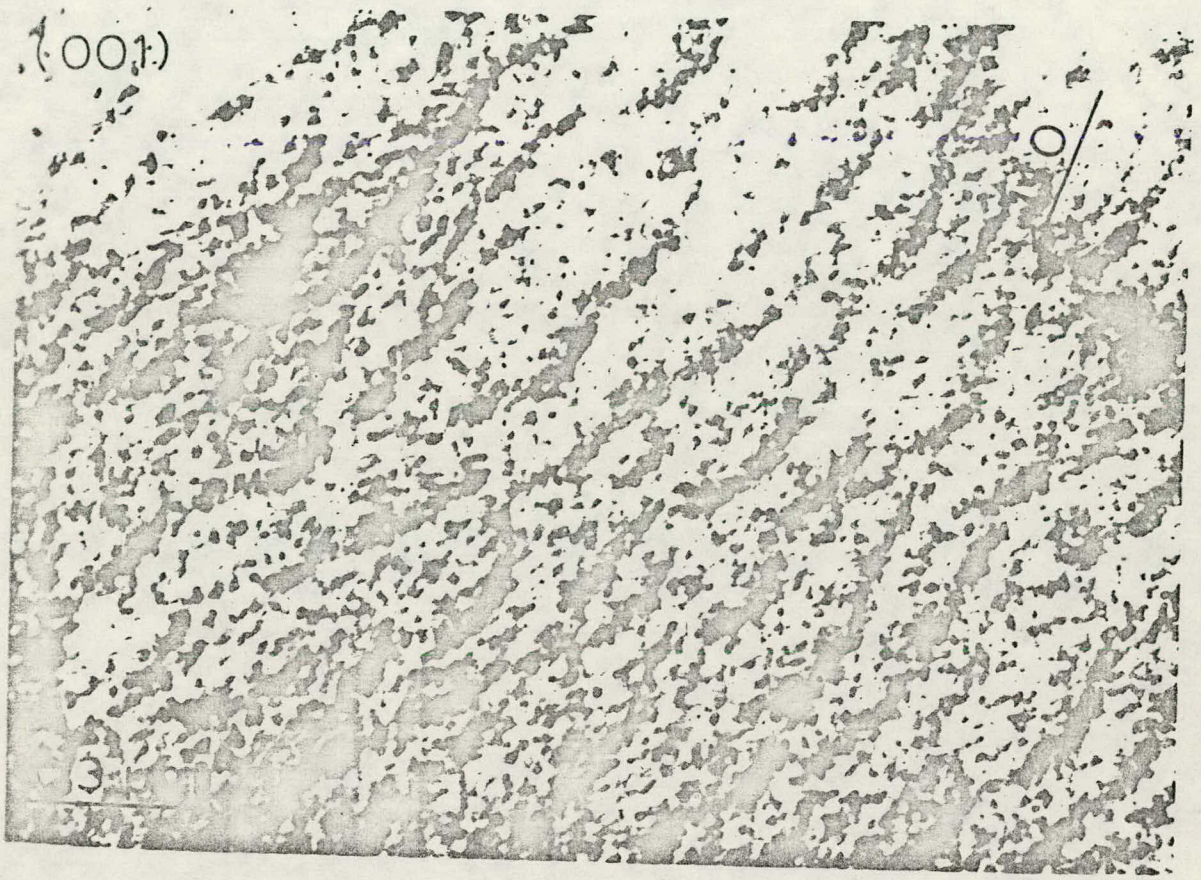

Fig. 76. Example of Typical Argon Ion-Milled Structure in Zr–15% Nb.

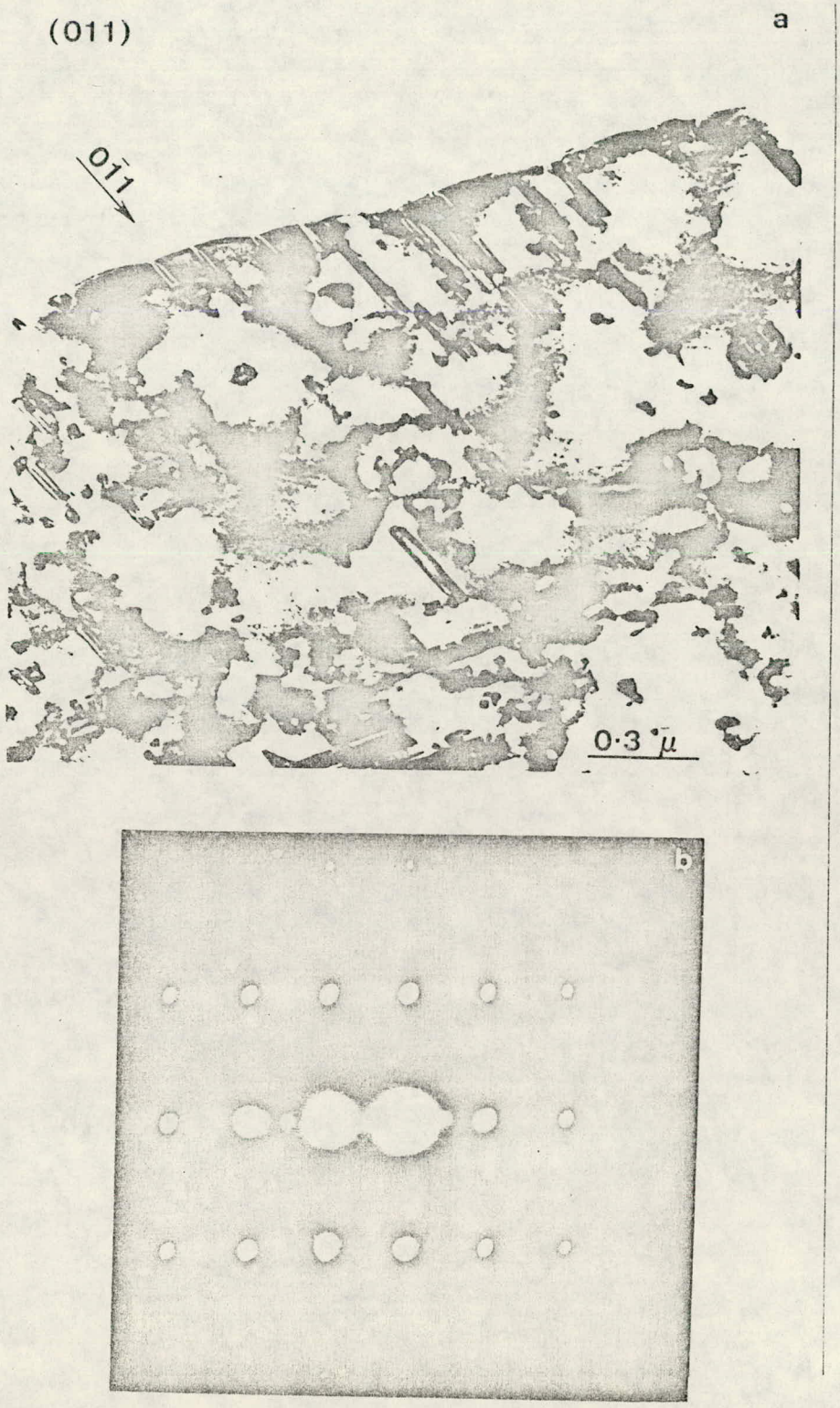

Fig. 77. Microstructure Associated with Compositional Inhomogeneities and Corresponding (011) Diffraction Pattern.

3.3.4 Phases Resulting from Incomplete Quenching

Several samples were observed to contain a coherent lath structure approximately 2500 Å in breadth aligned along a <011> direction of the bcc lattice as shown in Fig. 78. These structures were for the most part too small to analyze using conventional diffraction techniques and thus stationary micro-micro-diffraction was utilized. As can be seen in Fig. 79 these laths alternate between β and β + ω phase regions with an occasional hexagonal area being detected. STEM x-ray microanalyses of these laths indicate their composition to be Zr–15% Nb with no segregation between the alternate phases. The development of this structure is probably the result of incomplete quenching from the β field to room temperature.

3.3.5 Intermediate Structures

The second most frequent feature detected in β + ω containing samples is shown in the bright and dark-field micrographs of Fig. 80. As in Fig. 70, no distinct bright-field structure can be recognized; however, in this case dark-field images formed using an ω_{0002} reflection show a structure of approximately 10 Å periodicity aligned along [200] directions of the bcc lattice. Diffraction patterns from the ideal as-quenched ω structure and this sample are compared in Fig. 81. Satellites are clearly observed to develop just off ω_{0002} reflections and are aligned parallel to [222] directions. Dark-field images formed using an β ω_{0002} and a satellite reflection show a characteristic fringe

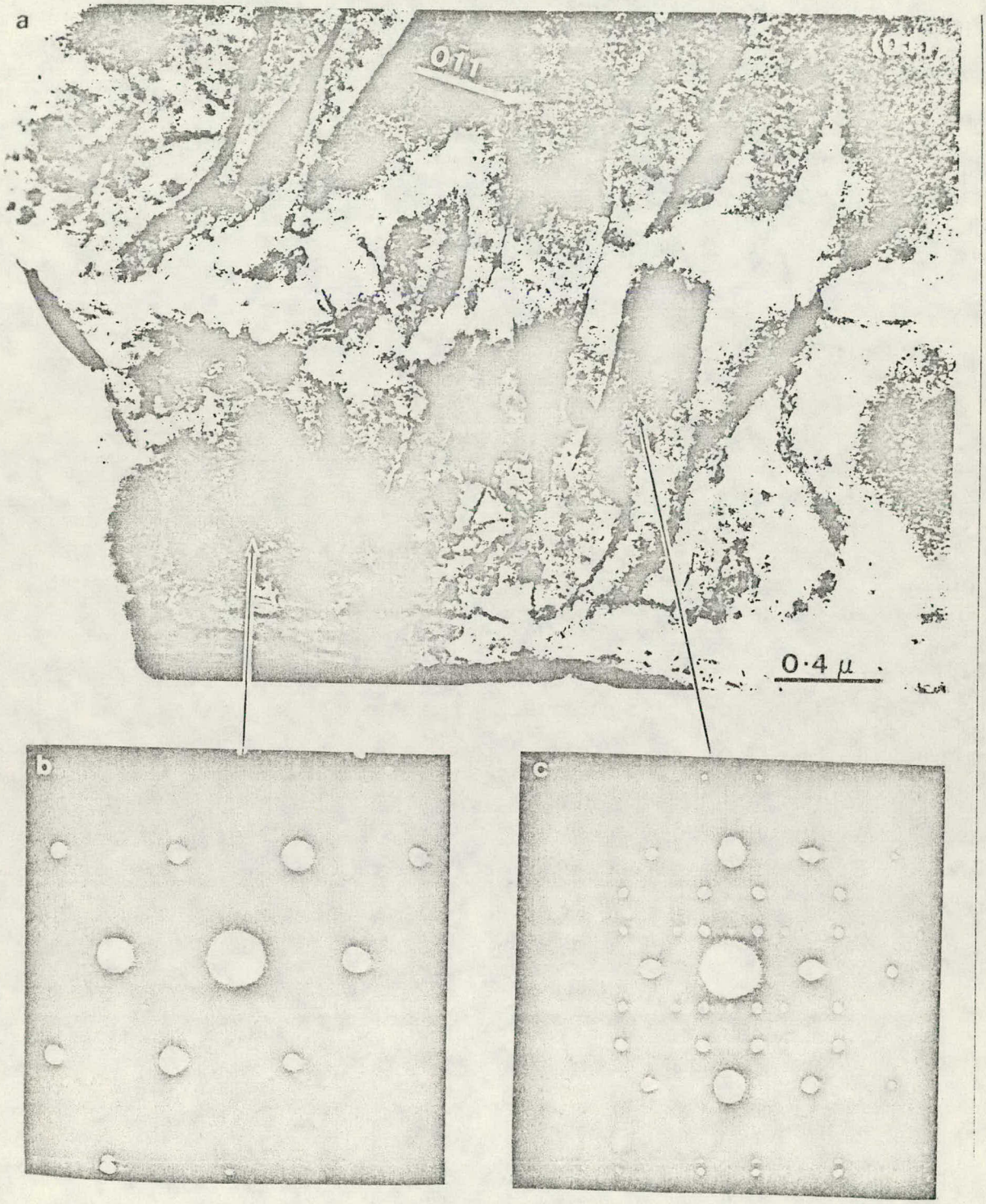

Fig. 78. Lath Structure and Diffraction Patterns Observed in Zr–15% Nb Alloy.

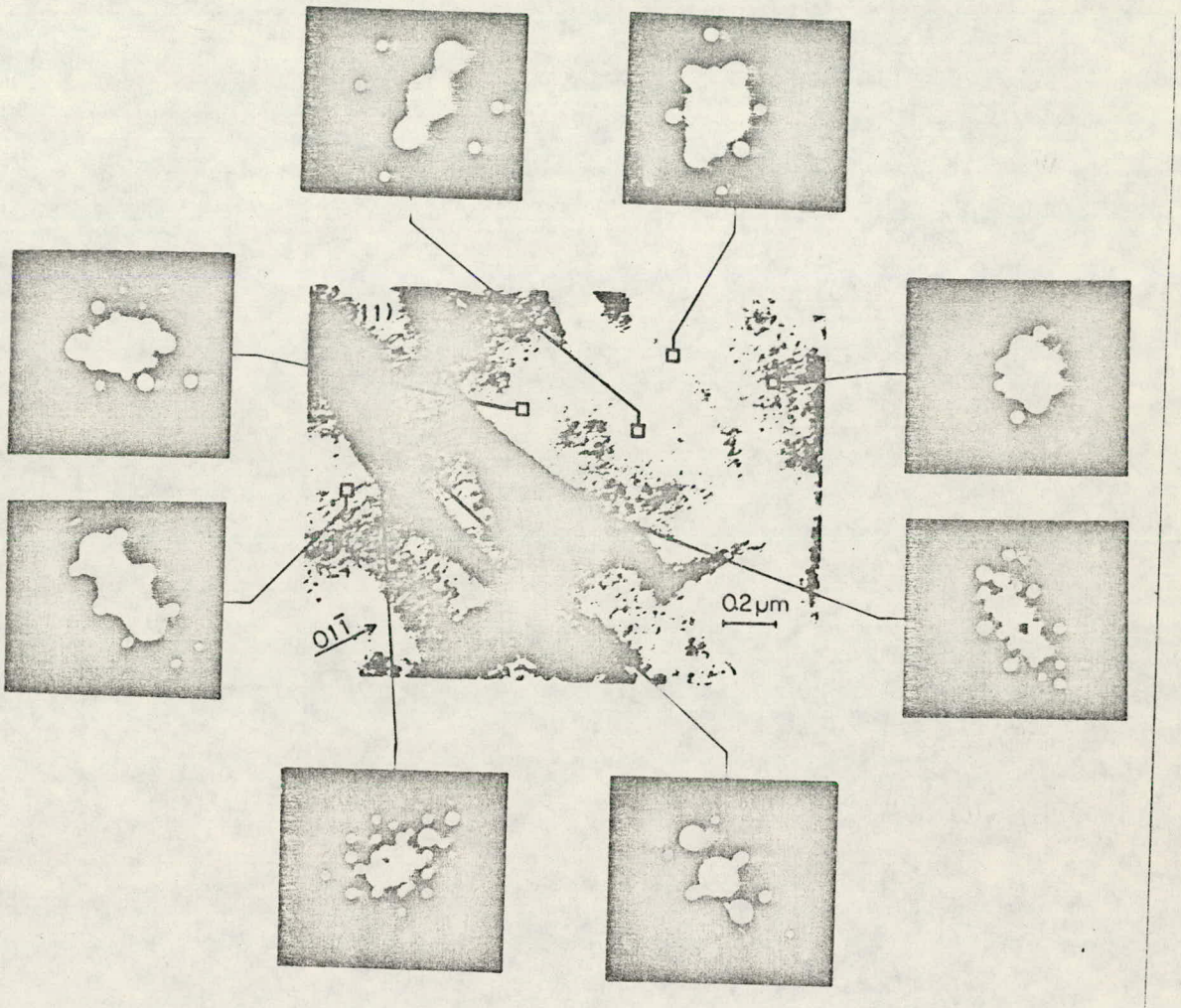

Fig. 79. Analysis of Lath Structure in Zr–15% Nb Using Stationary Diffraction Pattern Technique.

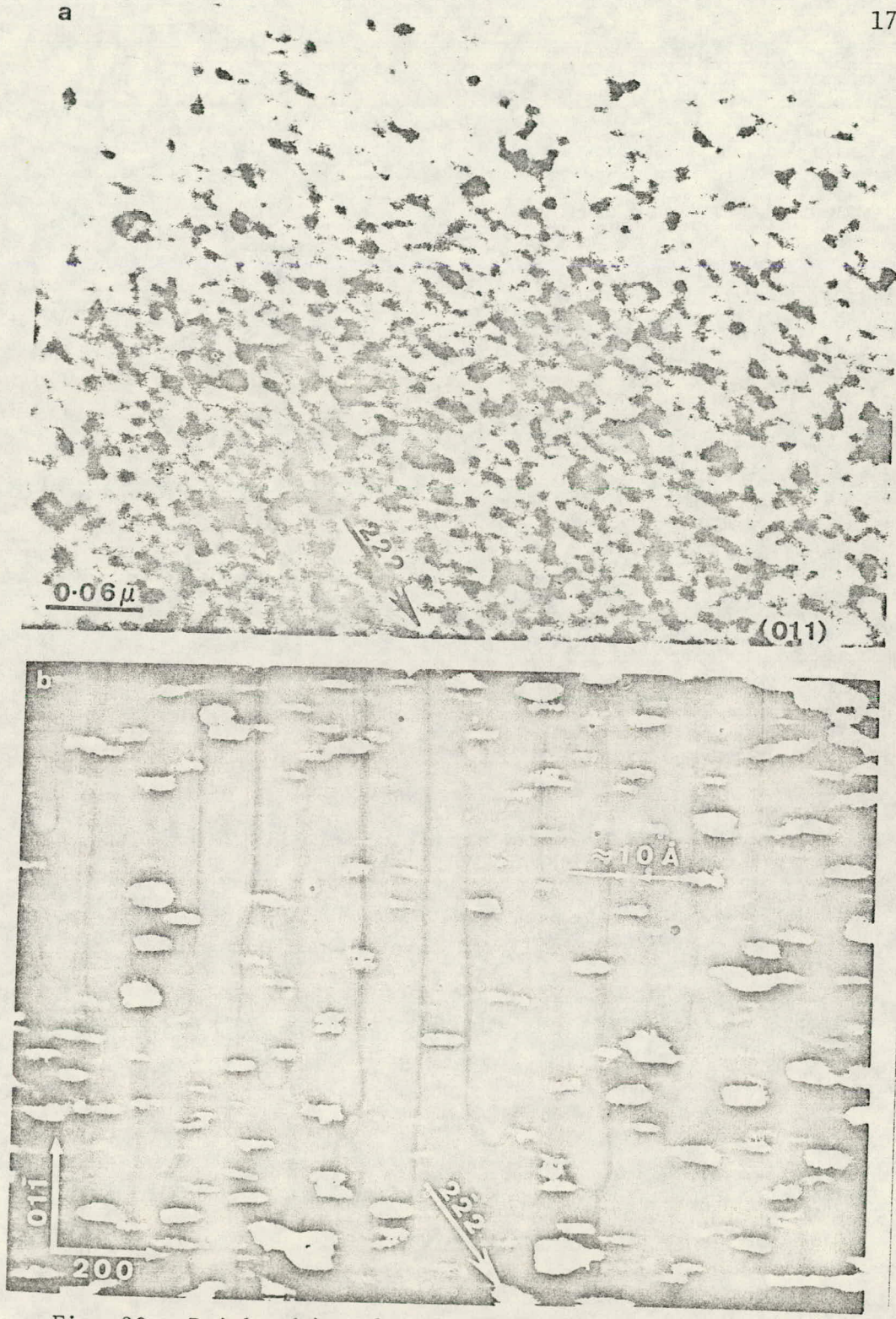

Fig. 80. Bright (a) and Dark-Field TEM Micrographs of Intermediate Structure in Zr–15% Nb.

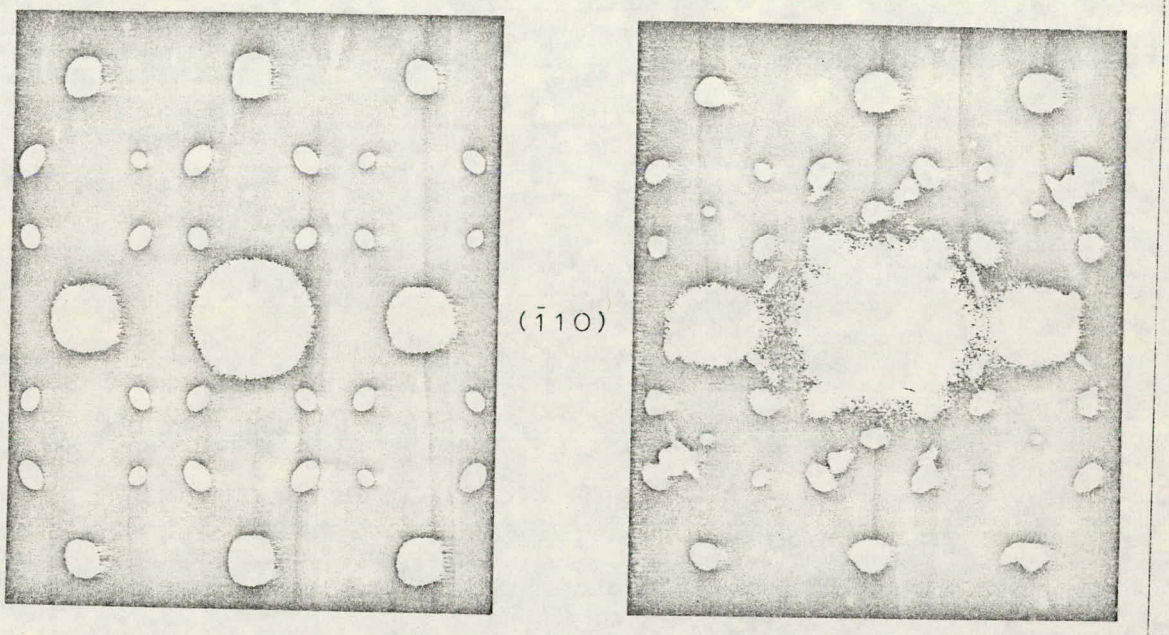

Fig. 81. Comparison of (1̄10) Electron Diffraction Patterns from As-Quenched ω (a) and Intermediate Phase (b) Morphology.

pattern perpendicular to the $[222]_\beta$ direction with a spacing of ∿25 Å as shown in Fig. 82. The observation of such a structure was initially interpreted as the formation of a long period ordered structure of alternating β and ω phase regions as predicted by Cook's[27–29] theory of the omega phase morphology in Zr-Nb. Thermal cycling experiments on prethinned specimens between –196 and +30°C failed to change the relative intensity of these ω satellite reflections. Furthermore it was not possible to consistently observe this morphology from one sample to another.

These inconsistencies were resolved when the existence of a thin hexagonal film was discovered on samples exhibiting identical ω satellite reflections. Figure 83 shows one of the few cases in which this film extended beyond the edge of the specimen. The diffraction pattern insert clearly indicates its hexagonal nature. STEM x-ray microchemical analysis of this region indicated a composition identical to the matrix (i.e., 15% Nb).

Electron energy loss measurements were then subsequently performed in order to check for the possible formation of an oxide layer. The energy loss spectrum labeled *a* in Fig. 84 was recorded from a contamination zone purposely formed on the film by allowing the STEM probe (in a VG HB5) to remain stationary on a region of the sample for ∿0.5 h. In this case a carbon κ loss edge is clearly observed. The second spectrum (*b*) was measured under identical operating conditions by simply translating the electron probe to a "clean" area of the specimen. The positions of the carbon and oxygen κ loss edges are indicated on both spectra and it seems that there is no significant oxygen concentration detectable in

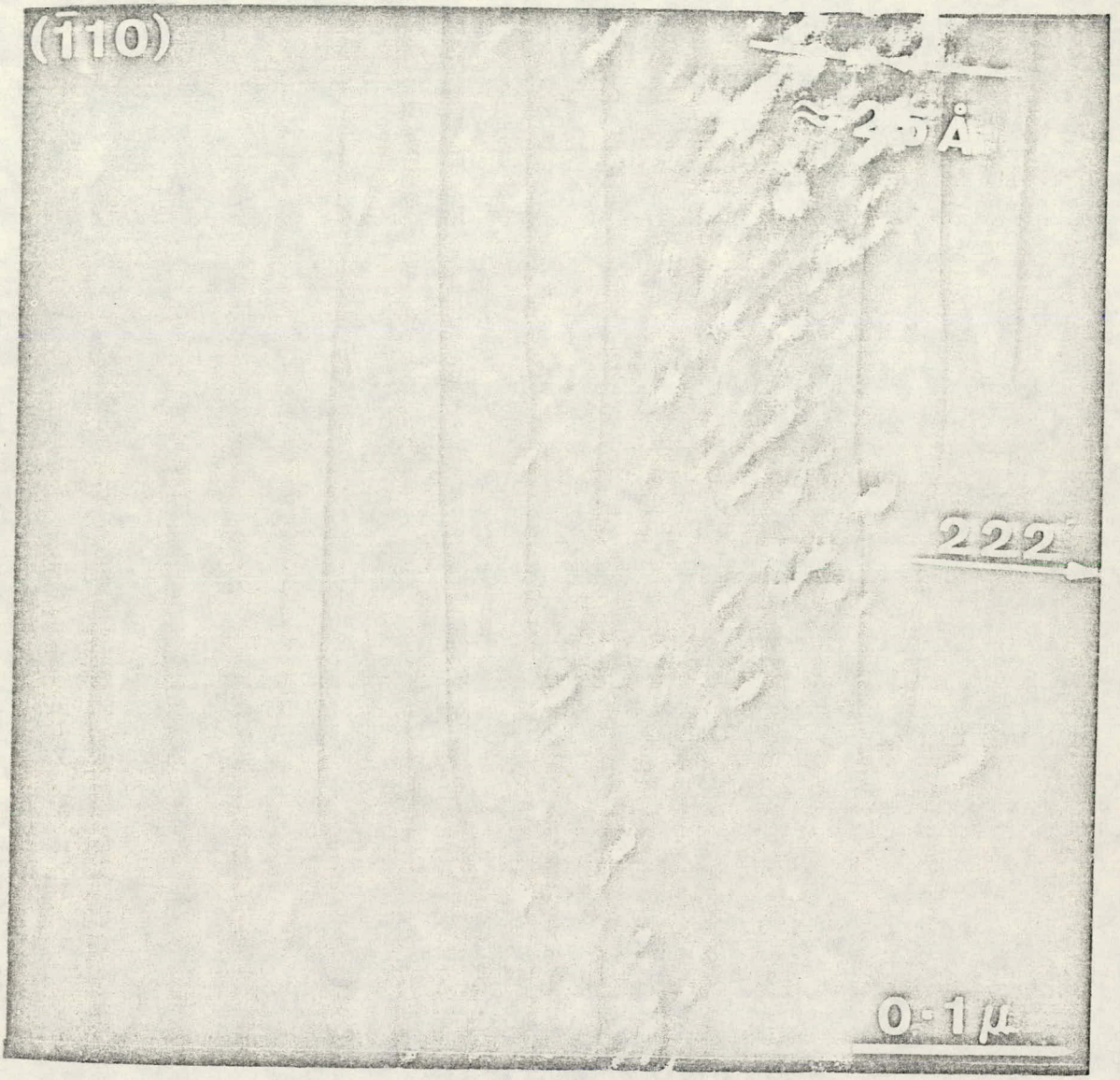

Fig. 82. 25 Å Spacing Fringes Obtained by Imaging Using ω_{0002} and the Corresponding Satellite Reflection from Fig. 83.

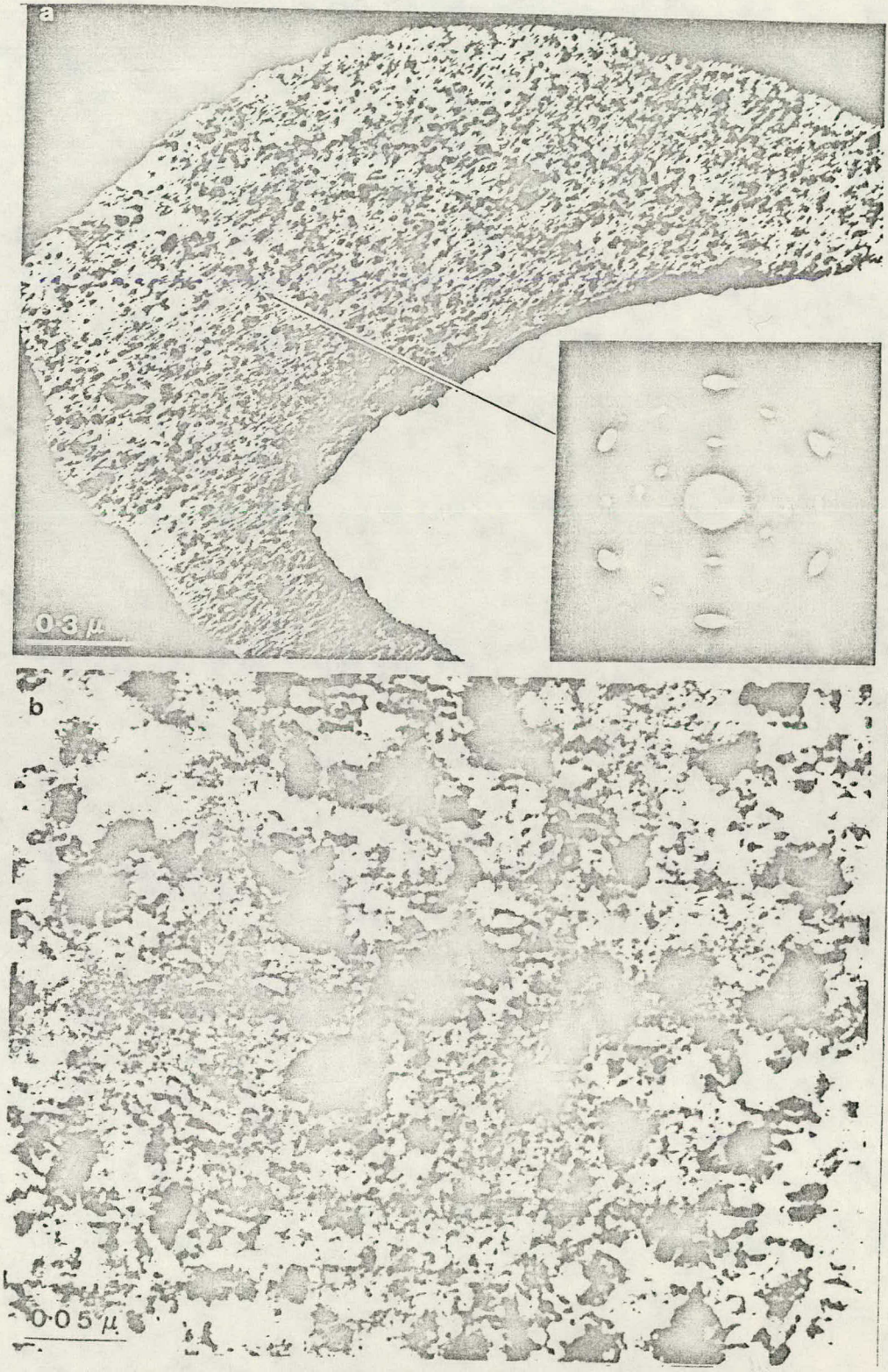

Fig. 83. Microstructure of Thin Crystalline Surface Film.

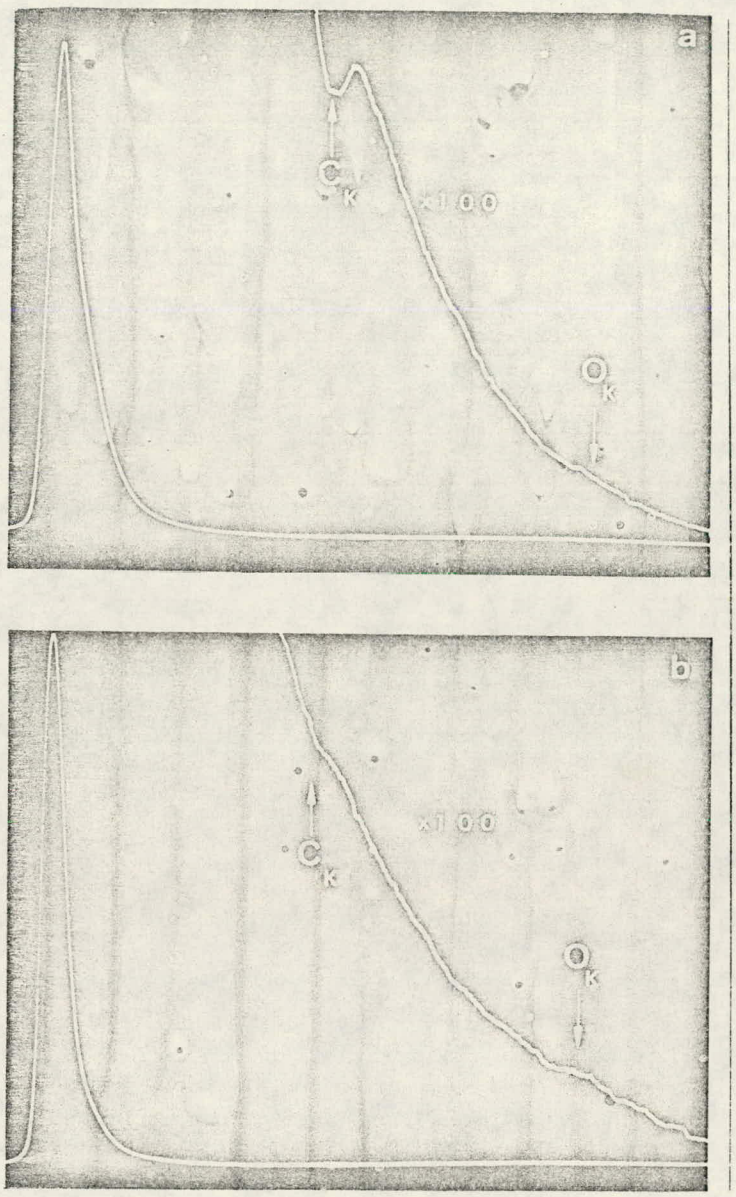

Fig. 84. Electron Energy Loss Measurements from Surface Film of Fig. 83. Spectrum (a) measured from contamination zone due to electron probe; spectrum (b) from "clean" area. Note absence of detectable oxygen K edge in both cases.

either case. The slight ripple near the position of the oxygen κ edge is due to electronic noise and was not reproducible on repeated scans.

The development of the ω satellites can now be interpreted by reference to Fig. 85. The diffraction pattern of Fig. 85(a) was recorded from the thick (dark) region of Fig. 83(a) and is a $(011)_{\beta+\omega}$ pattern. The hexagonal pattern (b) was recorded from the thin film shown on the same micrograph and is shown in the appropriate experimentally determined orientation with respect to the $\beta + \omega$ matrix. The diffraction pattern labeled (c) was produced by superimposing the negatives of Fig. 85(a) and (b) and the correspondence to the diffraction pattern of Fig. 81(b) is apparent. These results indicate that the ω satellite formation can be attributed to the existence of a thin crystalline surface film and not to the development of an ordered $\beta + \omega$ structure.

A second type of lath structure was also observed in some of the samples and is shown in Fig. 86. These laths have a width of approximately 500 Å and no compositional variation was noted between the features. A sequence of diffraction patterns over a standard stereographic triangle is reproduced in Fig. 87. These patterns can be indexed as the β and as-quenched ω structures together with an fcc phase having a lattice parameter of 5.01 Å. The orientation relationship between the fcc and bcc phases has been determined to be the following.

$$(011)_\beta \| (111)_{fcc} \qquad \text{and} \qquad [200]_\beta \| [\bar{1}01]_{fcc}$$

which differs only slightly from the Kurdjumov-Sacks relation

$$(011)_\beta \| (111)_{fcc} \qquad \text{and} \qquad [1\bar{1}1]_\beta \| [\bar{1}01]_{fcc}$$

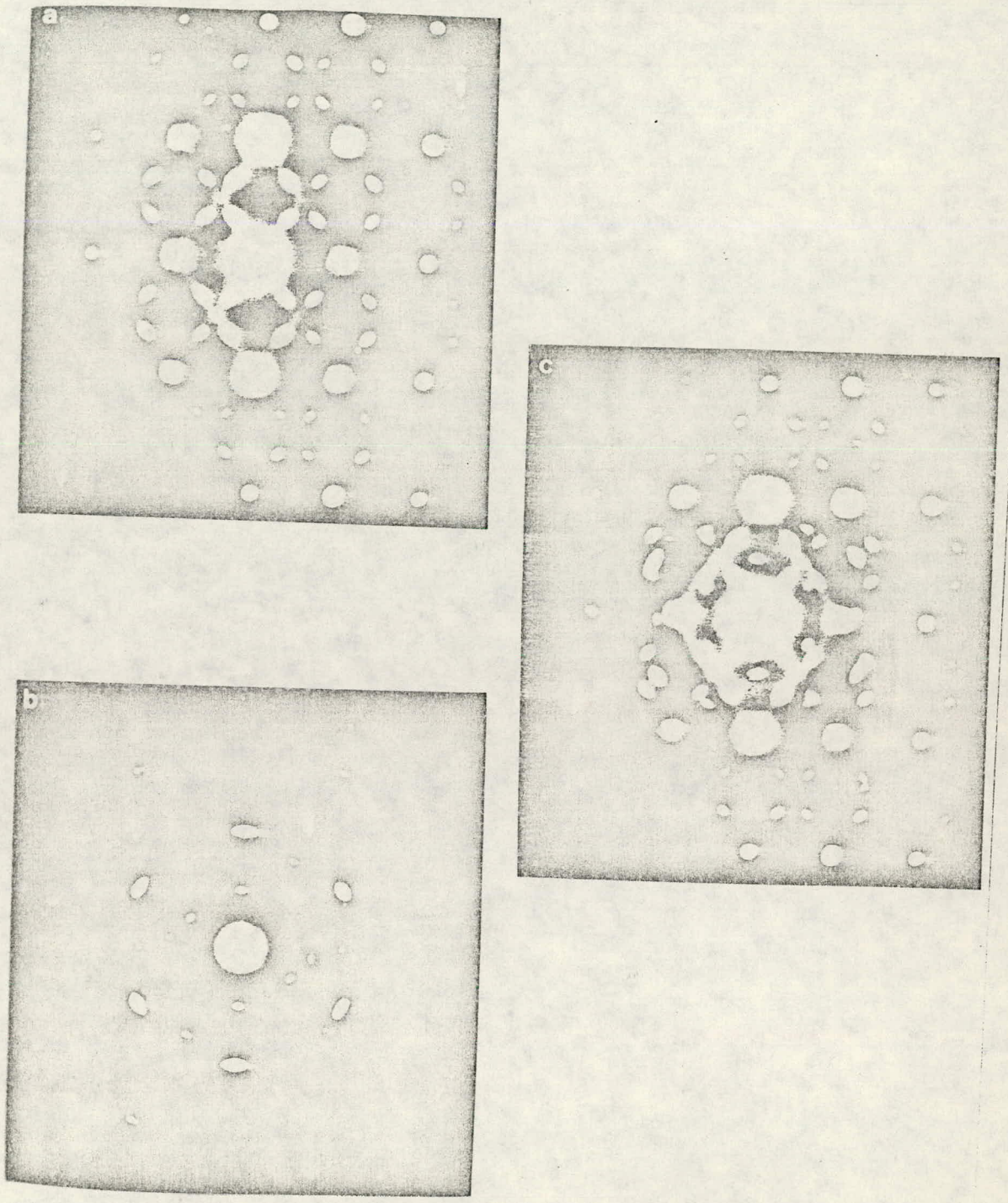

Fig. 85. Development of ω Satellite Reflections Due to Superposition of Hexagonal Pattern (b) on (011) β + ω Pattern (a) Resulting in Pattern (c).

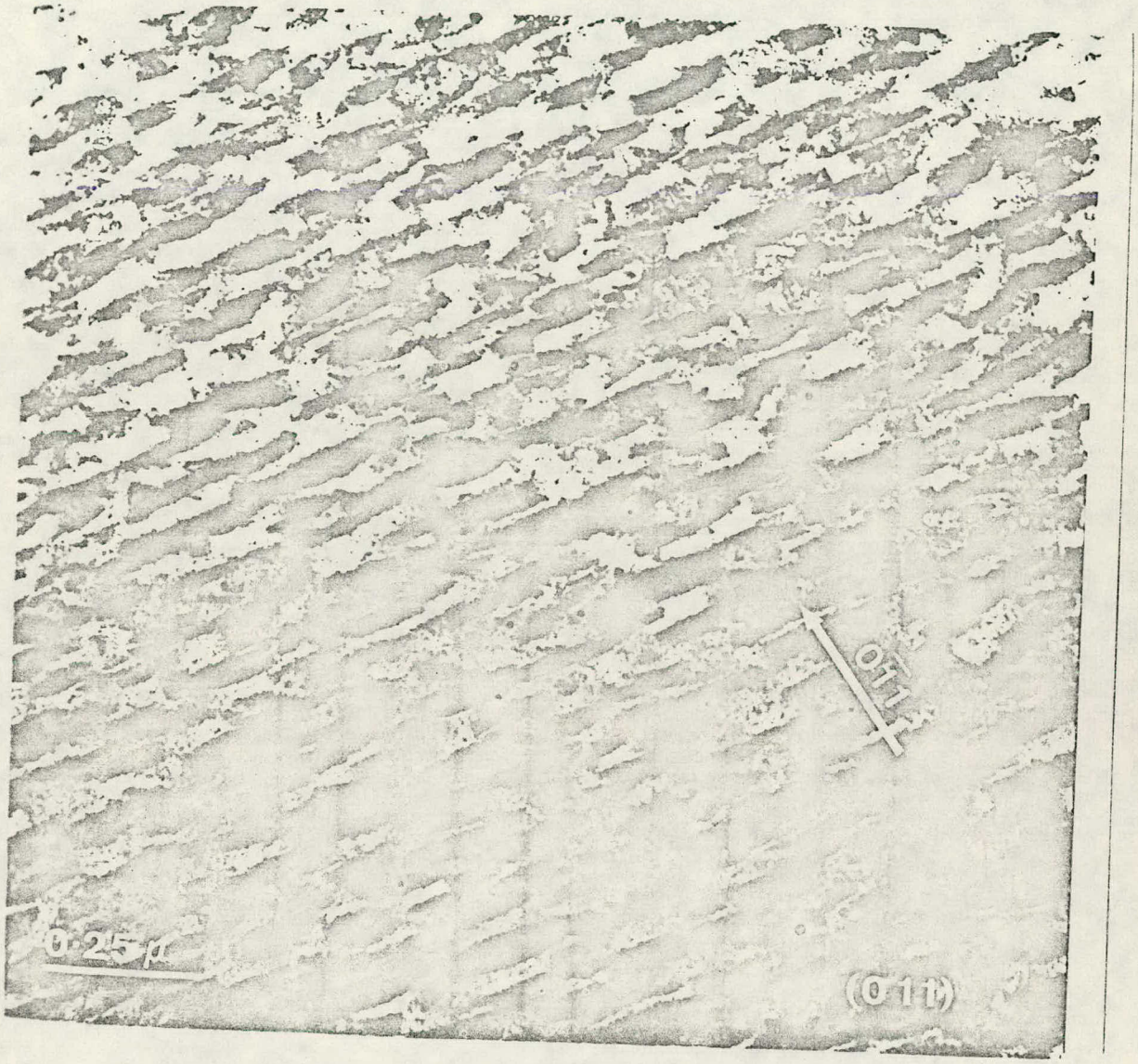

Fig. 86. Coherent Lath Structure Observed in Zr–15% Nb.

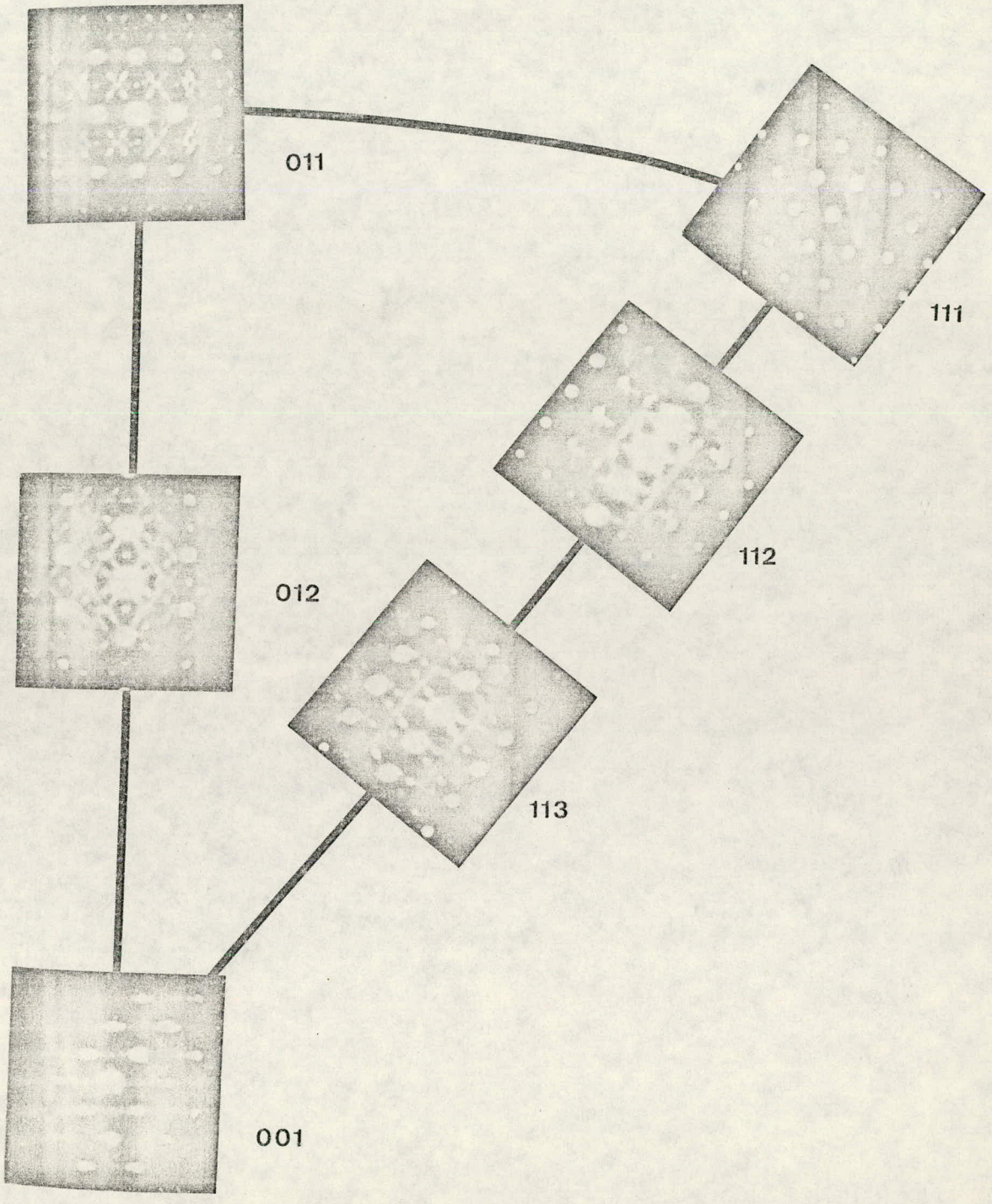
011
111
112
012
113
001

The periodic reflections along the [020] direction of the $(001)_\beta$ diffraction pattern are consistent with spiking effects from the $(011)_{fcc}$ reciprocal lattice plane only 10° off the $(001)_\beta$.

Argon ion-milling of the thinned disc for 1 h at 4 keV and 30 mA completely change the observed structure as shown in the TEM micrograph and corresponding diffraction patterns of Figs. 88 and 89. It was not possible to determine whether these changes were the result of the removal of a surface film or due to specimen heating effects. This structure can be a discontinuous form of the hexagonal film shown in Fig. 83 since the $(011)_\beta$ patterns of the two are extremely similar. It is possible that these structures are a form of the δ-hydride which in the zirconium-hydrogen system has an fcc crystal structure and a lattice parameter of 4.79 Å.

3.3.6 Precipitation of Coherent Isothermal Omega

Specimens aged for one year at room temperature developed a coherent precipitate consistent with the early stages of isothermal (aged) omega. These precipitates are shown in Fig. 90 and appear to be platelets approximately 200 Å in diameter and less than 100 Å thick. Their coherent nature can be identified by the absence of a sharp well-defined interface with the bcc matrix indicating the presence of a strain field at their perimeter. Interestingly, these platelets form a periodic structure along one of the {111} planes in the bcc lattice with an average spacing of 400 Å as shown in Fig. 91. Higher magnification images also indicate the presence of a thin crystalline surface film. This can be

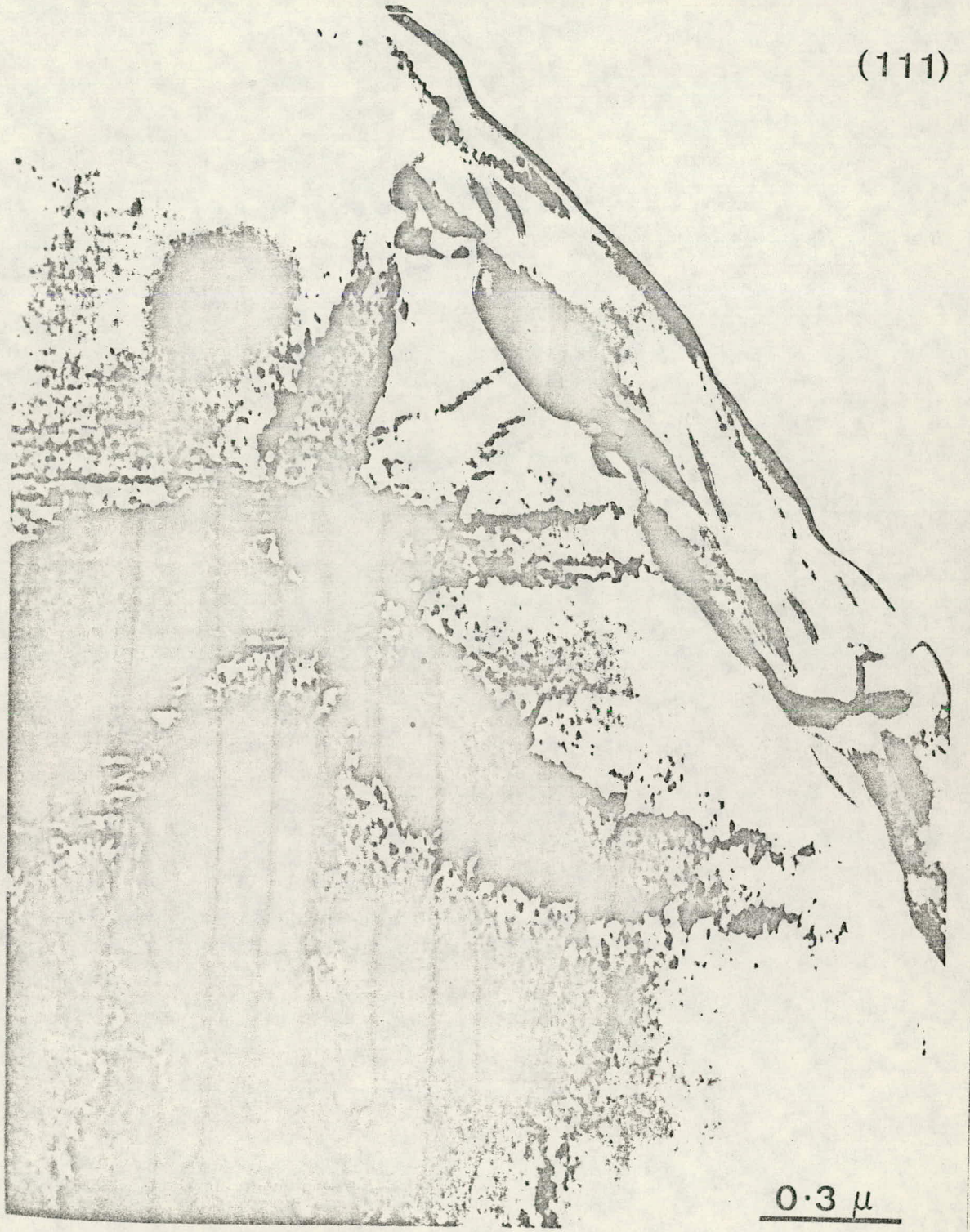

Fig. 88. Microstructural Changes Resulting from Argon Ion-Milling of Sample Shown in Fig. 86.

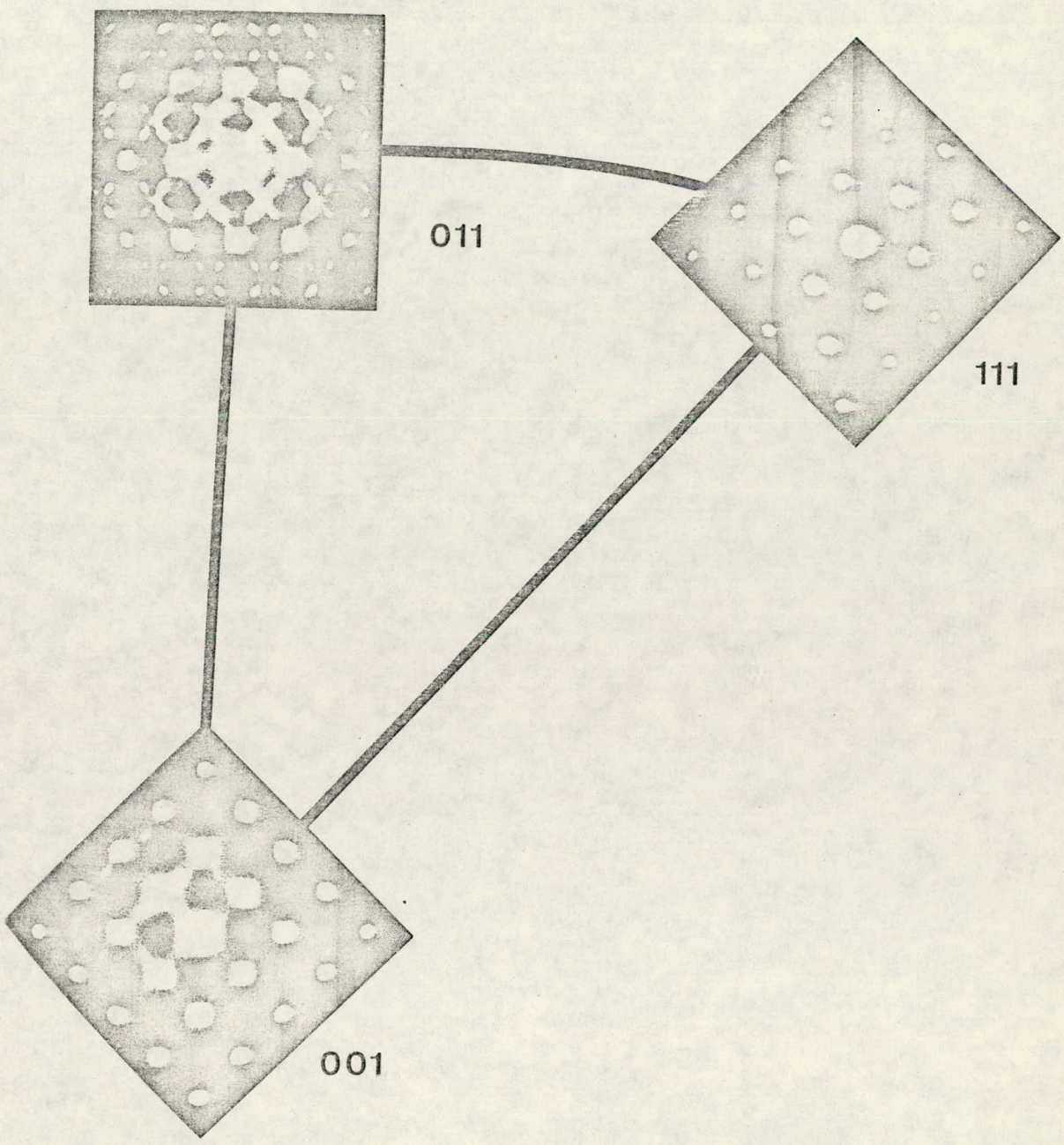

Fig. 89. Corresponding Electron Diffraction Patterns for the Microstructure of Fig. 88.

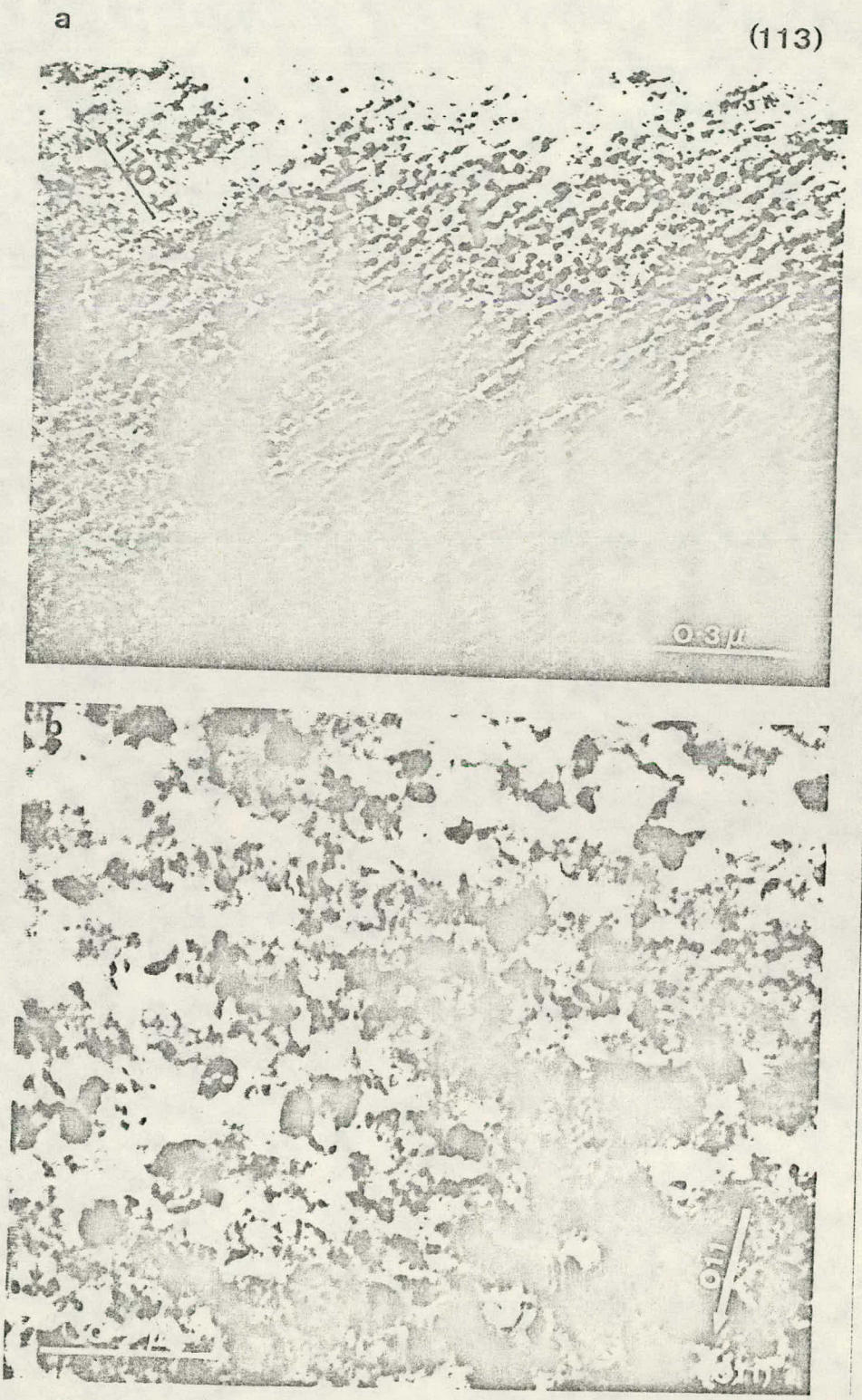

Fig. 90. Precipitation of Coherent Isothermal Omega in Zr–15% Nb.

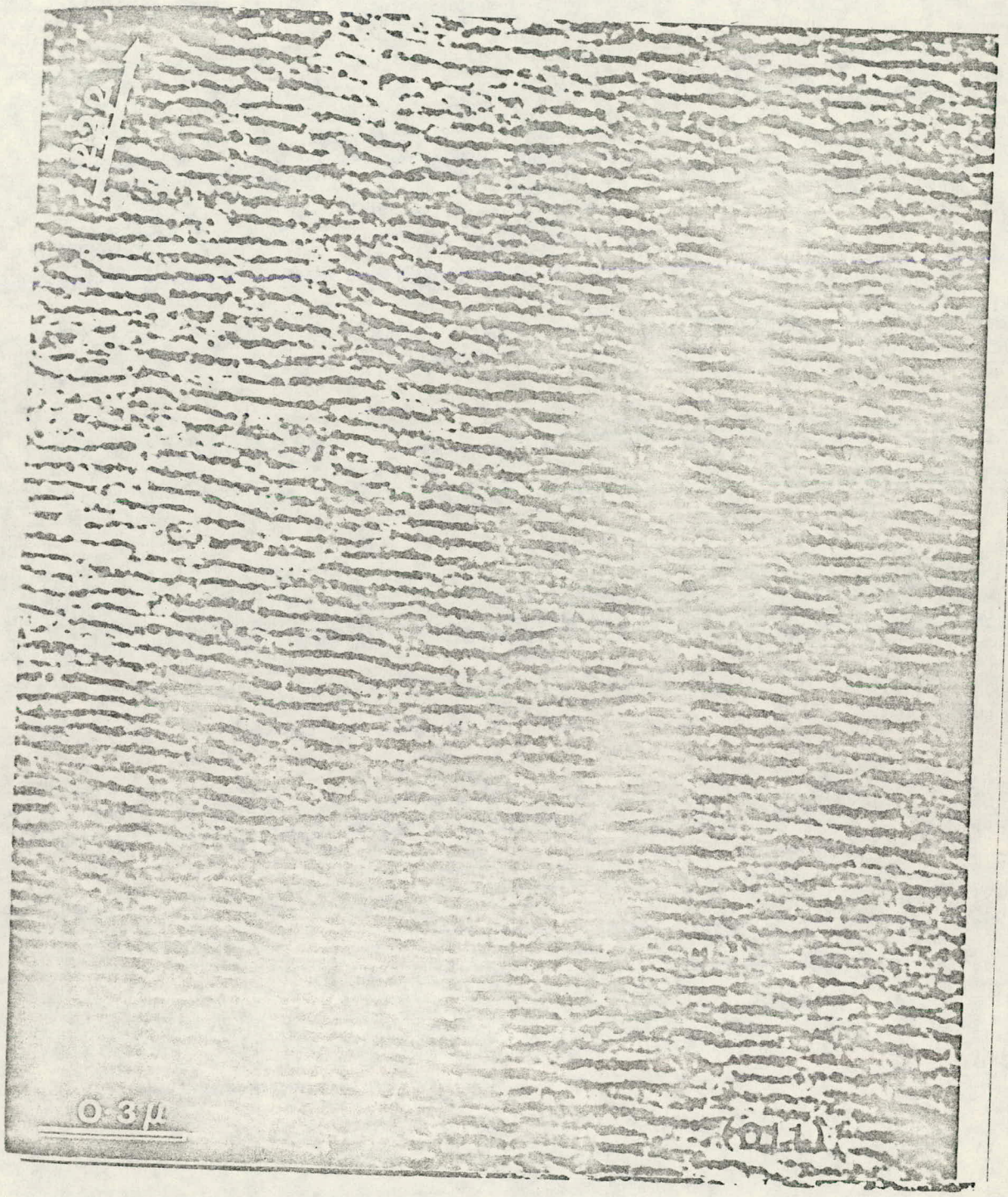

Fig. 91. Periodic Structure Formed in Samples Containing Coherent Isothermal Omega.

inferred from the discontinuous Moiré fringe pattern shown in the TEM bright field image of Fig. 92. Selected area diffraction measurements made as a function of sample thickness (Fig. 93) also indicate the presence of a thin surface film.

The electron diffraction patterns observed over a standard stereographic triangle for this sample are summarized in Fig. 94. The formation of <100> superlattice reflections as well as changes in the bcc lattice parameter ($a_0 \cong 3.41$ Å) are consistent with the occurrence of solute segregation followed by the formation of the coherent isothermal (aged) omega phase with a c/a ratio of ~ 0.615 and having the orientation relationship

$$(111)_\beta \| (0001)_\omega \qquad \text{and} \qquad [01\bar{1}]_\beta \| [11\bar{2}0]_\omega$$

It was not possible to confirm experimentally changes in composition of the matrix using x-ray microanalysis due to the high contamination rate in the JSEM 200. Electron energy loss measurements did not indicate the presence of oxygen in the sample. The $\frac{1}{6}$ <112> and $\frac{1}{2}$ <110> reflections in these patterns are due to the thin surface film and can be indexed as an ordered face-centered cubic structure having the following orientation relationship with the bcc lattice

$$(111)_\beta \| (011)_{fcc} \qquad \text{and} \qquad [1\bar{1}0]_\beta \| [200]_{fcc}$$

The corresponding lattice constant of this fcc structure is $a_0 = 4.82$ Å.

3.4 In-Situ Thermal Cycling Experiments

Samples characterized as containing only the as-quenched ω and β phases were used in the thermal cycling experiments described in this

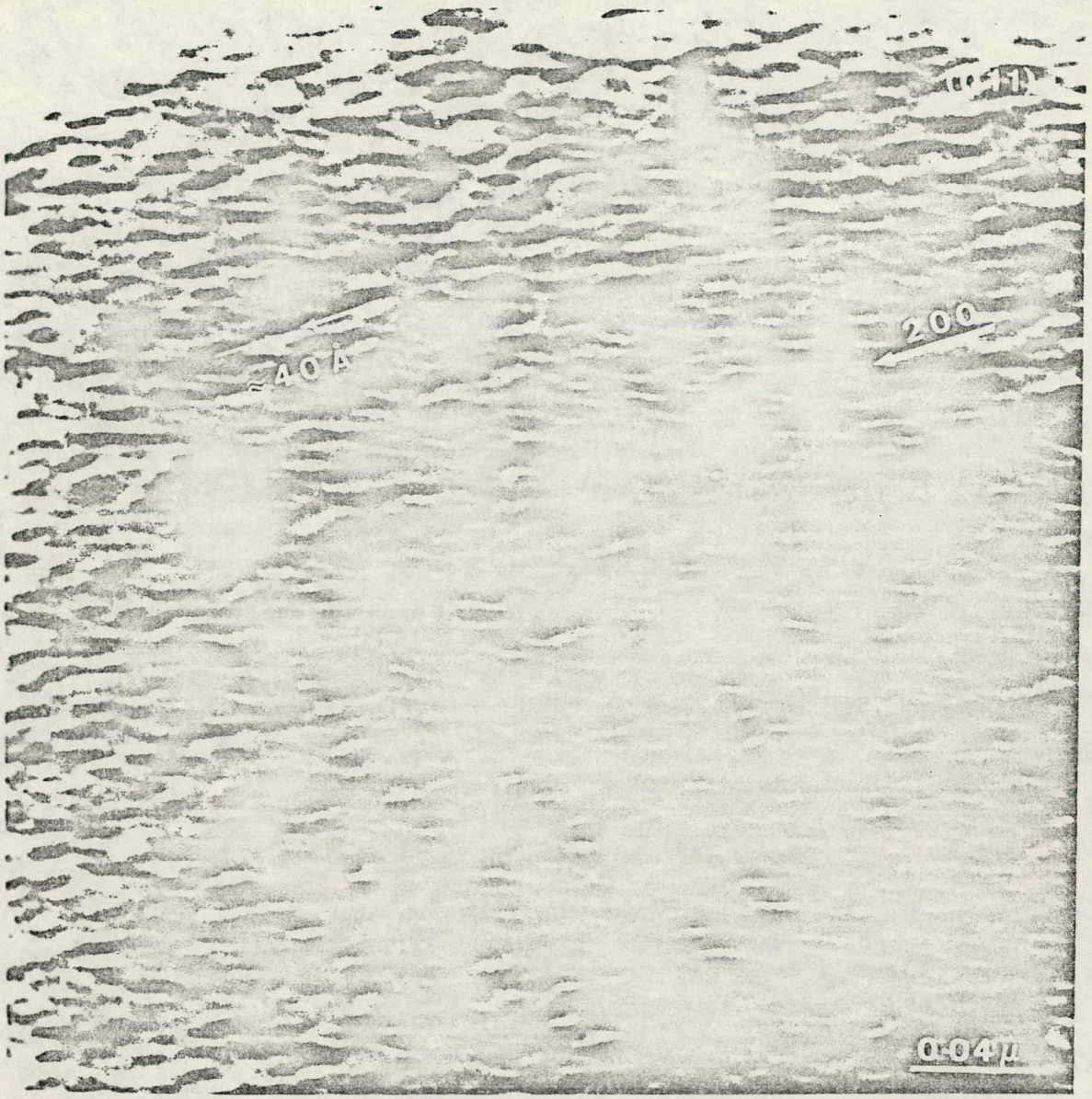

Fig. 92. 40 Å Moiré Fringe Pattern Possibly Due to the Formation of a Thin Surface Film.

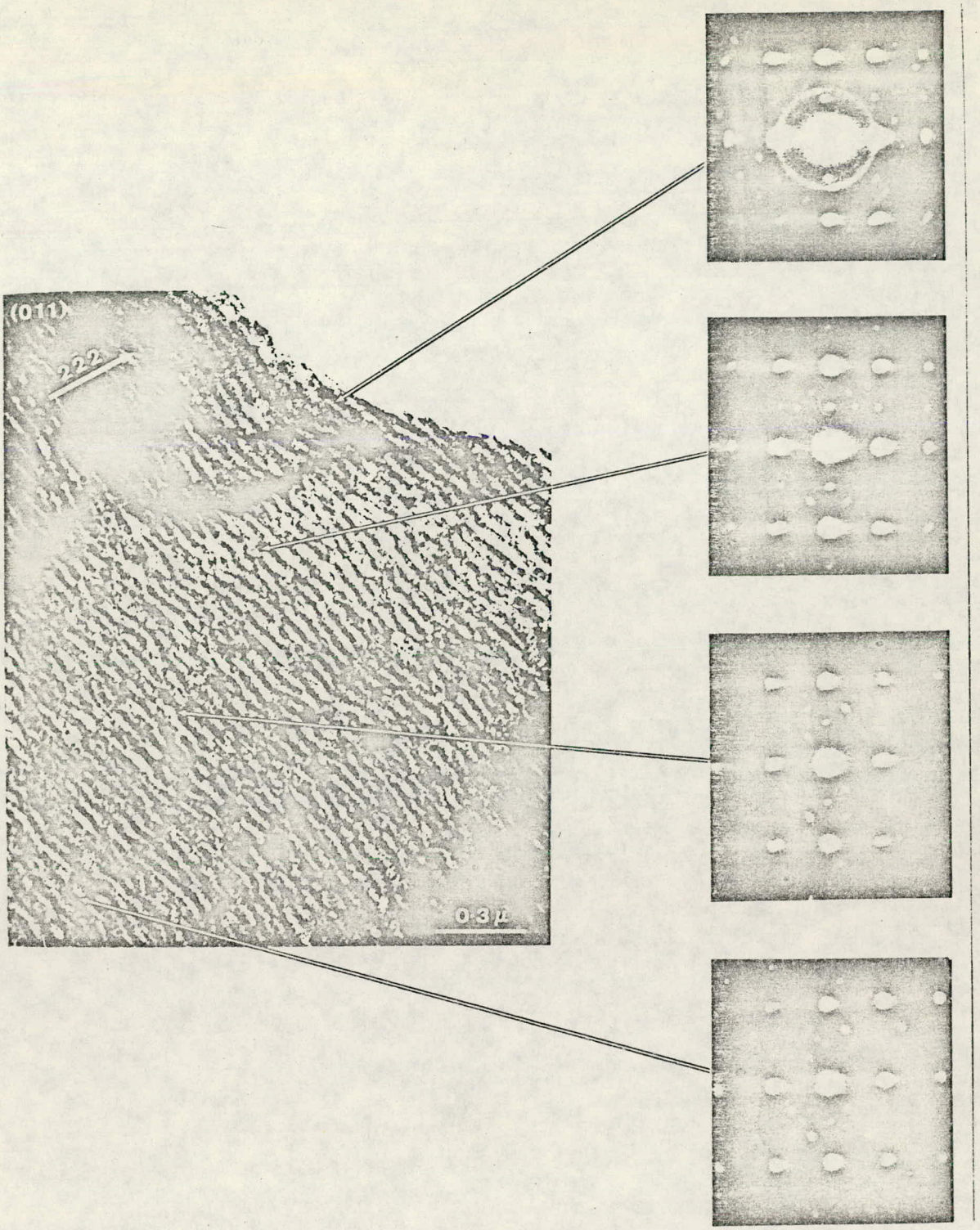

Fig. 93. Variation in Diffraction Patterns as a Function of Sample Thickness Indicating the Possibility of a Surface Film.

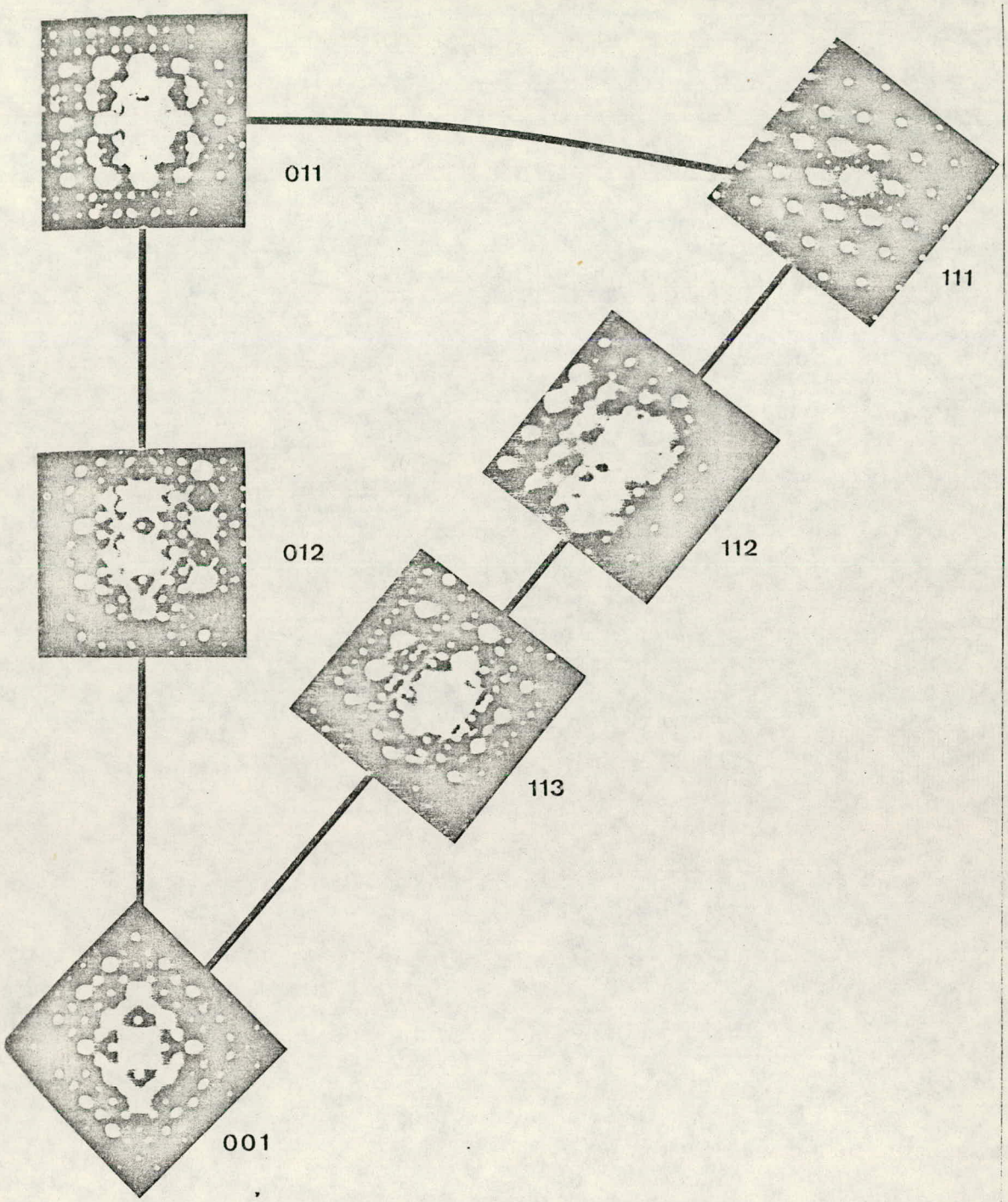

Fig. 94. Summary of Electron Diffraction Patterns from the Microstructure of Fig. 90.

section. Specimens were mounted in a single-tilt cooling state and measurements of the relative intensities of the ω and β reflections were made as a function of temperature using transmission scanning electron diffraction (TSED). All measurements were made along a <2$\bar{2}\bar{2}$> systematic row in an {011} reciprocal lattice plane, with the sample oriented for exact <2$\bar{2}\bar{2}$> Bragg scattering. The data were recorded on an ORTEC 6200 MCS and transferred for analysis on an LSI-11 microcomputer system using software listed in Appendix E.

In order to perform these TSED temperature measurements using the existing cooling stage it was necessary to orient the specimen so that an {011} pole could be reached using only the single-tilt axis available. This was accomplished by inserting the sample into the microscope and noting its crystallographic orientation relative to the tilt axis. The stage was then removed from the column and the specimen appropriately rotated (relative to the tilt axis). The sample was then reinserted into the TEM and the process repeated until a {011} pole could be successfully reached.

The temperature of the stage was monitored using a Copper-Constantan thermocouple attached to the cooling block in which the sample was mounted. The voltage drop across the thermocouple junction was measured using a LEED and NORTHRUP millivolt potentiometer. Temperature dependence studies were made unidirectionally from −196°C to room temperature by allowing the liquid nitrogen cooled stage to equilibrate to ambient temperatures via thermal conduction through the stage block. This was necessary because no temperature controlling facilities were

available for this stage. As a consequence of this, each temperature scan required approximately 12 h of continuous microscope operation. During this time the specimen position was periodically checked to ensure that all measurements were made at constant thickness and orientation. Due to the extremely long duration of each set of measurements, all intensities were normalized to that of the <222> Bragg reflection to compensate for changes in incident beam current. In this experiment, the intensity of the $<222>_{\beta}$ Bragg peak was monitored rather than the <000> transmitted beam intensity so that the system could operate at the maximum possible sensitivity. Thus the gain of the photomultiplier tube (PMT) was adjusted so that the <000> transmitted beam intensity was just short of saturating the detector. The remaining linear amplifiers were then used to amplify the $<222>_{\beta}$ intensity to the maximum level which can be processed by the voltage-to-frequency converter used to digitize the intensity measurements.

Figure 95 shows typical selected area diffraction patterns recorded at a (stage) temperature of −196 and +22°C from approximately an 1000-Å-thick region of the Zr−15% Nb alloy. No substantial differences between these two patterns can be visually detected. TSED measurements of the relative intensity ratio of the ω_{0002} and β_{222} reflections as a function of temperature are given in Fig. 96. A monotonic increase of the ω_{0002} peak relative to the β_{222} intensity with decreasing temperature is apparent. The variation of the intensity ratio of the ω_{0002} to the ω_{0001} reflection is essentially constant as indicated in Fig. 97. In-situ thermal cycling experiments were repeated on this sample four times with identical trends

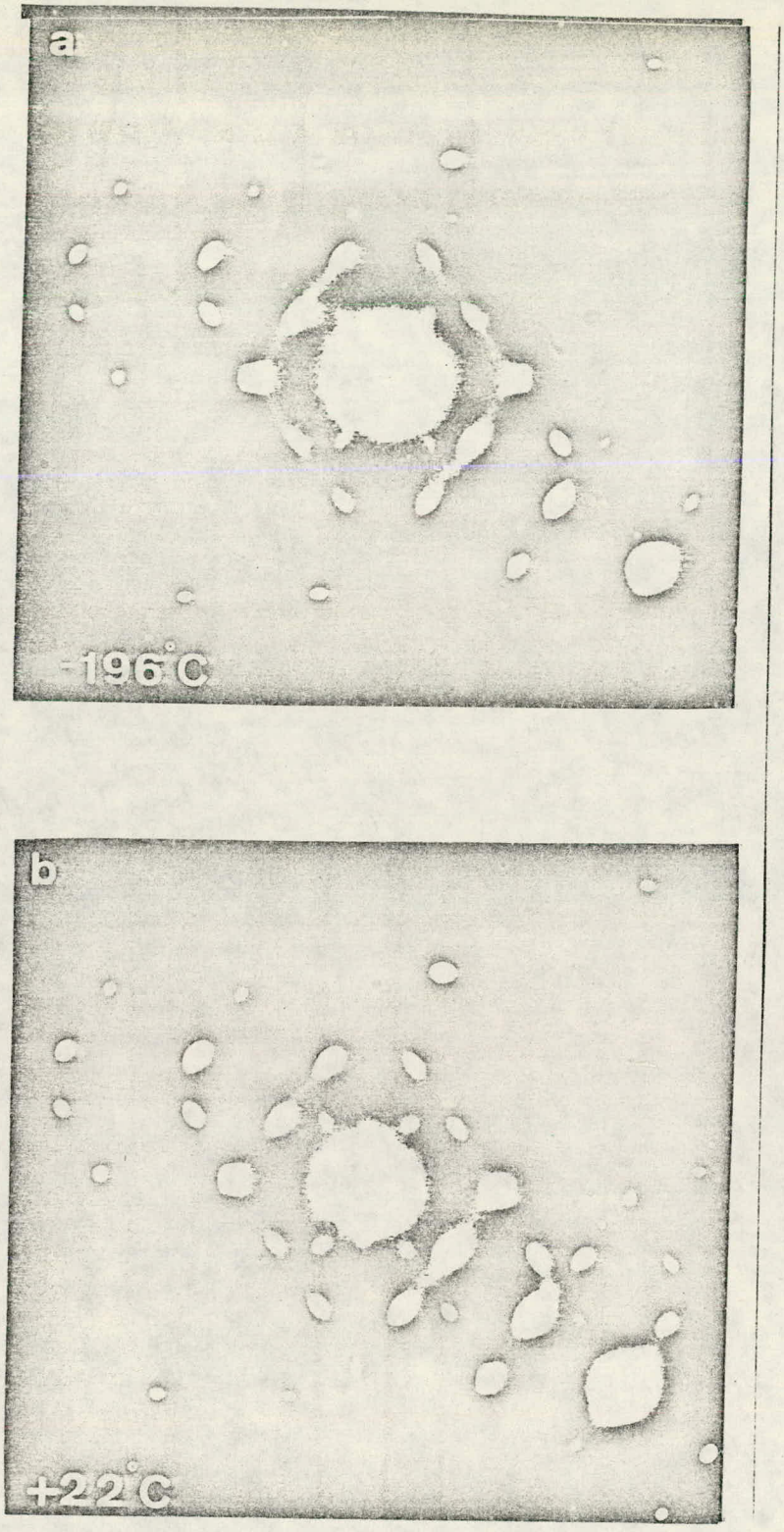

Fig. 95. Diffraction Patterns from the As-Quenched ω + β Morphology at −196 and +22°C.

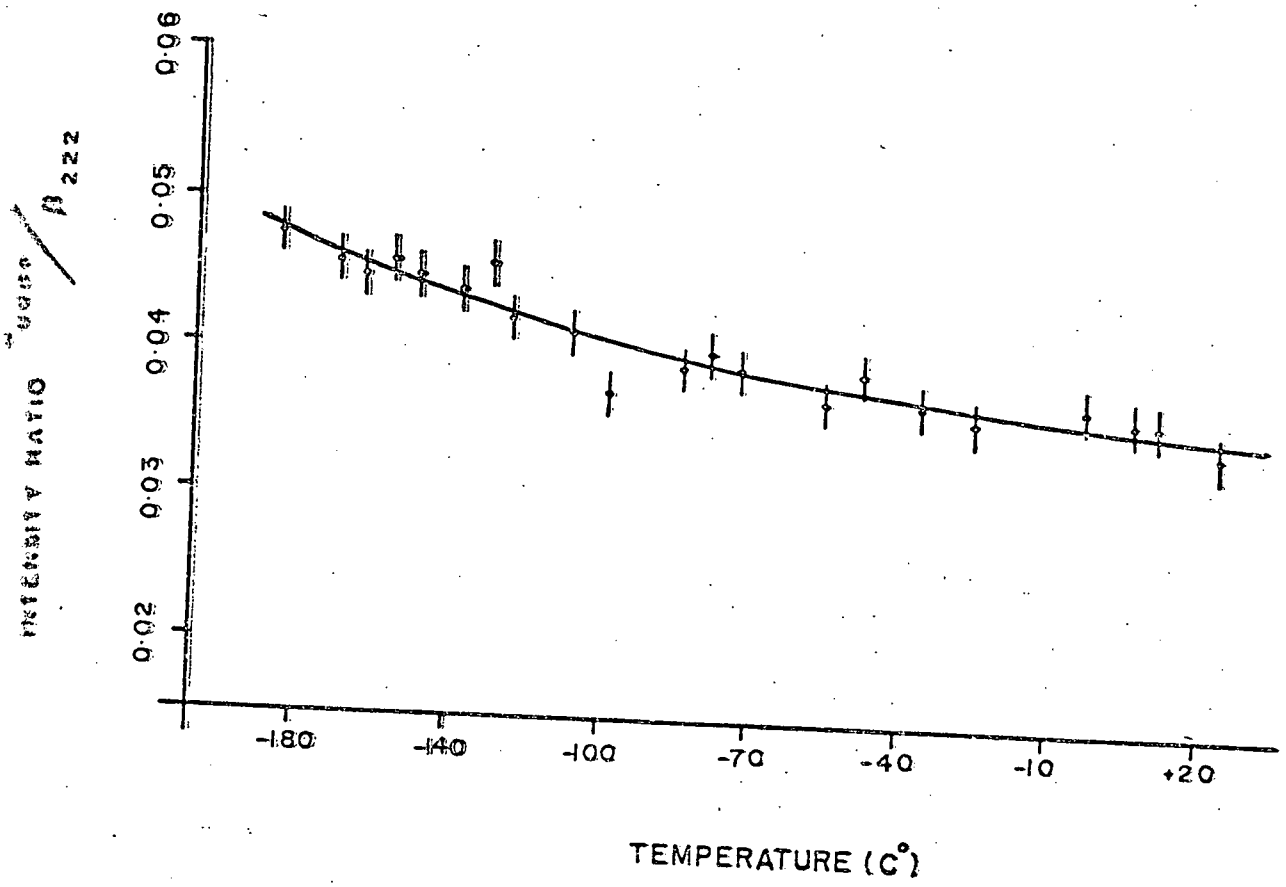

Fig. 96. Experimental Measurements of the Variation of $\omega_{0002}/\beta_{222}$ Intensity Ratio as a Function of Temperature.

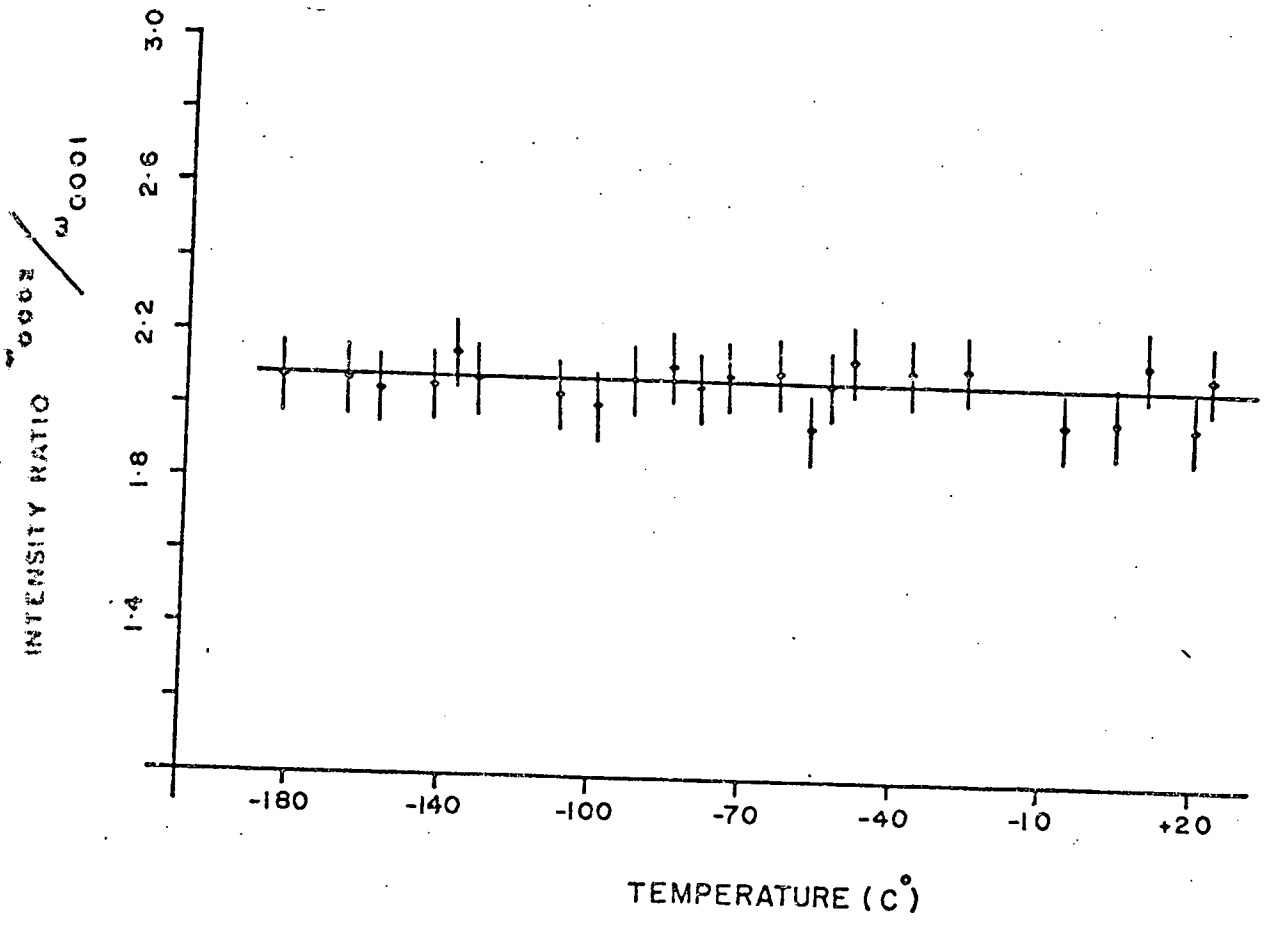

Fig. 97. Experimental Measurements of the $\omega_{0002}/\omega_{0001}$ Intensity Ratio as a Function of Temperature.

being observed. The accumulation of contamination on the sample, however, prohibited direct comparisons of these data from one measurement to another. In addition, prethinned samples thermally cycled at 12-h intervals between −196 and 30°C over a period of eight weeks exhibited identical trends when subsequently measured on the JSEM 200.

Structure factor calculations of the intensity distribution along a $\langle 222 \rangle_\beta$ direction for two different β + ω structures are schematically shown in Fig. 98. In this figure the relative intensity of a diffraction maxima (i.e., the square of the calculated structure factor) is linearly proportional to the radius of the circle used to represent a given reflection. The first set of calculations [Fig. 98(a)] illustrate the changes in diffracted intensity as a pure bcc structure ($\eta \equiv 0$) is subjected to a sinusoidal ω-forming displacement wave [Eq. (1.1)] as a function of order parameter (η). Thus if the bcc structure was completely transformed into the ω phase structure factor considerations predict the ratio of $\omega_{0002}/\omega_{0001}$ to be 9 to 1. Table 3 lists the ω_{0002} to ω_{0001} ratio for specific values of η. Figure 98(b) represents structure factor calculations along a $\langle 222 \rangle_\beta$ direction for an ordered phase of alternating β and ω regions. In this case it was assumed that these regions had a spatial extent of 24 Å (i.e., approximately four β cells = eight ω cells) along the <222> direction. This spatial extent is consistent with the experimental observations of omega domain size observed in this work as well as in the literature. Table 4 lists the calculated structure factor ratios for this periodic arrangement.

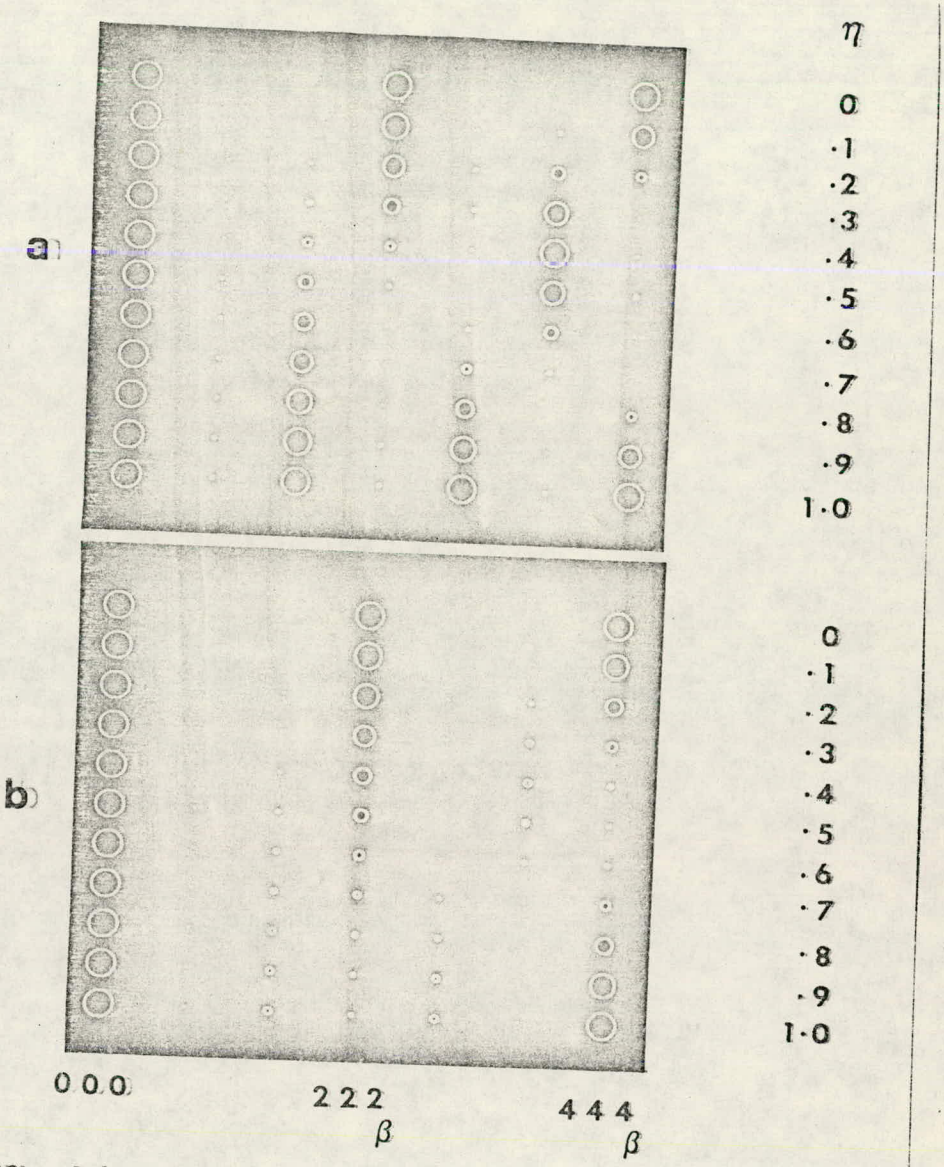

Fig. 98. Schematic Illustration of the Changes Along a <222> Direction in an Electron Diffraction Pattern for: (a) a Homogeneous Sample Changing from the Pure β Phase ($\eta = 0$) to the Ideal ω Phase ($\eta = 1$) and (b) to a Completely Ordered Structure of the β Plus ω Phase.

Table 3. Calculated Structure Factor Ratio for Ideal Omega Phase as a Function of Order Parameter (η)

Order Parameter (η)	Structure Factor Ratio $(\omega_{0002}/\omega_{0001})^2$
0	--
0.1	4.73
0.2	5.46
0.3	6.18
0.4	6.85
0.5	7.47
0.6	8.00
0.7	8.42
0.8	8.74
0.9	8.93
1.0	9.00

Table 4. Calculated Structure Factor Ratio for Long Period Ordered Structure of β + ω Phase as a Function of Order Parameter (η)

Order Parameter (η)	Structure Factor Ratio	
	$(\omega_{0002}/\omega_{0001})^2$	$(\omega_{0002}/\beta_{222})^2$
0	--	--
0.1	4.73	0.0041
0.2	5.47	0.0197
0.3	6.18	0.0544
0.4	6.86	0.123
0.5	7.47	0.250
0.6	8.00	0.476
0.7	8.42	0.943
0.8	8.74	1.41
0.9	8.94	1.98
1.0	9.00	2.25

Unfortunately the effects of double diffraction as well as inelastic scattering preclude a direct comparison of these calculations with experimental measurements; however, the following qualitative interpretation of the experimental data can be set forth. Since the ratio of the $\omega_{0002}/\omega_{0001}$ intensity remains essentially constant as a function of temperature, it can be concluded that no change in the degree of completion of the ω to β transformation has occurred due to changes in sample temperature. The monotonic increase in the ω_{0002} intensity relative to the β_{222} reflection can thus be interpreted as an increase of the total volume fraction of the ω phase in the sample with respect to the β phase. At no time during these measurements was it possible to detect an ordering of the ω phase relative to the β phase either through changes in relative intensities of diffraction peaks or by the development of ordering reflections corresponding to a long period structure.

CHAPTER 4

4. CONCLUSIONS

The results of this research can be divided into two parts – namely the study of the as-quenched omega phase morphology, and the work involved with the application of analytical electron microscopy to materials characterization. With regard to the omega phase, this research has shown that (1) the domain size of the as-quenched omega structure in Zr–15% Nb is on the order of 30 Å, (2) no alignment of omega domains along $\langle 222 \rangle_\beta$ directions is observed, and (3) samples having undergone thermal cycling experiments in thin foil form did not develop a long-period structure of alternating β and ω phases below the omega transformation temperature. The size of the omega domains noted in this work is consistent with that previously quoted in the literature, yet for a number of years it has been reported that these domains arrange themselves periodically along specific directions of the bcc lattice. It is difficult to simply resolve this discrepancy, but it was noted during this study that a wide variety of microstructural features can develop as a result of sample preparation and hence it is feasible to postulate that such effects could be responsible for the conflicting results. No coherent long-period β and ω structure immediately below the omega transformation temperature was detected; however, it is possible that thin film constraints may have inhibited the formation of such a metastable structure by shifting stability away from the ordered phase. The CTEM images and diffraction patterns

observed during this research included moderate inelastic scattering effects and thus it would be interesting to continue studies of this transformation using high resolution imaging combined with energy filtering. At present the only instruments capable of such experiments are the high resolution dedicated scanning transmission electron microscopes (DSTEM) equipped with electron energy loss spectrometers and the possibility of such work is being investigated.

Analytical electron microscopy has been shown to be an extremely powerful tool for the microcharacterization of materials. However, these techniques are not by any means without complications, and it was necessary to investigate the AEM system used in this work so that instrumental artifacts which invalidate the information produced in the microscope environment might be eliminated. Once these factors had been corrected, it was possible to obtain a wealth of information about the microvolume of material under investigation.

The instrumental problems, which were associated with x-ray analysis, in the AEM system used during this research included: fluorescence by uncollimated radiation, contamination formed under the influence of the electron probe, and the generation of system peaks in the immediate vicinity of the specimen. Of these factors, the single most important correction necessary to perform quantitative x-ray microanalysis is the reduction of uncollimated radiation. Without such a correction, true quantitative microanalysis is virtually impossible. The effects of contamination have been shown to be detrimental in all aspects of TEM-based analysis. Imaging, analytical spatial resolution, mass sensitivity, and quantitative

analysis all suffer in their ultimate performance due to the accumulation of foreign material on the sample surface. It has also been shown that the removal of system peaks, generated in the instrument, is an important aspect of microchemical analysis which should not be neglected.

Experimental measurements combined with theoretical calculations have shown that the optimum conditions for x-ray analysis in an AEM are realized at the highest attainable incident electron beam energy and by using a detector/specimen geometry which maximizes the detector observation angle. Furthermore, once all instrumental corrections have been applied to the AEM system, it is possible to obtain accurate quantitative results in "thin" specimens using the standardless analysis technique and the formalism presented in Chapter 2. The calculation of an absorption correction for a homogeneous semi-thick sample is not difficult, but, as most analyses involve multi-element phases of varying thicknesses, it becomes simpler to analyze thinner regions of the sample where such a correction is not required. Quantitative analysis using thin-film standards is potentially simple, although experimental aspects such as the accurate duplication or measurement of instrumental operating conditions complicates the development of this method.

Finally, two complementary methods of obtaining structural information about a specimen using electron diffraction have been investigated and refined. These methods – namely transmission scanning electron diffraction and the stationary diffraction pattern technique – when combined with appropriate calculations allows one to obtain information about the

nature of the sample not attainable using conventional selected-area-diffraction techniques.

The ability to perform simultaneously energy dispersive x ray as well as electron energy loss measurements will be one of the most important aspects of AEM to the materials scientist for development in the future. Using these two complementary techniques the potential to perform analysis of all atomic species of $Z \geq 3$ may be realized, and, in special cases, through systematic studies of plasmon losses it may be possible to analyze for the presence of hydrogenic compounds. Combining these microchemical analysis capabilities with the various electron diffraction techniques for crystallographic analysis makes analytical electron microscopy an essential part of any materials research program.

LIST OF REFERENCES

1. D. J. Cometto, G. L. Houze, and R. F. Hehemann, *Trans. AIME* 233, 30 (1965).

2. J. M. Silcock, *Acta Met.* 6, 481 (1958).

3. Y. A. Bagaryatskii, G. I. Nosava, and T. V. Tagunova, *Akad. Nauk. SSSR* 105, 1225 (1955).

4. B. A. Hatt and J. A. Roberts, *Acta Met.* 8, 575 (1960).

5. J. O. Stiegler, J. T. Houston, and M. L. Picklesimer, *J. Nucl. Mater.* 11, 32 (1964).

6. W. G. Brammer and C. G. Rhodes, *Phil. Mag.* 16, 477 (1967).

7. S. L. Sass, *Acta Met.* 17, 813 (1969).

8. C. W. Dawson and S. L. Sass, *Met. Trans.* 1, 2225 (1970).

9. K. K. McCabe and S. L. Sass, *Phil. Mag.* 23, 252 (1971).

10. A. T. Balcerzak and S. L. Sass, *Met. Trans.* 3, 1601 (1972).

11. S. L. Sass, *J. Less-Common Metals* 28, 157 (1972).

12. T. S. Kuan, R. R. Ahrens, and S. L. Sass, *Met. Trans.* 6A, 1767 (1975).

13. A.L.J. Chang, W. Krakow, and S. L. Sass, *Acta Met.* 24, 29 (1976).

14. D. deFontaine, N. E. Paton, and J. C. Williams, *Acta Met.* 19, 1153 (1971).

15. S. C. Moss, D. T. Keating, and J. D. Axe, *Phase Transformation 1973.* Penn State University, 23–25 May, Pergamon Press, Oxford, 1973.

16. B. W. Batterman, G. Maracci, A. Merlini, and S. Pace, *Phys. Rev. Letters,* 31, 227 (1973).

17. W. Lin, H. Spalt, and B. W. Batterman, *Phys. Rev.* (1976) (submitted).

18. D. deFontaine, *Acta Met.* 18, 275 (1970).

19. H. E. Cook and D. deFontaine, *Acta. Met.* 17, 915 (1969).

20. H. E. Cook and D. deFontaine, *Acta Met.* 19, 607 (1971).

21. E. S. Fisher and D. Dever, *Acta Met.* 18, 265 (1970).

22. D. deFontaine, N. E. Paton, and J. C. Williams, *Acta Met.* 19, 1153 (1971).

23. W. Vandermuelen and A. Deruyttere, *Met. Trans.* 4, 1659 (1972).

24. B. Borie, S. Sass, and A. Andreassen, *Acta Cryst.* A29, 585 (1973).

25. B. Borie, S. Sass, and A. Andreassen, *Acta Cryst.* A29, 594 (1973).

26. H. E. Cook, *Acta Met.* 21, 1445 (1973).

27. H. E. Cook, *Acta Met.* 22, 239 (1974).

28. H. E. Cook, *Acta Met.* 23, 1027 (1975).

29. H. E. Cook, *Acta Met.* 23, 1041 (1975).

30. J. Philibert and R. Tixier, *NBS No. 298*, 13 (1968).

31. J. Philibert and R. Tixier, *J. Phys. D* 1, 685 (1968).

32. G. Cliff and G. W. Lorimer, *Fifth European Conference on Electron Microscopy, 1972*, p. 136.

33. M. H. Jacobs and J. Baborovoska, *Fifth European Conference on Electron Microscopy, 1972*, p. 140.

34. P. Duncumb, *J. deMicroscopie* 7, 581 (1965).

35. R. H. Geiss and T. C. Huang, *J. Vac. Sci. Tech.* 12, 140 (1975).

36. P. Doig and J. W. Edington, *Phil. Mag.* 27, 285 (1975).

37. J. Philibert, *X-Ray Optics and Microanalysis*, Academic Press, New York, 1963, p. 379.

38. T. Namae, *J. Electron Microscopy* 24, 1 (1975).

39. D. J. Marshall and T. A. Hall, *J. Phys. D* 1, 1651 (1968).

40. W. Reuter, *Sixth Intern. Conference X-Ray Optics and Microanalysis*, Academic Press, New York, 1972, p. 121.

41. J. I. Goldstein and D. B. Williams, *SEM* 1, 651 (1977).

42. H. L. Fraser, N. J. Zaluzec, J. B. Woodhouse, and L. B. Sis, *33rd Proc. EMSA* (1975), p. 106.

43. N. J. Zaluzec and H. L. Fraser, *34th Ann. Proc. EMSA* (1976).

44. N. J. Zaluzec and H. L. Fraser, *8th Int. Conf. on X-Ray Optics and Microanalysis* (1977) (in press).

45. J. I. Goldstein, private communication.

46. H. S. Perlman, *Proc. Phys. Soc. (London)*, 76, 623 (1960).

47. A. M. Arthurs and B. L. Moiseiwitch, *Proc. Roy. Soc.* A247, 550 (1958).

48. N. Mott and H. Massey, *Theory of Atomic Collisions*, Oxford Press, London, 1949.

49. C. R. Worthington and S. G. Tomlin, *Proc. Phy. Soc. (London)*, 69, 401 (1956).

50. E.H.S. Burhop, *Proc. Cam. Phil. Soc.* 36, 43 (1940).

51. J. I. Goldstein, J. L. Costley, G. W. Lorimer, and S.J.B. Reed, *SEM* 1, 315 (1977).

52. C. J. Powell, *Rev. Mod. Phys.* 48, 33 (1976).

53. W. Hink and A. Ziegler, *Z. Physik* 226, 222 (1969).

54. L. T. Pockman, D. L. Webster, P. Kirkpatrick, and K. Harworth, *Phys. Rev.* 71, 330 (1947).

55. P. Kirkpatrick and A. V. Baez, *Phys. Rev.* 71, 521 (1947).

56. L. Landau, *J. Phys. Moscow* 8, 201 ( ).

57. H. A. Bethe, *Ann. Phys.* 5, 325 (1930); *H.d. Phys.* 24, 519 (1933).

58. V. E. Cosslett and R. N. Thomas, *Brit. J. Appl. Phys.* 15, 1283 (1964); 16, 779 (1965); 15, 883 (1964).

59. A. T. Nelms, National Bureau of Standards, Circular No. 577 (1956).

60. G. D. Archard and T. Mulvey, *3rd Int. Conf. on X-Ray Optics and Microanalysis*, Academic Press, 1962.

61. G. Wentzel, *Z. Phys.* 43, 524 (1927).

62. N. A. Dyson, *X-Rays in Atomic and Nuclear Physics*, Longman Group, Ltd., London, 1973.

63. J. Colby, *Advances in X-Ray Analysis* 11, 287 (1968) (Plenum Press).

64. R. W. Fink, R. C. Jopson, H. Mark, and C. D. Swift, *Rev. Mod. Phys.* 39, 125 (1967).

65. E.H.S. Burhop, *J. Phys. Radium* 16, 625 (1955).

66. V. W. Slivinsky and P. J. Ebert, *Phys. Rev. A* 5, 1581 (1972).

67. K.F.J. Heinrich, *Proc. 11th Conf. MAS* (1976), p. 29.

68. *Handbook of Chemistry and Physics*, 53rd ed. (ed. by R. Weast), Chemical Rubber Company, Cleveland, Ohio, 1973.

69. E. J. McGuire, *Phys. Rev. Letters* 33A, 288 (1970).

70. J. A. Crowther, *Proc. Roy. Soc.* A84, 226 (1910).

71. B. Cullity, *Elements of X-Ray Diffraction*, Chap. 2, Addison Wesley, Reading, MA, 1967.

72. A. Sommerfeld, *Ann. d. Physik* 11, 257 (1931).

73. R. Weinstock, *Phys. Rev.* 61, 584 (1942).

74. P. Kirkpatrick and L. Wiedmann, *Phys. Rev.* 67, 321 (1945).

75. JEOL, Ltd., Electron Microscope Division.

76. J. W. Sprys, *Rev. Sci. Inst.* 46, 773 (1975).

77. N. J. Zaluzec and H. L. Fraser, *J. Phys. E.* 9, 1051 (1976).

78. E. A. Kenik and J. Bentley, Metals and Ceramics Division, Oak Ridge National Laboratory, private communication (1977).

79. Philips Electronics Instruments, Inc., Electron Microscope Division.

80. Vacuum Generators, Ltd., Electron Microscope Division.

81. J. J. Hren, P. S. Ong, P. F. Johnson, and E. J. Jenkins, *34th Ann. Proc. EMSA, 1976*, Claitor's Publishing Company, Baton Rouge, LA, p. 418.

82. H. L. Fraser, M. H. Loretto, and R. E. Smallman, *Phil. Mag.* 28, 667 (1973).

83. N. J. Zaluzec and H. L. Fraser, *Workshop on Analytical Electron Microscopy*, Cornell, 1976.

84. *Workshop on Analytical Electron Microscopy, op. cit.* General discussion in open forum, summarized in *Proceedings*.

85. J. T. Fourie, *SEM/IITRI* (ed. by O. Johari), 1976, p. 53.

86. J. C. Russ, *SEM/IITRI* (ed. by O. Johari), 1976, p. 143.

87. J. C. Russ, *SEM/IITRI* (ed. by O. Johari), 1976, p. 335.

88. P. Duncumb, *Phil. Mag.* 7(84), 2101 (1962).

89. Th. Bronder and J. Jakschik, *Phys. Stat. Sol.* (a) 31, 503 (1975).

90. C. R. Hall, *Proc. Roy. Soc.* A295, 140 (1966).

91. H. L. Fraser and J. B. Woodhouse, *Proc. 2nd Workshop on AEM*, Cornell University (July 1978).

92. R. H. Geiss and T. C. Huang, IBM Technical Report No. 965-IBM-01 (1974).

93. R. H. Geiss, *Appl. Phys. Letters* 23, 283 (1973).

94. C.W.B. Grigson, *Rev. Sci. Inst.* 36, 1587 (1965).

95. D. M. Maher, *SEM/IITRI* (ed. by O. Johari), 1974, p. 215.

96. P. M. Kelly, A. Jostsons, R. G. Blake and J. G. Napier, *Phys. Stat. Sol.* (a) 31, 771 (1975).

97. B. F. Buxton, J. A. Eades, J. W. Steeds, and G. M. Rockham, *Phil. Trans. Roy. Soc.* 281, 171 (1976).

98. R. W. Carpenter and N. J. Zaluzec, *Proc. 2nd Workshop on AEM*, Cornell University (July 1978).

99. R. F. Egerton and M. J. Whelan, *Proc. 8th Int. Conf. on EM*, Canberra, Australia (1974), p. 384.

100. P. E. Flewitt, P. J. Ash, and A. G. Crocker, *Acta Met.* 24, 669 (1976).

101. T. Schober and V. Sorajic, *Metallography* 6, 183 (1973).

102. R. A. Spurling, G. G. Rhodes, and J. C. Williams, *Met. Trans.* 2597 (1974).

103. M. J. Blackburn and J. C. Williams, *Trans. TMS-AIME* 239, 287 (1967).

104. H. J. Rack, D. Kalish and R. Fike, *Mat. Sci. Eng.* 6, 181 (1970).

105. R. Ericksen, R. Taggart, and D. Polonis, *Trans. TMS-AIME* 245, 359 (1969).

APPENDIX A

Computer Program NEDS

Subroutine SINPUT

Subroutine SKLM

Subroutine SBGRND

Subroutine GSETUP

Subroutine GAUSS

APPENDIX A

Computer Program NEDS

This appendix contains documentation of the computer program NEDS which has been used to analyze all energy dispersive x-ray spectra during this research. The program is currently set up to analyze a 10 keV wide spectrum recorded at an energy resolution of 20 eV/channel; however, it can be easily modified should different operating conditions be required. An example of a partial analysis of and EDS spectrum is shown in Figs. 99 and 100. Figure 99(a) shows a typical EDS spectrum recorded from a thin foil in the JEOL JSEM 200, and Fig. 99(b) compares the fitted polynomial background curve [Eq. 2.52)] with the experimental data. The results of a partial analysis of this spectrum is shown graphically in Fig. 100(a), where the program has fitted Gaussian profiles to the NiL_{α}, AlK_{α} and SiK_{α} peaks recorded in the energy range 0.65 to 2.15 keV. Figure 100(b) compares the profile (sum) of these three peaks to the experimental data. Figure 101 is a simplified flow diagram for the program NEDS.

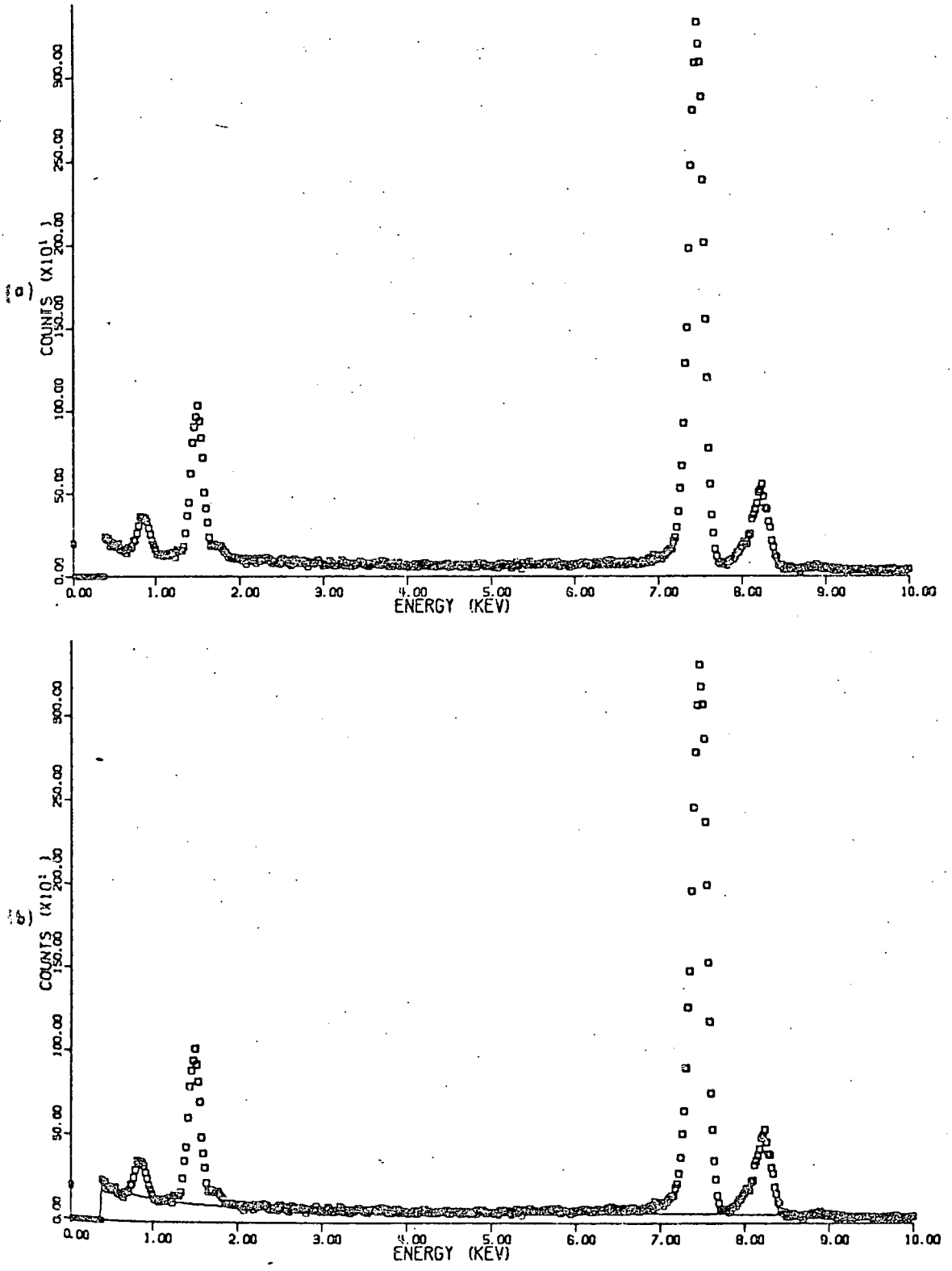

Fig. 99. (a) Typical X-Ray Spectrum Recorded from the JEOL JSEM 200. (b) Comparison of fitted polynomial background curve (solid line) to experimental data.

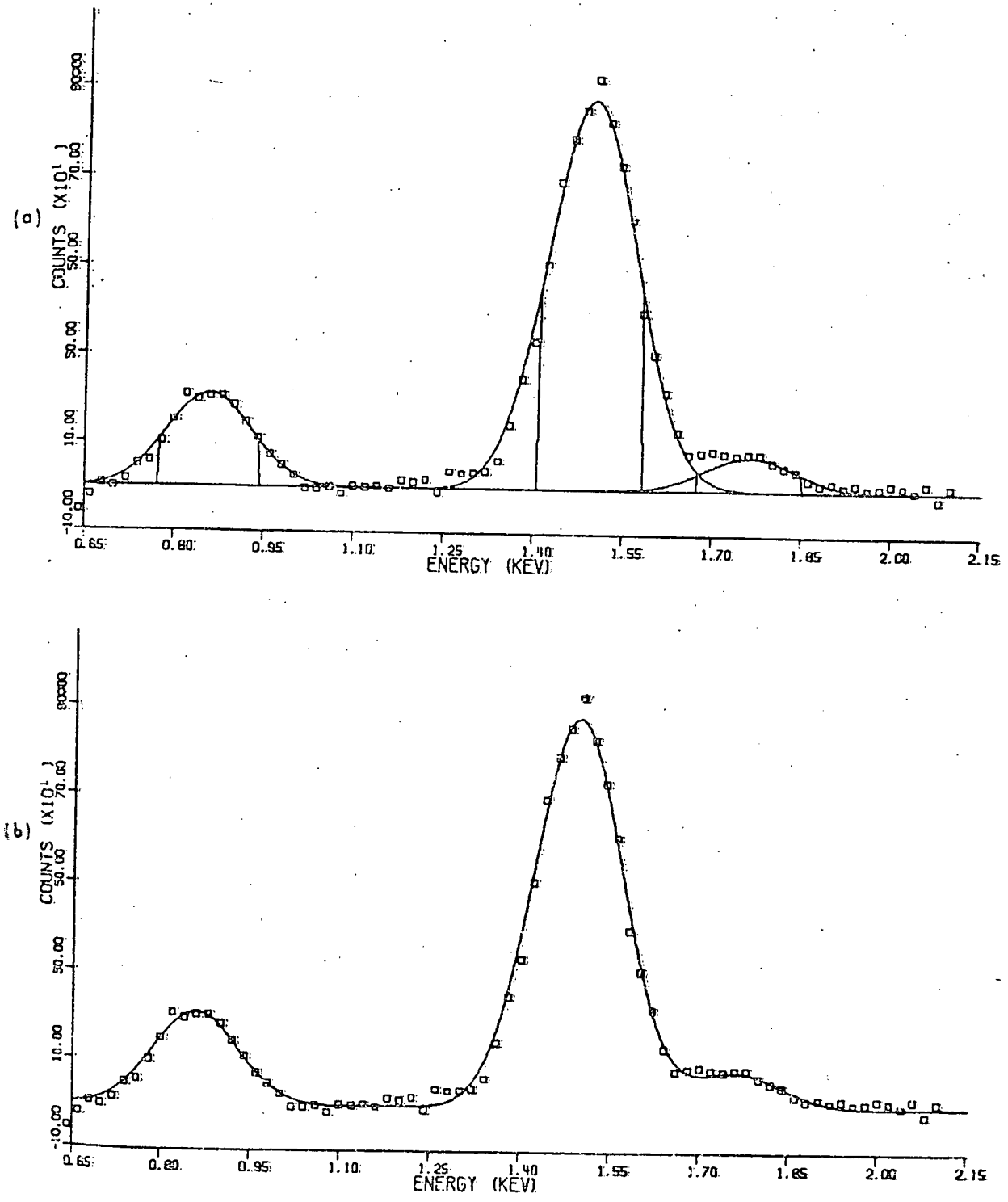

Fig. 100. (a) Fitted Gaussian Profiles for NiL_α (0.85 keV), AlK_α (1.47 keV), and SiK_α (1.75 keV) Compared to Experimental Data. FWHM region indicated on each Gaussian curve. (b) Sum of NiL_α, AlK_α, and $SiK\alpha$ profiles (solid line) compared to experimental data.

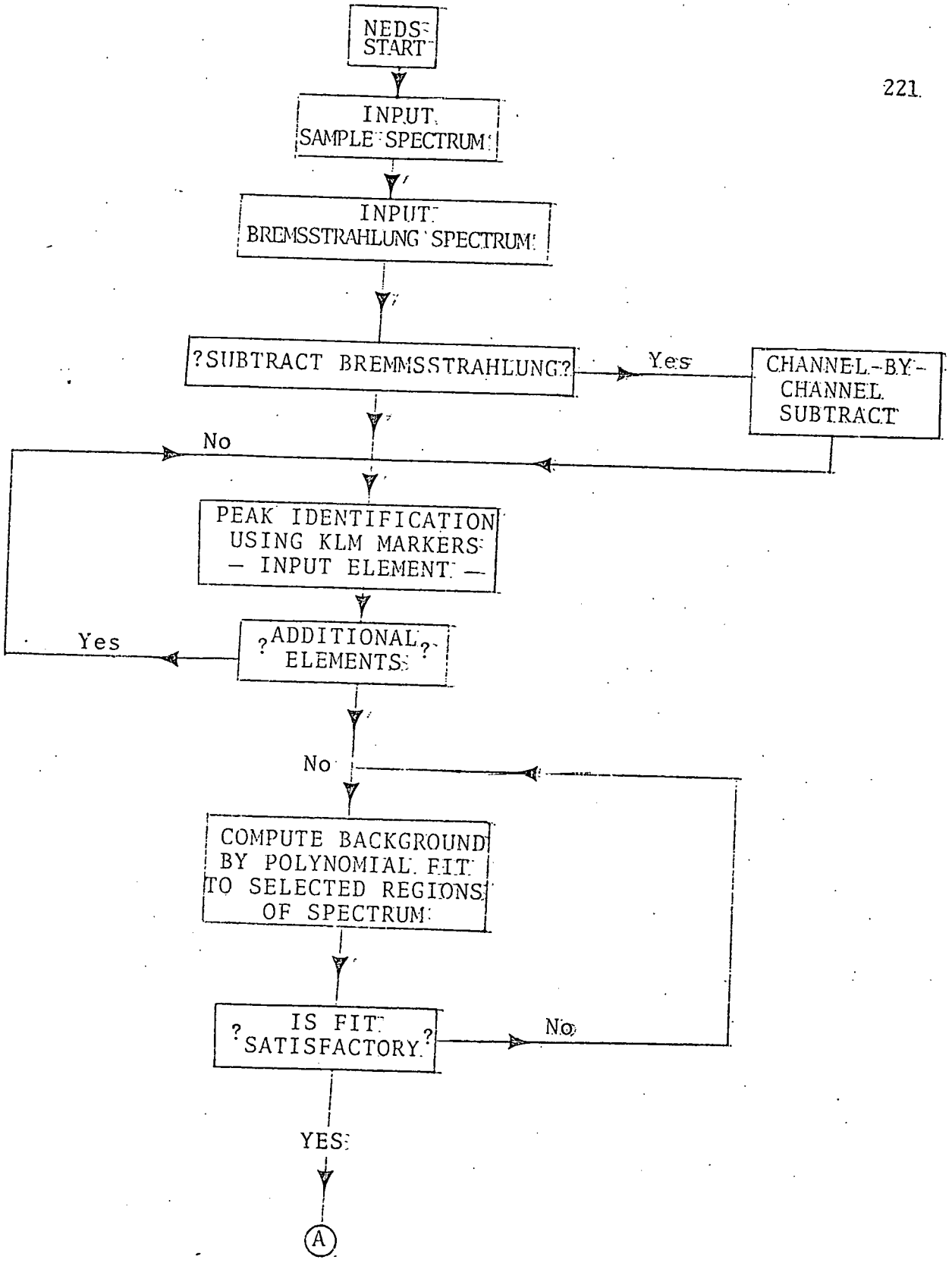

Fig. 101. Flow Diagram for the Program NEDS.

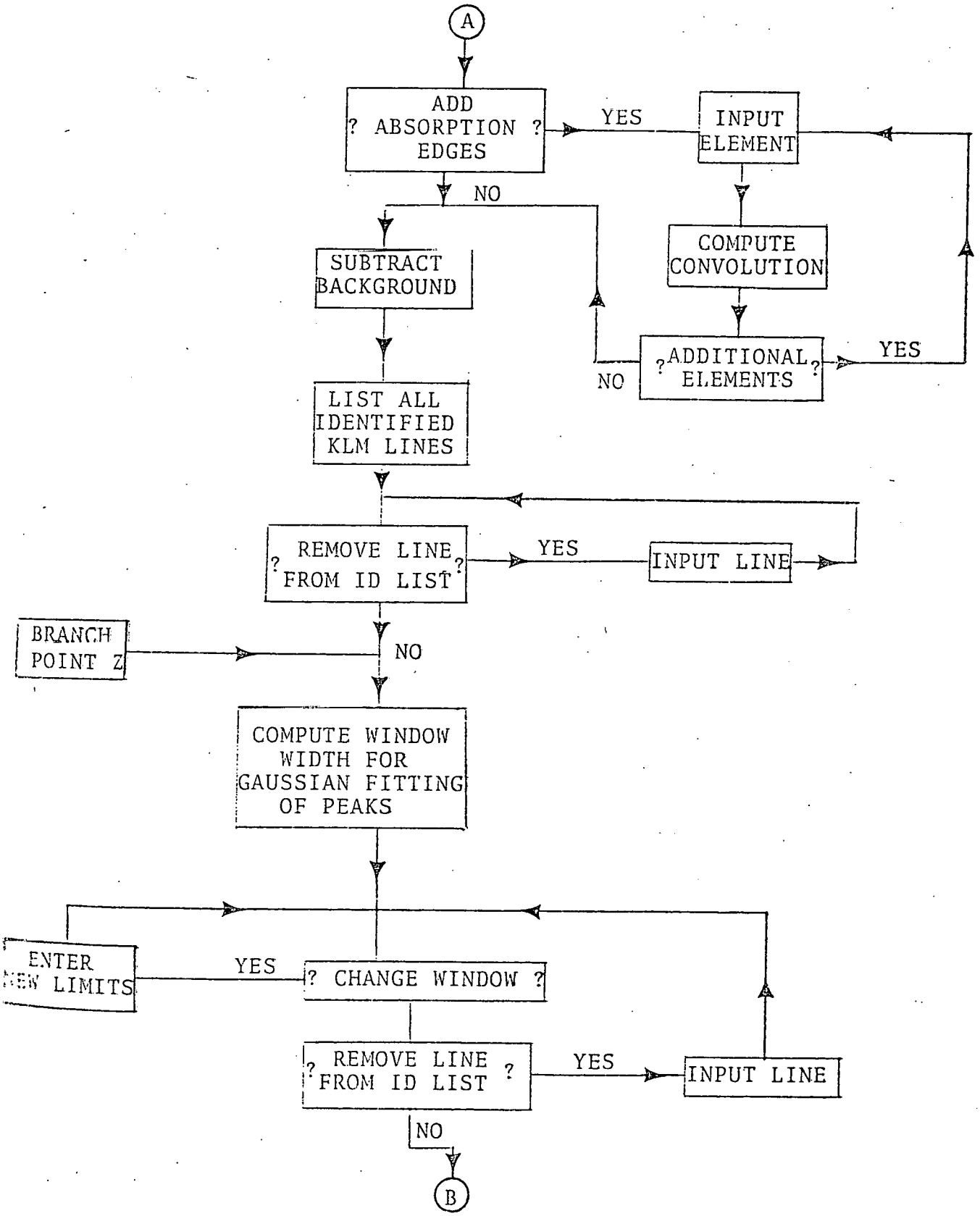

Fig. 101 (continued)

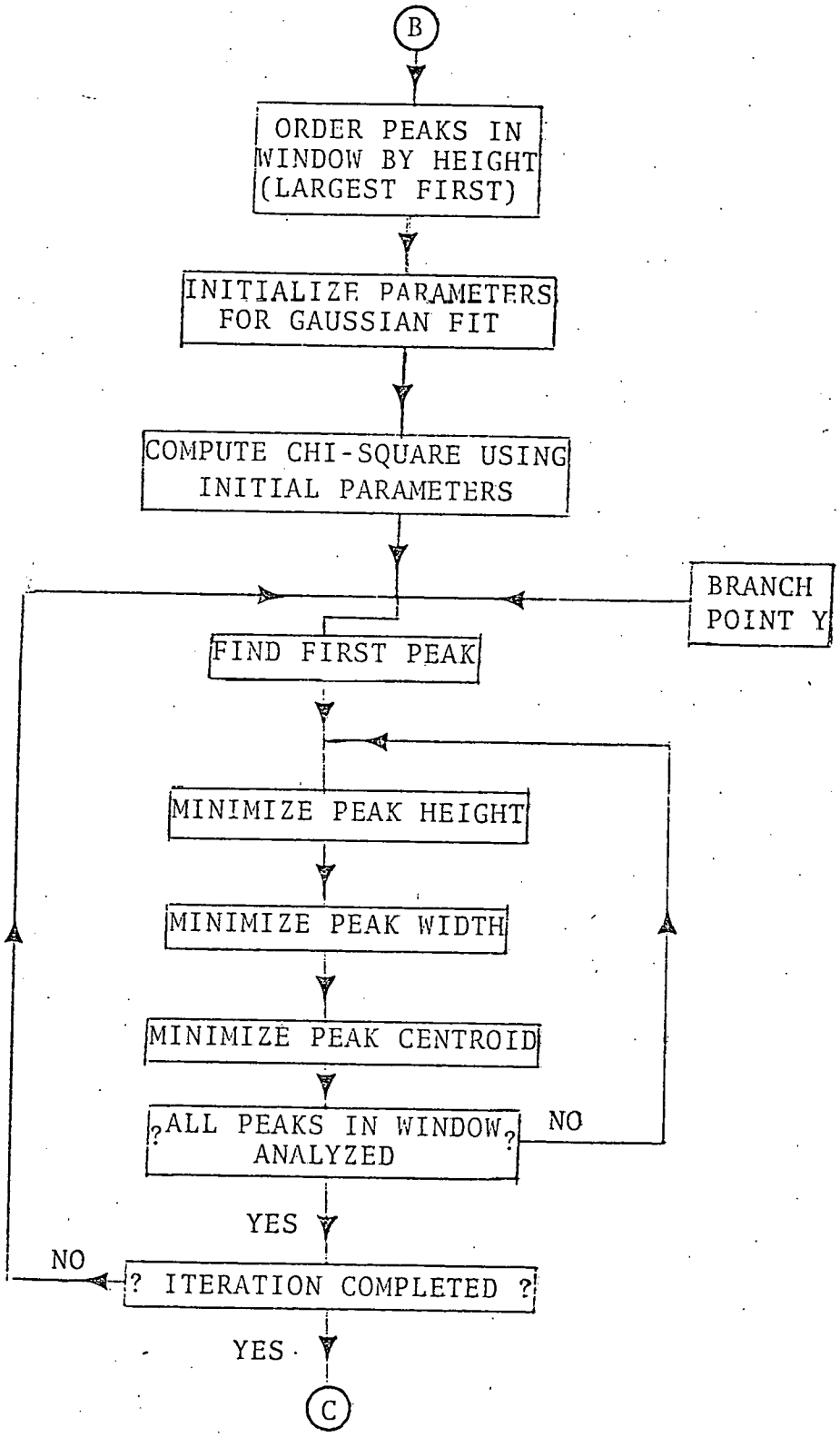

Fig. 101 (continued)

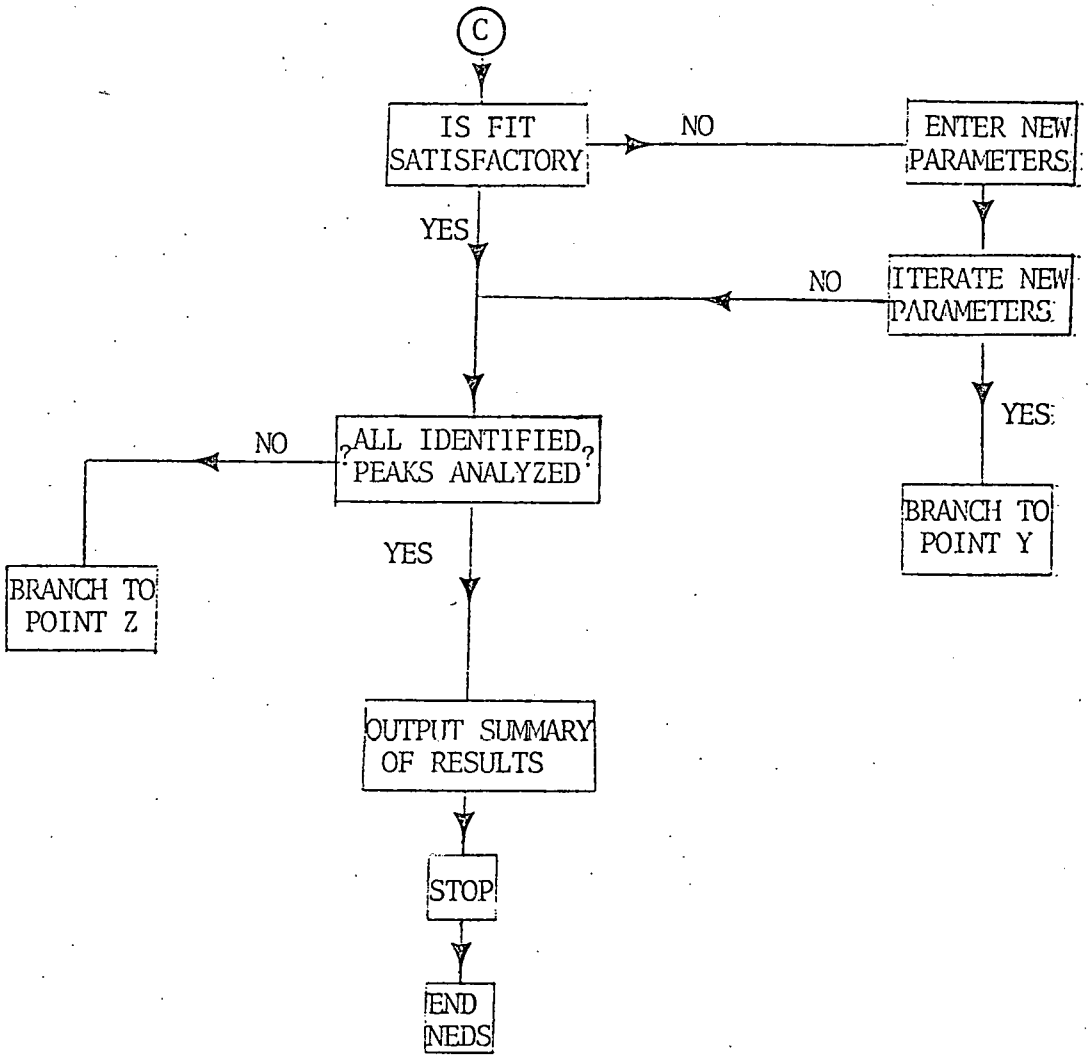

Fig. 101 (continued)

```
C
C                          EDS DATA ANALYSIS PROGRAM
C
C
C                                   7703010000
C
C                ALL QUESTIONS AND COMMENTS SHOULD BE DIRECTED TO:
C
C                                 NESTOR J. ZALUZEC
C                              DEPARTMENT OF METALLURGY
C                              UNIVERSITY OF ILLINOIS
C                                URBANA,ILLINOIS
C
C                          ALL RIGHTS RESERVED BY AUTHOR
C THIS PROGRAM IS WRITTEN IN FORTRAN IV  FOR USE ON A XEROX SIGMA 5
C OR PDP LSI-11 COMPUTER SYSTEM EQUIPPED WITH A TEKTRONIX 4010-1
C GRAPHICS DISPLAY TERMINAL .  THIS VERSION IS FOR USE ON A LSI-11.
C
C DATA INPUT USES THE FOLLOWING DCB'S
C  5=GRAPHICS TERMINAL (INPUT)
C  7=GRAPHICS TERMINAL (OUTPUT)
C 10=FILE CONTAINING BREMSSTRAHLUNG SPECTRUM
C 11=FILE CONTAINING SAMPLE(S) SPECTRUM
C 12=FILE USED FOR OUTPUT OF RESULTS
C
C TO RUN ON THE PDP LSI-11  THE FOLLOWING COMMAND WILL INITIATE THE
C SYSTEM CORRECTLY
C
C .RUN FD1:NEDS.SAV
C
C
C
C THIS PROGRAM CAN ANALYZE AT MOST 30 PEAKS
C NOTE THIS DOES NOT CORRESPOND TO 30 ELEMENTS
C ALL INPUT DATA FROM TERMINAL IS IN KEV
C SPECTRUM SET UP TO ANALYZE A 10 KEV REGION
C TO CHANGE RESOLUTION OF MCA CHANGE IRES (NOW SET AT 20EV/CHN)
C
C
C
C
      COMMON P(502),E(502),BG(502),EKLM(502),SUBID(76)
      COMMON SUBP(76),SUBE(76),AEN(30),AHT(30),AEL(31),AINT(30)
      COMMON SUME(760),SUMP(760),SUMID(760),ABG(30)
      COMMON ITAPE(72),INAME(72),YY,YN,
     1EKA(20),EKB(20),ELA(20),ELB(20),EMA(20),EMB(20),NUM(20)
      COMMON /ELEMNT/ CS(100),ALNID(6)
      COMMON /EDSVRB/ IRES,EO,EI,NFK,THICK,SYMBOL,Z,
     1EMAX,EMIN,MFLAG,BL1,BU1,BL2,BU2,BL3,BU3,AAA,BBB,CCC,EKABS,ELABS,
     2EMABS,EABS,BGL,BGU,LBGL,LBGU,S1,S2,R,SABS,EN,RR,RESLVE,FLAG,
     3EMIN2,EMAX2,EMIN1,EMAX1,NCHN,FN,MM,M,MIN,MAX,NMIN,NMAX,NPT,NP,AM,
     4IFN,IFFN,ATOM,NPTS,LAST,BRCKET,FF,ABSFF,CC,EL,EU,PB,ITH1,ITH2
      DATA YY,YN/'Y','N'/
```

```
      DATA IRES/20/
      DATA ALNID/'KA','KB','LA','LB','MA','MB'/
      DATA CS/' H','HE','LI','BE',' B',' C',' N',' O',' F','NE'
     1,'NA','MG','AL','SI',' P',' S','CL','AR',' K','CA','SC','TI',
     2' V','CR','MN','FE','CO','NI','CU','ZN','GA','GE','AS','SE',
     3'BR','KR','RB','SR',' Y','ZR','NB','MO','TC','RU','RH','PD',
     4'AG','CD','IN','SN','SB','TE',' I','XE','CS','BA','LA','CE',
     5'PR','ND','PM','SM','EU','GD','TB','DY','HO','ER','TM','YB',
     6'LU','HF','TA',' W','RE','OS','IR','PT','AU','HG','TL','PB',
     7'BI','PO','AT','RN','FR','RA','AC','TH','PA',' U','NP','PU',
     8'AM','CM','BK','CF','ES','FM'/
 999    CALL SINPUT
      IF(FLAG.EQ.9999.) GO TO 9999
      CALL SKLM
      IF(FLAG.EQ.9998.) GO TO 999
      CALL SBGRND
      EMIN1=0.
      EMAX1=0.
      NCHN=25
      FN=1.
 50   CALL GSETUP
      IF(FLAG.EQ.9997.) GO TO 99
      CALL GAUSS
C
C RETURN TO SEARCH TO FIND NEXT PEAK AND REPEAT ABOVE UNTIL
C ALL IDENTIFEID KLM PEAKS HAVE BEEN ANALYSED
C
       GO TO 50
C
C OUTPUT RESULTS OF BEST FIT PARAMETERS
C
 99   WRITE(7,74)
      WRITE(12,74)
 74   FORMAT(' PK NO.--ENERGY---STND.DEV.---HEIGHT--COUNTS---BGND',
     C' --PEAK/BGND')
      DO 75 I=1,IFPN
      PB=AINT(I)/ABG(I)
      WRITE(7,76) I,AEN(I),AEL(I),AHT(I),AINT(I),ABG(I),PB
      WRITE(12,76)I,AEN(I),AEL(I),AHT(I),AINT(I),ABG(I),PB
 76   FORMAT(2X,I2,3X,1F6.3,5X,1F6.2,3X,3(1F7.1,2X),1F6.2)
 75   CONTINUE
      WRITE(7,77) THICK,ITH1,ITH2
      WRITE(12,77)THICK,ITH1,ITH2
 77   FORMAT(' SAMPLE THICKNESS PROPORTIONAL TO ',1F10.2,
     C/,' (CONTINUUM COUNTS IN CHANNELS ',I4,'-',I4,')',5(/))
C
C READ IN NEXT SPECTRUM
C
 9999 STOP
      END
```

```
      SUBROUTINE SINPUT
      COMMON P(502),E(502),BG(502),EKLM(502),SUBID(76)
      COMMON SUBP(76),SUBE(76),AEN(30),AHT(30),AEL(31),AINT(30)
      COMMON SUME(760),SUMP(760),SUMID(760),ABG(30)
      COMMON    ITAPE(72),INAME(72),YY,YN,
     1EKA(20),EKB(20),ELA(20),ELB(20),CHA(20),CHB(20),NUM(20)
      COMMON /CDBVRB/ IRES,EO,EI,NPK,THICK,SYMBOL,Z,
     1EMAX,EMIN,MFLAG,BL1,BU1,BL2,BU2,BL3,BU3,AAA,BBB,CCC,EKABS,ELABS,
     2EMABS,EABS,BGL,BGU,LBGL,LBGU,S1,S2,R,SABS,EN,RR,RESLVE,FLAG,
     3EMIN2,EMAX2,EMIN1,EMAX1,NCHN,FN,MM,M,MIN,MAX,NMIN,NMAX,NPT,NP,AM,
     4IFN,IFFN,ATOM,NPTS,LAST,BRCKET,FF,ABSFF,CC,EL,EU,PB,ITH1,ITH2
      CALL ERASE
      WRITE(7,900)
  900  FORMAT(25X,29('*'),/,
     125X,'* EDS DATA ANALYSIS PROGRAM *',/,
     125X,'*       7709010000-NJZ       *',/,25X,29('*'),//)
      WRITE(7,901)
  901  FORMAT(18X,' ENTER NAME OF FILE WHICH CONTAINS BREMS. SPECTRUM' )
      CALL ASSIGN(10,' DUMMY' ,-6,'OLD','NC' ,1)
      WRITE(7,902)
  902 FORMAT(18X,' ENTER NAME OF FILE WHICH CONTAINS SAMPLE SPECTRUM' )
      CALL ASSIGN(11,' DUMMY' ,-6,'OLD','NC' ,1)
      WRITE(7,903)
  903 FORMAT(18X,' ENTER NAME OF FILE TO BE USED FOR OUTPUT SUMMARY' )
      CALL ASSIGN(12,' DUMMY' ,-6,'NEW','NC' ,1)
      AEL(31)=1000.
C
C INPUT BREMSTRALLUNG EXCITED SPECTRUM
C ITAPE =TAPE IDENTIFICATION NUMBER
C INAME= TAPE IDENTIFICATION
C
  999 READ (10,1,END=2)ITAPE
      READ(10,1,END=2)INAME
    1  FORMAT(72A1)
C
C EO=ACCELERATING VOLTAGE IN KEV
C EI=STARTING POINT OF SPECTRUM IN KEV (USUSALLY SET AT ZERO)
C NOTE THAT THIS PROGRAM ANALYZES A REGION 10 KEV WIDE
C FROM EI TO EI+10.0 KEV
C
      READ(10,3,END=2)  EO,EI
    3 FORMAT(2F7.3)
      DO 2 I=1,50
      K=I*10-9
      KK=K+9
      READ(10,4,END=2,ERR=2)(BG(N),N=K,KK)
    4 FORMAT(10(1F6.0,1X))
    2 CONTINUE
      REWIND 10
C
C INPUT SAMPLE SPECTRUM
C
```

```
      READ(11,1,END=9999,ERR=5) ITAPE
      READ(11,1,END=9999,ERR=5) INAME
      READ(11,3,END=9999,ERR=5) EO,EI
      EO=EO*1000.
      DO 5 I=1,50
      K=I*10-9
      KK=K+9
      READ(11,4,END=5,ERR=5)(P(N),N=K,KK)
C
C INITIALIZE ENERGY MATRIX
C
      DO 5 N=K,KK
      E(N)=(N-1)*IRES*.001 + EI
      EKLM(N)=1.
      IF (P(N).LE.0.5) P(N)=1.
 5    CONTINUE
      E(500)=10.0 +EI
      P(1)=1.0
C
C SCAN THROUGH SPECTRUM CHECK FOR OBVIOUS ERRORS
C
      DO 6 N=2,498
      IF((P(N).GE.(5*SQRT(P(N+1))+P(N+1))).AND.(P(N).GE.
     1(5*SQRT(P(N-1))+P(N-1))).AND.(P(N).GE.10.)) GO TO 7
      GO TO 6
 7    P(N)=(P(N+1)+P(N-1))/2.
 6    CONTINUE
      WRITE(7,1)ITAPE
      WRITE(7,1)INAME
      WRITE(12,1)  ITAPE
      WRITE(12,1)INAME
 10   FORMAT(31(/))
D     WRITE(7,11)
 11   FORMAT(//,$,' DO YOU WANT TO PROCESS THIS TAPE? YES-NO',2X)
      READ(5,302)   X
 301  FORMAT(1F12.6)
 302  FORMAT(1A1)
 261  FORMAT(6(1F10.5,1X))
      WRITE(12,3)  X
      IF (X.EQ.YN) GO TO 2
D     WRITE(7,13)
 13   FORMAT(5(/),$,' SUBTRACT BREMSSTRAHLUNG FLUORESCENCE? YES-NO',2X)
C
C SUBTRACT BREMSSTRAHLUNG SPECTRUM
C
      READ (5,302) X
      IF(X.EQ.YN) GO TO 14
      CALL MSUB(P,BG,P,500,1,0,0)
      CALL NEGTVE(P,500,0.)
C
C  SCALE SPECTRUM AND CHECK FOR REGIONS LESS THAN .5 KEV
C
```

```
   14   DO 12 I=2,25
        P(I)=P(25)
   12    CONTINUE
D       CALL ERASE
        CALL CRTPLT(150.,265.,E,P,500,0,0,1.,1.,E,P,500)
D       CALL PLOT (0.,767.,0)
        RETURN
 9999   FLAG=9999.
        RETURN
        END



        SUBROUTINE SKLM
        COMMON P(502),E(502),BG(502),EKLM(502),SUBID(76)
        COMMON SUBP(76),SUBE(76),AEN(30),AHT(30),AEL(31),AINT(30)
        COMMON SUME(760),SUMP(760),SUMID(760),ABG(30)
        COMMON ITAPE(72),INAME(72),YY,YN,
       1EKA(20),EKB(20),ELA(20),ELB(20),EMA(20),EMB(20),NUM(20)
        COMMON /ELEMNT/ CS(100),ALNID(6)
        COMMON /EDSVRB/IRES,E0,EI,NPK,THICK,SYMBOL,Z,
       1EMAX,EMIN,MFLAG,BL1,BU1,BL2,BU2,BL3,BU3,AAA,BBB,CCC,EKABS,ELABS,
       2EMABS,EABS,BGL,BGU,LBGL,LBGU,S1,S2,R,SABS,EN,RR,RESLVE,FLAG,
       3EMIN2,EMAX2,EMIN1,EMAX1,NCHN,PN,MM,M,MIN,MAX,NMIN,NMAX,NPT,NP,AM,
       4IPN,IFPN,ATOM,NPTS,LAST,BRCKET,FF,ABSFF,CC,EL,EU,PB,ITH1,ITH2
C
C READ IN ELEMNT AND CALCULATE K-L-M XRAY LINES
C
        NPK=1
C CALCULATE THICKNESS OF SPECIMEN I.E. BACKGROUND COUNTS IN CONTINUUM.
       THICK=0.
       WRITE(7,100)
  100   FORMAT(26(/),$,' ENTER ENERGY LIMITS FOR CONTINUUM'
      1,' MEASUREMENTS (IN KEV) EL,EU=  ')
       READ(5,101) E1,E2
  101   FORMAT(2F10.0)
       ITH1=E1*1000./IRES
       ITH2=E2*1000./IRES
       DO 114 I=ITH1,ITH2
       THICK=THICK+P(I)
  114  CONTINUE
   24   CONTINUE
       CALL PLOT(0.,767.,0)
D       WRITE(7,15)
   15  FORMAT (27(/),$,'  ENTER ELEMENT ' )
       READ(5,16)   SYMBOL
    3   FORMAT(A1)
   16  FORMAT(A2)
       Z=ATOMNR(SYMBOL)
```

```
      IF (Z.EQ.1000) GO TO 9999
      IF(Z.LE.0.5) GO TO 24
      EKA(NPK)=ENERGY(Z,1)
      EKB(NPK)=ENERGY(Z,4)
      ELA(NPK)=ENERGY(Z,2)
      ELB(NPK)=ENERGY(Z,5)
      EMA(NPK)=ENERGY(Z,3)
      EMB(NPK)=ENERGY(Z,6)
C
C IF (ALPHA-BETA) LESS THAN DETECTOR RESOLUTION DELETE BETA
C AND SHIFT ALPHA UPWARDS TO COMPENSATE
C
      IF((EKB(NPK)-EKA(NPK)).LE.0.1)EKA(NPK)=(EKA(NPK)+EKB(NPK))/2.
      IF((ELB(NPK)-ELA(NPK)).LE.0.1)ELA(NPK)=(ELA(NPK)+ELB(NPK))/2.
      IF((EMB(NPK)-EMA(NPK)).LE.0.1)EMA(NPK)=(EMA(NPK)+EMB(NPK))/2.
      IF((EKB(NPK)-EKA(NPK)).LE.0.1) EKB(NPK)=0.001
      IF((ELB(NPK)-ELA(NPK)).LE.0.1) ELB(NPK)=0.001
      IF((EMB(NPK)-EMA(NPK)).LE.0.1) EMB(NPK)=0.001
      NUM(NPK)=Z
C
C PLOT OF THESE LINES ON KNOWN SPECTRUM
C SCALE BETA INTENSITY TO FRACTION OF ALPHA INTENSITY
C
      EMAX=E(499)
      EMIN=E(10)
      IF(EKA(NPK).LE.EMAX)EKLM(ICHN(EKA(NPK),IRES))=ABS(P(ICHN(
     CEKA(NPK),IRES)))
      IF(EKB(NPK).LE.EMAX)EKLM(ICHN(EKB(NPK),IRES))=ABS(P(ICHN(
     CEKA(NPK),IRES)))*0.15
      IF(ELA(NPK).LE.EMAX)EKLM(ICHN(ELA(NPK),IRES))=ABS(P(ICHN(
     CELA(NPK),IRES)))
      IF(ELB(NPK).LE.EMAX)EKLM(ICHN(ELB(NPK),IRES))=ABS(P(ICHN(
     CELA(NPK),IRES)))*0.5
      IF(EMA(NPK).LE.EMAX)EKLM(ICHN(EMA(NPK),IRES))=ABS(P(ICHN(
     CEMA(NPK),IRES)))
      IF(EMB(NPK).LE.EMAX)EKLM(ICHN(EMB(NPK),IRES))=ABS(P(ICHN(
     CEMA(NPK),IRES)))*0.5
D     CALL CRTPLT(150.,265.,E,EKLM,500,1,1,1.,1.,E,P,500)
D     CALL PLOT (0.,767.,0)
D     WRITE(7,19)
 19   FORMAT(28(/),$,'  IS THIS CORRECT? YES-NO',2X)
      READ (5,3)   X
      IF(X.EQ.YY) GO TO 20
      IF(EKA(NPK).LE.EMAX)EKLM(ICHN(EKA(NPK),IRES))=1.0
      IF(EKB(NPK).LE.EMAX)EKLM(ICHN(EKB(NPK),IRES))=1.0
      IF(ELA(NPK).LE.EMAX)EKLM(ICHN(ELA(NPK),IRES))=1.0
      IF(ELB(NPK).LE.EMAX)EKLM(ICHN(ELB(NPK),IRES))=1.0
      IF(EMA(NPK).LE.EMAX)EKLM(ICHN(EMA(NPK),IRES))=1.0
      IF(EMB(NPK).LE.EMAX)EKLM(ICHN(EMB(NPK),IRES))=1.0
D     CALL ERASE
      CALL CRTPLT(150.,265.,E,P,500,0,0,1.,1.,E,P,500)
      CALL CRTPLT(150.,265.,E,EKLM,500,1,1,1.,1.,E,P,500)
```

```
D       CALL PLOT (0.,767.,0)
        GO TO 24
 20     CONTINUE
D       CALL PLOT (0.,767.,0)
D       WRITE(7,22)
 22     FORMAT(29(/),$,' ADDITIONAL ELEMENT? YES-NO',2X)
        READ(5,3)   X
        IF(X.EQ.YN) GO TO 23
        NPK=NPK+1
        GO TO 24
 23     CONTINUE
D       CALL PLOT (0.,767.,0)
        RETURN
 9999    FLAG=9998.
        RETURN
        END



        SUBROUTINE SBGRND
        COMMON P(502),E(502),BG(502),EKLM(502),SUBID(76)
        COMMON SUBP(76),SUBE(76),AEN(30),AHT(30),AEL(31),AINT(30)
        COMMON SUME(760),SUMP(760),SUMID(760),ABG(30)
        COMMON ITAPE(72),INAME(72),YY,YN,
       1EKA(20),EKB(20),ELA(20),ELB(20),EMA(20),EMB(20),NUM(20)
        COMMON /ELEMNT/ CS(100),ALNID(6)
        COMMON /EDSVRB/IRES,EO,EI,NPK,THICK,SYMBOL,Z,
       1EMAX,EMIN,MFLAG,BL1,BU1,BL2,BU2,BL3,BU3,AAA,BBB,CCC,EKABS,ELABS,
       2EMABS,EABS,BGL,BGU,LBGL,LBGU,S1,S2,R,SABS,EN,RR,RESLVE,FLAG,
       3EMIN2,EMAX2,EMIN1,EMAX1,NCHN,FN,MM,M,MIN,MAX,NMIN,NMAX,NPT,NP,AM,
       4IFN,IFFN,ATOM,NPTS,LAST,BRCKET,FF,ABSFF,CC,EL,EU,FB,ITH1,ITH2
C CALCULATE BACKGROUND BY POLYNOMINAL FIT AND DETECTOR EFF.
C
 44     CONTINUE
        MFLAG=0
D       WRITE (7,441)
 441    FORMAT(30(/),$,' REPLOT FOR BGRND FIT? YES-NO',2X)
        READ(5,3)   X
 269    IF(X.EQ.YN) GO TO 125
D       CALL ERASE
        CALL CRTPLT(150.,265.,E,P,500,0,0,1.,1.,E,P,500)
          MFLAG=1
 125       CALL PLOT (0.,767.,0)
D       WRITE(7,25)
 25     FORMAT(31(/),' SET 3 BGRND REGIONS')
        CALL CRSSHR(X,Y)
        CALL TRANXY(X,Y,BL1,Y)
        CALL CRSSHR(X,Y)
```

```
      CALL TRANXY(X,Y,BU1,Y)
      CALL CRSSHR(X,Y)
      CALL TRANXY(X,Y,BL2,Y)
      CALL CRSSHR(X,Y)
      CALL TRANXY(X,Y,BU2,Y)
      CALL CRSSHR(X,Y)
      CALL TRANXY(X,Y,BL3,Y)
      CALL CRSSHR(X,Y)
      CALL TRANXY(X,Y,BU3,Y)
      BL1=BL1*1000.
      BU1=BU1*1000.
      BL2=BL2*1000.
      BU2=BU2*1000.
      BL3=BL3*1000.
      BU3=BU3*1000.
      CALL BGRND1(EO,IRES,BL1,BU1,BL2,BU2,BL3,BU3,AAA,BBB,CCC)
      CALL CRTPLT(150.,265.,E,BG,500,1,1,1.,1.,E,P,500)
      MFLAG=0
D      CALL PLOT (0.,767.,0)
D      WRITE(7,28)
 28   FORMAT(32(/),$,' CHANGE BACKGROUND? YES-NO',2X)
      READ(5,3)   X
      IF (X.EQ.YY) GO TO 44
C
C ROUTINE TO ADD ABSROPTION EDGES TO BGND SPECTRUM
C BY CONVOLUTION OF EDGE WITH A GAUSSIAN RESPONSE FUNCTION OF DETECTOR
C
      CALL PLOT(0.,767.,0)
D      WRITE(7,32)
 32   FORMAT(33(/),$,' ADD ABSORPTION EDGES? YES-NO',2X)
      READ(5,3)   X
      IF(X.EQ.YN) GO TO 38
 33   CONTINUE
      CALL PLOT(0.,767.,0)
D      WRITE(7,21)
 21   FORMAT(27(/),$,35X,'ENTER ELEMENT',2X)
      READ(5,16)   SYMBOL
 16     FORMAT(A2)
 3    FORMAT(A1)
      Z=ATOMNR(SYMBOL)
      EKABS=12.37788/EDGE(Z,1)
      ELABS=12.37788/EDGE(Z,4)
      EMABS=12.37788/EDGE(Z,9)
      CALL PLOT(0.,767.,0)
D      WRITE(7,35)   EKABS,ELABS,EMABS
 35   FORMAT(28(/),35X,'K EDGE=',1F5.2,/,35X,'L EDGE=',1F5.2,/,35X,
     C,'M EDGE=',1F5.2,/,$,35X,'SELECT EDGE:NONE=0,K=1,L=2,M=3 ')
      READ(5,300)   X
 300   FORMAT(1F2.0)
      IF (X.EQ.0.) GO TO 33
      IF (X.EQ.1.) EABS=EKABS*1000.
```

```
      IF(X.EQ.2) EABS=ELABS*1000.
      IF (X.EQ.3) EABS=EMABS*1000.
      CALL PLOT(0.,767.,0)
D      WRITE(7,36)
 36   FORMAT(32(/),35X,'SET A BGND REGION PAST THIS EDGE' )
      CALL CRSSHR(X,Y)
      CALL TRANXY(X,Y,BGL,Y)
      CALL CRSSHR(X,Y)
      CALL TRANXY(X,Y,BGU,Y)
      LBGL=BGL*1000./IRES
      LBGU=BGU*1000./IRES
C
C CALCULATE DISCREPANCY RATION TRUE/FIT
C
      S1=0.
      S2=0.
      DO 37 I=LBGL,LBGU
      S1=S1+BG(I)
      S2=S2+P(I)
 37   CONTINUE
      R=S2/S1
C      WRITE(7,34)   R
C 34   FORMAT(' ERROR RATIO=' ,1F5.3)
C
C CALCULATE CONVOLUTION AND MULTIPLY BGND SPECTRUM BY R(E)
C
      SABS=SIGMA(EABS,0.)
      DO 39 I=2,500
      EN=(I-1.)*IRES
      IF(EN.LE.(EABS-5.*SABS)) RR=1.
      IF((EN.GE.(EABS-5.*SABS)).AND.(EN.LE.(EABS+5.*SABS)))
     1RR=CONV(EABS,SABS,IRES,EN,R)
      IF(EN.GE.(EABS+5.*SABS+0.0001)) RR=R
      BG(I)=BG(I)*RR
 39   CONTINUE
D     CALL ERASE
      CALL CRTPLT(150.,265.,E,P,500,0,0,1.,1.,E,P,500)
      CALL CRTPLT(150.,265.,E,BG,500,1,1,1.,1.,E,P,500)
D      CALL PLOT (0.,767.,0)
D      WRITE(7,32)
      READ(5,3)   X
      IF (X.EQ.YY) GO TO 33
 38   CONTINUE
C
C SUBTRACT FITTED BACKGROUND CURVE FROM EXPERIMENTAL DATA
C
      CALL MSUB(P,BG,P,500,1,0,0)
      CALL NEGTVE (P,500,-0.0)
      DO 61 I=2,20
      P(I)=1.
 61   CONTINUE
      RETURN
      END
```

```
      SUBROUTINE GSETUP
      COMMON P(502),E(502),BG(502),EKLM(502),SUBID(76)
      COMMON SUBP(76),SUBE(76),AEN(30),AHT(30),AEL(31),AINT(30)
      COMMON SUME(760),SUMP(760),SUMID(760),ABG(30)
      COMMON ITAPE(72),INAME(72),YY,YN,
     1EKA(20),EKB(20),ELA(20),ELB(20),EMA(20),EMB(20),NUM(20)
      COMMON /ELEMNT/ CS(100),ALNID(6)
      COMMON /EDSVRB/IRES,EO,EI,NPK,THICK,SYMBOL,Z,
     1EMAX,EMIN,MFLAG,BL1,BU1,BL2,BU2,BL3,BU3,AAA,BBB,CCC,EKABS,ELABS,
     2EMABS,EABS,BGL,BGU,LBGL,LBGU,S1,S2,R,SABS,EN,RR,RESLVE,FLAG,
     3EMIN2,EMAX2,EMIN1,EMAX1,NCHN,FN,MM,M,MIN,MAX,NMIN,NMAX,NPT,NP,AM,
     4IPN,IFPN,ATOM,NPTS,LAST,BRCKET,FF,ABSFF,CC,EL,EU,FB,ITH1,ITH2
C
C SEARCH SPECTRUM FOR IDENTIFIED PEAKS WHICH ARE SORTED BY
C ENERGY IN EKLM ARRAY
C SET UP A REFERENCE LEVEL FOR BGND
C
      IF(MFLAG.EQ.-1) GO TO 88
      IF(FLAG.EQ.9999) GO TO 153
C      WRITE(7,53)
C 53   FORMAT(29(/),' SET BGND REGION TO SET DET. LIMIT; BL,BU' ,
C     C'  NOT MORE THAN 1 KEV WIDE' )
C      CALL CRSSHR(X,Y)
C      CALL TRANXY(X,Y,BGL,Y)
C      CALL CRSSHR(X,Y)
C      CALL TRANXY(X,Y,BGU,Y)
 3     FORMAT(A1)
 26    FORMAT(2F7.5)
      LBGL=ICHN(BL3/1000.,IRES)
      LBGU=ICHN(BU3/1000.,IRES)
      RESLVE=-1.
      DO 54 I=LBGL,LBGU
      RESLVE=AMAX1(RESLVE,P(I))
 54   CONTINUE
      RESLVE=RESLVE + 3.*SQRT(RESLVE)
D      CALL ERASE
D     WRITE(7,541)
 541   FORMAT(' THE FOLLOWING PEAKS HAVE BEEN IDENTIFIED' )
      FLAG=1.0
      EMIN2=E(10)
      EMAX2=E(499)
      GO TO 164
 153  FLAG=0.0
C
C FIND THE LOWEST ENERGY PEAK BY CYCLING EKLM(N)
C
   50 DO 51 N=NCHN,500
      IF (N.GT.498) GO TO 99
      IF (NCHN.GE.500) GO TO 99
      IF(EKLM(N).GT.1.5)  GO TO 59
      GO TO 51
```

```
   59   MM=N
        GO TO 60
 51     CONTINUE
 60     NCHN=N+1
C
C DEFINE WIDTH OF DISPLAY WINDOW --SET LIMITS BASED ON PEAK
C WIDTH OR RESLVE LIMIT WHICH EVER IS LARGEST
C
        EN=E(N)*1000.
        EMIN=EN-4*SIGMA(EN,0.)
        EMAX=EN+4*SIGMA(EN,0.)
        M=MM
   55   MIN=M-1
        IF(P(MIN).LE.RESLVE) GO TO 56
        M=M-1
        GO TO 55
 56     M=MM
 57     MAX=M+1
        IF(P(MAX).LE.RESLVE) GO TO 58
        M=M+1
        GO TO 57
 58     EMIN=AMIN1(EMIN,E(MIN)*1000.)
        EMAX=AMAX1(EMAX,E(MAX)*1000.)
        IF(EMIN.LE.(EN-700.)) EMIN=EN-700.
C
C SET UP STARTING POINTS FOR PLOT
C
        EMIN2=(INT(EMIN/100.)-1.)/10.
C        EMAX2=(INT(EMAX/100.)+1.)/10.
        IF (EMIN2.LE.EMAX1) EMIN2=EMAX1
        EMAX2=EMIN2 +70.*IRES/1000.
 89     NMIN=ICHN (EMIN2,IRES)
        NMAX=ICHN(EMAX2,IRES)
        NPT=NMAX-NMIN
        IF(NPT.GE.76) GO TO 87
        GO TO 88
 87     CONTINUE
        EMAX2=EMIN2+70.*IRES/1000.
        GO TO 89
C
C COPY SUBSETS OF P AND E ARRAYS FOR PLOTTING
C
 88     CALL XCPY(P,SUBP,NMIN,1,NPT,1,500,1,0)
        CALL XCPY(E,SUBE,NMIN,1,NPT,1,500,1,0)
        SUBP(1)=SCALEN(NMIN,NMAX)
        SUBP(NPT)=0.
D       CALL ERASE
        CALL CRTPLT  (150.,265.,SUBE,SUBP,NPT,-5,0,1.,1.,SUBE,SUBP,NPT)
C
C COPY IDENTIFICATION K-L-M MARKERS WITHIN WINDOW AND PLOT
C
```

```
      CALL XCPY(EKLM,SUBID,NMIN,1,NPT,1,500,1,0)
D     CALL CRTPLT(150.,265.,SUBE,SUBID,NPT,1,1,1.,1.,SUBE,SUBP,NPT)
D      CALL PLOT (0.,767.,0)
      IF (MFLAG.EQ.-1) GO TO 157
C
C ORDER PEAKS WITHIN  WINDOW BY PEAK HEIGHT FOR EVENTUAL
C GAUSSIAN FITTING  MOST INTENSE PEAK FIRST
C NP=NUMBER OF PEAKS IN THE WINDOW
C PN=PEAK NUMBER OF THE FIRST PEAK IN THE WINDOW
C
      NP=0.
 161   AM=2.0
      JN=0
      DO 162 J=1,NPT
      AM=AMAX1(AM,SUBID(J))
      IF(SUBID(J).GE.AM) JN=J
 162  CONTINUE
      IF(JN.LE.0.5) GO TO 163
      IPN=PN+NP
      AEN(IPN)=SUBE(JN)
      AHT(IPN)=SUBID(JN)
      SUBID(JN)=1.0
      NP=NP+1
      GO TO 161
 163  IPN=PN
      IFPN=IPN+NP-1
 157  WRITE(7,63)   NP,EMIN2,EMAX2
 63   FORMAT(27(/),X,I2,' PEAK(S) HAVE BEEN IDENTIFIED BETWEEN' ,
     C1F5.2,'  TO ' ,1F5.2, '  KEV' )
C
C WRITE OUT WHICH PEAKS HAVE BEEN PREVIOUSLY IDENTIFIED
C
      Z=0.
 64   FORMAT (X,2(A2,2X),2X,1F7.4,' KEV' )
 164  DO 65 I=1,NPK
      ATOM=CS(NUM(I))
D      IF((EKA(I).GE.EMIN2).AND.(EKA(I).LE.EMAX2).
D     CAND.(EKLM(ICHN(EKA(I),IRES)).GE.2.))
D     CWRITE(7,64)   ATOM,ALNID(1),EKA(I)
D      IF((EKB(I).GE.EMIN2).AND.(EKB(I).LE.EMAX2).
D     CAND.(EKLM(ICHN(EKB(I),IRES)).GE.2.))
D     CWRITE(7,64)   ATOM,ALNID(2),EKB(I)
D      IF((ELA(I).GE.EMIN2).AND.(ELA(I).LE.EMAX2).
D     CAND.(EKLM(ICHN(ELA(I),IRES)).GE.2.))
D     CWRITE(7,64)   ATOM,ALNID(3),ELA(I)
D      IF((ELB(I).GE.EMIN2).AND.(ELB(I).LE.EMAX2).
D     CAND.(EKLM(ICHN(ELB(I),IRES)).GE.2.))
D     CWRITE(7,64)   ATOM,ALNID(4),ELB(I)
D      IF((EMA(I).GE.EMIN2).AND.(EMA(I).LE.EMAX2).
D     CAND.(EKLM(ICHN(EMA(I),IRES)).GE.2.))
D     CWRITE(7,64)   ATOM,ALNID(5),EMA(I)
```

```
D      IF((EMB(I).GE.EMIN2).AND.(EMB(I).LE.EMAX2).
D     CAND.(EKLM(ICHN(EMB(I),IRES)).GE.2.))
D     CWRITE(7,64)    ATOM,ALNID(6),EMB(I)
 65     CONTINUE
D      WRITE(7,651)
 651    FORMAT($,X,'DO YOU WANT TO ELIMINATE A PEAK? YES-NO',2X)
       READ(5,3)    X
       IF (X.EQ.YN) GO TO 107
D      WRITE(7,652)
 652     FORMAT($,X,'ENTER THE PEAK ENERGY IN -KEV-',2X)
       IF(X.EQ.YY) Z=1.
       READ(5,300)    X
 300    FORMAT(1F7.5)
       EKLM(ICHN(X,IRES))=1.0
       GO TO 65
 107   CONTINUE
       IF (MFLAG.EQ.-1) GO TO 159
       IF(FLAG.GE.0.5) GO TO 153
 159    WRITE(7,653)
 653    FORMAT($,X,'DO YOU WANT TO CHANGE WINDOW WIDTH? YES-NO',2X)
       READ(5,3)    X
       IF(X.EQ.YN) GO TO 106
D       WRITE(7,654)
 654    FORMAT(X,'SET NEW LIMITS EMIN,EMAX' )
       CALL CRSSHR(X,Y)
       CALL TRANXY(X,Y,EMIN2,Y)
       CALL CRSSHR(X,Y)
       CALL TRANXY(X,Y,EMAX2,Y)
       GO TO 89
 106   CONTINUE
       IF(MFLAG.EQ.-1) GO TO 158
       IF(Z.EQ.1) GO TO 88
       FN=IFPN+1
       NCHN=ICHN(EMAX2,IRES) +1
 158    IF (MFLAG.EQ.-1) MFLAG=0
       EMIN1=EMIN2
       EMAX1=EMAX2
       RETURN
 99     FLAG=9997.
       RETURN
       END
```

```
      SUBROUTINE GAUSS
      COMMON P(502),E(502),BG(502),EKLM(502),SUBID(76)
      COMMON SUBP(76),SUBE(76),AEN(30),AHT(30),AEL(31),AINT(30)
      COMMON SUME(760),SUMP(760),SUMID(760),ABG(30)
      COMMON ITAPE(72),INAME(72),YY,YN,
     1EKA(20),EKB(20),ELA(20),ELB(20),EMA(20),EMB(20),NUM(20)
      COMMON /ELEMNT/ CS(100),ALNID(6)
      COMMON /EDSVRB/IRES,CO,CI,NPK,THICK,SYMBOL,Z,
     1EMAX,EMIN,MFLAG,BL1,BU1,BL2,BU2,BL3,BU3,AAA,BBB,CCC,EKABS,ELABS,
     2EMABS,EABS,BGL,BGU,LBGL,LBGU,S1,S2,R,SABS,EN,RR,RESLVE,FLAG,
     3EMIN2,EMAX2,EMIN1,EMAX1,NCHN,PN,MM,M,MIN,MAX,NMIN,NMAX,NPT,NP,AM,
     4IPN,IFPN,ATOM,NPTS,LAST,BRCKET,FF,ABSFF,CC,EL,EU,PB
C
C BEGIN GAUSSIAN FITTING : NOTE THAT THERE ARE 6 ITERATIONS FOR THE FIT
C IPN=PEAK NUMBER OF THE FIRST PEAK IN THE WINDOW
C NP=NUMBER OF PEAKS IN THE WINDOW
C NPT= NUMBER OF DATA POINTS IN THE WINDOW
C
 166  CALL MLTFIT(IPN,NP,NPT)
C
C    PLOT FITTED CURVES
C
      NPTS=NPT*10
      LAST=NPTS+1
      DO 66 I=1,LAST
      SUME(I)=EMIN2+(I-1)*(EMAX2-EMIN2)/NPTS
       SUMID(I)=0.
 66    CONTINUE
      DO 68 I=IPN,IFPN
      DO 69 J=1,LAST
      BRCKET=(SUME(J)-AEN(I))*1000./SIGMA(AEN(I)*1000,AEL(31))
      SUMP(J)=AHT(I)*EXP(-BRCKET**2./2.)
      SUMID(J)=SUMID(J)+SUMP(J)
      FF=SUME(J)*1000.
      CALL MASSAB(FF,ABSFF)
      CC=(EO-FF)/FF
      BG(J)=(AAA*CC**2.+BBB*CC+CCC)*EXP(ABSFF)
 69   CONTINUE
      IF (I.GE.(IPN+1)) GO TO 169
      CALL CRTPLT(150.,265.,SUBE,SUBP,NPT,-5,0,1.,1.,SUBE,SUBP,NPT)
 169  CALL CRTPLT(150.,265.,SUME,SUMP,NPTS,1,1,1.,1.,SUBE,SUBP,NPT)
      EL=(AEN(I)*1000-(2.355*SIGMA(AEN(I)*1000,AEL(31)))/2.)*.001
      EU=(AEN(I)*1000+(2.355*SIGMA(AEN(I)*1000,AEL(31)))/2.)*.001
      AINT(I)=0.
      ABG(I)=0.
C IN ORDER TO GET AN INTEGRAL RATHER THAN SUM MULTIPLY
C SUMP(J) AND BG(J) BY THE FACTOR AH=(EMAX2-EMIN2)*1000/NPTS
C IN LINES 579-580
      DO 70 J=1,LAST
      IF((SUME(J).LE.EL).OR.(SUME(J).GE.EU)) BG(J)=0.
      IF((SUME(J).LE.EL).OR.(SUME(J).GE.EU)) SUMP(J)=0.
```

```
      IF(INT((J-1)/10.).EQ.((J-1)/10.)) AINT(I)=AINT(I)+SUMP(J)
      IF(INT((J-1)/10.).EQ.((J-1)/10.)) ABG(I)=ABG(I)+BG(J)
 70   CONTINUE
      CALL CRTPLT(150.,265.,SUME,SUMP,NPTS,1,1,1.,1.,SUBE,SUBP,NPT)
 68    CONTINUE
      CALL PLOT(0.,180.,0)
      PAUSE 'HIT RETURN TO CONTINUE'
       IF(NP.LE.1) GO TO 67
D      CALL ERASE
       CALL CRTPLT(150.,265.,SUBE,SUBP,NPT,-5,0,1.,1.,SUBE,SUBP,NPT)
      CALL CRTPLT(150.,265.,SUME,SUMID,NPTS,1,1,1.,1.,SUBE,SUBP,NPT)
D      CALL PLOT (0.,180.,0)
      PAUSE 'HIT RETURN TO CONTINUE'
 67    CONTINUE
      CALL PLOT(0.,155.,0)
      WRITE(7,800)
 800   FORMAT($,X,' IS THE FIT SATISFACTORY? Y-N  ')
      READ(5,799) X
 799   FORMAT(1A1)
      IF(X.EQ.YY) GO TO 801
      CALL PLOT(0.,155.,0)
      WRITE(7,802)
 802   FORMAT(35X,'PEAK NO.',2X,'ENERGY',2X,'STND DEV ',2X,'COUNTS')
      DO 803 I=IPN,IFPN
      WRITE(7,804) I,AEN(I),AEL(I),AHT(I)
 804  FORMAT(39X,I2,4X,1F6.3,5X,1F6.2,2X,1F8.1,/,$,X,'ENTER NEW VALUES:'
     1,' ENERGY,STND DEV,COUNTS:',4X)
      READ(5,805) AEN(I),AEL(I),AHT(I)
 805   FORMAT(3F10.0)
 803   CONTINUE
       AEL(31)=(AEL(IPN)*2.35482)**2.-AEN(IPN)*3489.25-25000.6
 809       CALL ERASE
      WRITE(7,806)
 806  FORMAT($,' ITERATE NEW VALUES? Y-N  ')
      READ(5,799) X
      IF(X.EQ.YY) GO TO 850
      IF(X.EQ.YN) GO TO 66
      GO TO 809
 850   MFLAG=-1
 801   CONTINUE
D      CALL ERASE
C
C RETURN TO SEARCH TO FIND NEXT PEAK AND REPEAT ABOVE UNTIL
C ALL IDENTIFIED K-L-M PEAKS HAVE BEEN ANALYSED
      FLAG=9999.
      RETURN
      END
```

APPENDIX B

Subroutine Library – NXRYL

Function ATOMNR

Function ATOMWT

Function ENERGY

Function EDGE

Function YIELD

Function BETA

Function CROSS

Function GEN

Function ABGEN

Function FWHM

Function SIGMA

Subroutine PARAM

Subroutine MASSAB

Subroutine QATR

Subroutine BKSCTR

Subroutine KWBGND

Subroutine KBGND

Subroutine MSUB

Subroutine XCPY

Subroutine LOC

Subroutine NEGTVE

Subroutine MLTFIT

Subroutine CHIMIN

Subroutine CHISQ

Subroutine BGRND1

Subroutine BGRND2

Function ICHN

Function CONV

Function SCALEN

APPENDIX B

Subroutine Library – NXRYL

This appendix contains a listing of a general x-ray analysis subroutine library common to the programs NEDS, NXRYRT, and NMCS, as well as important subroutines dealing with the various calculations presented in this research. For example, the calculation of the angular distribution of continuum intensity or the functional dependence of the theoretical peak-to-background ratio for thin foils can be duplicated by reference to these subroutines and Eqs. (2.47) through (2.51).

```
      FUNCTION ATOMNR(SYMBOL)
C
C OUTPUTS ATOMIC NUMBER OF ELEMENT WHICH CORRESPONDS TO SYMBOL
C
      DIMENSION SS(18),NUM(18)
      COMMON /ELEMNT/ CS(100),ALNID(6)
      DATA CS/' H','HE','LI','BE',' B',' C',' N',' O',' F','NE'
     1,'NA','MG','AL','SI',' P',' S','CL','AR',' K','CA','SC','TI',
     2' V','CR','MN','FE','CO','NI','CU','ZN','GA','GE','AS','SE',
     3'BR','KR','RB','SR',' Y','ZR','NB','MO','TC','RU','RH','PD',
     4'AG','CD','IN','SN','SB','TE',' I','XE','CS','BA','LA','CE',
     5'PR','ND','PM','SM','EU','GD','TB','DY','HO','ER','TM','YB',
     6'LU','HF','TA',' W','RE','OS','IR','PT','AU','HG','TL','PB',
     7'BI','PO','AT','RN','FR','RA','AC','TH','PA',' U','NP','PU',
     8'AM','CM','BK','CF','ES','FM'/
      DATA ALNID/'KA','LA','MA','KB','LB','MB'/
      DATA SS/'NO','H   ','B ','C ','N ','O ',
     9'F ','P ','S ','A ','K ','V ','Y ','I ','W ','U ',' A','CB' /
     9,NUM/1000,1,5,6,7,8,9,15,16,18,19,23,39,53,74,92,18,41/
      DO 1 I=1,100
      IF(SYMBOL-CS(I))1,5,1
1     CONTINUE
      DO 2 I=1,18
      IF (SYMBOL-SS(I))2,4,2
2     CONTINUE
        WRITE(7,3) SYMBOL
3      FORMAT (30X,'THE ELEMENT ',A2,' DOES NOT EXIST')
      GO TO 7
4     SYMBOL=CS(NUM(I))
      I=NUM(I)
5     ATOMNR=I
      GO TO 6
7     ATOMNR=0
6     RETURN
      END




      FUNCTION ATOMWT(Z)
C OUTPUTS ATOMIC WEIGHT OF ELEMENT Z
C
C
      DIMENSION A(100)
      DATA A/1.008,4.003,6.939,9.012,10.811,12.011,14.007,15.999,18.998
     120.183,22.990,24.312,26.982,28.086,30.974,32.064,35.453,39.948,
     239.102,40.080,44.956,47.900,50.942,51.996,54.938,55.847,58.933,
     358.710,63.540,65.370,69.720,72.590,74.922,78.960,79.909,83.800,
     485.470,87.620,88.905,91.220,92.906,95.940,99.000,101.070,102.905,
```

```
5106.400,107.870,112.400,114.820,118.690,121.750,127.600,126.904,
6131.300,132.905,137.340,138.910,140.120,140.907,144.240,147.000,
7150.350,151.960,157.250,158.924,162.500,164.930,167.260,168.934,
8173.040,174.970,178.490,180.948,183.850,186.200,190.200,192.200,
9195.090,196.967,200.590,204.370,207.190,209.980,210.000,210.000,
1222.000,223.000,226.000,227.000,232.038,231.000,238.030,237.000,
2244.000,243.000,247.000,247.000,251.000,254.000,253.000/
 I=Z
 ATOMWT=A(I)
 RETURN
 END



      FUNCTION ENERGY(Z,L)
C
C OUTPUTS ENERGY OF XRAY LINE OF ELEMENT Z, IF L=1,2,3,4,5,6
C THEN OUTPUTS KA,LA,MA,KB,LB,MB LINES RESPECTIVELY
C OUTPUTS ENERGY IN -KEV-
      GO TO (1,3,5,8,10,12),L
   1  IF(Z-3.)7,2,2
 2     WAVE=1./(-1.6745699E-03+Z*(-6.8467562E-05+Z*(6.281489E-04+
     1Z*(1.0809595E-05+Z*(-3.027904E-07+Z*(4.6637467E-09-2.6734801E-11
     2*Z))))))
       ENERGY=12.37788/WAVE
       RETURN
 3     IF(Z-8.)7,4,4
  4    WAVE=1./(1.9140411E-02+Z*(-3.8046413E-03+Z*(2.6884465E-04+
     1Z*(-3.9334536E-06+Z*(6.4498238E-08+Z*(-5.1038884E-10+
     2Z*1.582812E-12))))))
       ENERGY=12.37788/WAVE
       RETURN
 5     IF(Z-40.)7,6,6
 6     WAVE=1./(-.4326787+Z*(.023126494+Z*(-4.6580727E-04+
     1Z*(4.6345531E-06-1.5432413E-08*Z))))
       ENERGY=12.37788/WAVE
       RETURN
 7     ENERGY=0.
       RETURN
 8     IF(Z-11.)7,9,9
 9     WAVE=1./(1.90599E-2-Z*(6.072234E-3-Z*(1.194595E-3-Z*(9.651631
     1E-6-Z*(1.802092E-7-Z*1.037428E-9)))))
       ENERGY=12.37788/WAVE
       RETURN
10      IF(Z-20.)7,11,11
11      WAVE=1./(-2.535951E-2+Z*(2.33104E-3-Z*(6.181201E-5-Z*(4.97452E
     1-6-Z*(6.023248E-8-Z*(4.04167E-10-Z*8.23965E-13))))))
       ENERGY=12.37788/WAVE
       RETURN
12       IF(Z-50.)7,13,13
```

```
13    WAVE=1./(1.172996E-1-Z*(9.385426E-3-Z*(2.797442E-4-Z*(3.80862
     19E-6-Z*(2.812141E-8-Z*8.4532E-11)))))
      ENERGY=12.37788/WAVE
      RETURN
      END



      SUBROUTINE MASSAB(E,ABS)
C
C CALCUALTE MASS.ABS. COEFF FOR 0.7 - 20. KEV XRAYS
C TO CORRECTION FOR ABSORPTION EFFECTS DUE TO DETECTORS
C BE WINDOW, AU LAYER, AND SI DEAD LAYER
C THICKNESS USED = MANUFACTURERS SPECIFICATIONS
C INPUT ENERGY IN KEV;ABS= SUM(U(E).T)
C
      WL=12.3779/E
      ABE=0.350*WL**2.86
      IF (WL.LE.6.745) GO TO 50
      ASI=1.54*WL**2.73
      GO TO 51
 50   ASI=18.5*WL**2.77
 51     IF(WL.LE.0.863) GO TO 54
      IF((WL.GE.0.863).AND.(WL.LE.0.903))GO TO 55
      IF ((WL.GE.0.903).AND.(WL.LE.1.04))GO TO56
      IF((WL.GE.1.04).AND.(WL.LE.3.62)) GO TO 57
      IF((WL.GE.3.62).AND.(WL.LE.3.939))GO TO 58
      IF((WL.GE.3.939).AND.(WL.LE.4.522)) GO TO 59
      IF((WL.GE.4.522).AND.(WL.LE.5.415))GO TO 80
      IF ((WL.GE.5.415).AND.(WL.LE.6.157))GO TO 61
      IF ((WL.GE.6.157).AND.(WL.LE.8.3401)) GO TO 62
      AAU=20.1*WL**2.2
      GO TO 63
 54   AAU=272.*WL**2.59
      GO TO 63
 55   AAU=232.*WL**2.80
      GO TO 63
 56   AAU=167.*WL**2.80
      GO TO 63
 57   AAU=67.64*WL**2.80
      GO TO 63
 58   AAU=58.3*WL**2.80
      GO TO 63
 59   AAU=48.3*WL**2.80
      GO TO 63
 80   AAU=41.8*WL**2.80
      GO TO 63
 61   AAU=22.5*WL**2.2
      GO TO 63
 62   AAU=21.*WL**2.2
```

```
63    AAU=-AAU*38.6E-06
      ASI=-ASI*2.33E-05
      ABE=-ABE*1,4097E-03
      ABS=AAU+ASI+ABE
      RETURN
      END



      FUNCTION EDGE(Z,N)
C
C THIS FUNCTION CALCULATES THE WAVELENGTH OF CHARACTERISTIC
C ABSORPTION EDGE OF ELEMENTZ, N=1-9 CORRESPONDS TO K,L1,L2,L3,M1,M2,M3,
C M4,M5   WAVELENGTH IN ANGSTROMS.
      GO TO (1,2,3,4,5,6,7,8,9,10),N
 1    EDGE=-1.3047E-2+Z*(6.0888E-3-Z*(5.5706E-4-Z*(1.1428E-4
     1-Z*(4.3872E-6-Z*(8.3315E-8-Z*6.1105E-10)))))
      GO TO 11
 2    EDGE=1.3466E-2-Z*(2.9704E-3-Z*(2.801E-4-Z*(7.1603E-6-Z*(2.E-7
     1-Z*(2.2743E-9-Z*9.7452E-12)))))
      GO TO 11
 3    EDGE=-3.5441E-2+Z*(5.6833E-3-Z*(3.1012E-4-Z*(1.1498E-5
     1-Z*(1.1217E-7-Z*(3.6034E-10+Z*9.0739E-13)))))
      GO TO 11
 4    EDGE=-9.3211E-2+Z*(1.5753E-2-Z*(9.5002E-4-Z*(3.1576E-5
     1-Z*(4.492E-7-Z*(3.1953E-9-Z*8.9014E-12)))))
      GO TO 11
 5    EDGE=-.54974+Z*(6.8436E-2-Z*(3.3998E-3-Z*(8.6866E-5-Z*(1.1779E-6
     1-Z*(8.2E-9-Z*2.2796E-11)))))
      GO TO 11
 6    EDGE=-.64464+Z*(7.7538E-2-Z*(3.74E-3-Z*(9.2964E-5-Z*(1.2345E-6-
     1-Z*(8.4477E-9-Z*2.3158E-11)))))
      GO TO 11
 7    EDGE=-.97256+Z*(.1103-Z*(5.0823E-3-Z*(1.221E-4-Z*(1.5894E-6
     1-Z*(1.0735E-8-Z*2.933E-11)))))
      GO TO 11
 8    EDGE=-.98122+Z*(.109385-Z*(4.9342E-3-Z*(1.1555E-4-Z*(1.4681E-6
     1-Z*(9.6993E-9-Z*2.5961E-11)))))
      GO TO 11
 9    EDGE=-.73755+Z*(8.2784E-2-Z*(3.7622E-3-Z*(8.8875E-5-Z*(1.1372E-6
     1-Z*(7.5702E-9-Z*2.0419E-11)))))
      GO TO 11
10    EDGE=6.2696E-2-Z*(7.5868E-3-Z*(3.5136E-4-Z*(8.2023E-6
     1-Z*(1.0477E-7-Z*(6.6909E-10-Z*1.7612E-12)))))
11    EDGE=1./EDGE
      IF(N-1) 12,12,15
 12    IF(Z-57.) 15,15,13
13    EDGE=0.00000001
14    RETURN
```

```
 15    IF(EDGE) 16,14,17
 16    EDGE=999.
 17    IF(EDGE-999.) 18,14,16
 18    IF(Z-2.*(2*N-1)) 16,16,14
       RETURN
       END
C
C
C
       FUNCTION YIELD(Z,L)
C THIS FUNCTION CALCULATES THE FLUORESCENCE YIELD OF ELEMENT Z FOR
C LINE L
       GO TO (1,2,3,1,2,3),L
 1     D=-0.037948+Z*(0.034256-Z*Z*0.116342E-05)
       GO TO 4
 2     D=-0.111065+Z*(0.013680-Z*Z*0.217720E-06)
       GO TO 4
 3     D=-0.00036+Z*(0.00386+Z*Z*0.20101E-06)
 4     D=D**4.
       YIELD=D/(1.+D)
       RETURN
       END



       FUNCTION BETA(Z,J)
C THIS FUNCTION CALCULATES THE RATION BETA/ALPHA LINE
C INTENSITY RATION FOR ELEMENT Z LINE J
       GOTO(1,4,5,1,4,5),J
 1     IF(Z-17.) 3,2,2
 2       X=ALOG(Z)
       BETA=-14.695958+X*(15.603086+X*(-6.2366705+X*
      1(1.1166658-X*0.074854434)))
       RETURN
 3     BETA=0.01
       RETURN
 4     BETA=-0.015+0.00575*Z
       RETURN
 5     BETA=0.5
       RETURN
       END


 SUBROUTINE PARAM(EO,EC,L,ZR,RO,RB,AN,DEN,W,F,S,ABSC,TH,CP,ATW,BE)
 COMMON P(16)
 P(1)=EO
 P(2)=ZR
 P(3)=EC
 P(4)=RB
 P(5)=1.-RO/RB
```

```
      P(6)=AN
      P(7)=DEN
      P(8)=W
      P(9)=F
      P(10)=S
      P(11)=ABSC
      P(12)=TH
      P(13)=CP
      P(14)=ATW
      P(15)=BE
      P(16)=L
      RETURN
      END



      FUNCTION CROSS(TYPE,Z,EO,EC,L)
C CALCULATE THE IONIZATION CROSS SECTION FOR THE GIVEN PARA.
C       IF TYPE=0. CLASSICAL CROSS SECTION USED FOR MICROPROBE
C                    WITH CORRECTIONS BY MOTT&MASSEY,BURHOP,
C                   & WORTHINGTON & TOMLIN
C       IF TYPE=1. MODIFIED BY ZALUZEC TO ACCOUNT FOR RELATIVITY
C                   BY CHANGING CONSTANTS (EMPIRICAL FIT)
C IF L=1 CALCULATE K SHELL CROSS SECTION
C IF L=2 CALCULATE L SHELL CROSS SECTION
C BK=CONSTANT RELATED TO RADIUS OF SHELL
C NZ=NUMBER OF ELECTRONS IN FULL SHELL
C Z=REDUCED PATHLENGTH PARAMETER =FRACTION OF ELECTRON RANGE
C EO= INCIDENT ENERGY (KEV)
C EC= CRITICAL EXCITATION ENERGY(KEV)
C
C

      AK=6.4924E-20
      IF(L.EQ.1) BK=0.35
      IF(L.EQ.2) BK=0.25
      IF(L.EQ.1) NZ=2
      IF(L.EQ.2) NZ=8
      EZ=EO*(1.-Z)**0.667
      IF (EZ.LE.EC) GO TO 9
      BT=1.-(1./(1.+EZ/511.))**2.
      BZ=(1.65 +2.35*EXP(1.-EZ/EC))
      IF (TYPE.EQ.0) BT=0.
      UZ=EZ/EC
      IF(TYPE.EQ.1.) BZ=(5.*(1.-EXP(-EC/2.))/UZ)*
        (1.-EXP(-(1250/EC)/(UZ)**2.))
```

```
      CROSS=AK*BK*NZ*(ALOG(4.*EZ/(BZ*EC))-ALOG(1.-BT)-BT)/(EC*EZ)
       RETURN
9      CROSS=0.
      RETURN
      END


      FUNCTION GEN(T)
      COMMON P(16)
      Z=1.E04*T/P(2)
      QZ=CROSS(1.,Z,P(1),P(3),P(16))
      RZ=P(4)*(1.-P(5)*EXP(-P(10)*P(7)*Z/4.))
      IF (RZ.EQ.0.) RZ=1.
      ZN=EXP(-P(10)*P(7)*Z)
      GEN=0.005625*QZ*RZ*ZN*P(6)*P(7)*P(8)*P(9)*P(13)/P(14)
      RETURN
      END


         FUNCTION ABGEN(T)
         COMMON P(16)
         Z=1.E04*T/P(2)
         BE=P(15)/57.295779
         TH=P(12)/57.295779
         CORR=SIN(BE)/SIN(TH)
         AZ=EXP(-P(11)*P(7)*CORR*Z)
         ABGEN=GEN(T)*AZ
         RETURN
         END
C
CC    ..................................................................
CC
CC       SUBROUTINE QATR
CC
CC       PURPOSE
CC          TO COMPUTE AN APPROXIMATION FOR INTEGRAL(FCT(X), SUMMED
CC          OVER X FROM XL TO XU).
CC
CC       USAGE
CC          CALL QATR (XL,XU,EPS,NDIM,FCT,Y,IER,AUX)
CC        . PARAMETER FCT REQUIRES AN EXTERNAL STATEMENT.
CC
CC       DESCRIPTION OF PARAMETERS
CC          XL      -',THE LOWER BOUND OF THE INTERVAL.
CC          XU      - THE UPPER BOUND OF THE INTERVAL.
CC          EPS     - THE UPPER BOUND OF THE ABSOLUTE ERROR.
CC          NDIM    - THE DIMENSION OF THE AUXILIARY STORAGE ARRAY AUX.
CC                    NDIM-1 IS THE MAXIMAL NUMBER OF BISECTIONS OF
CC                    THE INTERVAL (XL,XU).
CC          FCT     - THE NAME OF THE EXTERNAL FUNCTION SUBPROGRAM USED.
C           Y       - THE RESULTING APPROXIMATION FOR THE INTEGRAL VALUE.
```

```
C            IER    - A RESULTING ERROR PARAMETER.
C            AUX    - AN AUXILIARY STORAGE ARRAY WITH DIMENSION NDIM.
C
C        REMARKS
C           ERROR PARAMETER IER IS CODED IN THE FOLLOWING FORM
C           IER=0  - IT WAS POSSIBLE TO REACH THE REQUIRED ACCURACY.
C                    NO ERROR.
C           IER=1  - IT IS IMPOSSIBLE TO REACH THE REQUIRED ACCURACY
C                    BETACAUSE OF ROUNDING ERRORS.
C           IER=2  - IT WAS IMPOSSIBLE TO CHECK ACCURACY BETACAUSE NDIM
C                    IS LESS THAN 5, OR THE REQUIRED ACCURACY COULD NOT
C                    BETA REACHED WITHIN NDIM-1 STEPS. NDIM SHOULD BETA
C                    INCREASED.
C
C        SUBROUTINES AND FUNCTION SUBPROGRAMS REQUIRED
C           THE EXTERNAL FUNCTION SUBPROGRAM FCT(X) MUST BETA CODED BY
C           THE USER. ITS ARGUMENT X SHOULD NOT BETA DESTROYED.
C
C        METHOD
C           EVALUATION OF Y IS DONE BY MEANS OF TRAPEZOIDAL RULE IN
C           CONNECTION WITH ROMBERGS PRINCIPLE. ON RETURN Y CONTAINS
C           THE BETAST POSSIBLE APPROXIMATION OF THE INTEGRAL VALUE AND
C           VECTOR AUX THE UPWARD DIAGONAL OF ROMBERG SCHEME.
C           COMPONENTS AUX(I) (I=1,2,...,IEND, WITH IEND LESS THAN OR
C           EQUAL TO NDIM) ECOME APPROXIMATIONS TO INTEGRAL VALUE WITH
C           DECREASING ACCURACY BY MULTIPLICATION WITH (XU-XL).
C           FOR REFERENCE, SEE
C           (1) FILIPPI, DAS VERFAHREN VON ROMBERG-STIEFEL-BAUER ALS
C               SPEZIALFALL DES ALLGEMEINEN PRINZIPS VON RICHARDSON,
C               MATHEMATIK-TECHNIK-WIRTSCHAFT, VOL.11, ISS.2 (1964),
C               PP.49-54.
C           (2) BAUER, ALGORITHM 60, CACM, VOL.4, ISS.6 (1961), PP.255.
C
C     ..................................................................
C
      SUBROUTINE QATR(XL,XU,EPS,NDIM,FCT,Y,IER,AUX)
C
C
      DIMENSION AUX(1)
C
C     PREPARATIONS OF ROMBERG-LOOP
      AUX(1)=.5*(FCT(XL)+FCT(XU))
      H=XU-XL
      IF(NDIM-1)8,8,1
    1 IF(H)2,10,2
C
C     NDIM IS GREATER THAN 1 AND H IS NOT EQUAL TO 0.
    2 HH=H
      E=EPS/ABS(H)
      DELT2=0.
      P=1.
```

```
      JJ=1
      DO 7 I=2,NDIM
      Y=AUX(1)
      DELT1=DELT2
      HD=HH
      HH=.5*HH
      F=.5*F
      X=XL+HH
      SM=0.
      DO 3 J=1,JJ
      SM=SM+FCT(X)
    3 X=X+HD
      AUX(I)=.5*AUX(I-1)+F*SM
C     A NEW APPROXIMATION OF INTEGRAL VALUE IS COMPUTED BY MEANS OF
C     TRAPEZOIDAL RULE.
C
C     START OF ROMBERGS EXTRAPOLATION METHOD.
      Q=1.
      JI=I-1
      DO 4 J=1,JI
      II=I-J
      Q=Q+Q
      Q=Q+Q
    4 AUX(II)=AUX(II+1)+(AUX(II+1)-AUX(II))/(Q-1.)
C     END OF ROMBERG-STEP
C
      DELT2=ABS(Y-AUX(1))
      IF(I-5)7,5,5
    5 IF(DELT2-E)10,10,6
    6 IF(DELT2-DELT1)7,11,11
    7 JJ=JJ+JJ
    8 IER=2
    9 Y=H*AUX(1)
      RETURN
   10 IER=0
      GO TO 9
   11 IER=1
      Y=H*Y
      RETURN
      END


      SUBROUTINE BKSCTR(ZAV,EO,ECA,RO,RB)
C     THIS SUBROUTINE CALCULATES THE ELECTRON SCATTERING
C     CORRECTION FACTORS TO X-RAY CALCULATIONS
C     AS DERIVED BY REUTER
      ETA=-0.0254+0.016*ZAV-1.86E-04*ZAV**2.+8.3E-07*ZAV**3.
      RO=1.+2.8*(1.-.9*(ECA/EO))*ETA
      RB=3.+4.05E-10*ZAV**5.
      RETURN
      END
```

```
      FUNCTION FWHM(ENZ)
C     THIS FUNCTION CALCULATES THE FWHM OF AN XRAY PEAK
C     DUE TO DETECTOR BROADENING
C     ENZ=ENERGY OF XRAY LINE IN KEV
C      RESULT FWHM IN KEV
      FWHM=SQRT(ENZ*3489.25 +28000.)/1000.
      RETURN
      END




      SUBROUTINE KWBGND(Z,EO,E,DE,ANGLE,BG)
C     CALCULATE BGRND INTENSITY FROM K&W EQUATIONS
C Z=ATOMIC NUMBER
C EO=INCIDENT ENERGY
C E= CONTINUUM ENERGY
C DE =CONTINUUM ENERGY WINDOW ABOUT E
C
C      SPECIAL NOTE ALL ENERGY IN UNITS OF -EV-
C
C ANGLE= ANGLE FROM INCIDENT BEAM DIRECTION (FORWARD=0.0 DEGREES)
C NOTE THAT K& W USE GAUSSIAN UNITS MUST DIVIDE E BY 300.
C ALSO MUST DIVIDE THEIR Q BY E*H TO GET CORRECT UNITS
C
C UNITS ON Q ARE NOW      CM**2./(STERADIAN*ATOM)
C
C
      ZC=EO/(300.*Z**2.)
      U=E/EO
      Y3=-0.00259+0.00776/(ZC+.116)
      Y2=0.067+0.023/(ZC+.75)
      Y1=0.22*(1.-0.39*EXP(-26.9*ZC))
      YH=(-0.214*Y1 + 1.21*Y2-Y3)/(1.43*Y1-2.43*Y2+Y3)
      YJ=(1.+2.*YH)*Y2-2.*(1.+YH)*Y3
      YK=(1.+YH)*(Y3+YJ)
      YI=(-YJ+YK/(U+YH))/ZC
      A=EXP(-0.223*ZC)-EXP(-57.*ZC)
      B=EXP(-0.0828*ZC)-EXP(-84.9*ZC)
      AA=1.47*B-0.507*A-0.833
      BB=1.70*B-1.09*A-0.627
      XI=(0.252+AA*(U-0.135)-BB*(U-0.135)**2)/ZC
      BT=SQRT(1.-(1./(EO/5.11E05+1))**2.)
      THETA=ANGLE/57.295779
      S=(SIN(THETA))**2/(1.-BT*COS(THETA))**4
      C=1.+ (COS(THETA))**2/(1.-BT*COS(THETA))**4
      BG=(XI*S+YI*C)*DE/E
```

```
C
C MULTIPLE BY CONVERSION FACTOR
C     10**-50./(1.6021E-12 ERGS/EV *4.136E-15 EV SEC)
C
C     10**-50.= K& W CONSTANT
C
C
      DC=DC*1.5091E-24
      RETURN
      END



      SUBROUTINE KBGND(ZAV,EO,E,DE,BG)
C       CALCULATE BGRND INTENSITY FROM KRAMERS EQUATION
C ZAV= ATOMIC NUMBER OF MATRIX
C EO= INCIDENT ENERGY
C E = CONTINUUM ENERGY
C DE = CONTINUUM WINDOW WIDTH
C
C     SPECIAL NOTE ALL UNITS OF ENERGY ARE IN -EV-
C
C      UNITS ON Q ARE    CM**2./(STERADIAN ATOM)
C
      DATA PI/3.14159/
      AK=1.4286E-21/(4.*PI)
      ZAV2=ZAV*ZAV
      BG=AK*ZAV2*DE/(EO*E)
       RETURN
      END



      FUNCTION SIGMA(EN,EL)
C
C THIS FUNCTION CALCULATES THE STND DEV OF EDS PEAK  FOR
C DETECTOR SYSTEM. HERE PEAK ENERGY IS IN EV SIGHMA IS IN EV , EL IS
C A VARIATION PARAMETER FOR GAUSSIAN FITTING
      SIGMA=SQRT(EN*3.46925+25000.6+EL)/2.35482
      RETURN
      END
```

```
C
C     .....................................................................
C
C        SUBROUTINE MSUB
C
C        PURPOSE
C           SUBTRACT TWO MATRICES ELEMENT BY ELEMENT TO FORM RESULTANT
C           MATRIX
C
C        USAGE
C           CALL MSUB(A,B,R,N,M,MSA,MSB)
C
C        DESCRIPTION OF PARAMETERS
C           A - NAME OF INPUT MATRIX
C           B - NAME OF INPUT MATRIX
C           R - NAME OF OUTPUT MATRIX
C           N - NUMBER OF ROWS IN A,B,R
C           M - NUMBER OF COLUMNS IN A,B,R
C           MSA - ONE DIGIT NUMBER FOR STORAGE MODE OF MATRIX A
C                 0 - GENERAL
C                 1 - SYMMETRIC
C                 2 - DIAGONAL
C           MSB - SAME AS MSA EXCEPT FOR MATRIX B
C
C        REMARKS
C           NONE
C
C        SUBROUTINES AND FUNCTION SUBPROGRAMS REQUIRED
C           LOC
C
C        METHOD
C           STRUCTURE OF OUTPUT MATRIX IS FIRST DETERMINED. SUBTRACTION
C           OF MATRIX B ELEMENTS FROM CORRESPONDING MATRIX A ELEMENTS
C           IS THEN PERFORMED.
C           THE FOLLOWING TABLE SHOWS THE STORAGE MODE OF THE OUTPUT
C           MATRIX FOR ALL COMBINATIONS OF INPUT MATRICES
C                        A                B                R
C                   GENERAL          GENERAL          GENERAL
C                   GENERAL          SYMMETRIC        GENERAL
C                   GENERAL          DIAGONAL         GENERAL
C                   SYMMETRIC        GENERAL          GENERAL
C                   SYMMETRIC        SYMMETRIC        SYMMETRIC
C                   SYMMETRIC        DIAGONAL         SYMMETRIC
C                   DIAGONAL         GENERAL          GENERAL
C                   DIAGONAL         SYMMETRIC        SYMMETRIC
C                   DIAGONAL         DIAGONAL         DIAGONAL
C
C     .....................................................................
C
      SUBROUTINE MSUB(A,B,R,N,M,MSA,MSB)
      DIMENSION A(1),B(1),R(1)
```

```
C
C        DETERMINE STORAGE MODE OF OUTPUT MATRIX
C
      IF(MSA-MSB) 7,5,7
    5 CALL LOC(N,M,NM,N,M,MSA)
      GO TO 100
    7 MTEST=MSA*MSB
      MSR=0
      IF(MTEST) 20,20,10
   10 MSR=1
   20 IF(MTEST-2) 35,35,30
   30 MSR=2
C
C        LOCATE ELEMENTS AND PERFORM SUBTRACTION
C
   35 DO 90 J=1,M
      DO 90 I=1,N
      CALL LOC(I,J,IJR,N,M,MSR)
      IF(IJR) 40,90,40
   40 CALL LOC(I,J,IJA,N,M,MSA)
      AEL=0.0
      IF(IJA) 50,60,50
   50 AEL=A(IJA)
   60 CALL LOC(I,J,IJB,N,M,MSB)
      BEL=0.0
      IF(IJB) 70,80,70
   70 BEL=B(IJB)
   80 R(IJR)=AEL-BEL
   90 CONTINUE
      RETURN
C
C        SUBTRACT MATRICES FOR OTHER CASES
C
  100 DO 110 I=1,NM
  110 R(I)=A(I)-B(I)
      RETURN
      END
C
C     ..................................................................
C
C        SUBROUTINE XCPY
C
C        PURPOSE
C           COPY A PORTION OF A MATRIX
C
C        USAGE
C           CALL XCPY(A,R,L,K,NR,MR,NA,MA,MS)
C
```

```
C         DESCRIPTION OF PARAMETERS
C            A  - NAME OF INPUT MATRIX
C            R  - NAME OF OUTPUT MATRIX
C            L  - ROW OF A WHERE FIRST ELEMENT OF R CAN BE FOUND
C            K  - COLUMN OF A WHERE FIRST ELEMENT OF R CAN BE FOUND
C            NR - NUMBER OF ROWS TO BE COPIED INTO R
C            MR - NUMBER OF COLUMNS TO BE COPIED INTO R
C            NA - NUMBER OF ROWS IN A
C            MA - NUMBER OF COLUMNS IN A
C            MS  - ONE DIGIT NUMBER FOR STORAGE MODE OF MATRIX A
C                    0 - GENERAL
C                    1 - SYMMETRIC
C                    2 - DIAGONAL
C
C         REMARKS
C            MATRIX R CANNOT BE IN THE SAME LOCATION AS MATRIX A
C            MATRIX R IS ALWAYS A GENERAL MATRIX
C
C         SUBROUTINES AND FUNCTION SUBPROGRAMS REQUIRED
C            LOC
C
C         METHOD
C            MATRIX R IS FORMED BY COPYING A PORTION OF MATRIX A. THIS
C            IS DONE BY EXTRACTING NR ROWS AND MR COLUMNS OF MATRIX A,
C            STARTING WITH ELEMENT AT ROW L, COLUMN K
C
C     ..................................................................
C
      SUBROUTINE XCPY(A,R,L,K,NR,MR,NA,MA,MS)
      DIMENSION A(1),R(1)
C
C        INITIALIZE
C
      IR=0
      L2=L+NR-1
      K2=K+MR-1
C
      DO 5 J=K,K2
      DO 5 I=L,L2
      IR=IR+1
      R(IR)=0.0
C
C        LOCATE ELEMENT FOR ANY MATRIX STORAGE MODE
C
      CALL LOC(I,J,IA,NA,MA,MS)
C
C        TEST FOR ZERO ELEMENT IN DIAGONAL MATRIX
C
      IF(IA) 4,5,4
    4 R(IR)=A(IA)
    5 CONTINUE
      RETURN
      END
```

```
C
C     ..................................................................
C
C        SUBROUTINE LOC
C
C        PURPOSE
C           COMPUTE A VECTOR SUBSCRIPT FOR AN ELEMENT IN A MATRIX OF
C           SPECIFIED STORAGE MODE
C
C        USAGE
C           CALL LOC (I,J,IR,N,M,MS)
C
C        DESCRIPTION OF PARAMETERS
C           I    - ROW NUMBER OF ELEMENT
C           J    - COLUMN NUMBER  OF ELEMENT
C           IR   - RESULTANT VECTOR SUBSCRIPT
C           N    - NUMBER OF ROWS IN MATRIX
C           M    - NUMBER OF COLUMNS IN MATRIX
C           MS   - ONE DIGIT NUMBER FOR STORAGE MODE OF MATRIX
C                  0 - GENERAL
C                  1 - SYMMETRIC
C                  2 - DIAGONAL
C
C        REMARKS
C           NONE
C
C        SUBROUTINES AND FUNCTION SUBPROGRAMS REQUIRED
C           NONE
C
C        METHOD
C           MS=0    SUBSCRIPT IS COMPUTED FOR A MATRIX WITH N*M ELEMENTS
C                   IN STORAGE (GENERAL MATRIX)
C           MS=1    SUBSCRIPT IS COMPUTED FOR A MATRIX WITH N*(N+1)/2 IN
C                   STORAGE (UPPER TRIANGLE OF SYMMETRIC MATRIX). IF
C                   ELEMENT IS IN LOWER TRIANGULAR FORTION, SUBSCRIPT IS
C                   CORRESPONDING ELEMENT IN UPPER TRIANGLE.
C           MS=2    SUBSCRIPT IS COMPUTED FOR A MATRIX WITH N ELEMENTS
C                   IN STORAGE (DIAGONAL ELEMENTS OF DIAGONAL MATRIX).
C                   IF ELEMENT IS NOT ON DIAGONAL (AND THEREFORE NOT IN
C                   STORAGE), IR IS SET TO ZERO.
C
C     ..................................................................
C
      SUBROUTINE LOC(I,J,IR,N,M,MS)
C
      IX=I
      JX=J
      IF(MS-1) 10,20,30
   10 IRX=N*(JX-1)+IX
      GO TO 36
   20 IF(IX-JX) 22,24,24
```

```
 22 IRX=IX+(JX*JX-JX)/2
    GO TO 36
 24 IRX=JX+(IX*IX-IX)/2
    GO TO 36
 30 IRX=0
    IF(IX-JX) 36,32,36
 32 IRX=IX
 36 IR=IRX
    RETURN
    END



      SUBROUTINE NEGTVE(XA,NPT,RIMIT)
C
C  THIS SUBROUTINE SETS THE MAXIMUN NEGTVE VALUE
C  STORED IN THE ARRAY XA WITH NPT NUMBER OF POINTS
      DIMENSION XA(1)
      DO 1 I=1,NPT
      IF(XA(I).LE.(-1.*RIMIT)) XA(I)=-1.*RIMIT
 1    CONTINUE
      RETURN
      END



      FUNCTION ICHN(EN,IRES)
C
C THIS FUNCTION CALCULATES THE CHNNEL NO. WHICH CORRESPONDS TO
C THE ENERGY EN, AT RESOLUTION RES,EN IN  -KEV-
      ICHN=INT(EN*1000./IRES)
      RETURN
      END



      FUNCTION CONV(EABS,SABS,IRES,EN,R)
C
C THIS FUNCTION CONVOLUTES A STEP FUNCTION WHICH CHANGES
C IT VALUE FROM 1 TO R AT AN ENERGY EABS. CONVOLUTION IS WITH A
C STANDARD GAUSSIAN CHARACTERISTIC OF DETECTOR IRESPONSE.
C ALL ENERGIES IN -EV-
      S1=0.
      S2=0.
      MIN=EABS-5.*SABS
      MAX=EABS+5.*SABS
      MID=EABS
      DO 1 I=MIN,MID,IRES
      S1=S1+EXP(-((EN-I)/SIGMA(EN,0.))**2./2.)
```

```
 1     CONTINUE
       DO 2 I=MID,MAX,IRES
       S2=S2+EXP(-((EN-I)/SIGMA(EN,0.))**2./2.)
 2     CONTINUE
       RN1=S1/S2
       RN2=S2/S1
       CONV=1./(1.+RN2) + R/(1.+RN1)
       RETURN
       END
C
C
C
C
C
C
C
C
      FUNCTION SCALEN(MIN,MAX)
C
C THIS FUNCION FINDS MAD OF ARRAY P BETWEEN MIN,MAX
      COMMON P(502),E(502),BG(502),EKLM(502),SUBID(76)
      SCALEN=0
      DO 1 I=MIN,MAX
      SCALEN=AMAX1(SCALEN,P(I))
 1    CONTINUE
      SCALEN=SCALEN*1.0
      RETURN
      END
C
C
C
C
C
      SUBROUTINE MLTFIT(IPN,NP,NPT)
C
C THIS SUBROUTINE FITS MULTIPLE GAUSSIANS TO EXPERIMENTAL
C DATA THE GAUSSIAN PEAKS FITTED ARE THOSE WHICH HAVE BEEN
C IDENTIFIED IN THE K-L-M MARKER MODE OF THIS PROGRAM.
C IPN= IS THE PEAK NUMBER OF THE FIRST PEAK IN THE WINDOW
C NP= THE REMAINING NUMBER OF PEAKS WITHIN THE WINDOW
C NPT= NUMBER OF DATA POINTS WITHIN THE WINDOW.
C THE ENERGY OF THE PEAK IS AEN(I)
C THE PEAK HEIGHT IS AHT(I)
C THE PEAK WIDTH IS RELATED TO ENERGY BUT VARIED BY AEL(I)
C NOTE THE FIRST TWO   ITERATIONS HOLD PEAK ENERGY CONSTANT
      COMMON P(502),E(502),BG(502),EKLM(502),SUBID(76)
      COMMON SUBP(76),SUBE(76),AEN(30),AHT(30),AEL(31),AINT(30)
      COMMON SUME(760),SUMP(760),SUMID(760),ABG(30)
      IFPN=IPN+NP-1
      COUNT=0.
```

```
D       CALL ERASE
 1     DO 3 J=IPN,IFPN
C  MINIMIZE PEAK HEIGHTS
       DELTA=(SQRT(AHT(J)))/5.
       CALL CHIMIN(IPN,NP,NPT,AHT(J),DELTA)
C MINIMIZE PEAK WIDTHS
       ALPHA=AEL(31)*0.05
       CALL CHIMIN(IPN,NP,NPT,AEL(31),ALPHA)
C MINIMIZE  PEAK ENERGY
       BETA=0.005
       IF(COUNT.LE.1.5) BETA=0.
       CALL CHIMIN(IPN,NP,NPT,AEN(J),BETA)
 3     CONTINUE
C       OUTPUT RESULTS
       WRITE(7,5) (I,I=IPN,IFPN)
       WRITE(7,105) (AEN(I),I=IPN,IFPN)
       WRITE(7,205) (AEL(I),I=IPN,IFPN)
       WRITE(7,305)(AHT(I),I=IPN,IFPN)
 5     FORMAT(' PEAK NO.= ',5(8X,I3))
 105    FORMAT(' ENERGY  = ',5(4X,1F7.2))
 205     FORMAT(' STND DEV= ',5(4X,1F7.2))
 305     FORMAT(' PEAK HT.= ',5(4X,1F7.0))
       WRITE(7,405)
 405    FORMAT(X,72('*'))
       COUNT=COUNT+1
       IF(COUNT.GE.5.5) GO TO 9
       GO TO 1
  9    RETURN
       END
C
C
C
C
C
       SUBROUTINE CHIMIN(IPN,NP,NPT,V,DELTA)
C
C THIS ROUTINE MINIMIZES THE FITTING PARAMETERS V FOR THE LEAST
C SQUARES ANALYSIS OF THE DATA FOUND IN SUBP,SUBEBY THE
C INCREMENTS OF DELTA
C NOTE THAT V IS NEVER ALLOWED TO BE LESS THAN DELTA*3
       COMMON P(502),E(502),BG(502),EKLM(502),SUBID(76)
       COMMON SUBP(76),SUBE(76),AEN(30),AHT(30),AEL(31),AINT(30)
       COMMON SUME(760),SUMP(760),SUMID(760),ABG(30)
       AM=0.6*V
       AMM=V+0.4*V
       CALL CHISQ(IPN,NP,NPT,X1)
       V=V-DELTA
       IF(V.LE.AM)      GO TO 2
       IF(DELTA.EQ.0) GO TO 2
       CALL CHISQ(IPN,NP,NPT,X2)
```

```
      IF(X2-X1) 1,2,3
    1   CALL CHISQ(IFN,NP,NFT,X1)
      V=V-DELTA
      IF(V.LE.AM)       GO TO 2
       CALL CHISQ(IFN,NP,NFT,X2)
      IF(X2-X1) 1,2,4
    3   V=V+DELTA*2.
      IF(V.GE.AMM)      GO TO 2
    7   CALL CHISQ(IFN,NP,NFT,X1)
      V=V+DELTA
      IF(V.GE.AMM)      GO TO 2
      CALL CHISQ(IFN,NP,NFT,X2)
      IF(X2-X1) 7,2,5
    4   V=V+DELTA/2.
      GO TO 2
    5   W=V-DELUA/2.
    2   RETURN
      END
C
C
C
C
C
      SUBROUTINE CHISQ(IFN,NP,NFT,XSQ)
C
C THIS SUBROUTINE CALCULATES THE CHI-SQUARED VALUES OF THE
C  GAUSSIANS GIVEN
C SKIP 1ST AND LAST POITS
      COMMON P(502),E(502),BG(502),EKLM(502),SUBID(76)
      COMMON SUBP(76),SUBE(76),AEN(30),AHT(30),AEL(31),AINT(30)
      COMMON SUME(760),SUMP(760),SUMID(760),ABG(30)
      LAST=NFT-2
      XSQ=0.
      IFPN=IFN+NP-1
      DO 1 I=2,LAST
      SUM=0.
      DO 2 J=IFN,IFPN
      AEL(J)=SIGMA(AEN(J)*1000.,AEL(31))
      BRCKET=(SUBE(I)-AEN(J))*1000./AEL(J)
      SUM =SUM+AHT(J)*EXP(-BRCKET**2./2.)
    2   CONTINUE
      XSQ=XSQ+(SUBP(I)-SUM)**2.
    1   CONTINUE
      RETURN
      END
C
C
C
C
C
```

```
      SUBROUTINE BGRND1(EO,IRES,BL1,BU1,BL2,BU2,BL3,BU3,AAA,BBB,CCC)
C
C CALCULATES BACKGROUND BY POLYNOMIAL FIT TO 3 REGIONS/
C INCLUDING EFFECTS OF DETECTOR EFFICIENCY
C ALL ENERGIES IN -EV-
      COMMON P(502),E(502),BG(502),ENLM(502),SUBID(76)
C  CALCULATE BG PARAMETERS FOR EACH ENERGY RANGE
      CALL BGRND2 (EO,IRES,BL1,BU1,E11,E12,E13,E1,E23,E2,E33,E3)
      CALL BGRND2 (EO,IRES,BL2,BU2,F11,F12,F13,F1,F23,F2,F33,F3)
      CALL BGRND2 (EO,IRES,BL3,BU3,G11,G12,G13,G1,G23,G2,G33,G3)
      H11=E11+F11+G11
      H12=E12+F12+G12
      H13=E13+F13+G13
      H1=E1+F1+G1
      H21=H12
      H22=H13
      H23=E23+F23+G23
      H2=E2+F2+G2
      H31=H13
      H32=H23
      H33=E33+F33+G33
      H3=E3+F3+G3
      DELTA1=H11*(H22*H33-H32*H23)
      DELTA2=H12*(H21*H33-H31*H23)
      DELTA3=H13*(H21*H32-H31*H22)
      DELTA=DELTA1-DELTA2+DELTA3
      A1=H1*(H22*H33-H32*H23)
      A2=H12*(H2*H33-H3*H23)
      A3=H13*(H2*H32-H3*H22)
      AAA=(A1-A2+A3)/DELTA
      B1=H11*(H2*H33-H3*H23)
      B2=H1*(H21*H33-H31*H23)
      B3=H13*(H21*H3-H31*H2)
      BBB=(B1-B2+B3)/DELTA
      C1=H11*(H22*H3-H32*H2)
      C2=H12*(H21*H3-H31*H2)
      C3=H1*(H21*H32-H31*H22)
      CCC=(C1-C2+C3)/DELTA
      CALL PLOT(525.,180.,0)
C      WRITE (7,88)
C 88   FORMAT(' CALCULATED POLYNOMIAL COEFFICIENTS:')
C     WRITE(7,89)   AAA,BBB,CCC
C 89   FORMAT(2X,3(1X,1PE10.3))
      DO 90 I=2,500,1
      FF=(I-1.)*IRES
      CALL MASSAB(FF,ABSFF)
      CC=(EO-FF)/FF
      BG(I)=(AAA*CC**2+BBB*CC+CCC)*EXP(ABSFF)
      IF(BG(I).LE.0) BG(I)=1.0
      IF (I.LE.25.) BG(I)=BG(26)
```

```
 90   CONTINUE
      BG(1)=1.
      RETURN
      END
C
C
C
C
C
      SUBROUTINE BGRND2(EO,IRES,BL1,BU1,S11,S12,S13,S1,S23,S2,S33,S3)
C
C CALCULATES POLYNOMINAL FIT PARAMETERS FOR BGND EQ.
      COMMON F(502),E(502),BG(502),EKLM(502),SUBID(76)
      LBL1=BL1
      LBU1=BU1
      S11=0.
      S12=0.
      S13=0.
      S1=0.
      S23=0.
      S2=0.
      S33=0.
      S3=0.
      DO 855 I=LBL1,LBU1,IRES
      J=I/IRES
      F=I
      EF=(EO-F)/F
      CALL MASSAB(F,ABSF)
      S11=S11+EF**4.*EXP(2.*ABSF)
      S12=S12+EF**3.*EXP(2.*ABSF)
      S13=S13+EF**2.*EXP(2.*ABSF)
      S1=S1+F(J)*EF**2.*EXP(ABSF)
      S23=S23+EF*EXP(2.*ABSF)
      S2=S2+F(J)*EF*EXP(ABSF)
      S33=S33+EXP(2.*ABSF)
      S3=S3+F(J)*EXP(ABSF)
 855  CONTINUE
      RETURN
      END
```

APPENDIX C

Subroutine Library – NGRAPH

Subroutine CRTPLT

Subroutine SYMPLT

Subroutine PLRPLT

Subroutine ERASE

Subroutine PLOT

Subroutine XYTRAN

Subroutine TRANXY

Subroutine CRSSHR

Subroutine POINT

Subroutine SPOINT

Subroutine LINE

Subroutine SYMBOL

Subroutine SCALE

Subroutine RSCALE

Subroutine OFFSET

Subroutine AXIS

Subroutine TICS

Subroutine LABEL

Subroutine TINPUT

Subroutine TOUTPT

APPENDIX C

Subroutine Library – NGRAPH

This appendix documents the graphics subroutine library written for use on the DEC LSI-11 microcomputer and Tektronics 4010-1 graphics terminal for use in conjunction with the data analysis programs described elsewhere in these appendices. These routines can also be used on a stand-alone basis for graphics display of calculations performed on the computer system.

```
C
C
C      GRAPHICS LIBRARY FOR PDP LSI-11 MICROCOMPUTER
C              ANY QUESTIONS AND/OR COMMENTS
C                 SHOULD BE DIRECTED TO
C
C
C              NESTOR J. ZALUZEC
C              DEPARTMENT OF METALLURGY
C              MATERIALS RESEARCH LABORATORY
C              UNIVERSITY OF ILLINOIS
C              URBANA , ILLINOIS 61801
C
C
      SUBROUTINE CRTPLT (XZ,YZ,XA,YA,NPT,NMODE,IRPLT,XM,YM,SXA,SYA,NS,
     1ILX,NILX,ILY,NILY)
C
C     THIS IS THE GRAPHICS CONTROL SUBROUTINE WHICH  WILL
C     PRODUCE A COMPLETE GRAPH ON THE TEKTRONIX 4010-1 TERMINAL
C     INCLUDING AXII,TIC MARKS AND LABELS
C
C      XZ= ORIGIN OF GRAPH (X AXIS) IN ABSOLUTE SCREEN UNITS (50.-1023.)
C      YZ=    "       "    (Y AXIS)  "   "        "       "   (50.-770.)
C      XA= ARRAY OF DATA FOR X AXIS
C      YA=   "   "   "    "  Y AXIS
C      NPT= NUMBER OF POINTS IN XA & YA TO BE PLOTTED
C      NMODE= DESCRIBES TYPE OF PLOT
C           0= DATA PLOTTED AS DOTS
C           1= DATA PLOTTED AS CONTINUOUS LINE
C     -NMODE= DATA PLOTTED AS SYMBOL (I.E. NMODE IS NEGATIVE)
C             SEE SUBROUTINE SYMBOL FOR LIST OF SYMBOLS
C      IRPLT= SUPERPOSITION CONTROL
C           0= NEW GRAPH ERASE SCREEN AND DRAW AXII ETC
C           1= SUPERIMPOSE DATA ON TOP OF OLD GRAPH
C              (USE SCALE FACTORS FROM OLD GRAPH FOR PLOTTING)
C      XM=AUXILIARY MAGNIFICATION CHANGE (OVERRIDES
C              CALCULATED SCALE FACTORS IF DIFFERENT FROM 1.0) X AXIS
C      YM= AS XM BUT Y AXIS
C      SXA= DATA ARRAY USED TO SCALE X AXIS (CAN BE DIFFERENT FROM XA)
C      SYA= AS SXA BUT Y AXIS
C      NS= NUMBER OF POINTS IN SXA & SYA TO BE USED FOR SCALING
C      ILX= ARRAY CONTAINING THE LABEL FOR THE X AXIS (2 HOLLERITH
C              CHARACTERS PER ARRAY ELEMENT)
C      NILX= NUMBER OF CHARACTERS IN ILX
C      ILY= ARRAY CONTAINING THE LABEL FOR THE Y AXIS (1 HOLLERITH
C              CHARACTER PER ARRAY ELEMENT)
C      NILY= NUMBER OF CHARACTERS IN ILY
C
C
C
```

```
      DIMENSION XA(1),YA(1),SXA(1),SYA(1),ILX(1),ILY(1)
      COMMON /CRTLST/ XMIN,DX,YMIN,DY,OFFX,OFFY,XL,YL
C
C     GRAPH LENGTH X AXIS = 800 UNITS
C     GRAPH LENGTH Y AXIS = 500 UNITS
C
      XL=800.
      YL=500.
C
C     CALCULATE SCALE FACTORS
C
      CALL SCALE(XMIN,DX,NS,SXA,XL)
      CALL RSCALE(YMIN,DY,NS,SYA,YL)
      DX=DX*XM
      DY=DY*YM
      CALL OFFSET(XMIN,DX,YMIN,DY,XZ,YZ,XL,YL)
C
C     CHECK FOR SUPERPOSITION
C
      IF (IRPLT.EQ.1) GO TO 2
      CALL ERASE
      CALL AXIS(1)
      CALL TICS
      CALL LABEL(ILX,NILX,ILY,NILY)
C
C     DRAW DATA
C
 2    IF(NMODE.EQ.0) CALL POINT(NPT,XA,YA)
      IF(NMODE.EQ.1) CALL LINE(NPT,XA,YA)
      IF(NMODE.LT.0) NSYM=-1*NMODE
      IF(NMODE.LT.0) CALL SPOINT(NPT,XA,YA,NSYM,8.)
       RETURN
      END
C
C
C
C
      SUBROUTINE SYMPLT(XZ,YZ,XA,YA,NPT,NSM,IRPLT,DK,YM,X,NX,Y,NY)
C
C     THIS SUBROUTINE IS SIMILIAR TO CRTPLT HOWEVER INSTEAD
C     OF PLOTTING Y VS. X IT DRAWS A SYMBOL THE SIZE OF WHICH
C     IS PROPORTIONAL TO THE INTENSITY OF Y  VS. X POSITION
C
C     ITS SPECIFIC USE IS IN STRUCTURE FACTOR CALCULATIONS
C     IN ELECTRON DIFFRACTION PATTERNS
C
C     XZ,YZ,XA,YA,NPT,IRPLT,YM AS DEFINED IN CRTPLT
C
C     NSM= TYPE OF SYMBOL TO BE PLOTTED
C     DK= IS THE DARK LEVEL INDICATOR
C        I.E. A VALUE OF YA(I)< DK IS CONSIDERED TO BE ZERO INTENSITY
```

```
C     X=SCALING ARRAY FOR X AXIS
C     NX= NUMBER OF PTS IN X
C     Y=SCALING ARRAY FOR Y AXIS
C     NY= NUMBER OF PTS IN Y
C
C
      DIMENSION XA(1),YA(1),X(1),Y(1)
C
C     SET X AXIS LENGTH =600. UNITS
C     SET MAXIMUM SYMBOL SIZE = 40. UNITS
C
      XL=800.
      YL=40.
      CALL SCALE(YMIN,DY,NY,Y,YL)
      CALL SCALE(XMIN,DX,NX,X,XL)
      DY=DY*YM
      IF(IRPLT.EQ.0) CALL ERASE
C
C     CALCULATE POSITION OF SYMBOL ON SCREEN
C
      DO 1 I=1,NPT
      XPT=XZ +(XA(I)-XMIN)*DX
      YPT=YZ
      SIZE=(YA(I)-YMIN)*DY
C
C      NOTE ASSUME ANY SIZE LESS THAN DK=0.00
C
      IF(SIZE.LT.DK) GO TO 1
C
C     PLOT SYMBOL
C
      CALL SYMBOL(XPT,YPT,SIZE,NSM)
    1 CONTINUE
      RETURN
      END



      SUBROUTINE PLRPLT(XZ,YZ,XA,YA,NPT,NSM,IRPLT,XM,YM,X,NX,Y,NY)
C
C      THIS SUBROUTINE PLOTS DATA IN A POLAR COORDINATE SYSTEM
C     XZ,YZ,XA,YZ,NPT,NSM,IRPLT,XM,YM,X,NX,Y,NY AS IN CRTPLT & SYMPLT
C
C     XA = ANGLE THETA IN DEGREES (0  = HORIZONTAL; CCW= + DIRECTION)
C     YA = INTENSITY AS FUNCTION OF THETA
C
C      DATA PLOTTED AS A CONTINUOUS LINE WITH 10 SYMBOLS (NSM)
C           SUPERIMPOSED EVERY  0.1*NPT DEGREES
C
C
C
C
```

```
      DIMENSION XA(1),YA(1)
C
C      MAXIMUM  RADIUS = 400 UNITS
C
      YL=400.
      YUL=YZ+YL
      YLL=YZ-YL
      XUL=XZ+YL
      XLL=XZ-YL
      CALL SCALE (YMIN,DY,NY,Y,YL)
      IF (IRPLT.EQ.0) CALL ERASE
C
C     MOVE POINTER TO FIRST POSITION
C
      RO=(YA(1)-YMIN)*DY
      A= XA(1)/57.29
      XPT=XZ+RO*COS(A)
      YPT=YZ +RO*SIN(A)
      IF(XPT.LE.XLL) XPT=XLL
      IF(XPT.GE.XUL) XPT=XUL
      IF(YPT.LE.YLL) YPT=YLL
      IF(YPT.GE.YUL) YPT=YLL
      CALL TOUTPT(29)
      CALL XYTRAN (XPT,YPT)
      NPP=NPT+1
C
C      PLOT DATA
C
      DO 1 I=1,NPP
      R=(YA(I)-YMIN)*DY
      A=(XA(I))/57.29
      XPT=XZ + R*COS(A)
      YPT=YZ + R*SIN(A)
      IF(XPT.GE.XUL) XPT=XUL
      IF(XPT.LE.XLL) XPT=XLL
      IF(YPT.GE.YUL) YPT=YUL
      IF(YPT.LE.YLL) YPT=YLL
      CALL XYTRAN (XPT,YPT)
    1 CONTINUE
      DO 3 I=1,10
      CALL TOUTPT(22)
    3 CONTINUE
      CALL TOUTPT (31)
C
C     PLOT SYMBOL ON TOP OF DATA CURVE
C
      INC=0.1*NPP
      DO 2 I=1,NPP,INC
      R=(YA(I)-YMIN)*DY
      A=(XA(I))/57.29
```

```
      XPT=XZ+R*COS(A)
      YPT=YZ+R*SIN (A)
      IF(XPT.GE.XUL) XPT=XUL
      IF(XPT.LE.XLL) XPT=XLL
      IF(YPT.GE.YUL) YPT=YUL
      IF(YPT.LE.YLL) YPT=YLL
      CALL SYMBUL (XPT,YPT,8.,NSM)
 2     CONTINUE
      RETURN
      END
C
C
C
C
C
      SUBROUTINE ERASE
C
C      THIS SUBROUTINE ERASES THE TEKTRONIX TERMINAL
C OUTPUT (ESC) (FF) TO SCOPE FOR NEW PAGE
C
      CALL TOUTPT(7)
      CALL TOUTPT(27)
      CALL TOUTPT(12)
C
C     TIME DELAY FOR BAUD RATE PURPOSES
C
      DO 1 I=1,1000
 1    CALL TOUTPT(22)
      CALL PLOT(0.,767.,0)
C RESET TO ALPHA MODE
      CALL TOUTPT(31)
      RETURN
      END



      SUBROUTINE PLOT (X,Y,NMODE)
C
C      THIS SUBROUTINE MOVES THE POINTER TO A POSITION
C      X,Y (ABSOLUTE UNITS) ON THE SCREEN
C      IF NMODE =0 MOVE TO POSITION
C               =1 MOVE TO POSITION AND PLOT A POINT
C
C TURN ON GS
      CALL TOUTPT(31)
      CALL TOUTPT(29)
C TEST FOR MOVE, POINT PLOT, : 0,1
      IF(NMODE.EQ.0) GO TO 1
      IF(NMODE.EQ.1) GO TO 2
C PLOT LINE FROM LAST TO NEW
```

```
 2     CALL XYTRAN (X,Y)
 1     CALL XYTRAN (X,Y)
C TURN OFF GS
      CALL TOUTPT(31)
      RETURN
      END



      SUBROUTINE XYTRAN(X,Y)
C
C     THIS SUBROUTINE TRANSMITS COORDINATE INFORMATION
C     TO THE TEKTRONIX TERMINAL IN THE APPROPRIATE MANNER
C
C BREAK UP X,Y INTO HI/LO COMPONENTS
      IX=X
      IY=Y
      LOX=MOD(IX,32)+64
      IHOX=MOD(IX/32,32)+32
      LOY=MOD(IY,32)+96
      IHOY=MOD(IY/32,32)+32
C TRANSMITT TO TEKSCOPE
      CALL TOUTPT(IHOY)
      CALL TOUTPT(LOY)
      CALL TOUTPT(IHOX)
      CALL TOUTPT(LOX)
      RETURN
      END



      SUBROUTINE TRANXY(X,Y,XPT,YPT)
C
C  THIS SUBROUTINE CONVERTS ABSOLUTE SCREEN COORDINATES
C OBTAINED BY USING THE CROSSHAIR INTO DATA VALUES APPROPRIATE
C TO THE LAST SET OF SCALE FACTORS USED FOR PLOTTING DATA
C X=ABSOLUTE SCREEN COORDINATE X AXIS
C Y=     "       "       "       Y   "
C XPT= DATA VALUE X AXIS
C YPT= DATA VALUE Y AXIS
C
C
      COMMON/CRTLST/ XMIN,DX,YMIN,DY,OFFX,OFFY,XL,YL
      XPT=(X-OFFX)/DX + XMIN
      YPT=(Y-OFFY)/DY + YMIN
      RETURN
      END
```

```
      SUBROUTINE CRSSHR(X,Y)
C
C THIS SUBROUTINE LIGHTS UP THE CROSSHAIR
C POSITION THE CROSSHAIR BY MOVING THE THUMBWHEELS
C ON THE TERMINAL THEN STRIKE ANY PRINTING KEY (OR HIT RETURN)
C THE VALUE OF THE ABSOLUTE SCREEN COORDINATE ARE THEN TRANSMITTED
C TO X & Y
C X=X AXIS ABSOLUTE COORDINATE
C Y=Y AXIS ABSOLUTE COORDINATE
      CALL TOUTPT(27)
      CALL TOUTPT(26)
      CALL TINPUT(IC,IHX,ILX,IHY,ILY)
      X=32*(IHX-160)+(ILX-160)
      Y=32*(IHY-160)+(ILY-160)
      RETURN
      END



      SUBROUTINE POINT(NPT,AX,YA)
C
C THIS SUBROUTINE PLOTS AN ARRAY OF POINTS WHERE
C NPT=NUMBER OF POINTS IN THE ARRAY
C AX= ARRAY OF DATA FOR THE X AXIS
C YA= ARRAY OF DATA FOR THE Y AXIS
C
C SPECIAL NOTE: THE VALUES OF XMIN,DX,YMIN,DY,OFFX,OFFY,XL,YL
C WHICH ARE REQUIRED FOR PLOTTING ARE INTERNALLY SET BY
C CALLING THE SUBROUTINES SCALE AND OFFSET
C
C
      COMMON /CRTLST/ XMIN,DX,YMIN,DY,OFFX,OFFY,XL,YL
      DIMENSION AX(NPT),YA(NPT)
      XEND=OFFX+XL
      YEND=OFFY+YL
      DO 1 I=1,NPT
      XPT=OFFX+(AX(I)-XMIN)*DX
      YPT=OFFY+(YA(I)-YMIN)*DY
      XPT=INT(XPT)
      YPT=INT(YPT)
       IF(XPT.GE.XEND) XPT=XEND
      IF(YPT.GE.YEND) YPT=YEND
      IF(XPT.LE.OFFX) XPT=OFFX
      IF(YPT.LE.OFFY) YPT=OFFY
      CALL TOUTPT(29)
      CALL XYTRAN(XPT,YPT)
      CALL XYTRAN(XPT,YPT)
      CALL TOUTPT(31)
    1 CONTINUE
      RETURN
      END
```

```
      SUBROUTINE SPOINT(NPT,AX,YA,NTYPE,SIZE)
C
C THIS SUBROUTINE PLOTS AN ARRAY OF POINTS WHERE
C NPT=NUMBER OF POINTS IN THE ARRAY
C AX= ARRAY OF DATA FOR THE X AXIS
C YA= ARRAY OF DATA FOR THE Y AXIS
C NTYPE=SYMBOL TO BE PLOTTED AT THE POINT
C SIZE=SIZE OF THE SYMBOL TO BE PLOTTED
C
C SPECIAL NOTE: THE VALUES OF XMIN,DX,YMIN,DY,OFFX,OFFY,XL,YL
C WHICH ARE REQUIRED FOR PLOTTING ARE INTERNALLY SET BY
C CALLING THE SUBROUTINES SCALE AND OFFSET
C
C
      COMMON /CRTLST/ XMIN,DX,YMIN,DY,OFFX,OFFY,XL,YL
      DIMENSION AX(NPT),YA(NPT)
      XEND=OFFX+XL
      YEND=OFFY+YL
      DO 1 I=1,NPT
      XPT=OFFX+(AX(I)-XMIN)*DX
      YPT=OFFY+(YA(I)-YMIN)*DY
      XPT=INT(XPT)
      YPT=INT(YPT)
       IF(XPT.GE.XEND) XPT=XEND
      IF(YPT.GE.YEND) YPT=YEND
      IF(XPT.LE.OFFX) XPT=OFFX
      IF(YPT.LE.OFFY) YPT=OFFY
      CALL SYMBOL(XPT,YPT,SIZE,NTYPE)
    1 CONTINUE
      RETURN
      END



      SUBROUTINE LINE (NPT,AX,AAY)
C
C THIS SUBROUTINE DRAWS A CONTINUOUS LINE FROM DATA POINT TO DATA POINT
C NPT=NUMBER OF DATA POINTS
C AX=ARRAY OF DATA FOR X AXIS
C AAY=ARRAY OF DATA FOR Y AXIS
C
C SPECIAL NOTE: THE VALUES OF XMIN,DX,YMIN,DY,OFFX,OFFY,XL,YL
C ARE SET BY CALLS TO THE SUBROUTINES SCALE AND OFFSET
C
      COMMON /CRTLST/ XMIN,DX,YMIN,DY,OFFX,OFFY,XL,YL
      DIMENSION AX(NPT),AAY(NPT)
      XEND=OFFX+XL
      YEND=OFFY+YL
```

```
      XLAST=OFFX+(AX(1)-XMIN)*DX
      YLAST=OFFY+(AAY(1)-YMIN)*DY
      IF(XLAST.GE.XEND) XLAST=XEND
      IF(YLAST.GE.YEND) YLAST=YEND
      IF(XLAST.LE.OFFX) XLAST=OFFX
      IF(YLAST.LE.OFFY) YLAST=OFFY
      CALL TOUTPT(29)
      CALL XYTRAN(XLAST,YLAST)
      DO 1 I=1,NPT
      XPT=OFFX+(AX(I)-XMIN)*DX
      YPT=OFFY+(AAY(I)-YMIN)*DY
      IF(XPT.GE.XEND) XPT=XEND
      IF(YPT.GE.YEND) YPT=YEND
      IF(XPT.LE.OFFX) XPT=OFFX
      IF(YPT.LE.OFFY) YPT=OFFY
      CALL XYTRAN(XPT,YPT)
 1    CONTINUE
C INSERT TIME DELAY FOR BAUD RATE PURPOSES
      DO 2 I=1,10
 2    CALL TOUTPT(22)
      CALL TOUTPT(31)
      RETURN
      END



      SUBROUTINE SYMBOL(X,Y,HGHT,NTYPE)
C
C THIS SUBROUTINE DRAWS SYMBOLS AT THE POINT X,Y
C SIZE IS THE SIZE OF THE CHARACTER (WIDTH=HEIGHT) IN
C ABSOLUTE SCREEN UNITS . NTYPE IS THE TYPE OF SYMBOL TO BE DRAWN
C 1=SQUARE
C 2=TRIANGLE
C 3= X
C 4= +
C 5= HEXAGON
C 6=DIAMOND
C 7=STAR
C 8=CIRCLE
C 9=DOT
C
      CALL TOUTPT(29)
      SIZE=HGHT/2.
      FLAG=0.
      GO TO (1,2,3,4,5,6,7,9,8),NTYPE
```

```
C
C       DRAW HEXAGON
C
 5     CALL XYTRAN(X-SIZE/2.,Y+SIZE)
       CALL XYTRAN(X-SIZE/2.,Y+SIZE)
       CALL XYTRAN(X+SIZE/2.,Y+SIZE)
       CALL XYTRAN(X+SIZE,Y+SIZE/2.)
       CALL XYTRAN(X+SIZE,Y-SIZE/2.)
       CALL XYTRAN(X+SIZE/2.,Y-SIZE)
       CALL XYTRAN(X-SIZE/2.,Y-SIZE)
       CALL XYTRAN(X-SIZE,Y-SIZE/2.)
       CALL XYTRAN(X-SIZE,Y+SIZE/2.)
       CALL XYTRAN(X-SIZE/2.,Y+SIZE)
       GO TO 99
C
C       DRAW DIAMOND
C
 6     CALL XYTRAN(X,Y+SIZE)
       CALL XYTRAN(X,Y+SIZE)
       CALL XYTRAN(X+SIZE,Y)
       CALL XYTRAN(X,Y-SIZE)
       CALL XYTRAN(X-SIZE,Y)
       CALL XYTRAN(X,Y+SIZE)
       GO TO 99
C
C       DRAW .( DOT )
C
 8     CALL XYTRAN(X,Y)
       CALL XYTRAN(X,Y)
       GO TO 99
C
C       DRAW CIRCLE
C
 9       CALL XYTRAN(X+SIZE,Y)
       DO 11 I=1,91
       THETA=0.069813*(I-1)
       XPT=SIZE*COS(THETA) + X
       YPT=SIZE*SIN(THETA) + Y
 11    CALL XYTRAN(XPT,YPT)
       GO TO 99
C
C
C     INSERT TIME DELAY
C
C
 99     DO 98 I=1,10
 98    CALL TOUTPT(22)
       CALL TOUTPT(31)
       RETURN
       END
```

```
      SUBROUTINE SCALE(XMIN,DX,NPT,AAX,XL)
C
C THIS SUBROUTINE CALCULATES THE APPROPRIATE SCALING FACTORS
C FOR PLOTTING DATA USING A LINEAR SCALE ON THE TEKSCOPE
C XMIN=MIN. VALUE IN ARRAY AAX
C DX=SCALE FACTOR FOR PLOTTING IN POINTS/UNIT OF DATA
C NPT=NUMBER OF DATA POINTS IN AAX
C AAX=ARRAY CONTAINING DATA
C XL=LENGTH OVER WHICH DATA IS TO BE PLOTTED
C     NOTE THIS VALUE IS IN ABSOLUTE SCREEN UNITS
C       X AXIS=1024 SCREEN UNITS (MAX)
C       Y AXIS= 780 SCREEN UNITS (MAX)
C
C
      DIMENSION AAX(NPT)
      XMIN=1. E38
      DO 1 I=1,NPT
 1    XMIN=AMIN1(XMIN,AAX(I))
      XMAX=-1.E38
      DO 2 I=1,NPT
 2    XMAX=AMAX1(XMAX,AAX(I))
      IF(XMAX-XMIN) 3,3,4
 4    CONTINUE
      DX=XL/(XMAX-XMIN)
      RETURN
 3    DX=XL/10.
      RETURN
      END
```

```
      SUBROUTINE  RSCALE(XMIN,DX,NPT,AAX,XL)
C
C THIS SUBROUTINE CALCULATES THE APPROPRIATE SCALING FACTORS
C FOR PLOTTING DATA USING A LINEAR SCALE ON THE TEKSCOPE
C       NOTE THAT THIS ROUTINE ROUNDS ONLY THE UPPER LIMIT
C XMIN=MIN. VALUE IN ARRAY AAX
C DX=SCALE FACTOR FOR PLOTTING IN POINTS/UNIT OF DATA
C NPT=NUMBER OF DATA POINTS IN AAX
C AAX=ARRAY CONTAINING DATA
C XL=LENGTH OVER WHICH DATA IS TO BE PLOTTED
C     NOTE THIS VALUE IS IN ABSOLUTE SCREEN UNITS
C       X AXIS=1024 SCREEN UNITS (MAX)
C       Y AXIS= 780 SCREEN UNITS (MAX)
C
C
```

```
      DIMENSION AAX(NPT)
      XMIN=1. E38
      DO 1 I=1,NPT
1     XMIN=AMIN1(XMIN,AAX(I))
      XMAX=-1.E38
      DO 2 I=1,NPT
2     XMAX=AMAX1(XMAX,AAX(I))
      IF(XMAX-XMIN) 3,3,4
4     CONTINUE
      IF(ABS(XMAX).GE.100.) GO TO 5
      IF(ABS(XMAX).LT.1.0) GO TO 9
      XMAX=10.*INT(XMAX/10. +1.)
      GO TO 6
9     CNT=-1.
11    XMAX=XMAX*10.
      IF(ABS(XMAX).LT.1.0) GO TO 10
      XMAX=INT(XMAX +1.)*10.**CNT
      GO TO 6
10    CNT=CNT-1.
      GO TO 11
5     CNT=1.
7     XMAX=XMAX/10.
      IF (ABS(XMAX).LT.100.) GO TO 8
      CNT=CNT+1.
      GO TO 7
8     XMAX=INT(XMAX +1.)*10.**CNT
6     CONTINUE
      DX=XL/(XMAX-XMIN)
      RETURN
3     DX=XL/10.
      RETURN
      END



      SUBROUTINE OFFSET(A,B,C,D,E,F,G,H)
C
C THIS SUBROUTINE STORES THE VALUES OF XMIN,DX,YMIN,DY,OFFX,OFFY,XL,YL
C IN THE APPROPRIATE ORDER
C XMIN =MIN VALUE OF DATA ARRAY FOR X AXIS
C DX=SCALE FACTOR FOR X AXIS
C YMIN=MIN. VALUE FOR Y AXIS
C DY=SCALE FACTOR FOR Y AXIS
C OFFX=OFFSET OF ORIGIN USED FOR SHIFTING THE ORIGIN ALONG X AXIS
C OFFY=OFFSET OF ORIGIN ALONG Y AXIS
C       NOTE THAT OFFX AND OFFY MUST BE IN UNITS OF
C       ABSOLUTE SCREEN COORDINATS
C
```

```
      COMMON /CRTLST/ XMIN,DX,YMIN,DY,OFFX,OFFY,XL,YL
      XMIN=A
      DX=B
      YMIN=C
      DY=D
      OFFX=E
      OFFY=F
      XL=G
      YL=H
      RETURN
      END
```

```
      SUBROUTINE AXIS(ITYPE)
C
C THIS SUBROUTINE DRAWS X AND Y AXII BASED ON VALUES
C OBTAINED FROM THE OFFSET SUBROUTINE
C XL=LENGTH OF X AXIS IN ABSOLUTE SCREEN UNITS
C YL=LENGTH OF Y AXIS IN ABSOLUTE SCREEN UNITS
C ITYPE= TYPE OF AXIS 0=OPEN 1=CLOSED
C
C NOTE TIC MARKS ARE NOT DRAWN WITH THIS ROUTINE
C
C
      COMMON /CRTLST/ XMIN,DX,YMIN,DY,OFFX,OFFY,XL,YL
      XEND=OFFX+XL
      YEND=OFFY+YL
      CALL TOUTPT(29)
      CALL XYTRAN(XEND,OFFY)
      CALL XYTRAN(XEND,OFFY)
      CALL XYTRAN(OFFX,OFFY)
      CALL XYTRAN(OFFX,YEND)
      IF(ITYPE.EQ.0) GO TO 1
      CALL XYTRAN(XEND,YEND)
      CALL XYTRAN(XEND,OFFY)
1     CONTINUE
C INSERT TIME DELAY FOR BAUD RATE PURPOSES
      DO 2 I=1,10
2     CALL TOUTPT(22)
      CALL TOUTPT(31)
      RETURN
      END
```

```
      SUBROUTINE TICS
C
C THIS SUBROUTINE DRAWS TIC MARKS ALONG THE X AND Y AXIS OF A GRAPH
C USING THE VALUES OBTAINED FROM THE OFFSET ROUTINE
C XL=X AXIS LENGTH
C YL=Y AXIS LENGTH
C NOTE THAT THE TIC MARKS ALWAYS HAVE
C THE SAME DENSITY ALONG THE VARIOUS AXII
C THAT IS THERE ARE ALWAYS THE SAME NUMBER (20)
C AND ALTERNATE ONES ARE OF DIFFERENT LENGTH
C
C
      COMMON /CRTLST/ XMIN,DX,YMIN,DY,OFFX,OFFY,XL,YL
      IX=OFFX
      IY=OFFY
      IEX=IX+XL
      IEY=OFFY+YL
      INCX=-XL/20.
C
C      DRAW X AXIS TICS
C
      DO 1 I=IEX,IX,INCX
      S=1.
      A=(I-IX)*10./XL
      IF(A.EQ.INT(A)) S=2.
      TCLGTH=10.*S
      YPT=OFFY-TCLGTH
      XPT=I
      YPT=INT(YPT)
      CALL TOUTPT(29)
      CALL XYTRAN(XPT,OFFY)
      CALL XYTRAN(XPT,OFFY)
      CALL XYTRAN(XPT,YPT)
      CALL TOUTPT(31)
 1    CONTINUE
C
C      DRAW Y AXIS TICS
C
      INCY=-YL/20.
      DO 2 J=IEY,IY,INCY
      S=1.
      A=(J-IY)*10./YL
      IF(A.EQ.INT(A)) S=2.
      TCLGTH=10.*S
      XPT=OFFX-TCLGTH
      YPT=J
      XPT=INT(XPT)
      CALL TOUTPT(29)
      CALL XYTRAN(OFFX,YPT)
      CALL XYTRAN(OFFX,YPT)
```

```
      CALL XYTRAN(XPT,YPT)
      CALL TOUTPT(31)
 2    CONTINUE
      RETURN
      END



      SUBROUTINE LABEL(ILX,NILX,ILY,NILY)
C
C THIS SUBROUTINE LABELS THE AXII OF THE GRAPH
C
C ILX=ARRAY OF CHARACTERS FOR LABELING X AXIS
C     STORED AS 2 HOLLERITH CHARACTERS PER ARRAY ELEMENT
C NILX=NUMBER OF CHARACTERS IN ILX
C ILY=ARRAY OF CHARACTERS FOR LABELING Y AXIS
C     STORED AS 1 HOLLERITH CHARACTER PER ARRAY ELEMENT
C NILY=NUMBER OF CHARACTERS IN ILY
C
C
C                          EXAMPLE
C      STORE THE X AXIS LABEL ENERGY(KEV) IN ILX
C      AND THE Y AXIS LABEL COUNTS IN ILY
C
C         FOR LABELING THE X AND Y AXII RESPECTIVELY
C
C         DIMENSION ILX(6),ILY(6)
C         DATA ILX/'EN','ER','GY',' (','KE','V)'/
C         DATA ILY/'C','O','U','N','T','S'/
C         CALL LABEL (ILX,12,ILY,6)
C
C
C
C XL=X AXIS LENGTH
C YL=Y AXIS LENGTH
C
C THE ROUTINE LABELS THE MIN AND MAX OF EACH AXIS AND OUTPUTS
C THE VALUE OF THE INCREMENT (MINOR TIC) IN UNITS OF THE ORIGINAL DATA
C NOTE THAT THIS ROUTINE HAS ALSO BEEN SETUP TO WRITE ASCII
C CHARACTERS TO LABEL THE TITLES OF THE AXII
C FOR READABILITY ALL LABELING IS DONE USING THE NORMAL TTY OUTPUT
C THE GRAPHICS ROUTINE ARE USED IN ORDER TO POSITION THE OUTPUT
C WITH RESPECT TO THE COORDINATE SYSTEM
C
      COMMON /CRTLST/ XMIN,DX,YMIN,DY,OFFX,OFFY,XL,YL
      DIMENSION ILX(1),ILY(1)
      XEND=OFFX+XL-75.
```

```
      YEND=OFFY+YL+75.
      YS=OFFY-25.
      XS=0.
      XXS=OFFX-75.
      XMAX=XL/DX+XMIN
      YMAX=YL/DY+YMIN
      DELTAX=XL/DX/20.
      DELTAY=YL/DY/20.
C
C     LABEL X AXIS
C
      CALL PLOT(XXS,YS,0)
      WRITE(7,1) XMIN
 1    FORMAT(1X,1PE10.3)
      CALL PLOT(XEND,YS,0)
      WRITE(7,10) XMAX
 10   FORMAT(' ',1PE10.3)
      XMID=OFFX +XL/2.
      XTOP=XMID - 15.*(NILX/2.)
      CALL PLOT(XTOP,YS,0)
      NL=NILX/2.
      WRITE(7,200) (ILX(I),I=1,NL)
 200  FORMAT(X,50A2)
      XMID=XMID-120.
      YS=YS-22.
      CALL PLOT(XMID,YS,0)
      WRITE(7,3) DELTAX
 3    FORMAT(' TIC = ',1PE9.2)
C
C      LABEL Y AXIS
C
      CALL PLOT(XS,YEND,0)
      WRITE(7,11) YMAX
  11  FORMAT(' ',1PE9.2)
      YM=OFFY+11.
      CALL PLOT(0.,YM,0)
      WRITE(7,11) YMIN
      YMID=OFFY + YL/2.
      YTOP=YMID + 22.*(NILY/2.)
      DO 201 I=1,NILY
      CALL PLOT(20.,YTOP,0)
      WRITE(7,202) ILY(I)
 202  FORMAT(X,50A1)
      YTOP=YTOP-22.
 201  CONTINUE
      YEND=YEND-110.
      CALL PLOT(0.,YEND,0)
      WRITE(7,30) DELTAY
 30   FORMAT(' TIC = ',/,1PE9.2)
      RETURN
      END
```

```
        .TITLE  TOUTPT
        .GLOBL  TOUTPT
        .MCALL  .REGDEF,..V2..
        ..V2..
        .REGDEF
TOUTPT: TST     (R5)+           ;ADVANCE R5
WAIT:   TSTB    @#177564        ;BIT 7 SET?
        BMI     WRIT            ;IF YES WRITE
        BR      WAIT            ;IF NO WAIT FOR SCOPE
WRIT:   MOV     @(R5)+,@#177566 ;WRITE TO SCOPE
        RTS     PC              ;RESET PROGRAM
        .END    TOUTPT
```

```
        .TITLE TINPUT
        .GLOBL TINPUT
        .MCALL .REGDEF,..V2..
        ..V2..
        .REGDEF
TINPUT: TST     (R5)+           ;IGNORE ARG NUMBER
        MOV     #0,COUNT
        MTPS    #200            ;BLOCK INTERRUPTS
TEST:   TSTB     @#177560       ;DOES CONSOLE HAVD A CHARACTER?
        BMI     READ            ;READ IF IT DOES
        BR      TEST            ;TRY AGAIN
READ:   MOV     @#177562,@(R5)+ ;PUT NUMBER IN ARG.
        INC     COUNT           ;COUNT/5 ARGUMENTS
        CMP     #5,COUNT
        BNE     TEST
        MTPS    #0              ;NORMAL INTERRUPT CONDITIONS
        RTS PC                  ;RESET PROGRAM CONDITIONS
COUNT:  .WORD   0
        .END    TINPUT
```

APPENDIX D

Computer Program NXRYRT

APPENDIX D

Computer Program NXRYRT

This appendix contains documentation of the computer program NXRYRT which can be used to convert experimentally determined x-ray intensity ratios into composition ratios using a standardless analysis approach. In addition, the program can be used to predict experimental intensity ratios once the sample composition is entered. Comment lines are appropriately dispersed within the text and a simple flow diagram precedes the documentation (Fig. 102). An example of analysis using this program is given in Chapter 2, Section 2.2.8.

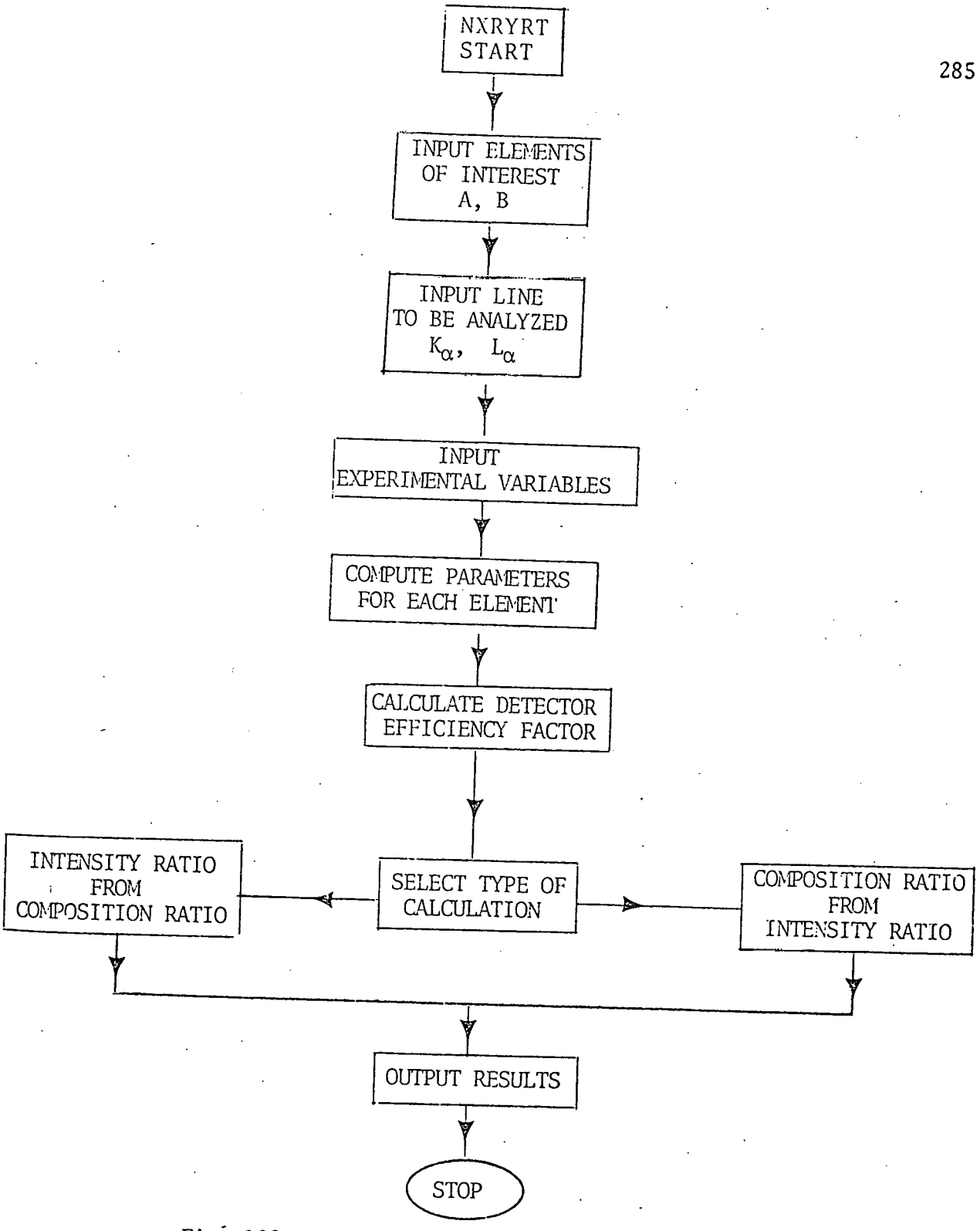

Fig. 102. Flow Diagram for the Program NXRYRT.

```
C       CALCULATION OF X-RAY EMISSION
C
C       THIS PROGRAM CALCULATES THE K(L)-ALPHA XRAY INTENSITY
C       RATIO EMITTED FROM A THIN FOIL GIVEN THE COMPOSITION
C       OR GIVEN THE MEASURED K(L)-ALPHA INTENSITY RATIO
C       IT WILL CALCULATE THE COMPOSITION OF THE ALLOY (BINARY)
C
C       THE CALCULATION OF K(L)-ALPHA INTENSITY REQUIRES SEVERAL
C       PARAMETERS TO BE DEFINED THE PROGRAM REQUESTS THESE AS
C       NEEDED.   IF THE CHARACTERISTICS OF THE BINARY SYSTEM ARE
C       COMPLETELY DEFINED IT IS POSSIBLE TO ITERATE THE CALCULATION
C       WITH THICKNESS.  IF NOT ONLY A THIN FOIL CALCULATION
C       CAN BE PERFORMED I.E. ONE MUST ASSUME THAT THE EFFECTS
C       OF ABSORPTION AND SCATTERING CAN BE NEGLECTED.
C
C
C       THE CALCULATION OF COMPOSITION FROM K RATIOS
C       USES THE THIN FILM APPROXIMATION IN ORDER TO
C       OBTAIN A COMPOSITION RATIO. ASSUMING A BINARY
C       SYSTEM THIS IS CONVERTED INTO CONCENTRATIONS.
C
C
C
      COMMON /ELEMNT/CS(100),ALNID(6)
      COMMON P(16),AUX(1000)
      EXTERNAL GEN,ABGEN
      DATA YY,YN,EX,COMP,CINT/'Y','N','E','C','I'/
      DATA CS/' H','HE','LI','BE',' B',' C',' N',' O',' F','NE'
     1,'NA','MG','AL','SI',' P',' S','CL','AR',' K','CA','SC','TI',
     2' V','CR','MN','FE','CO','NI','CU','ZN','GA','GE','AS','SE',
     3'BR','KR','RB','SR',' Y','ZR','NB','MO','TC','RU','RH','PD',
     4'AG','CD','IN','SN','SB','TE',' I','XE','CS','BA','LA','CE',
     5'PR','ND','PM','SM','EU','GD','TB','DY','HO','ER','TM','YB',
     6'LU','HF','TA',' W','RE','OS','IR','PT','AU','HG','TL','PB',
     7'BI','PO','AT','RN','FR','RA','AC','TH','PA',' U','NP','PU',
     8'AM','CM','BK','CF','ES','FM'/
      DATA ALNID/'KA','LA','MA','KB','LB','MB'/
C
C
C
C EO= INCIDENT BEAM VOLTAGE
C BO= RELATIVISTIC CORRECTION FACTOR V/C
C ECA= CRITICAL EXCITATION ENERGY OF K SHELL OF ELEMENT A
C ECB=  SAME EXCEPT FOR ELEMENT B
C RO= BACKSCATTER SURFACE CORRECTION FACTOR
C RB= BACKSCATTER BULK CORRECTION FACTOR
C ETA=BACKSCATTER COEFFICIENT OF AB ALLOY
C AN= AVAGADRO'S NUMBER
C WA =FLUORESCENCE YIELD OF K SHELL OF ELEMENT A
C WB= SAME BUT ELEMENT B
```

```
C RAKBKA= RATIO OF BETA TO ALPHA LINE FOR ELEMENT A
C RBKBKA= SAME BUT ELEMENT B
C FA= K ALPHA FRACTION OF THE TOTAL K SHELL EMISSION FOR A
C FB= SAME BUT ELEMENT B
C CA=CONCENTRATION OF ELEMENT A IN WT. %
C CB= SAME FOR ELEMENT B
C DEN=APPROXIMATE DENSITY OF AB ALLOY
C ZAV=APPROXIMATE AVERAGE ATOMIC # OF AB ALLOY
C ABSA= MASS ABS. COEFF FOR K ALPHA XRY OF ELEMENT A IN ALLOY AB;
C ABSB= SAME EXCEPT FOR K ALPHA XRY OF ELEMENT B
C                NOTE THAT ALL ENERGIES SHOULD BE ENTERED IN KEV
C
C
C
      WRITE(7,11)
 11   FORMAT(///,18X,'****************************************',
     1/,18X,'*K(L) ALPHA X-RAY INTENSITY RATIO PROGRAM*',
     1/,18X,'*              7706010000-NJZ              *',
     1/,18X,'****************************************')
 1    WRITE(7,111)
 111  FORMAT(//,$,10X,'ENTER 2 ELEMENTS A,B (EXIT=NONE)  ')
      READ(5,12) A,B
 12   FORMAT(A2,1X,A2)
      FLAG=0.
      FFLAG=0.
 112   FORMAT(/,18X'*************************',
     1/,18X,'* THIN FILM APPROXIMATION *',
     1/,18X,'*************************')
C
C      CALCULATE VARIOUS PARAMETERS FOR THE ELEMENTS A & B
C
C
C
      ZA=ATOMNR(A)
      IF(ZA.EQ.1000.) GO TO 9999
      ZB=ATOMNR(B)
      IF((ZA.EQ.0.).OR.(ZB.EQ.0)) GO TO 1
C
C
C      CHOOSE LINE FOR ANALYSIS IF Z<45 K(L)-ALPHA
C      IF Z>/45 L-ALPHA IS SUGGESTED
C
C
      LA=0
      LB=0
 215  WRITE(7,212) A
 212  FORMAT($,10X,'ENTER ',A2,' LINE TO BE ANALYZED (KA,LA)  ')
      READ(5,214) ALINE
 214  FORMAT(A2)
      IF(ALINE.EQ.ALNID(1)) LA=1
      IF(ALINE.EQ.ALNID(2)) LA=2
```

```
      IF(LA.EQ.0) GO TO 215
      IF((ZA.LT.26.).AND.(LA.EQ.2)) GO TO 217
      IF((ZA.GT.45.).AND.(LA.EQ.1)) GO TO 217
  216 WRITE(7,212) B
      READ(5,214) ALINE
      IF(ALINE.EQ.ALNID(1)) LB=1
      IF(ALINE.EQ.ALNID(2)) LB=2
      IF(LB.EQ.0) GO TO 216
      IF((ZB.LT.26.).AND.(LA.EQ.2)) GO TO 219
      IF((ZB.GT.45.).AND.(LA.EQ.1)) GO TO 219
      GO TO 220
  217 WRITE(7,218) A,ALNID(LA)
  218 FORMAT(X,'ANALYSIS OF ',A2,X,A2,' IS NOT PRACTICAL ON A ',
     1'SI(LI) X-RAY DETECTOR SYSTEM')
      GO TO 215
  219 WRITE(7,218) B,ALNID(LB)
      GO TO 216
  220 CONTINUE
      ECA=12.37788/EDGE(ZA,LA)
      ECB=12.37788/EDGE(ZB,LB)
      EKA=ENERGY(ZA,LA)
      EKB=ENERGY(ZB,LB)
      WA=YIELD(ZA,LA)
      WB=YIELD(ZB,LB)
      RAKBKA=BETA(ZA,LA)
      RBKBKA=BETA(ZB,LB)
      FA=1./(1.+RAKBKA)
      FB=1./(1.+RBKBKA)
      ATWA=ATOMWT(ZA)
      ATWB=ATOMWT(ZB)
      AN=6.023E23
C
C
C      READ IN ACCELERATING VOLTAGE
C
C
      WRITE(7,15)
   15 FORMAT($,10X,'ENTER ACCELERATING VOLTAGE IN KEV  ')
      READ(5,16) EO
   16 FORMAT(1F7.0)
   18 FORMAT(1F7.0)
C
C
C      CHOOSE TYPE OF CALCULATION
C
C
  179 WRITE(7,182)
  182 FORMAT(10X,'INDICATE TYPE OF CALCULATION',/,
     12X,'COMPOSITION FROM MEASURED K(L)-ALPHA RATIOS',
     1'= COMPOSITION',/,
     1$,2X,'K(L)-ALPHA INTENSITY RATIO FROM COMPOSITION',
```

```
     1'= INTENSITY  ')
      READ(5,121) RES
      IF(RES.EQ.COMP) GO TO 184
      IF(RES.EQ.CINT) GO TO 22
      GO TO 179
C
C
C      READ IN NECESSARY PARAMETERS INORDER TO CALCULATE
C      INTENSITY AS A FUNCTION OF THICKNESS
C
C
 22   WRITE(7,20) A,B
 20   FORMAT($,10X,'ENTER COMPOSITION ',1A2,',',1A2,
     1' IN FRACT. WEIGHT %  ')
      READ(5,21) CA,CB
 21   FORMAT(2F7.0)
      IF((CA+CB).LE.0.99) GO TO 22
      IF((CA+CB).GE.1.01) GO TO 22
      ZAV=ZA*CA +ZB*CB
      WRITE(7,31)
 31   FORMAT(10X,'ENTER VALUE OF ALLOY DENSITY',/,
     1$,18X,'IF UNKNOWN ENTER DENSITY AS 0. ')
      READ(5,18) DEN
      IF (DEN.EQ.0.) FFLAG=1.
      IF(FFLAG.EQ.1.) GO TO 184
      EC=AMIN1(ECA,ECB)
      CALL BKSCTR(ZAV,EO,EC,RO,RB)
      WRITE(7,30)
 30   FORMAT(10X,'ENTER ANGLES OF ELECTRON INCIDENCE (WRT NORMAL)',/,
     1$,10X,'AND X-RAY TAKE-OFF (WRT SURFACE)     ')
      READ (5,211) BTH,TH
 211  FORMAT(2F7.0)
C
C
C      CALCULATE APPROXIMATE VALUES OF ELECTRON ATT. COEFF (S)
C      AND ELECTRON RANGE (ZR) BASED ON BEST FIT EQUATIONS FROM
C       LOWER VOLTAGE DATA
C
C
      S=2.39E05/(EO**1.5-(AMIN1(ECA,ECB))**1.5)
      ZR=.144*ATOMWT(ZAV)*EO**2./(DEN*ZAV*2.*ALOG(101.*EO/ZAV))
      ZS=4.6E04/(S*DEN)
      S=S*ZR*1.E-04
      WRITE(7,23) A,ALINID(LA),A,A,ALNID(LA),B
 23   FORMAT(10X,'ENTER MASSAB COEFF. OF ',1A2,'-',A2,' IN ',1A2,
     1' AND ',1A2,'-',A2,' IN ',1A2)
      READ(5,24) UAA,UAB
 24   FORMAT(2F7.0)
      WRITE(7,23)B,ALNID(LB),A,B,ALNID(LB),B
      READ(5,24) UBA,UBB
```

```
C
C       CALCULASTE MASS ABS COEFF. OF BINARY ALLOY
C
        ABSA=UAA*CA + UAB*CB
        ABSB=UBA*CA + UBB*CB
C
C
C        CALCULATE DETECTOR EFFICIENCY FOR K ALPHA LINES IN QUESTION
C        I.E. CALCULATE ABSORPTION EFFECTS OF BE,AU,SI
C        ALSO SCALE ABSA & ABSB IN UNITS OF ZR
C
C
  184   CALL MASSAB(EKA,AABS)
        CALL MASSAB(EKB,BABS)
        DEFF=EXP(AABS-BABS)
        IF(FFLAG.EQ.1) GO TO 185
        ABSA=ABSA*ZR*1.E-04
        ABSB=ABSB*ZR*1.E-04
        IF(RES.EQ.COMP) GO TO 185
        WRITE(7,40) ZR
   40   FORMAT(5X,'BETHE ELECTRON RANGE (ZR) = ',1F7.3,
       1' MICRONS')
        WRITE(7,400) ZS
  400   FORMAT(5X,'DEPTH OF PENETRATION (ZS) = ',1F7.3,' MICRONS')
  185   WRITE(7,41) DEFF
   41   FORMAT(/,10X,' DETECTOR EFF. FACTOR= ',1F7.4,//)
        WRITE(7,13)
        WRITE(7,14) A,ZA,ALNID(LA),EKA,ECA,WA,FA,ATWA
        WRITE(7,14) B,ZB,ALNID(LB),EKB,ECB,WB,FB,ATWB
   13   FORMAT(/,' ELEMENT  Z  LINE  ENERGY   EDGE    YIELD ',
       1'A/SHELL    AT.WT.')
   14   FORMAT(4X,1A2,3X,1F3.0,2X,1A2,2X,1F7.3,1X,1F7.3,2X,1F6.4,2X,1F6.4,
       12X,1F7.2)
        IF(RES.EQ.COMP) GO TO 186
        IF(FFLAG.EQ.1.) GO TO 175
  104   WRITE(7,100)
  100   FORMAT(/,' TABULATE AS A FUNCTION OF Z/ZR? YES-NO-EXIT')
        READ(5,121) ANS
  121   FORMAT(1A1)
        IF(ANS.EQ.YN) FLAG=1.
        IF (ANS.EQ.EX) GO TO 1
        IF(ANS.EQ.YY) GO TO 103
        WRITE(7,101)
  101   FORMAT(/,' ENTER THICKNESS IN ANGSTROMS')
        READ (5,18) THICK
C
C
C        SCALE THICKNESS TO ZR
C
C
```

```
      Z=THICK*1.E-04/ZR
  103 CONTINUE
  175 IF(FFLAG.EQ.1.) WRITE(7,112)
      WRITE(7,10)
      IF(FFLAG.EQ.1) GO TO 102
   10 FORMAT(//,3X,'Z/ZR',2X,'U(Z)',5X,'Q(Z)',6X,'GEN(Z)',4X,
     1'ABGEN(Z)',3X,'INT(GEN)',3X,'INT(ABGEN) ER')
      IF(FLAG.EQ.1.) GO TO 102
C
C
C     CALCULATE INTENSITY BY NUMERICAL INTEGRATION OF APPROPRIATE
C     EQUATIONS
C
C
      DO 25 I=1,5
      DO 25 J=2,10,2
      Z=0.00001*J*10.**(I-1.)
  102 T=Z*ZR*1.E-04
      IF(T.EQ.0) FFLAG=1.
      CALL PARAM(EO,ECA,LA,ZR,RO,RB,AN,DEN,WA,FA,S,ABSA,TH,CA,ATWA,BTH)
      IF (Z.GE.0.999) Z=0.999
  275 IF(FFLAG.EQ.1.) Z=0.00
      UA=EO*(1.-Z)**0.667/ECA
      QA=CROSS(1.,Z,EO,ECA,LA)
      IF(FFLAG.EQ.1.) GO TO 176
      XA=GEN(T)
      AX=ABGEN(T)
      IF(AX.LE.1.E-30) AX=1.E-30
      IF(XA.LE.1.E-30) XA=1.E-30
      ER1=GEN(T)*T*.01
      ER2=ABGEN(T)*T*.01
      CALL QATR(0.,T,ER1,1000,GEN,GFA,IER1,AUX)
      CALL QATR(0.,T,ER2,1000,ABGEN,AGFA,IER2,AUX)
  176 CALL PARAM(EO,ECB,LB,ZR,RO,RB,AN,DEN,WB,FB,S,ABSB,TH,CB,ATWB,BTH)
      UB=EO*(1.-Z)**0.667/ECB
      QB=CROSS(1.,Z,EO,ECB,LB)
      IF(FFLAG.EQ.1.) GO TO 177
      XB=GEN(T)
      BX=ABGEN(T)
      ER1=GEN(T)*T*.01
      ER2=ABGEN(T)*T*.01
      IF(XB.LE.1.E-30) XB=1.E-30
      IF(BX.LE.1.E-30) BX=1.E-30
      CALL QATR(0.,T,ER1,1000,GEN,GFB,IER3,AUX)
      CALL QATR(0.,T,ER2,1000,ABGEN,AGFB,IER4,AUX)
      GO TO 178
C
C
C     SETUP CALCULATION OF INTENSITY IN THE THIN
C     FILM APPROXIMATION I.E. WHEN DENSITY HAS BEEN ENTERED
```

```
C       AS UNKNOWN.
C
C
 177  AX=0.
      GFA=0.
      AGFA=0.
      IER1=0.
      IER2=0.
      BX=0.
      GFB=0.
      AGFB=0.
      IER3=0.
      IER4=0.
      XA=QA*AN*WA*FA*CA/ATWA
      XB=QB*AN*WB*FB*CB/ATWB
C
C
C
 178  WRITE(7,2) Z,UA,QA,XA,AX,GFA,AGFA,IER1,IER2
      WRITE(7,200) UB,QB,XB,BX,GFB,AGFB,IER3,IER4
 2    FORMAT(/,1F7.5,1X,1F6.2,5(2X,1PE9.3),1X,2I1)
 200  FORMAT(8X,1F6.2,5(2X,1PE9.3),1X,2I1)
      R1= XA/XB
      IF(FFLAG.EQ.1) GO TO 169
      IF(BX.LE.1.E-30) GO TO 201
      GO TO 202
 201  R11=9.999E30
      GO TO 203
 202  R11=AX/BX
 203  R2=GFA/GFB
      R3= AGFA/AGFB
      GO TO 180
 169  R2=0.
      R11=0.
      R3=0.
 180  WRITE(7,3) A,B,R1,R11,R2,R3
 3    FORMAT(/,' GENERATED RATIO ',1A2,'/',1A2,'=',2X,4(2X,1PE9.2))
 300  FORMAT(' DETECTED  RATIO ',1A2,'/',1A2,'=',2X,4(2X,1PE9.2))
      R1=R1*DEFF
      R11=R11*DEFF
      R2=R2*DEFF
      R3=R3*DEFF
      WRITE(7,300) A,B,R1,R11,R2,R3
 4    FORMAT(18X,4(1X,1PE9.2),//)
      IF(T.EQ.0) FFLAG=0.
      IF(T.EQ.0) GO TO 104
      IF(FFLAG.EQ.1.) GO TO 1
      IF (FLAG.EQ.1.) GO TO 104
 25   CONTINUE
      GO TO 1
```

```
C
C
C       BEGIN CALCULATION OF COMPOSITION FROM INTENSITY MEASUREMENTS
C       NOTE: THIS ASSUMES THAT ALL ABSORPTION EFFECTS IN THE
C       SAMPLE CAN BE IGNORED AND MUST ONLY CALCULATE
C       EFFECTS OF OVERVOLTAGE (U)
C
C
 186    WRITE(7,187) A,B
 187    FORMAT(/,5X,'ENTER MEASURED K(L)-ALPHA INTENSITY RATIO OF ',
     11A2,'/',1A2)
        READ (5,18) RAT
        RAT=RAT/DEFF
        WRITE(7,188) RAT
 188    FORMAT(/,'   GENERATED K(L)-ALPHA RATIO (DETECTOR CORRECTION)= ',
     11F9.4)
        AI=1./RAT
        BI=1.
        UA=EO/ECA
        QA=CROSS(1.,0.,EO,ECA,LA)
        XA=QA*WA*FA*AI/ATWA
        XA=1./XA
        UB=EO/ECB
        QB=CROSS(1.,0.,EO,ECB,LB)
        XB=QB*WB*FB*BI/ATWB
        XB=1./XB
        CRATWT=XA/XB
        CBWT=100./(1.+CRATWT)
        CAWT=CBWT*CRATWT
        CAA=CAWT/ATWA
        CBA=CBWT/ATWB
        CAAT=100.*CAA/(CAA+CBA)
        CBAT=100.*CBA/(CAA+CBA)
        CRATAT=CAAT/CBAT
        WRITE(7,112)
        WRITE(7,191)
        WRITE(7,189)A,UA,QA,CAWT,CAAT
        WRITE(7,189)B,UB,QB,CBWT,CBAT
        WRITE(7,190) A,B,CRATWT,A,B,CRATAT
 191    FORMAT(//,5X,'ELEMENT',7X,'U(0)',7X,'Q(0)',9X,'WT %',7X,'AT %')
 189    FORMAT(8X,1A2,5X,1F9.3,3X,1PE9.3,2X,0PF9.3,2X,1F9.3)
 190    FORMAT(/,18X,'COMPOSITION RATIO ',1A2,'/',1A2,'  WT%= ',1F9.4,/,
     118X,'COMPOSITION RATIO ',1A2,'/',1A2,'  AT%= ',1F9.4)
        GO TO 1
 9999   STOP
        END
```

APPENDIX E

Computer Program NMCS

APPENDIX E

Computer Program NMCS

This appendix documents the computer program NMCS which is used for data analysis of spectra recorded in a multichannel scaler. Thus the program can be used for simple analysis and/or display of TSED, ELS, and EDS data. Comment lines are appropriately dispersed within the text; the program is set up to respond to a simple command structure which includes the following instructions: *graph, data, integrate, window, smooth, exit,* and *function.* The *graph* command allows the replotting of the data at scale factors other than calculated by the graphics library, while the *data* and *integrate* instructions provide a means of reading data points or integrals from specific regions of the spectrum. *Window* allows regions of the spectrum to be expanded to fill the screen, and *smooth* performs a five-point smoothing of the data. The *function* instruction allows the data arrays to be operated on by the following *functions*: exp(Y), ℓn(Y), and Y^{POWER} along both axes if desired. This is particularly useful in the case of ELS data which when graphed on a log-log plot yields a linear background dependence and can thus be analyzed using the *integrate* command.

```
C
C MCS DATA ANALYSIS PROGRAM
C
C THIS PROGRAM GRAPHS DATA OBTAINED FROM THE MCA WHEN USED
C IN THE MULTICHANNEL SCALING MODE.
C IT IS SETUP FOR LOOKING AT T.S.E.D. DATA IN PARTICULIAR
C BUT CAN ALSO BE USED TO DISPLAY X-RAY DATA SINCE THE DATA
C FORMAT IS CORRECT.
C
      COMMON ITAPE(72),INAME(72),SX(2),SY(2)
      COMMON AX(1020),AY(1020),BX(1020),BY(1020),NMODE,IRFLT,XM,YM,FLAG
     1,NNPT
      COMMON /CRTLST/ XMIN,DX,YMIN,DY,OFFX,OFFY,XL,YL
      DIMENSION ILX(6),ILY(6)
      DATA ILX/'CH','AN','NE','L ', 'NO','. '/
      DATA ILY/'C','O','U','N','T','S'/
      DATA G,D,W,R,S,DINT,YES,NO,E/'G','D','W','R','S','I','Y','N','E'/
      DATA FUNCT,CAL,DLN,PWR,HOR,VER/'F','C','L','P','H','V'/
      CALL ERASE
 9991 WRITE(7,1)
 1     FORMAT(18X,'*******************************',/,
     118X,'* MCS DATA ANALYSIS PROGRAM  *',/,
     118X,'*       7707070000-NJZ       *',/,
     118X,'*******************************',///,
     125X,'ENTER DATA FILE (FD1:FILE.DAT)')
      CALL ASSIGN(10,'DUMMY',-6,'OLD','NC',1)
C
C      READ IN RAW DATA AND GRAPH
C
      CALL TUPNIS
      WRITE(7,9992)
 9992 FORMAT($,' HAS VERTICAL INPUT BEEN RECORDED USING LOG (BASE 10)',
     1'AMPLIFIER? Y-N ')
      READ(7,13) RES
      IF(RES.NE.YES) GO TO 9993
      DO 9994 I=1,NNPT
      BY(I)=10.**(BY(I))
 9994 CONTINUE
 9993  HFLAG=0.
       VFLAG=0.
 999  CALL CRTPLT(150.,250.,BX,BY,NNPT,NMODE,IRFLT,XM,YM,BX,BY,NNPT,
     1ILX,12,ILY,6)
      WFLAG=0.
 11   CALL PLOT(0.,180.,0)
      IRFLT=0
      YM=1.
C
C     SETUP COMMAND STRUCTURE
C
```

```
      WRITE(7,12)
   12 FORMAT($,' COMMAND:GRAPH,DATA,INTEGRATE,WINDOW,RESET,SMOOTH,EXIT
     1,FUNCTION  ')
      READ(5,13) RES
   13 FORMAT(1A1)
      IF(RES.EQ.W) GO TO 30
   18 IF (FLAG.EQ.0) IL=1
      IF(FLAG.EQ.0) IU=NNPT
      NPT=0
      DO 17 I=IL,IU
      J=I-IL+1
      AX(J)=BX(I)
      AY(J)=BY(I)
      NPT=NPT+1
   17 CONTINUE
C
C     GO TO COMMAND SUBSECTION
C
      IF (RES.EQ.G) GO TO 14
      IF (RES.EQ.D) GO TO 15
      IF(RES.EQ.R) FLAG=0.
      IF(RES.EQ.R) GO TO 999
      IF (RES.EQ.S) GO TO 40
      IF (RES.EQ.W) GO TO 33
      IF (RES.EQ.DINT) GO TO 100
      IF(RES.EQ.FUNCT) GO TO 9990
      IF(RES.EQ.E) GO TO 9999
      GO TO 11
C
C     WINDOW RESET COMMAND
C     USE CROSSHAIR TO SET WINDOW LIMITS
C
C
C
   30 WFLAG=1.
      CALL PLOT(0.,150.,0)
      WRITE(7,31)
   31 FORMAT(2X,'SET WINDOW  LIMITS')
      CALL CRSSHR(X1,Y1)
      CALL CRSSHR(X2,Y2)
      CALL TRANXY(X1,Y1,DX1,DY1)
      CALL TRANXY(X2,Y2,DX2,DY2)
      DX3=BX(1)
      DX4=BX(1020)
      IF(HFLAG.EQ.1.) GO TO 231
      IF(HFLAG.EQ.2.) GO TO 232
      IF(HFLAG.EQ.3.) GO TO 233
      GO TO 234
  231 DX1=ALOG(DX1)
      DX2=ALOG(DX2)
      DX3=ALOG(DX3)
```

```
      DX4=ALOG(DX4)
      GO TO 234
  232 DX1=EXP(DX1)
      DX2=EXP(DX2)
      DX3=EXP(DX3)
      DX4=EXP(DX4)
      GO TO 234
  233 RWP=1./POWER
      DX1=DX1**RWP
      DX2=DX2**RWP
      DX3=DX3**RWP
      DX4=DX4**RWP
  234 SLP=(DX4-DX3)/1019.
      IL=INT((DX1-DX3)/SLP)
      IU=INT((DX2-DX3)/SLP)
      FLAG=1.
      GO TO 18
C
C
C     DATA POINT COMMAND
C     READ DATA FROM GRAPH USING CROSSHAIR ROUTINES
C     NOTE MUST HAVE PREVIOUSLY SET A WINDOW TO RUN
C
C
   15 IF(WFLAG.EQ.0) GO TO 11
      WRITE(7,151)
  151 FORMAT($,' ENTER NUMBER OF DATA POINTS(<=6) ')
      READ (5,152) NDP
  152 FORMAT(I1)
      CALL CRTPLT(150.,250.,AX,AY,NPT,NMODE,0,XM,YLAST,AX,AY,NPT,
     1ILX,12,ILY)
      CALL PLOT(0.,158.,0)
      DO 154 J=1,NDP
      CALL CRSSHR(X,Y)
      YH=158.-J*22.
      CALL PLOT(0.,YH,0)
      CALL TRANXY(X,Y,XPT,YPT)
      XP=XPT
      YP=YPT
      IF(HFLAG.EQ.1) XPT=ALOG(XPT)
      IF(VFLAG.EQ.1) YPT=ALOG(YPT)
      IF(HFLAG.EQ.2) XPT=EXP(XPT)
      IF(VFLAG.EQ.2) YPT=EXP(YPT)
      IF(HFLAG.EQ.3) XPT=XPT**(1./POWER)
      IF(VFLAG.EQ.3) YPT=YPT**(1./POWER)
      IX=(XPT-DX3)/SLP
      IF(HFLAG.EQ.0) XPT=BX(IX)
      IF(VFLAG.EQ.0) YPT=BY(IX)
C
```

```
C      WRITE  VALUES OF CROSSHAIR INTERSECTION POINT
C      AND NEAREST DATA ARRAY VALUE
       WRITE(12,155) XPT,YPT,XP,YP
       WRITE(7,155) XPT,YPT,XP,YP
 155   FORMAT(1X,'*',4(1F12.3,1X),'*')
 154   CONTINUE
       YH=158.-(NDP+1)*22.
       CALL PLOT(0.,YH,0)
       GO TO 11
C
C
C
C      SMOOTH COMMAND
C      PERFORM 5 POINT DATA SMOOTHING OF ENTIRE ARRAY
C
C
C
 40    CALL SMOOTH(BY,NNPT,AY)
       CALL SMOOTH(AY,NNPT,BY)
       DO 41 I=IL,IU
       J=I-IL+1
       AY(J)=BY(I)
 41    CONTINUE
       NMODE=1
       IRPLT=1
       YM=YLAST
       GO TO 33
C
C       INTEGRATE COMMAND
C        PERFORMS A SUMMATION OF # COUNTS ABOVE BACKGROUND IN
C        SELECTED AREA
C
 100   CALL CRTPLT (150.,250.,AX,AY,NPT,0,0,XM,YLAST,AX,AY,NPT,
      1ILX,12,ILY,6)
       CALL PLOT(0.,155.,0)
       WRITE(7,101)
 101   FORMAT($,' SET LOWER & UPPER BGRND PTS.')
       CALL CRSSHR(XLL,YLL)
       CALL CRSSHR(XU,YU)
       CALL TRANXY(XLL,YLL,XLL,YLL)
       CALL TRANXY(XU,YU,XU,YU)
C
C      CALCULATE SLOPE & INTERCEPT OF
C      STRAIGHT LINE THROUGH THESE POINTS
C
       SL=(YU-YLL)/(XU-XLL)
       B=YLL-SL*XLL
       YMAX=YL/DX +YMIN
       SX(1)=XLL
       SX(2)=XU
```

```
      SY(1)=YLL
      SY(2)=YU
      CALL CRTPLT(150.,250.,SX,SY,2,1,1,XM,YLAST,AX,AY,NPT,
     1ILX,12,ILY,6)
      CALL PLOT(0.,111.,0)
      WRITE(7,102)
  102 FORMAT($,' IS THIS CORRECT? YES,NO ')
      READ (5,13) IRES
      IF (IRES.EQ.NO) GO TO 100
      IF(HFLAG.NE.0) GO TO 103
      LL=INT(XLL)-IL
      LU=INT(XU)-IL
      DMAX1=-100.
      DMIN=1.E15
      NS=LU-LL
      DO 103 J=1,NS
      I=LL+J-1
      AY(I)=AY(I)-SL*AX(I)-B
      DMAX=AMAX1(DMAX1,AY(I))
      DMIN=AMIN1(DMIN,AY(I))
      IF(DMAX.GT.DMAX1) DMAX1=DMAX
      IF(AY(I).EQ.DMAX1) IFLAG=J
  103 CONTINUE
      CALL PLOT(512.,111.,0)
      WRITE(7,202)
  202 FORMAT($,' INTEGRATE FWHM? Y-N  ')
      READ (7,13) RES
      IF (RES.NE.YES) GO TO 203
      IF(HFLAG.NE.0) GO TO 203
C
C      FIND CHANNEL CONTAINING MAX# COUNTS,FWHM,CENTROID,
C      SUM OVER FWHM COUNTS ABOVE BG,
C      AND # COUNTS IN BG
C
      HALF=DMAX1/2.
      IIFLAG=LL+IFLAG-1
      DO 104 J=1,IFLAG
      I=LL+J-1
      IF(AY(I).GE.HALF) GO TO 105
  104 CONTINUE
  105 LLU=J
      DO 106 J=IFLAG,NS
      I=LL+J-1
  106 IF(AY(I).LE.HALF) GO TO 107
  107 LUL=J
      LLI=LLU+LL
      LLJ=LLI-1
      S1=AY(LLI)-AY(LLJ)
      B1=AY(LLI)-S1*AX(LLI)
      LLI=LUL+LL
      LLJ=LLI-1
```

```
      S2=AY(LLI)-AY(LLJ)
      B2=AY(LLI)-S2*AX(LLI)
      XLL=(HALF-B1)/S1
      XU=(HALF-B2)/S2
      FWHM=XU-XLL
      CNTR=XLL+FWHM/2.
      BG=0.
      SUM=0.
      LLX=LUL-1
      DO 108 JJ=LLU,LLX
      J=JJ+LL-1
      GB=SL*AX(J)+B
      F=AY(J)+GB
      IF(VFLAG.EQ.1) F=ALOG(F)
      IF(VFLAG.EQ.2) F=EXP(F)
      IF(VFLAG.EQ.3) F=F**(1./POWER)
      IF(VFLAG.EQ.1) GB=ALOG(GB)
      IF(VFLAG.EQ.2) GB=EXP(GB)
      IF(VFLAG.EQ.3) GB=GB**(1./POWER)
      SUM=SUM+F-GB
      BG=BG+GB
108    CONTINUE
      GO TO 204
203    CALL PLOT(512.,180.,0)
      WRITE(7,205)
205    FORMAT(' SET LOW LIMIT')
      CALL CRSSHR(XL,YL)
      CALL TRANXY(XL,YL,XP,YP)
      IF(HFLAG.EQ.1) XP=ALOG(XP)
      IF(HFLAG.EQ.2) XP=EXP(XP)
      IF(HFLAG.EQ.3) XP=XP**(1./POWER)
      ILCH=(XP-DX3)/SLP
      CALL PLOT(512.,155.,0)
      WRITE(7,206)
206   FORMAT($,' ENTER WIDTH (# CHN) ')
      READ(7,810) WIDTH
      IUCH=ILCH+WIDTH
      SX(1)=BX(ILCH)
      SX(2)=BX(ILCH)
      SY(1)=DMIN
      SY(2)=BY(ILCH)*2.
      CALL CRTPLT(150.,250.,SX,SY,2,1,1,XM,YLAST,AX,AY,NPT,ILX,12,ILY,6)
      SX(1)=BX(IUCH)
      SX(2)=BX(IUCH)
      CALL CRTPLT(150.,250.,SX,SY,2,1,1,XM,YLAST,AX,AY,NPT,ILX,12,ILY,6)
      CALL PLOT(512.,130.,0)
      WRITE(7,102)
      READ(7,13) IRES
      IF(IRES.EQ.NO) GO TO 203
      SUM=0.
      BG=0.
```

```
      CNTR=BX(ILCH)+(BX(IUCH)-BX(ILCH))/2.
      FWHM=WIDTH
      DMAX1=0.
      IIFLAG=ILCH
      DO 209 JJ=ILCH,IUCH
      P=BY(JJ)
      IF(VFLAG.EQ.1) P=ALOG(P)
      IF(VFLAG.EQ.2) P=EXP(P)
      IF(VFLAG.EQ.3) P=P**(1./POWER)
      GB=SL*BX(JJ)+B
      IF(VFLAG.EQ.1) GB=ALOG(GB)
      IF(VFLAG.EQ.2) GB=EXP(GB)
      IF(VFLAG.EQ.3) GB=GB**(1./POWER)
      BG=BG+GB
      SUM=SUM+P-GB
  209  CONTINUE
  204 ERS=SQRT(SUM)
      ERB=SQRT(BG)
      SB=SUM/BG
      ERSB=SB*SQRT(1./SUM +1./BG)
C
C      WRITE RESULT & APPROXIMATE ERROR =SQRT(#COUNTS)>TRUE ERROR
C
      CALL PLOT(0.,111.,0)
      WRITE(12,109) AX(IIFLAG),DMAX1,CNTR,FWHM,SUM,BG,SB,ERS,ERB,ERSB
      WRITE(7,109) AX(IIFLAG),DMAX1,CNTR,FWHM,SUM,BG,SB,ERS,ERB,ERSB
  109  FORMAT(1X,71('*'),/,1X,'*',3X,'MAX',4X,'CNTS',7X,'CNTR'
     1,5X,'FWHM',5X,'PEAK',6X,'BGRND',7X,'P/BG',4X,'*',/
     1,1X,'*',1F6.1,1X,1PE10.3,1X,0PF8.3,1X,1F8.3,1X,
     13(1PE10.3,1X),'*',/,1X,'*',36X,3(1PE10.3,1X),'*',/,1X,71('*'))
      GO TO 11
C
C
C      DRAW MODIFIED GRAPH
C
C
C
  14  CONTINUE
      CALL PLOT(0.,155.,0)
      WRITE(7,6)
   6  FORMAT($,' ENTER SUPERIMPOSE(Y-N),',
     1' MAGNIFICATION (Y-AXIS): ')
      READ(5,66) RES,YM
      IF(YM.EQ.0) YM=1.
  66  FORMAT(1A1,1X,1F7.0)
      IF(RES.EQ.NO) IRPLT=0
      IF (RES.EQ.YES) IRPLT=1
  33  CALL CRTPLT(150.,250.,AX,AY,NPT,NMODE,IRPLT,XM,YM,AX,AY,NPT,
     1ILX,12,ILY,6)
      YLAST=YM
      NMODE=0
```

```
      GO TO 11
C
C
C
C      FUNCTION COMMAND
C
C
 9990   CALL PLOT(0.,155.,0)
      WRITE(7,800)
 800   FORMAT($,1X,'ENTER FUNCTION:CALIB-X AXIS,EXP,LN,POWER  ')
      READ(7,13) RES
      IF(RES.EQ.CAL) GO TO 805
      CALL PLOT(650.,155.,0)
      WRITE(7,801)
 801  FORMAT($,1X,'ENTER AXIS: HORIZ.,VERT. ')
      HF=HFLAG
      VF=VFLAG
      READ(7,13) ARES
      IF(RES.EQ.E) GO TO 802
      IF(RES.EQ.LN) GO TO 803
      IF(RES.EQ.PWR) GO TO 804
      GO TO 11
C
C     CALCULATE EXP OF AXIS NOTE: IF PREVIOUS WAS LN THEN INVERT ASSUMED
C
 802  IF(ARES.EQ.HOR) HFLAG=1.
      IF(ARES.EQ.VER) VFLAG=1.
      IF(HF.EQ.2.) HFLAG=0.
      IF(VF.EQ.2.) VFLAG=0.
       DO 807 I=1,1020
      IF(ARES.EQ.HOR) BX(I)=EXP(BX(I))
 807   IF(ARES.EQ.VER) BY(I)=EXP(BY(I))
      GO TO 816
C
C     CALCULATE LN OF AXIS NOTE: IF PREVIOUS WAS EXP THEN INVERT ASSUMED
C
 803  IF(ARES.EQ.HOR) HFLAG=2.
      IF(ARES.EQ.VER) VFLAG=2.
      IF(HF.EQ.1.) HFLAG=0.
      IF(VF.EQ.1.) VFLAG=0.
       DO  808 I=1,1020
      IF(ARES.EQ.HOR) BX(I)=ALOG(BX(I))
 808    IF(ARES.EQ.VER) BY(I)=ALOG(BY(I))
      GO TO 816
C
C     CALCULATE PWR OF AXIS NOTE:IF PREVIOUS WAS PWR THEN INVERT ASSUMED
C
 804  IF(ARES.EQ.HOR) HFLAG=3.
      IF(ARES.EQ.VER) VFLAG=3.
      IF(HF.EQ.3.) HFLAG=0.
      IF(VF.EQ.3.) VFLAG=0.
```

```
      WRITE(7,809)
 809   FORMAT($,1X,'ENTER POWER  ')
      READ(7,810) POWER
 810  FORMAT(1F10.0)
      DO 811 I=1,1020
      IF(ARES.EQ.HOR) BX(I)=BX(I)**POWER
 811  IF(ARES.EQ.VER) BY(I)=BY(I)**POWER
      GO TO 816
C
C     CALIBRATE X AXIS: NOTE IF NON-LINEAR CANNOT CALIBRATE
C
 805   IF(HFLAG.GT.0.) GO TO 11
      CALL PLOT(0.,50.,0)
      WRITE(7,812)
 812   FORMAT(1X,'SELECT CALIB. PT.')
      CALL CRSSHR(CX1,CY1)
      CALL TRANXY(CX1,CY1,CCX1,CCY1)
      CALL PLOT(256.,50.,0)
      WRITE(7,813)
 813  FORMAT($,1X,'ENTER VALUE:  ')
      READ(7,810) XVAL1
      CALL PLOT(0.,25.,0)
      WRITE(7,812)
      CALL CRSSHR(CX2,CY2)
      CALL TRANXY(CX2,CY2,CCX2,CCY2)
      CALL PLOT(256.,25.,0)
      WRITE(7,813)
      READ(7,810) XVAL2
      DDX=(XVAL2-XVAL1)/(CCX2-CCX1)
      BDX=XVAL1-DDX*CCX1
      DO 814 I=1,1020
 814  BX(I)=BX(I)*DDX +BDX
 816      DO 815 I=IL,IU
      J=I-IL+1
      AX(J)=BX(I)
 815  AY(J)=BY(I)
      IRPLT=0
      GO TO 33
C
C
C
9999    CALL ERASE
      STOP
      END
```

```
      SUBROUTINE TUFNIS
C
C
C     THIS SUBROUTINE READS IN THE INPUT DATA FROM
C     THE FILE DEFINED IN MAIN AND DEFINES THE OUTPUT FILE

      COMMON ITAPE(72),INAME(72),SX(2),SY(2)
      COMMON AX(1020),AY(1020),BX(1020),BY(1020),NMODE,IRPLT,XM,YM,FLAG
     1,NNPT
      READ (10,2) ITAPE
      READ (10,2) INAME
      READ (10,2) BD,GV
    2 FORMAT(72A1)
    3 FORMAT(2F7.0)
      NMODE=0
      IRPLT=0
      XM=1.
      YM=1.
      FLAG=0
      WRITE(7,20) ITAPE
      WRITE(7,20) INAME
   20 FORMAT(1X,72A1)
      DO 4 I=1,102
      K=I*10-9
      KK=K+9
      READ (10,5,END=4) (BY(N),N=K,KK)
    5 FORMAT(10(1F6.0,1X))
      DO 4 N=K,KK
      BX(N)=N
    4 CONTINUE
      NNPT=KK
      CALL CLOSE(10)
      WRITE(7,900)
  900 FORMAT(1X,//,25X,'ENTER OUTPUT FILE (FD1:OUTPUT.OUT)')
      CALL ASSIGN (12,'DUMMY',-6,'NEW',NC,1)
      WRITE(12,20) ITAPE
      WRITE(12,20) INAME
      WRITE(12,20) BD,GV
      RETURN
      END



      SUBROUTINE SMOOTH (XA,NPT,SXA)
C
C     THIS SUBROUTINE DOES A E POINT SMOOTHING OF THE
C     ARRAY XA , THE RESULT IS THE STORED IN THE
C     ARRAY SAX .  THE SMOOTHING IS USING A BINOMIAL DISTRIB. FNCT.
```

```
C       NOTE CALLING SMMOTH TWICE IS EQUIVALENT TO A
C       5 POINT SMMOTHING
C
      DIMENSION XA(1),SXA(1)
      IU=NPT-2
      DO 1 I=3,IU
      SXA(I)=0.5*XA(I)+0.25*XA(I-1)+0.25*XA(I+1)
    1 CONTINUE
      RETURN
      END
```

APPENDIX F

Computer Program MCA

APPENDIX F

Computer Program MCA

This appendix documents the macro-program MCA which is used to read data from the ORTEC multichannel analyzer and which stores the data into a specified file on a floppy disc. The program was developed by Peggy Mochel and John Woodhouse of the Materials Research Laboratory in conjunction with these research and is included for completeness.

```
        .TITLE MCA
        .MCALL  .REGDEF,..V2..
        .REGDEF
        ..V2..
        .MCALL  .PRINT,.WRITW,.CLOSE,.CSIGEN,.EXIT,.WAIT,.TTYIN
        .GLOBL MCA
        DRCSR=167770
        WBUF=167772
        CARD1=20
        FLAG=20000
        MASK=200
        EOS=203
        BLANK=40
        LF=12
        CR=15
MCA:    MOV     #DRCSR,R3
        MOV     #1,COUNT
        MOV     #0,CNT
        MOV     #0,BLOCK
        CLR     (R3)+           ;ZERO DRCSR
        MOV     #CARD1,(R3)+    ;SET CARD NO,READ SR
        BIT     #FLAG,(R3)      ;CARD THERE?
        BNE     HALT
        TSTB    -4(R3)
        BPL     HALT            ;BIT 7 HI BIN READY
        MOV     #100,-(SP)      ;NORMAL LEVELS
        MOV     #0,-(SP)        ; I/O
        MOV     #100,-(SP)      ;NORMAL
        MOV     #104,-(SP)      ;STOP
        MOV     #100,-(SP)
WRIT:   TSTB    @#DRCSR         ;LOOK AT WBUF
        BPL     WRIT
        MOV     #50000,TIME     ;ADJUST RESPONSE TIME DELAY
        MOV     #2,@#DRCSR      ;LOOK AT WBUF
        MOV     (SP)+,@#WBUF    ;LOAD WBUF
        MOV     #0,@#DRCSR      ;LOOK AT CR
        MOV     #100022,@#WBUF  ;WRITE TO BBX CARD 22
        INC     CNT             ;COUNT COMMANDS
        CMP     #5,CNT          ;DONE?
        BEQ     FILE
DELAY:  INC     TIME            ;ORTEC RESPONSE TIME
        BPL     DELAY
        JMP     WRIT
FILE:   .PRINT #MSG4
        .CSIGEN #DEVSPC,#DEFEXT  ;CSI TO GET AND OPEN OUTPUT FILE
        .WAIT   #0              ;CHANNEL 0 OPENED?
        MOV     #AREA,R5        ;EMT ARGUMENT LIST
        MOV     #BUFFER,R1
BUFCLR: CLR     (R1)+           ;CLEAR BUFFER
        CMP     R1,#BUFEND      ;DONE?
```

```
        BLO     BUFCLR          ;LOOP IF NOT
        MOV     #BUFFER,R1       ;1ST BUFFER ADDRESS
        .PRINT #MSG6
SETUP:  .TTYIN                  ;GET TTY INPUT
        MOVB    R0,(R1)+        ;PUT IT IN BUFFER
        CMPB    #12,R0           ;WAS IT LF
        BNE     SETUP           ;IF NOT GET ANOTHER
        .PRINT #MSG7
SET2:   .TTYIN
        MOVB    R0,(R1)+
        CMPB    #12,R0
        BNE     SET2
        .PRINT #MSG8
SET3:   .TTYIN
        MOVB    R0,(R1)+
        CMPB    #12,R0
        BNE     SET3
        JMP     BEGIN
HALT:   .PRINT #MSG1
        .EXIT
BEGIN:  MOV     #20,@#167772        ;READ BYTE
        MOV     #0,@#167770         ;LOOK AT SR
        BIT     #40000,@#167774     ;BUSY?
        BNE     BEGIN               ;YES,TRY AGAIN
        MOV     #1,@#167770        ;NO,LOOK AT DATA
        INC     CNT                  ;LOOK FOR START OF TEXT
        CMP     CNT,#50              ;50 TIMES
        BEQ     ERR                  ;THEN QUIT
        CMP     #202,@#167774       ;START OF TEXT
        BEQ     WEED                 ;REMOVE 4 ZEROS,CR,LF
        CMP     CNT,#5               ;ELIM. 4 ZEROS,CR,LF
        BEQ     READ
        BR      BEGIN                ;NO,TRY AGAIN
WEED:   CLR     CNT                  ;RESET COUNTER
        BR      BEGIN
READ:   MOV     #20,@#167772
        MOV     #0,@#167770
        BIT     #40000,@#167774
        BNE     READ
        MOV     #1,@#167770         ;167774 SEES DATA
        CMP     #203,@#167774       ;IS IT END OF TEXT
        BEQ     FIN                 ;YES,CLOSE FILE
        MOV     @#167774,R2        ;DATA TO R2
        BIC     #MASK,R2            ;MASK OFF MSB
        MOVB    R2,(R1)+            ;PUT BYTE IN BUFFER
BTIN:   CMP     R1,#BUFEND     ;BUFFER FULL
        BLO     LINE                 ;NO,GO ON
        .WRITW R5,#0,#BUFFER,#400,BLOCK  ;PUT IT ON DISC
        INC     BLOCK              ;INCREMENT BLOCK
        CMP     #20,BLOCK           ;UPPER LIMIT ON FILE SIZE
        BEQ     ERR
```

```
        MOV     #BUFFER,R1
CLEAR:  CLR     (R1)+           ;CLEAR THE BUFFER
        CMP     R1,#BUFEND      ;DONE
        BLO     CLEAR
        MOV     #BUFFER,R1
LINE:   CMP     #BLANK,R2
        BNE     READ
        INC     COUNT
        CMP     #13,COUNT       ;10 CHANELS PER LINE
        BNE     LIN
        MOVB    #CR,(R1)+       ;CARRIAGE RETN
        JMP     BTIN
LIN:    CMP     #14,COUNT
        BNE     READ
        CLR     COUNT
        MOVB    #LF,(R1)+       ;LINE FEED
        JMP     BTIN
ERR:    .PRINT #MSG2
FIN:    MOVB    #CR,(R1)+
        MOVB    #LF,(R1)+
        .WRITW   R5,#0,#BUFFER,#400,BLOCK  ;WRIT LAST BLOCK
        .CLOSE #0           ;CLOSE OUTPUT FILE
        .PRINT #MSG5
REPEAT: .PRINT #MSG9        ;CONTINUE OR EXIT
        .TTYIN
        MOV     R0,R3           ;SAVE TTY INPUT
        .TTYIN              ;EXTRA CR
        .TTYIN                  ;EXTRA LF
        CMP     #60,R3          ;STOP?
        BEQ     EXIT
        CMP     #61,R3          ;CONTINUE-GO BACK TO BEGINNING
        BNE     REPEAT
        JMP     MCA
EXIT:   .EXIT
BUFFER: .=.+1000
BUFEND:.
DEFEXT: .WORD   0,0,0,0
BLOCK:  .WORD   0
COUNT:  .WORD   0
CNT:    .WORD 0
TIME:   .WORD   0
MSG1:   .ASCIZ  /NO CARD IN SLOT 20 OR BIN OFF/
        .EVEN
MSG2:    .ASCIZ /INPUT ERROR/
        .EVEN
MSG4:    .ASCIZ  /SPECIFY OUTPUT FILE, EG. FD1:DATA.DAT=/
        .EVEN
MSG5:   .ASCIZ  /OUTPUT COMPLETE/
        .EVEN
MSG6:    .ASCIZ  /ENTER TAPE IDENTIFICATION NUMBER/
```

```
        .EVEN
MSG7:   .ASCIZ  /ENTER SAMPLE IDENTIFICATION NUMBER/
        .EVEN
MSG8:   .ASCII  /ENTER INCIDENT BEAM VOLTAGE,/
        .BYTE   15,12
        .ASCIZ  /INITIAL VALUE OF X-RAY ENERGY/
        .EVEN
MSG9:    .ASCIZ  /STORE ANOTHER SPECTRUM? YES=1 NO=0/
        .EVEN
AREA:   .BLKW  10
DEVSPC=.
        .END    MCA
```

APPENDIX G

Circuit Diagram for TSED/TSEM Measurements

APPENDIX G

Circuit Diagram for TSED/TSEM Measurements

The schematic diagram of Fig. 103 shows the electronic circuit used to control the scanning system for TSED/TSEM measurements. A digital ramp from the ORTEC 6200 MCS, which is synchronized with the sequential channel advance, is routed through the first stage of the scanning system providing a continuously variable scan amplitude adjustment. The signal is then split into a ratioed x and y signal which effectively produces a continuously variable rotation capability. The final stage of the circuit adds a variable dc offset to both the x and y scans, which is finally routed to the intermediate alignment coils on the JSEM 200. The net result of this system is that scans of continuously variable amplitude, orientation and position can be produced about any point for intensity measurements. Figure 104 summarizes the remaining components of the TSED/TSEM system.

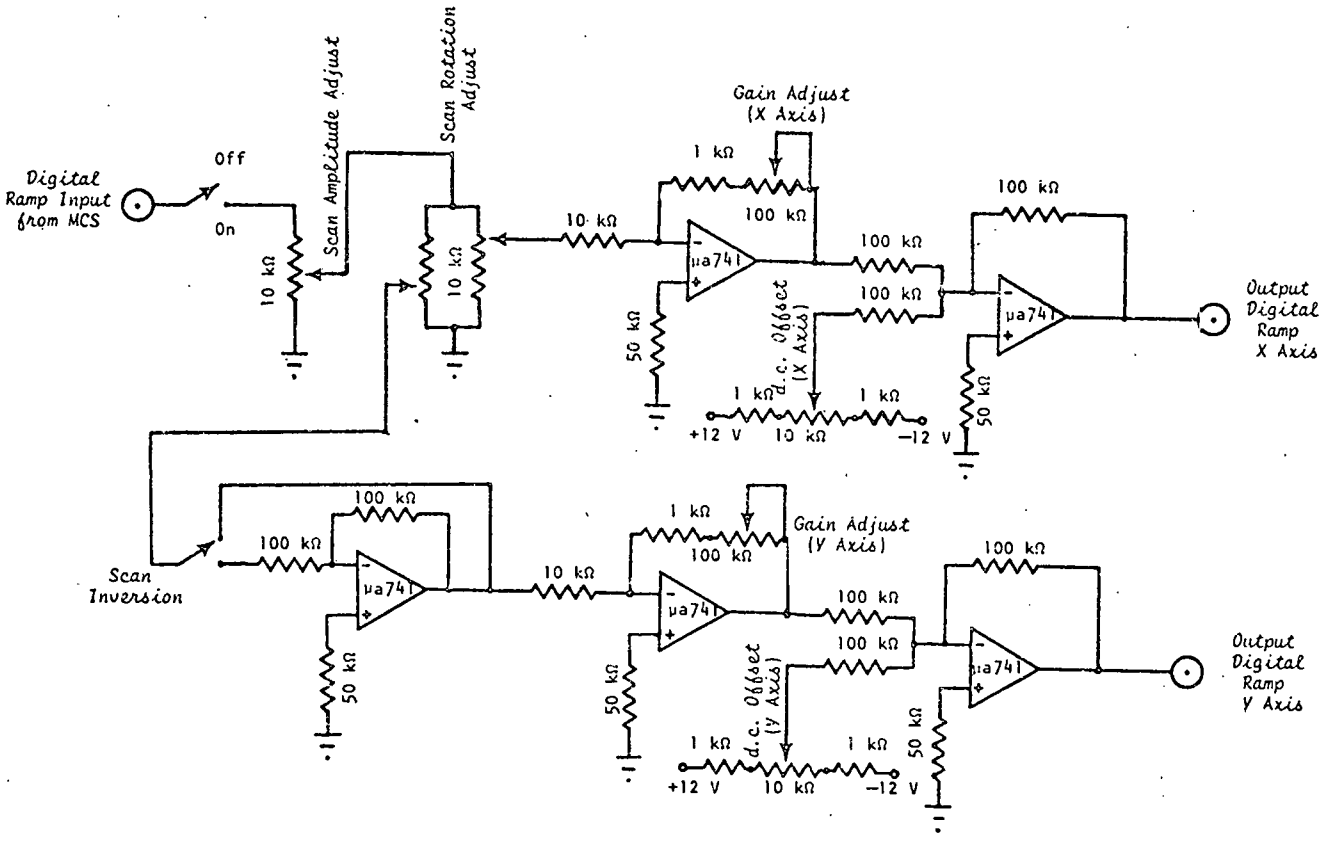

Fig. 103. Circuit Diagram for TSED/TSEM Scanning System.

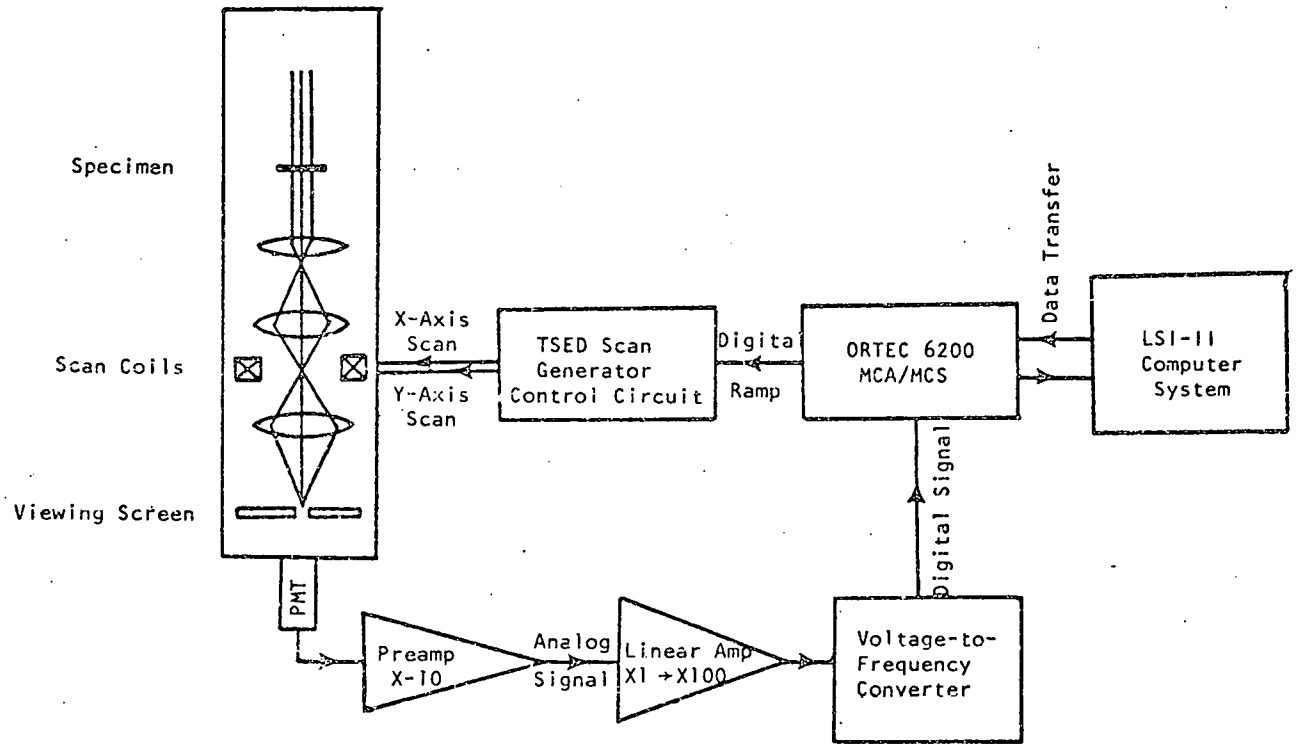

Fig. 104. Block Diagram of TSED/TSEM System.

VITA

Nestor John Zaluzec

attended Mendel Catholic High School where he graduated with honors in May 1969. He was awarded a Bachelor of Science degree in Physics with honors from Illinois Institute of Technology in May 1973, during which time he also attained the level of Senior Laboratory Technician in the Analytical Research Department of the Sherwin-Williams Research Center. In August of 1973 he became a research assistant in the Department of Metallurgy at the University of Illinois and was subsequently awarded a J&L Fellowship in Metallurgy for 1975. During his graduate studies he also served as a graduate teaching assistant responsible for laboratory courses in elementary x-ray diffraction and electron microscopy. Currently he is a Eugene P. Wigner fellow in the Radiation Effects and Microstructural Analysis Group of the Metals and Ceramics Division at Oak Ridge National Laboratory. He is the coauthor of the following publications.

"The Origin of Dislocations with b = <110> in Single Crystals of β-NiAl Compressed Along <001> at Elevated Temperatures," N. J. Zaluzec, H. L. Fraser, *Scripta Met.* 8, 1049 (1974).

"On the Feasibility of Quantitative Microchemical Analysis of Thin Metal Foils," H. L. Frazer, N. J. Zaluzec, J. B. Woodhouse, L. B. Sis, *33rd Ann. Proc. of EMSA, Las Vegas, 1975*, p. 106 (ed., G. W. Bailey).

"Examples of Microdiffraction Using the Stationary Diffraction Pattern Technique in STEM," N. J. Zaluzec, H. L. Fraser, *1st Workshop on Analytical Electron Microscopy,* Cornell University, 1976, p. 217 (eds., J. Silcox, D. M. Maher, D. C. Joy, M. S. Isaacson, R. H. Geiss, H. L. Fraser).

"X-Ray Absorption Effects in Thin Metal Foils," N. J. Zaluzec, H. L. Fraser, *1st Workshop on Analytical Electron Microscopy,* Cornell University, 1976, p. 118 (eds., J. Silcox, D. M. Maher, D. C. Joy, M. S. Isaacson, R. H. Geiss, H. L. Fraser).

"Microchemical Analysis of Thin Metal Foils," N. J. Zaluzec, H. L. Fraser, *34th Ann. Proc. of EMSA,* Miami, 1976, p. 420 (ed., G. W. Bailey).

"A Modified Stage for X-Ray Analysis in a TEM," N. J. Zaluzec, H. L. Fraser, *J. Phys. E.* 9, 1051 (1976).

"Comments on 'Energy Dispersive X-Ray Measurements of Thin Metal Foils'," N. J. Zaluzec, J. B. Woodhouse, H. L. Fraser, *Scripta Met.* 11, 257 (1977).

"Contamination and Absorption Effects in X-Ray Microchemical Analysis of Thin Metal Foils," N. J. Zaluzec, H. L. Fraser, *8th Int. Conf. on X-Ray Optics and Microanalysis,* Boston, 1977, Science Press (ed., D. Beamans, R. Ogilvie, D. Wittry).

"The Application of DSTEM to Materials Characterization at the University of Illinois," Invited Presentation, N. J. Zaluzec, *Annual Meeting of MRS,* Boston, 1977.

"Optimizing Conditions for X-Ray Microchemical Analysis in Analytical Electron Microscopy," N. J. Zaluzec, *9th Int. Conf. on Electron Microscopy*, 1, 548 (1978), Toronto.

"X-Ray Microanalysis Using an HVEM," N. J. Zaluzec, E. A. Kenik, J. Bentley, *2nd Workshop on Analytical Electron Microscopy*, Cornell University, 1978 (eds., J. Silcox, D. M. Maher, C. D. Joy, M. S. Isaacson, R. H. Geiss, H. L. Fraser).

"Transmission Scanning Electron Diffraction and Microscopy in a TEM/STEM Instrument," R. W. Carpenter, N. J. Zaluzec, *2nd Workshop on Analytical Electron Microscopy*, Cornell University, 1978 (eds., J. Silcox, D. M. Maher, C. D. Joy, M. S. Isaacson, R. H. Geiss, H. L. Fraser).

"On the Effects of Contamination on X-Ray Analysis," N. J. Zaluzec, H. L. Fraser, *2nd Workshop on Analytical Electron Microscopy*, Cornell University, 1978 (eds., J. Silcox, D. M. Maher, C. D. Joy, M. S. Isaacson, R. H. Geiss, H. L. Fraser).

"Gaussian Optics Calculations of the Parameters of a Magnetic Sector Energy Analyzer," N. J. Zaluzec, *2nd Workshop on Analytical Electron Microscopy*, Cornell University, 1978 (eds., J. Silcox, D. M. Maher, C. D. Joy, M. S. Isaacson, R. H. Geiss, H. L. Fraser).

AN ANALYTICAL ELECTRON MICROSCOPE STUDY OF THE OMEGA PHASE TRANSFORMATION IN A ZIRCONIUM-NIOBIUM ALLOY

NESTOR JOHN ZALUZEC, Ph.D.
Department of Metallurgy and Mining Engineering
University of Illinois at Urbana-Champaign, 1979

An *in-situ* study of the as-quenched omega phase transformation in Zr–15% Nb was conducted between the temperatures of 77 and 300°K using analytical electron microscopy. The domain size of the omega regions observed in this investigation was on the order of 30 Å, consistent with previous observations in this system. No alignment of omega domains along <222> directions of the bcc lattice was observed and furthermore *in-situ* thermal cycling experiments failed to produce a long period structure of alternating β and ω phase regions as predicted by one of the most recent theories of this transformation.

During this investigation, several techniques of microstructural analysis were developed, refined, and standardized. Grouped under the general classification of *Analytical Electron Microscopy (AEM)* they provide the experimentalist with a unique tool for the microcharacterization of solids, allowing semiquantitative to quantitative analysis of the morphology, crystallography, elemental composition, and electronic structure of regions as small as 20 Å in diameter. However, these techniques are not by any means without complications, and it was necessary to study the AEM system used in this work so that instrumental artifacts which invalidate the information produced in the microscope environment might be eliminated. Once these factors had been corrected, it was

possible to obtain a wealth of information about the microvolume of material under investigation.

The microanalytical techniques employed during this research include: energy dispersive x-ray spectroscopy (EDS) using both conventional and scanning transmission electron microscopy (CTEM, STEM), transmission scanning electron diffraction (TSED), the stationary diffraction pattern technique, and electron energy loss spectroscopy (ELS) using a dedicated scanning transmission electron microscope (DSTEM).